Controls on Width in Bedrock Rivers

by

Tingan Li

M.Sc. (Geology), China University of Petroleum-Beijing, 2017

B.Sc. (Geology), China University of Petroleum-Beijing, 2014

Thesis Submitted in Partial Fulfillment of the

Requirements for the Degree of

Doctor of Philosophy

in the

Department of Geography

Faculty of Environment

SIMON FRASER UNIVERSITY

Summer 2022

Declaration of Committee

Name:	**Tingan Li**
Degree:	**Doctor of Philosophy**
Title:	**Controls on Width in Bedrock Rivers**
Committee:	**Chair:** **Nicholas Blomley** Professor, Geography
	Jeremy Venditti Supervisor Professor, Geography
	Leonard Sklar Committee Member Adjunct Professor, Environmental Science
	Michael Church Committee Member Professor Emeritus, Geography University of British Columbia
	Gwenn Flowers Committee Member Professor, Earth Sciences
	Brendan Murphy Examiner Assistant Professor, Environmental Science
	Taylor Perron External Examiner Professor, Earth, Atmospheric and Planetary Sciences Massachusetts Institute of Technology

Abstract

One of the fundamental open questions in geomorphology is: What controls the width of bedrock rivers? Landscape evolution models scale width with drainage area, which is used as a proxy for channel discharge, but observations often do not support the width-drainage area scaling. This study explores controls on width in bedrock rivers by 1) developing mechanistic models for lateral erosion by bedload and suspended load impacts, 2) partitioning shear stresses on the bed and banks using model simulations and field observations, and 3) proposing a method for predicting steady-state channel width. A numerical model is developed for lateral erosion by bedload particles that are deflected by bed roughness, which reproduces the erosional patterns observed in the flume experiments. An analytical solution of the numerical model is derived, which shows that lateral erosion rate dominates at high sediment supply when the bed is near fully covered, while vertical erosion dominates at low-to-intermediate sediment supply when the bed is largely exposed to particle impacts. Partitioning bed and wall stresses, which are the key parameters of the lateral erosion model, shows that the observed wall stress is larger than the observed bed stress in many studied canyons due to the complex three-dimensional flow structure and rough bedrock walls in natural bedrock rivers. A lateral erosion model for lateral erosion by bedload and suspended load advected by turbulence eddies is developed to incorporate the role of suspended load and is combined with the model for lateral erosion by bedload impacts. The combined model shows that finer sediment dominates lateral erosion at low sediment supply, but coarser sediment plays an important role at high sediment supply. The model for lateral erosion from bedload impacts is coupled with the vertical erosion model to predict steady channel width at local and drainage basin scale. Results reveal that local channel width is controlled by sediment supply instead of water discharge. Channel width scales sediment supply and caliber at drainage basin scale, which can give the appearance of width-drainage area scaling.

Keywords: bedrock rivers; mechanistic models; lateral erosion; shear stress; channel width

Dedication

To that young kid, after leaving the small village and entering a big world since secondary school, you tried to be cool and fit in, you felt empty inside after the big laughs, and you lost yourself, but you have started to feel happy from your heart, you are proud of yourself and you are pursuing your dream through this journey.

Acknowledgements

I would like to thank my supervisor first, Jeremy Venditti. Jeremy has always been there whenever I need help. I have enjoyed numerous meetings with Jeremy, where we discussed research ideas and tried to solve research problems together. He has given many useful comments of my drafts, which not only improved the quality of my papers but also taught me how to be a good scientist. I appreciate his financial support that allows me to focus on my research, the freedom that allows me to explore all the research possibilities, and his encouragement whenever I feel down or am lost. I am especially grateful for the invitation of Christmas dinner from Jeremy, Andrea and Sofia, which warms my heart as an international student who lives far away from my family.

Leonard Sklar also play an important role in this study. Chatting with Leonard has inspired me to explore new ideas in my thesis and to some extent reshaped my views on publications and doing research. Leonard's detailed comments have been very helpful to lift my papers. Mike Church has provided constructive comments of my drafts and been very helpful in answering my questions about rivers. I am also grateful to Peter Nelson, Mike Lamb, Colin Rennie and Gwenn Flowers for discussions around this work.

I thank the staff in the Geography Department for their help, B-Jae Kelly, John NG, Justin Song, Anke Baker, Erin Rodgers, Joyce Chen, Erin Huddleston and Curtis Platson. I am grateful to colleagues in river dynamics group, Max Hurson, Eric Cao, Kirsti Fairweather, Kyle Kusack, Mike Curran, Lizzie Dingle, Ryan Bradley, Morgan Wright, Dan Murphy, Sahar Karimi, Laurie Solkoski and Ray Kostaschuk, Rebecca Ho, Brendan Murphy and Shawn Chartrand in School of Environmental Science, and my friends, Alex Smith, Shuoge Shen, Aspen Anderson, Kingston Chen, Tina Cao, Xi Zhao and climbing buddies for all their help, encouragement and company.

Finally, I would like to thank my parents for the foundation they provided me with and giving me a happy childhood full of adventures in the mountains, rivers and lakes, my sisters and my brother for always making me feel like the specialist person in the world, my nephews and niece for the joy they bring to me, and my partner Son Tung Nguyen and dog Roscoe for waiting for me at home with well prepared dinner in every late evening when I was tied up with research, going on these crazy backpacking adventures with me, and mostly importantly their love.

Table of Contents

List of Tables

List of Figures

List of Notations

a	coefficient in the Manning-Strickler formula (dimensionless)
A	drainage area (km^2)
A_0	drainage area at the channel head (km^2)
A_l	cross-sectional area of the particle perpendicular to lateral velocity (m^2)
A_c	projected area of grid cell (m^2)
A_p	total projected area of the deflector surface onto the plane that is parallel to the upward motion of saltation particles, following the plane that is parallel to the downward motion of saltation particles (m^2)
A_w	impact area on the wall (m^2)
$A_a(T)$	wetted area at time period T (m^2)
b	drainage area-downstream distance scaling power dependency (dimensionless)
c	volumetric sediment concentration (dimensionless)
c_b	Near-bed volumetric sediment concentration (dimensionless)
C_d	drag deceleration coefficient (ms^{-2})
C_g	gravitational acceleration coefficient (ms^{-2})
C_1	drag parameter (dimensionless)
C_2	parameter for natural sediment (dimensionless)
C_3	parameter for natural sediment (dimensionless)
C_r	restitution coefficient (dimensionless)
C_ϵ	constant originating from the Richardson-Kolmogorov cascade under the assumption that turbulence is at equilibrium
d	distance between two adjacent roughness elements (m)
D	grain size of bedload particles (m)
D_0	grain size at the channel head (m)
D_{84}	84^{th} percentile of the surface bed material
D_r	grain size of roughness elements (m)
D_v	empirical coefficient for vertical variation of lateral flow turbulence intensity

e	the ratio of lateral to vertical erosion rate (dimensionless)
E_a	lateral erosion rate predicted by the advection-abrasion model (ms^{-1})
E_b	bulk erosion rate (m^2s^{-1})
E_c	instantaneous total erosion rate from one cell (m^3s^{-1})
E_{cd}	eroded cross-sectional area per unit time for the deflection-abrasion model (m^2s^{-1})
E_{ca}	eroded cross-sectional area per unit time for the advection-abrasion model (m^2s^{-1})
E_{cb}	eroded cross-section area per unit time within the bedload layer (m^2s^{-1})
E_{cs}	eroded cross-section area per unit time within the suspended load layer (m^2s^{-1})
E_{ct}	total eroded cross-section area per unit time (m^2s^{-1})
E_d	lateral erosion rate predicted by the deflection-abrasion model (ms^{-1})
E_l	lateral erosion rate (ms^{-1})
E_l^*	nondimensional lateral erosion rate (ms^{-1})
E_{lu}	lateral erosion rate for uniformly distributed alluvium (ms^{-1})
E_{lu}^*	nondimensional lateral erosion rate for uniformly distributed alluvium (dimensionless)
E_{lpa}	lateral erosion rate on the adjacent wall for patchy alluvium (ms^{-1})
E_{lpa}^*	nondimensional lateral erosion rate on the adjacent wall for patchy alluvium (dimensionless)
E_{lpo}	lateral erosion rate on the opposite wall for patchy alluvium (ms^{-1})
E_{lpo}^*	nondimensional lateral erosion rate on the opposite wall for patchy alluvium (dimensionless)
E_i	local erosion rate due to individual bedload particles deflected by each deflector of the alluvium (ms^{-1})
E_t	total erosion rate (ms^{-1})
E_v	vertical erosion rate (ms^{-1})
E_v^*	nondimensional vertical erosion rate (ms^{-1})
E_z	lateral erosion rate at elevation z (ms^{-1})
f	total friction factor (dimensionless)

f_a	friction factor for alluvium (dimensionless)
f_b	friction factor for bedrock surface (dimensionless)
f_r	friction factor for roughness element (dimensionless)
F_a	fraction of alluvium (dimensionless)
F_b	fraction of sediment load that is transported as bedload (dimensionless)
F_0	the bedload fraction of the total load at the channel head (dimensionless)
F_r	fraction of roughness elements (dimensionless)
g	gravity acceleration (ms^{-2})
h	water depth
h_c	impact elevation on the roughness element (m)
h_d	height of bedload particle during collision with the deflector (m)
h_{max}	maximum impact height on the wall (m)
h_s	saltation hop height (m)
I	impact rate of particles advected by turbulence eddies ($m^{-2}s^{-1}$)
I_c	impact rate on grid cell (s^{-1})
I_p	impact rate on the upward trajectory plane ($m^{-2}s^{-1}$)
I_w	impact rate on the wall (s^{-1})
$\boldsymbol{i_s}$	incoming saltation velocity vector (ms^{-1})
$\boldsymbol{i_o}$	outgoing saltation velocity vector (ms^{-1})
$\boldsymbol{IL}$	impact position vector (ms^{-1})
$\boldsymbol{IV}$	impact velocity vector (ms^{-1})
k_a	alluvium roughness length scale (m)
k_A	empirical parameter in Hack's law (dimensionless)
k_b	bedrock roughness length scale (m)
k_c	coefficient that describes water and sediment density, threshold of motion and boundary roughness ($m^{3/7}s^{-6/7}$)
k_d	coefficient that links grain size with drainage area (depend on m_d)
k_e	rock erodibility (Pa^{-1})
k_p	measure of river base flow (depends on m_q)

k_r	rock strength parameter (Pa)
k_s	hydraulic roughness length scale (m)
k_t	fraction of time that erosion occurs (dimensionless)
k_v	rock resistance coefficient (dimensionless)
k_w	ratio of width to sediment supply rate (ms/kg)
l	integral length scale (m)
l_s	saltation hop length (m)
l_{sd}	saltation hop length of the downward trajectory (m)
l_{su}	saltation hop length of the upward trajectory (m)
L	length of upward trajectory plane (m)
m_1	coefficient for downstream width variation (dimensionless)
m_2	coefficient for downstream slope variation (dimensionless)
m_d	downstream fining parameter (dimensionless)
m_q	discharge-drainage area scaling power dependency (dimensionless)
m_s	empirical parameter that describes the downstream change of the portion of sediment transported as suspended load (dimensionless)
M	mass of bedload particles (kg)
$\hat{\boldsymbol{n}}$	surface normal vector (dimensionless)
n	empirical coefficient that relates hydraulic roughness to fractions of grain size coarser than the median grain size (dimensionless)
n_x	downstream component of the unit vector $\hat{\boldsymbol{n}}$ (dimensionless)
n_y	lateral component of the unit vector $\hat{\boldsymbol{n}}$ (dimensionless)
n_z	vertical component of the unit vector $\hat{\boldsymbol{n}}$ (dimensionless)
N	number of grids (dimensionless)
N_u	total number of deflectors that contributes to lateral erosion for uniformly distributed alluvium (dimensionless)
$\boldsymbol{p}$	projection of the incoming velocity vector onto the surface normal vector (ms^{-1})
P	the Rouse number (dimensionless)
$P(T)$	wetted perimeter at time period T (m)
q	sediment supply per unit width ($kgm^{-1}s^{-1}$)

q_s	bedload sediment supply per unit width ($kgm^{-1}s^{-1}$)
Q_s	total sediment supply (kgs^{-1})
q_t	transport capacity per unit width ($kgm^{-1}s^{-1}$)
Q_t	total transport capacity (kgs^{-1})
Q_w	water discharge ($m^3\ s^{-1}$)
r	semi-circle radius cut along the roughness element (m)
r'	lateral distance between each slice of the deflector surface and the center of the deflector (m)
r_s	radius of each slice of the deflector surface (m)
R	hydraulic radius (m)
R_b	nondimensional buoyant density (dimensionless)
S	channel slope (dimensionless)
S_t	Stokes number (dimensionless)
t	time (s)
t_l	eddy turnover time (s)
u	instantaneous downstream velocity (ms^{-1})
u^*	shear velocity (ms^{-1})
u_i	downstream impact velocity (ms^{-1})
u_o	outgoing downstream velocity (ms^{-1})
u_s	saltation downstream velocity (ms^{-1})
$u'(z)$	flow velocity at depth z (ms^{-1})
$\bar{u}$	mean flow velocity (ms^{-1})
$\bar{u}(T)$	flow velocity at time period T (ms^{-1})
U	uplift rate (mm/year)
v	instantaneous lateral velocity (ms^{-1})
v_{min}	minimum wall-normal particle velocity limit (ms^{-1})
v'_{min}	minimum wall-normal flow velocity limit (ms^{-1})
v_i	wall-normal impact velocity (ms^{-1})
v_l	lateral component of wall-normal impact velocity (ms^{-1})
v_v	vertical component of wall-normal impact velocity (ms^{-1})
v_o	outgoing wall-normal velocity (ms^{-1})

v_p	impact velocity advected by turbulence eddies (ms^{-1})
v_s	saltation lateral velocity (ms^{-1})
v'	lateral turbulent flow velocity fluctuations (ms^{-1})
V	volume eroded per particle impact advected by turbulence eddies (m^3)
V_p	volume of spherical sediment grains (m^3)
V_l	volume eroded per particle impact (m^3)
w	instantaneous vertical velocity (ms^{-1})
w_0	outgoing vertical velocity (ms^{-1})
w_f	fall velocity (ms^{-1})
w_i	vertical impact velocity (ms^{-1})
w_s	saltation vertical velocity (ms^{-1})
w_b	bottom channel width of a trapezoid channel (m)
$\bar{w}$	mean surface width of a trapezoid channel (m)
W	channel width (m)
x	downstream distance (km)
x_0	unchanneled distance from the drainage divide to the channel head (km)
x_l	downstream impact position (ms^{-1})
y	lateral distance from the wall (m)
y_a	the distance between the furthest deflector and the adjacent wall for patchy alluvium (m)
y_o	the distance between the furthest deflector and the opposite wall for patchy alluvium (m)
y_u	lateral distance between the deflector and the eroded wall for uniformly distributed alluvium (m)
y_l	lateral impact position (m)
y_{max}	maximum lateral distance from the wall (m)
Y	Young's modulus of elasticity ($kgm^{-1}s^{-2}$)
z	vertical distance from the bed (m)
z_0	a function of the boundary roughness (m)
z_l	vertical impact position (m)

z_{lmax}	maximum erosion height on the wall (m)
ρ_s	sediment density (kgm^{-3})
ρ_w	water density (kgm^{-3})
σ_T	rock tensile strength (Pa)
τ	boundary shear stress (Pa)
τ^*	nondimensional form of shear stress τ (dimensionless)
τ_{Tot}	total shear stress (Pa)
τ_{bed}	bed shear stress (Pa)
τ_l	local shear stress (Pa)
τ_{wall}	wall shear stress (Pa)
τ_s	shear stress due to skin friction (Pa)
τ_s^*	nondimensional shear stress due to skin friction (dimensionless)
τ_c^*	critical shields stress for incipient sediment motion (dimensionless)
ΔT	time period (min)
Δt	time step (s)
Δz	vertical interval on the wall (m)
Θ	angle of the upward trajectory plane (°)
β	angle of the downward trajectory plane (°)
α	bank angle (°)
κ	Karman's constant (dimensionless)
η	kinematic viscosity of the fluid (m^2s^{-1})
ξ	empirical coefficient that scales bedrock roughness to grain size (dimensionless)
φ	the ratio of wall stress to bed stress (dimensionless)
Ψ	coefficient describing the portion of particles near the banks that are advected toward the banks (dimensionless)
Ψ_v	coefficient describing the portion of particles near the banks that move downwards (dimensionless)
σ_T	tensile yield strength (Pa)
σ_v	standard deviation of lateral flow velocity fluctuations perpendicular to the banks

ϵ	the rate at which energy transferred from macroscale structures to the microstructures
Υ	dimensionless factor that accounts for differences between the diffusivity of momentum and sediment (dimensionless)
χ	integral relating suspended sediment flux to the parameters of the flow and sediment concentration within the bedload layer (dimensionless)
λ	coefficient of width-drainage area scaling relation (depend on μ)
μ	power of width-drainage area scaling relation (dimensionless)
δ	channel steepness (depend on θ)
θ	channel concavity (dimensionless)

Preface

The research conducted in this thesis was lead by the author, Tingan Li, and the work presented in Chapters 1-7 was conducted with contribution from Professor Jeremy G. Venditti. Professor Michael Church provided early reviews of Chapters 1-4 and discussions of Chapter 5, Professor Leonard S. Sklar provided early reviews of Chapters 2-5, Professor Peter A. Nelson and Colin Rennie provided early reviews of Chapter 4, and Professor Michael P. Lamb provided early reviews of Chapter 5.

Chapter 2 is a reprint from Journal of Geophysical Research: Earth Surface, Li, T., Fuller, T. K., Sklar, L. S., Gran, K.B., & Venditti, J. G. (2020). A mechanistic model for lateral erosion of bedrock channel banks by bedload particle impacts. Journal of Geophysical Research: Earth Surface, 125, e2019JF005509. https://doi.org/10.1029/2019JF005509.

Chapter 3 is a reprint from Journal of Geophysical Research: Earth Surface, Li, T., Venditti, J. G., & Sklar, L.S. (2021). An analytical model for lateral erosion from saltating bedload particle impacts. Journal of Geophysical Research: Earth Surface,126, e2020JF006061. https://doi.org/10.1029/2020JF006061.

Chapter 4 is a reprint from Journal of Geophysical Research: Earth Surface, Li, T., Venditti, J. G., Rennie, C. D., & Nelson, P. A. (2022). Bed and bank stress partitioning in bedrock rivers. Journal of Geophysical Research: Earth Surface, 127, e2021JF006360. https://doi.org/10.1029/2021JF006360.

Chapter 5 is a reprint from Journal of Geophysical Research: Earth Surface, Li, T., Venditti, J. G., Sklar, L.S. & Lamb, M. P. (in review). Lateral erosion of bedrock channel banks by bedload and suspended load.

Chapter 6 will be submitted to Nature under the title “What sets the width and slope of bedrock rivers?” with Li, T., Venditti, J. G., & Sklar, L.S. as the authors.

Chapter 1. Scope and Objectives

The central question of this dissertation is: What controls the width in bedrock rivers? Despite decades of effort, predictions of width in bedrock rivers commonly rely on scaling relations that link width to discharge (Whipple, 2004; Wohl & David, 2008; Rennie et al., 2018; Wright et al., 2022) or metrics of drainage area and slope (stream power) (Finnegan et al., 2005; Wobus et al., 2006; Turowski et al., 2007). These relations allow for large-scale predictions of landscape evolution over geologic time scales, but fail to predict the local width variability because they lump the influence of variables on width into poorly constrained parameters not related to a specific physical mechanism. There are also analytical approaches where width is calculated by iteratively solving equations that describe sediment cover and vertical erosion (Turowski, 2018, 2020). However, the lateral erosion process responsible for eroding banks of bedrock rivers is not represented in existing approaches to width prediction.

The central question is addressed by development of mechanistic models and field observations. The specific objectives of the research are to:

1) Develop a numerical model for lateral erosion by saltating bedload and couple it with the vertical erosion model;

2) Derive an analytical solution of the numerical model and explore the implications for channel width and slope dynamics;

3) Partition bed and wall shear stresses using field observations and the ray-isovel model;

4) Develop a model for lateral erosion by bedload and suspended load that compare the roles of finer and coarser sediments in eroding bedrock riverbanks;

5) Develop a method for predicting local and downstream width and slope variation.

In Chapter 2, a mechanistic model for lateral erosion by bedload particle impacts is developed. The model is tested using experiments by Fuller et al. (2016). The model is then coupled with the Sklar & Dietrich (2004) vertical erosion model to explore the competition between vertical and lateral erosion in bedrock channels.

Chapter 3 derives an analytical solution of the model developed in Chapter 2. The analytical model predicts a nonlinear dependence of lateral erosion rate on sediment supply, shear stress and grain size. The analytical model is applied to a natural bedrock channel, Boulder Creek, CA, to see if the model can reproduce observed width variations caused by a change in sediment supply rate and grain size.

Chapter 4 develops methods for partitioning bed and wall stresses using field observations and the ray-isovel model that predicts the cross-sectional distribution of velocity. Observed bed and wall stresses are calculated for 26 bedrock canyons in the Fraser River, and the results are compared with modelled stresses. A shear stress partitioning framework is proposed to help guide prediction of bed and wall shear stresses in a bedrock river reach.

Chapter 5 develops a mechanistic model for lateral erosion by bedload and suspended load impacts that are advected by turbulent eddies. This model is combined with the bedload deflection model (Chapters 2 & 3) to explore the relative importance of finer and coarser sediments in eroding bedrock channel banks.

Chapter 6 presents a method to predict channel width and slope at steady state, by coupling models for lateral erosion and vertical erosion by bedload impacts. The method is further expanded to explore the downstream variations of width and slope at large scales.

Chapter 7 summarizes the major findings of the thesis.

Chapter 2. A Mechanistic Model for Lateral Erosion of Bedrock Channel Banks by Bedload Particle Impacts

Abstract

Bedrock incision plays a key role in determining the pace of landscape evolution. Much is known about how bedrock rivers incise vertically, but less is known about lateral erosion. Lateral erosion is widely thought to occur when the bed is alluviated, which prevents vertical erosion and deflects the downstream transport of bedload particles into channel walls. Here we develop a model for lateral erosion by bedload particle impacts. The lateral erosion rate is the product of the volume eroded per particle impact and the impact rate. The volume eroded per particle impact is modelled by tracking the motion of bedload particles from collision with roughness elements to impacts on the wall. The impact rate on the wall is calculated from deflection rates on roughness elements. The numerical model further incorporates the co-evolution of wall morphology, shear stress and erosion rate. The model predicts the undercut wall shape observed in physical experiments. The non-dimensional lateral erosion rate is used to explore how lateral erosion varies under different relative sediment supply (ratio of supply to transport capacity) and transport stage conditions. Maximum lateral erosion rates occur at high relative sediment supply rates (~0.7) and moderate transport stages (~10). The competition between lateral and vertical erosion is investigated by coupling the saltation-abrasion vertical erosion model with our lateral erosion model. The results suggest that vertical erosion dominates under near 75% of supply and transport stage conditions, but is outpaced by lateral erosion near the threshold for full bed coverage.

2.1. Introduction

Bedrock river incision sets the pace of landscape evolution in unglaciated landscapes (Willett, 1999; Whipple, 2004). Bedrock rivers are laterally

constrained by rock banks and have intermittently exposed rock beds that incise vertically (Turowski et al., 2008; Meshkova et al., 2012). Bedrock rivers form the lower boundary of hillslopes (Perron et al., 2008) and thus are hard points in the landscape that must be cut through to lower the elevation of the whole landscape (Rennie et al., 2018; Venditti et al., 2019). Incision rates of bedrock rivers are commonly modelled as a function of stream power (Seidl & Dietrich, 1992; Anderson, 1994; Tucker & Slingerland, 1994; Willett, 1999; Hancock & Anderson, 2002) or boundary shear stress parametrized from basin slope-area relations (Howard & Kerby, 1983; Howard, 1994; Moglen & Bras, 1995; Stark, 2006; Tucker & Slingerland, 1996; Whipple & Tucker, 1999; Wobus et al., 2006). These models allow for large-scale predictions of landscape evolution over geologic time scales, but mask physical processes responsible for bedrock river incision. This makes the predictions of these models difficult to evaluate because the actual erosional processes may differ in important ways from the model assumptions. Process-based models are needed to investigate the relative role of controlling variables such as rock strength, grain size, roughness, water discharge and sediment supply and to provide more detailed physical explanations (Whipple et al., 2000; Whipple, 2004; Sklar & Dietrich, 2004, 2006; Nelson & Seminara, 2011; Huda & Small, 2014; Beer & Turowski, 2015; Turowski, 2018).

Vertical erosion processes are well known and several models exist to represent them. Whipple et al. (2000) summarized the processes of vertical incision: abrasion by sediment impacts of bedload or suspended load; plucking from the bed by hydraulic forces; chemical and physical weathering; cavitation; and debris-flow scour. Detailed models of the physics of individual incision processes have been developed to predict bedrock river dynamics, including: saltation abrasion model (Sklar & Dietrich, 2004); total-load abrasion model (Lamb et al., 2008); plucking model based on the block topple-sliding mechanism (Lamb et al., 2015; Larsen & Lamb, 2016); bedload abrasion, macroabrasion and plucking model (Chatanantavet & Parker, 2009); and weathering model (Hancock et al., 2011). These models have been used to predict how vertical incision in

bedrock channels changes in response to changing boundary conditions (Whipple, 2004; Sklar & Dietrich, 2006, 2008; Egholm et al., 2013; Huda & Small, 2014; Larsen & Lamb, 2016).

However, bedrock rivers can also erode laterally, and adjust their width. Undercut walls are evidence of active, local width adjustment (Figure 2.1). Local variations in bedrock river width can induce highly turbulent plunging flow as water enters the narrow part of bedrock rivers, which can in turn promote erosion of the bed and sidewalls by bedload particle impacts (Venditti et al., 2014). Lateral incision has also been observed to be responsible for formation of strath terraces (Fuller et al., 2009), creation of wide valley bottoms (Snyder & Kammer, 2008) and planation of valley bottoms (Cook et al., 2014) at large scales. Therefore, understanding lateral erosion mechanisms is crucial for exploring bedrock width dynamics and its influence on fluvial processes from local (reach) to large scales. In comparison to what is known about vertical erosion, however, comparatively little is known about lateral erosion mechanisms. Previous studies mostly relate the bedrock bank erosion to local conditions, such as flood events (Stark et al., 2010), high alluvial cover (Gilbert, 1877; Shepherd, 1972), meander migration (Finnegan & Dietrich, 2011), weak lithology (Montgomery, 2004; Stark et al., 2010) or bank strength (Limaye & Lamb, 2014). Existing lateral erosion models rely on the stream power law to link stream power or parametrized shear stress to erosion rates with various degrees of sophistication (Hancock & Anderson, 2002; Finnegan et al., 2005; Stark, 2006; Wobus et al., 2006; Turowski et al., 2009; Lague, 2010; Langston & Tucker, 2018; Yanites, 2018; Croissant et al., 2019). Most of these models ignore the influence of sediment supply on lateral erosion by simply scaling the lateral erosion rate with shear stress (e.g. Stark, 2006; Wobus, 2006) or the rate of energy dissipation per unit area of the channel wall created by centripetal acceleration around a bend (Langston & Tucker, 2018). Others have introduced the influence of alluvial cover on limiting lateral erosion in high sediment supply environments (Hancock & Anderson, 2002; Lague, 2010; Yanites, 2018), but did not include a quantitative relation between sediment supply and lateral erosion rate because the

fundemental relation was unknown. Turowski (2020) recently developed a lateral bank erosion model due to bedload particle impacts, deflected by gravel bars. The model does not include the physics of deflections, but rather treats the gravel alternate bars as a source of roughness capable of deflecting particles in an otherwise straight bedrock channel. In the limit of small degrees of cover, this produces decreasing lateral erosion rates with increasing extent of alluvial cover because gravel bars increase their length as the cover gets greater due to the assumption of constant aspect ratio of gravel bars.

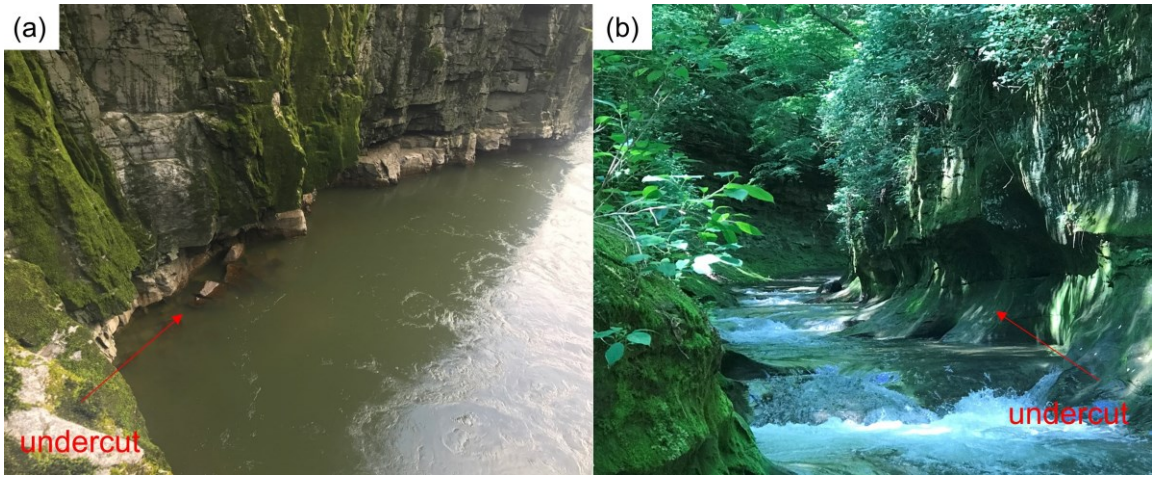

Figure 2.1 Examples of undercut walls in a) Fraser Canyon, British Columbia (~165 m wide; undercut is ~2 m high). b) Fall Creek Gorge, Indiana (~3 m wide; undercut is about 1.5 m high). Undercut walls are highlighted by red arrows.

Gilbert (1877) first suggested that a bedrock channel will incise laterally when the channel bed is covered with transient alluvial deposits. Recent research on lateral erosion has focused on the role of sediment supply on setting the relative rates of vertical and lateral erosion (Turowski et al., 2007; Fuller et al., 2009; Finnegan & Balco, 2013). These investigations suggest lateral erosion dominates in high sediment supply environments, but is limited in low sediment supply environments. None of these studies propose a specific process or mechanism to explain how the high sediment supply drives lateral erosion. Physical experiments have documented channel widening by bedload abrasion (Finnegan et al., 2007; Johnson & Whipple, 2010). Enlighted by these

experiments, Fuller et al. (2016) further explored the erosional mechanism of deflection of saltating bedload particles into the channel wall by roughness elements, and concluded that it is an effective mechanism for lateral erosion into bedrock when the bed is covered by alluvium or composed of large protruded roughness elements. This mechanism explains why lateral erosion dominates in high sediment supply environments where intermittent alluvial cover likely occurs. The downstream transport of bedload particles is deflected by alluvial cover and obtains lateral momentum to erode the wall. In low sediment supply environments, alluvial cover may not be available to deflect bedload particles. This newly identified mechanism for lateral erosion opens the door for a mechanistically-based lateral erosion model.

Here we develop a mechanistic model to explore the potential efficacy of bedload particle impacts as a mechanism of lateral erosion in bedrock channels and test the model using the Fuller et al. (2016) flume experiments, referred to as Fuller Experiments hereafter. Our model only considers the collision between bedload particles and bed roughness elements as the sole process by which saltating bedload particles obtains lateral momentum to erode the wall. We acknowledge that other lateral erosion mechanisms certainly exist, such as plucking (e.g. Beer et al., 2017), but abrasion is the dominant process in massive crystalline rock. We also recognize that channel curvature may enhance particle impacts with the wall (Cook et al., 2014; Turowski, 2018; Langston & Tucker, 2018; Mishra et al., 2018), but have elected not to include that effect to enable a solution to our model. The numerical model is formulated by determining the initial velocity of bedload particles before collision with bed roughness elements from empirical relations (Sklar & Dietrich, 2004), estimating the momentum transfer during collision from a simplified reflection methodology, and tracking the movement of bedload particles from collision with bed roughness elements to impact on the wall using force balance equations. This allows the distribution of lateral erosion on the wall to be calculated. The model is implemented with and without co-evolution of wall morphology, shear stress, and erosion rate to explore how channel change influences the results. After we show how our lateral

erosion model works, we then couple it with the Sklar & Dietrich (2004) vertical incision model to investigate the competition between vertical and lateral erosion with transport stage and relative sediment supply.

2.2. Model Development

The model is based on the saltation-abrasion mechanism of bedrock erosion and the well-known tools and cover effect (Sklar & Dietrich, 2004). Erosion rates are a function of sediment supply, transport stage, grain size and rock strength (Sklar & Dietrich, 2004; 2008). When the bed is relatively free of cover, impacts of saltating bedload particles are capable of detaching rock particles from the surface. Vertical erosion is limited at high sediment supply rates, when the bed is covered. However, when covered, downstream transport of saltating bedload particles can be deflected by particles that make up the alluvial cover (referred to as roughness elements) and directed towards channel walls, which induces lateral erosion. Following the saltation-abrasion vertical erosion model formulation (Sklar & Dietrich, 2004), we assume that the flow, sediment transport and distribution of roughness element are uniform in a bedrock channel with a planar bed and straight walls. We use a hybrid approach to model lateral erosion by impacts of saltating bedload particles. First, we model all the possible individual deflection trajectories from discrete parts of the roughness elements for a given hydraulic condition. Then we apply these results in a continuum model by calculating the deflection rates on each cell of the roughness surface and calculate the resultant erosion rates as a function of locations on the wall.

2.2.1. Initial hydraulic, flow resistance and bedload transport conditions

We assume that bed roughness elements are composed of immobile semi-spheres with diameter of D_r and an areal fraction of F_r, arranged in uniformly distributed rows and columns with a spacing of d (Figure 2.2). The

distance between the wall and the center of the first roughness element is the same as the spacing between two adjacent roughness elements (Figure 2.2), for simplicity. We tested the effects of this simplification by setting distance to the wall from the first defector to $d - D_r$ and found it had a negligible effect on the erosion rates (< 1%). Initial hydraulic conditions are calculated from six input variables: water discharge Q_w, channel width W, channel slope S, areal fraction F_r of roughness elements, roughness element diameter D_r, and bedload particle diameter D. In natural bedrock rivers, D and D_r would be the grain size of the transported bed load and deposited bed material, respectively.

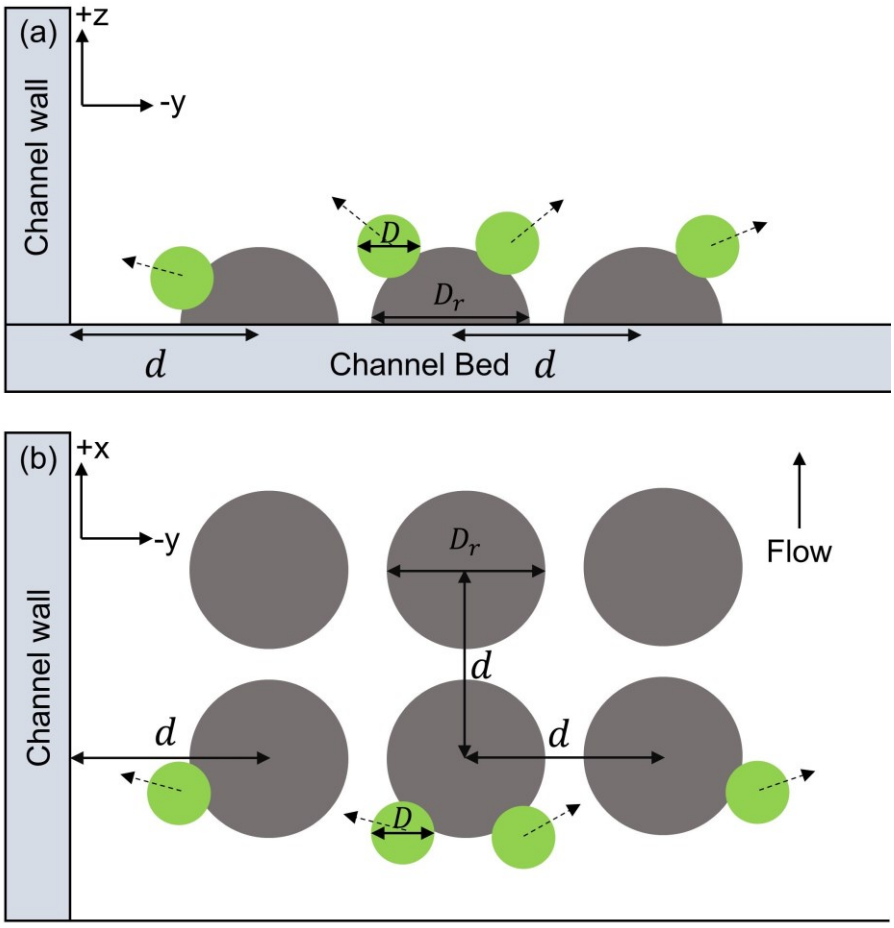

Figure 2.2 a) Cross section view and b) plan view of model setup in an idealized rectangular channel eroded by saltating bedload particles that are deflected by roughness elements distributed on the channel bed. The grey semi-spheres represent roughness elements with diameter of D_r, which are equally distributed in rows and columns with the same distance d. The green spheres represent bedload particles that impact roughness elements. Only one side of the channel walls is shown here and used for simulation, assuming that the walls are symmetrical.

Asumming steady uniform flow, the total shear stress τ is given as

$$\tau = \rho_w g h S \qquad \text{(Equation 2.1)}$$

where ρ_w is water density, g is gravity acceleration, h is water depth.

τ can also be expressed as a function of Darcy-Weisbach hydraulic friction factor f and mean flow velocity $\bar{u}$

$$\tau = \frac{\rho_w f \bar{u}^2}{8} \qquad \text{(Equation 2.2)}$$

In a bedrock channel with roughness elements and transported bedload particles, the flow resistance is derived from the bedrock surface, roughness elements, alluvial cover and channels walls. To calculate the contribution of each source, flow resistance has been weighted by its areal proportion (Tanaka & Izumi, 2013; Inoue et al., 2014; Johnson, 2014; Ferguson et al., 2019). Here we adopted the Johnson (2014) method and assumed the wall flow resistance is negligible, which is valid for a channel that is wide relative to its depth. f can be expressed as a weighted average of the spatial fractions of different sources of flow resistance in the channel

$$f = (1 - F_r - F_a) f_b + F_r f_r + F_a f_a \qquad \text{(Equation 2.3)}$$

where F_a is the fraction of alluvium, f_b, f_r and f_a are friction factors for bedrock, roughness elements, and alluvium, respectively. Because the deposition of alluvial cover was observed to be negligible in the Fuller Experiments, Equation 2.3 for that case can be simplified to

$$f = (1 - F_r) f_b + F_r f_r. \qquad \text{(Equation 2.4)}$$

f_b and f_r can be modelled using appropriate roughness length scales in any preferred flow resistance relation. For simplification, they are used here as fitting parameters to calibrate the model to the Fuller Experiments.

Combining Equations 2.1-2.4 with the continuity equation for a rectangular channel ($Q_w = Wh\bar{u}$), h, $\bar{u}$ and τ can be solved as

$$h = \left(\frac{Q_w}{W}\right)^{2/3} (8gS)^{-1/3}[(1-F_r)f_b + F_r f_r]^{1/3} \quad \text{(Equation 2.5)}$$

$$\bar{u} = \left(\frac{Q_w}{W}\right)^{1/3} (8gS)^{1/3}[(1-F_r)f_b + F_r f_r]^{-1/3} \quad \text{(Equation 2.6)}$$

$$\tau = \frac{\rho_w}{8}\left(\frac{Q_w}{W}\right)^{2/3} (8gS)^{2/3}[(1-F_r)f_b + F_r f_r]^{1/3}. \text{(Equation 2.7)}$$

Assuming the roughness elements cause flow separation and contribute form drag, the shear stress available to transport sediment τ_s can be obtained from replacing f in Equation 2.2 with $(1-F_r)f_b$

$$\tau_s = \frac{\rho_w}{8}\left(\frac{Q_w}{W}\right)^{2/3} (8gS)^{2/3}[(1-F_r)f_b + F_r f_r]^{-2/3}(1-F_r)f_b. \quad \text{(Equation 2.8)}$$

Initial bedload transport conditions, including the saltation hop height h_s, saltation hop length l_s, bedload particle velocity u_s, are estimated from the empirical relations of Sklar & Dietrich (2004)

$$\frac{l_s}{D} = 8.0\left(\frac{\tau_s^*}{\tau_c^*} - 1\right)^{0.88}\left(1 - \left(\frac{u^*}{w_f}\right)^2\right)^{-0.50} \quad \text{(Equation 2.9)}$$

$$\frac{h_s}{D} = 1.44\left(\frac{\tau_s^*}{\tau_c^*} - 1\right)^{0.56} \quad \text{(Equation 2.10)}$$

$$\frac{u_s}{\left(\left(\frac{\rho_s}{\rho_w} - 1\right)gD\right)^{0.5}} = 1.56\left(\frac{\tau_s^*}{\tau_c^*} - 1\right)^{0.56} \quad \text{(Equation 2.11)}$$

where ρ_s is the sediment density, $u^* = \sqrt{ghS}$ is the flow shear velocity, $\tau_s^* = \tau_s/(\rho_s - \rho_w)\, gD$ is the non-dimensional shear stress available for sediment transport, τ_c^* is τ_s^* at the threshold of motion for particle movement, w_f is the particle fall velocity, which is calculated from the empirical method developed by Dietrich (1982), assuming values of Cory shape factor (0.8) and Powers scale

(3.5) typical for natural gravel grains. Auel et al. (2017a, b) recently updated the Sklar & Dietrich (2004) equations, but calibrated hop lengths, heights and velocities to shear stress for supercritical flows with Froude numbers up to 5. The relations notably produce symmetric particle trajectories, which are different from the low velocity, asymmetric trajectories typical of subcritical and transcritical flows we consider here. Application of our model to in supercritical flows may require re-parameterization.

The bed-normal velocity w_s is calculated from the difference between the gravitational acceleration of the particle and deceleration due to drag (Lamb et al., 2008a)

$$w_s = \sqrt{\frac{C_\mathrm{g}}{C_\mathrm{d}}(1 - e^{-2C_2(h_s - h_c)})} \qquad \text{(Equation 2.12)}$$

where $C_\mathrm{g} = (\frac{\rho_s}{\rho_w} - 1)g$ is the gravitational acceleration coefficient, $C_\mathrm{d} = 3C_d D\frac{\rho_w}{\rho_s}$ is the drag deceleration coefficient, C_1 (0.45) is the drag coefficient, h_c is the height above the bed of the point of collision with the roughness element ($h_c = 0$ for collisions with the bed).

2.2.2. Collision between bedload particles and roughness elements

Assuming that the saltating bedload particles have negligible lateral momentum during the normal course of a downstream hop, the saltation lateral velocity v_s before collision is zero. Thus, the incoming saltation velocity vector $\boldsymbol{i_s}$ has two non-zero components

$$\boldsymbol{i_s} = (u_s, 0, w_s). \qquad \text{(Equation 2.13)}$$

During collision with roughness elements in water, bedload particles experience an inelastic rebound that can be modelled by the sum of an elastic and a viscous force (Cundall & Strack, 1979). For simplicity, the elastic response is modelled using a reflection methodology to calculate the outgoing saltation velocity vector after collision with a roughness element as

$$\boldsymbol{i_o} = C_r(\boldsymbol{i_s} - \mathbf{2}\boldsymbol{p}) \qquad \text{(Equation 2.14)}$$

where $\boldsymbol{p}$ is the projection of the incoming particle velocity vector onto the surface normal vector, at the point of collision (defined by the normal vector $\hat{\boldsymbol{n}}$) calculated from

$$\boldsymbol{p} = \left(\frac{\boldsymbol{i_s} \cdot \hat{\boldsymbol{n}}}{\hat{\boldsymbol{n}} \cdot \hat{\boldsymbol{n}}}\right)\hat{\boldsymbol{n}} \qquad \text{(Equation 2.15)}$$

assuming that the tangential force during collision is negligible. The coefficient of restitution (C_r) describes the retention of particle momentum during the collision between bedload particles and roughness elements. We choose a value $C_r = 0.9$ based on experimental observations (Niño et al., 1994; Schmeeckle et al., 2001; Joseph et al., 2001; Joseph & Hunt, 2004), which means that the particle loses $1 - C_r^2 = 19\%$ of its incident kinetic energy during an impact.

The magnitude and direction of $\boldsymbol{i_o} = (u_o, v_o, w_0)$ are controlled by incoming velocity $\boldsymbol{i_s}$ and normal vector $\hat{\boldsymbol{n}}$ at the point of collision (Figure 2.3). Consider a bedload particle that collides near the base of the roughness element, at the roughness element centerline. The magnitude of $\boldsymbol{i_s}$ for this case is maximized because the collision occurs near the bed where w_s is the greatest, which will maximize the magnitude of $\boldsymbol{i_o}$ for given hydraulic conditions. However, the collision will create an $\boldsymbol{i_o}$ for this case that points in the upstream direction with negligible lateral velocity v_o, because $\hat{\boldsymbol{n}}$ is pointing upstream (Figure 2.3). In contrast, when $\hat{\boldsymbol{n}}$ is rotated to 45 degrees relative to the centerline of the roughness element (Figure 2.3), $\boldsymbol{i_o}$ will have a substantial wall-normal velocity component v_o with negligible downstream velocity component u_0. Therefore, to incorporate the variation of $\boldsymbol{i_s}$, $\hat{\boldsymbol{n}}$ and hence $\boldsymbol{i_o}$ at the point of collision with the roughness element, the surface of each roughness element is discretized into N approximately uniform triangular grid cells ($N \approx 2000$ is selected here for a balance of efficiency and accuracy). Within each cell, the potential impact position and impact angle are assumed to be represented the cell centroid, and the outgoing velocity $\boldsymbol{i_o}$ of individual bedload particles is calculated in each grid cell from Equations 2.13-2.15.

Not all cells on the surface of a semi-spherical roughness element are subject to collisions. To estimate which cells will experience collisions, and the impact rate on each grid cell as a function of the bedload flux, we begin by assuming that the trajectory of bedload particles before impacting on the roughness element is composed of two components: upward trajectory and downward trajectory (Sklar & Dietrich, 2004). The upward trajectory has a hop height of h_s and a hop length of l_{su}, and the downward trajectory has a hop height of h_s and a hop length of l_{sd}. Assuming these two trajectories together form a triangle, with a total hop length of l_s and hop height of h_s (Figure 2.4), l_{su} and l_{sd} can be approximated from l_s as (Sklar & Dietrich, 2004)

$$l_{su} = \frac{1}{3} l_s \qquad \text{(Equation 2.16)}$$

$$l_{sd} = \frac{2}{3} l_s \qquad \text{(Equation 2.17).}$$

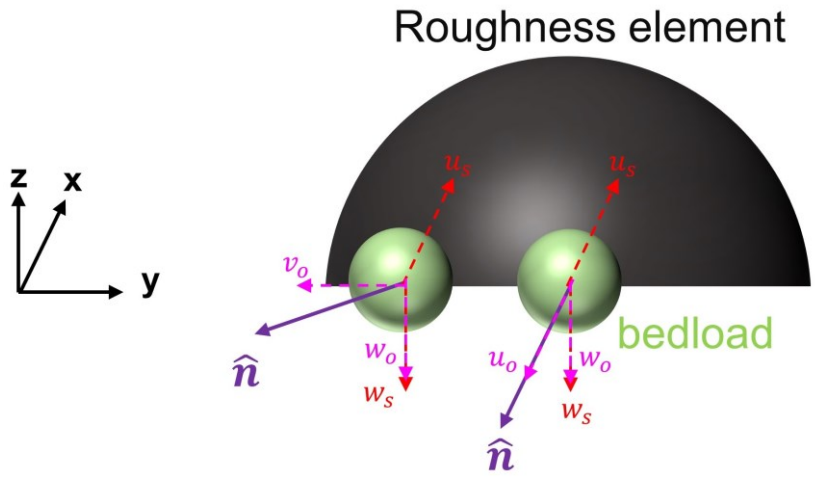

Figure 2.3 Schematic diagram of collision between roughness element (black) and bedload particles (green). The incoming velocity $\boldsymbol{i_s = (u_s, 0, w_s)}$, where $\boldsymbol{u_s}$ is incoming downstream velocity and $\boldsymbol{w_s}$ is incoming vertical velocity. The outgoing velocity $\boldsymbol{i_o = (u_o, v_o, w_o)}$, where $\boldsymbol{u_0}$ is outgoing downstream velocity, $\boldsymbol{v_0}$ is outgoing lateral velocity and $\boldsymbol{w_0}$ is outgoing vertical velocity. Two examples of collision are shown here: collision with the roughness element head resulting in $\boldsymbol{v_o \approx 0}$ and collision with 45 degrees relative to the base of the roughness element head resulting in $\boldsymbol{v_o \gg 0}$.

Three planes are formed by the triangular trajectory of bedload particles: 1) the plane parallel to the upward trajectory; 2) the plane parallel to the

downward trajectory; and 3) the plane parallel to the bed (Figure 2.4). All upward moving particles must move parallel to the first plane and all downward moving particles must cross the first plane. In contrast, only upward moving particles will cross the second plane and all downward moving particles will follow the second plane. The third plane, the channel bed, is where the particles turn around. Our model only incorporates the impacts of downward moving particles on the roughness element surface. The length L of the first plane for intercepting the downward moving particles is

$$L = \sqrt{h_s^2 + l_{su}^2} \qquad \text{(Equation 2.18)}$$

and its angle Θ intersecting with the bed is

$$\Theta = \arctan\frac{h_s}{l_{su}} \qquad \text{(Equation 2.19)}$$

The impact rate, with dimensions of collisions per unit time per unit area on the first plane, can be expressed as

$$I_p = \frac{q_s}{ML} \qquad \text{(Equation 2.20)}$$

where q_s is sediment supply per unit width, and M is the mass of a bedload particle. The area of each grid cell is projected onto the first plane, along a vector parallel to the downward trajectory of bedload particles, to calculate the impact rate on each grid cell. The angle β of the projected direction intersecting with the bed is (Figure 2.4)

$$\beta = \arctan\frac{h_s}{l_{sd}} \qquad \text{(Equation 2.21).}$$

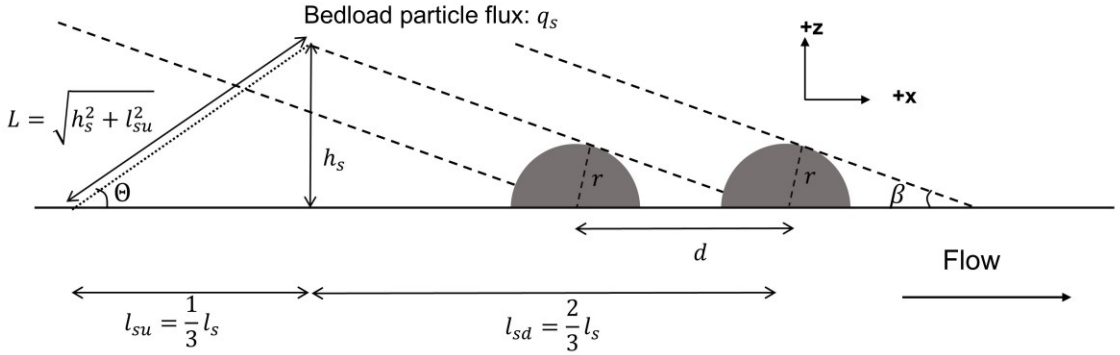

Figure 2.4 Sketch of calculating the impact rate on the roughness element (grey semi-circle). The trajectory for bedload particle flux is simplified as a triangle, formed by upward l_{su} and downward portion l_{sd} of the total hop length l_s and total hop height h_s. Three planes are defined here, including the plane parallel to the upward trajectory (dotted line) intersected with the bed from an angle Θ, the plane parallel to the downward trajectory (dashed line) intersected with the bed from an angle β, and the plane of the bed where the particles turn around (solid line). Each plane is as wide as the channel.

The projected area for each grid cell is defined as A_c. The impact rate on each grid cell of the roughness element surface I_c can hence be expressed as

$$I_c = I_p A_c \qquad \text{(Equation 2.22)}$$

The variation of impact rates I_c is illustrated in Figure 2.5, where the 10 mm roughness element from the Fuller Experiments is used as an example. The center of each grid cell is projected onto a horizontal 2D surface from the plan view (Figure 2.5a) and onto a vertical 2D surface from the along-stream view (Figure 2.5b). There is no impact on most of the downstream facing part of the semi-sphere surface (Figure 2.5a-b) because it is below the tangent point of downward-moving trajectory. Meanwhile, the impact rate is zero near the vertex of the upstream facing part of the roughness element (Figure 2.5a-b), because the impacts here are in the shadow of downward-moving trajectory when the roughness elements are too close to each other (Figure 2.4). The impacts decrease from the center to the edge of the roughness element (Figure 2.5a), due to the decrease of the shadow effect as the radius r of a circle for a longitudinal slice through the sphere reduces to zero at the edge of the roughness. The impact rate also decreases with distance downstream because the impact area A_c goes to zero when the surface cell gets tangential (parallel) to the flux trajectory (Figure 2.5b).

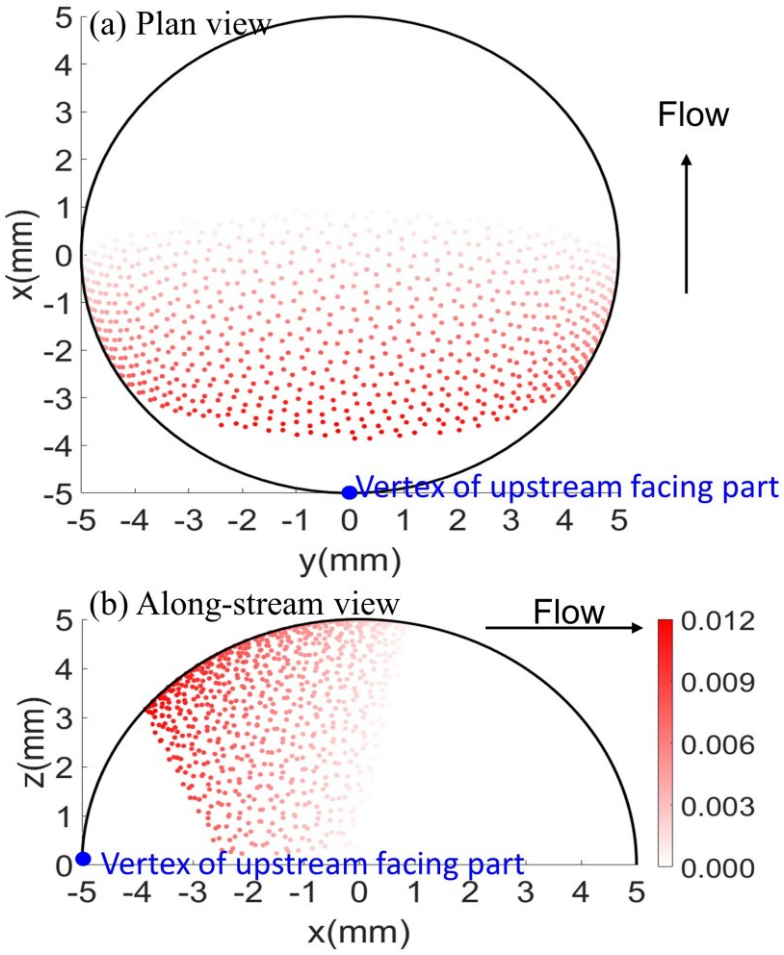

Figure 2.5 a) Plan view and b) along-stream view showing the distribution of impact rates on each grid cell of roughness elements with diameter 10.0 mm using models inputs from the Fuller Experiments. Black lines are the boundary of the roughness elements.

2.2.3. Movement of bedload particles from collision with roughness element to impact on the wall

After collision, the movement of bedload particles is modelled from force balance equations and tracked over each time step Δt. We assume that fluid drag and gravity are the dominant forces affecting instantaneous downstream velocity u, lateral velocity v and vertical velocity w. The change in particle velocities with time are given by

$$-\frac{du}{dt} = C_{\mathrm{d}}(\bar{u} - u'(\mathrm{z}))^2 \qquad \text{(Equation 2.23)}$$

$$-\frac{dv}{dt} = C_{\mathrm{d}} v^2 \qquad \text{(Equation 2.24)}$$

$$-\frac{dw}{dt} = \begin{cases} C_{\mathrm{d}} w^2 + C_{\mathrm{g}} & for\ w > 0 \\ C_{\mathrm{d}} w^2 - C_{\mathrm{g}} & for\ w \leq 0 \end{cases} \qquad \text{(Equation 2.25)}$$

where $u'(z)$ is the downstream flow velocity at height z above the bed. For turbulent boundary layer flow in a channel, $\bar{u}_z$ can be calculated from the law of the wall

$$u'(z) = \frac{u^*}{\kappa} \ln\left(\frac{30z}{k_{\mathrm{s}}}\right) \qquad \text{(Equation 2.26)}$$

where κ is von Karman's constant (~ 0.41), k_{s} is the hydraulic roughness length scale which can be obtained from friction factor f using a general Manning-Strickler formula

$$k_{\mathrm{s}} = h(8f)^3 \qquad \text{(Equation 2.27)}$$

(Johnson, 2014). Equations 2.22-2.25 can be numerically integrated at each time step Δt to solve for the velocity and position of individual bedload particles. The time step used in the simulation is $\Delta t = 10^{-5}$s. Smaller time steps were also tested, which substantially increase the computational time but do not change the results. A minimum wall-normal velocity v_{min} is adopted here to distinguish between impacts that cause erosion and impacts that are viscously damped, which is a function of the particle Stokes number S_t (Davis et al., 1986; Schmeeckle et al., 2001; Joseph & Hunt, 2004):

$$v_{min} = \frac{9 S_t \rho_w \eta}{\rho_s D} \qquad \text{(Equation 2.28)}$$

where η is the kinematic viscosity of the fluid (10^{-6} m^2s^{-1}), and a value of $S_t = 100$ is selected here from Schmeeckle et al. (2001) and Joseph & Hunt (2004). At each time step, a bedload particle may be rebounded by the channel bed or other roughness elements before it impacts on the wall (Figure 2.6). In this situation, the rebounded velocity is simulated using the same method used for the original collision with the roughness element, taking into account that the normal vector for the bed is vertical. The simulation runs until a bedload particle has impacted the wall or its lateral velocity is below the velocity limit v_{min} before

reaching the wall. When bedload particles impact the wall, the impact velocity vector $\boldsymbol{IV} = (u_i, v_i, w_i)$ and impact position vector $\boldsymbol{IL} = (x_l, y_l, z_l)$ are recorded for calculation of lateral erosion rate of different locations on the wall.

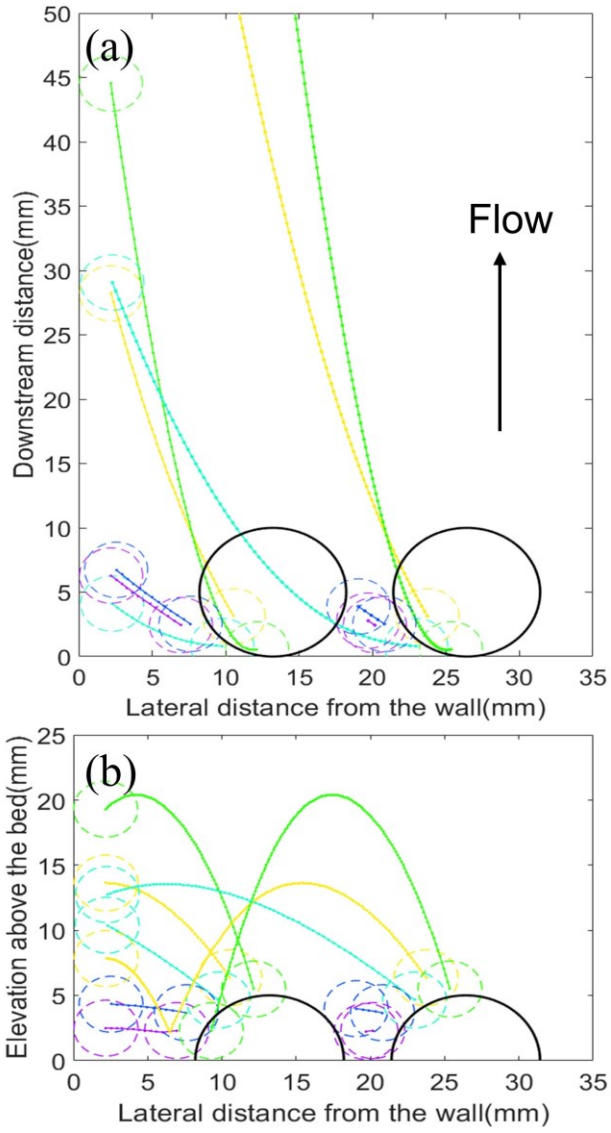

Figure 2.6 a) Plan view and b) downstream view of the deflection trajectories of bedload particles (colorful circles with dashed lines) for a range of deflection positions on the roughness elements (black circles and semi-circles with solid lines). The roughness size is 10.0 mm and the bedload particle size is 4.3 mm. The model inputs are from the Fuller Experiments.

The deflection trajectories of bedload particles vary with the impact positions on the same roughness element. Bedload particles impacting on the

part that is near 45 degrees relative to the centerline of roughness element travel a shorter downstream distance because the particles have larger lateral velocity and can impact on the wall faster (Figure 2.6a). Meanwhile, bedload particles deflected by the higher part of the roughness element can impact higher on the wall due to the higher initial height before deflection and the upward moving velocity after deflection here (Figure 2.6b). When the roughness elements are located further from the wall, more impacts are viscously damped and are rebounded by the bed before impacting on the wall due to more loss of momentum on the way to the wall (Figure 2.6). The bedload particles deflected by the roughness elements further from the wall also impact lower on the wall (Figure 2.6a), and impact further downstream on the wall as it takes longer to impact on the wall (Figure 2.6b).

2.2.4. Calculation of instantaneous lateral erosion rate

Assuming the channel wall is fully exposed to impacts, the erosion rate E_c due to deflections from one grid cell on a roughness element, can be expressed as the product of two terms: the volume eroded per particle impact V_c and the number of particle impacts per unit time I_w (Sklar & Dietrich, 2004)

$$E_c = V_c I_w \qquad \text{(Equation 2.29)}$$

where V_c can be calculated as a function of impact velocity v_i, and rock parameters, including Young's modulus of elasticity of the bedrock Y, dimensionless bedrock strength coefficient k_v, and tensile yield strength σ_T

$$V_c = \frac{\pi \rho_s D^3 v_i^2 Y}{6 k_v \sigma_T^2}\,. \qquad \text{(Equation 2.30)}$$

I_w can be determined from I_c depending on whether the movement of bedload particle deflected by each cell will lead to an impact on the wall or not. If the bedload particle deflected by the roughness element does not impact on the wall, its impact rate on the wall I_w is zero. However, if the bedload particle obtains enough momentum to reach the wall, its impact rate on the wall I_w is the same with that on the roughness element I_c.

$$I_w = \begin{cases} I_c & impacts\ on\ the\ wall \\ 0 & not\ impacts\ on\ the\ wall \end{cases} \qquad \text{(Equation 2.31)}$$

E_c varies with each grid cell on a roughness element (Figure 2.7). Only the 1/4 of the semi-sphere roughness element that faces upstream and toward the near wall contributes to E_c due to the concentration of impacts on the upstream facing part of the semi-sphere (Figure 2.5) and the deflection of bedload particles towards the other side of the channel if they impact on the roughness element surface that faces against the wall (Figure 2.7). E_c is highest at the impact position that has a normal vector $\hat{\boldsymbol{n}}$ facing 45 degrees relative to the longitudinal centerline of the roughness element in planview, and is close to the base of the roughness element, because the rebounded velocity (Figure 2.3) and the impact rate (Figure 2.5) are highest there. E_c decreases with the increasing distance between the roughness element and the wall due to the loss of lateral momentum of bedload particles when travelling towards the wall (Figure 2.7).

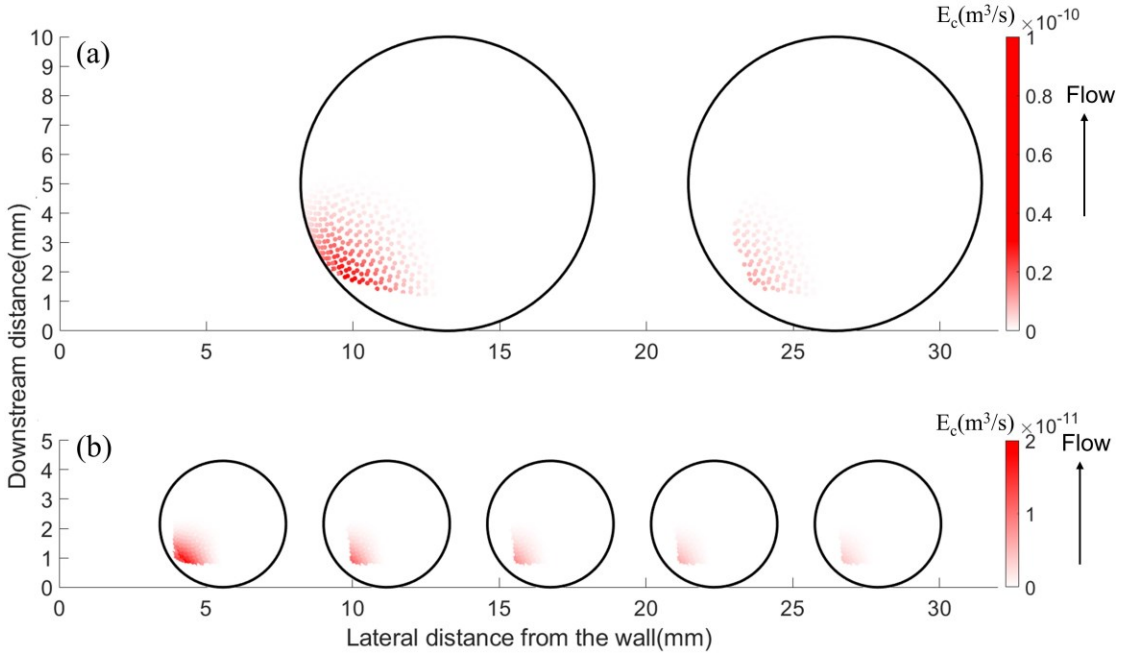

Figure 2.7 Variation of E_c with each grid cell on the a) 10.0 mm roughness elements and b) 4.3 mm roughness elements using inputs from the Fuller et al. (2016) experiments.

Assuming that bed roughness elements are uniformly distributed in rows comprised of equally spaced semi-spheres (Figure 2.2), and transported bedload

is uniformly distributed across the channel, each row of roughness elements deflects same number of bedload particles and causes same amount of lateral wall erosion. Therefore, only one row of roughness elements is used for calculating the instantaneous local lateral erosion rate E_c and the total erosion rate E_t due to the existence of one row of roughness elements is simply the sum of all E_c, the local erosion rates due to individual bedload particles deflected by each grid cell on the roughness elements

$$E_t = \sum E_c \qquad \text{(Equation 2.32)}$$

Because the total erosion rate due to multiple rows of roughness elements is the superposition of the lateral erosion rate due to a single row of roughness elements, and the lateral erosion rate in the longitudinal direction repeats for the downstream distance d between two adjacent rows of roughness elements, the integrated lateral erosion rate within d due to multiple rows of roughness element is equal to E_t. Therefore, the averaged area of material removed from the channel cross section per unit time (referred to as bulk erosion rate E_b) within d can be expressed as

$$E_b = \frac{E_t}{d} \qquad \text{(Equation 2.33)}$$

Bedload particles impact on the wall at many different elevations and downstream locations (Figure 2.6). To calculate the average lateral erosion rate E_z at a given elevation z, the wall is divided into a uniform grid with a vertical interval Δz from the base of the wall to the maximum erosion height on the wall z_{lmax}. A value of $\Delta z = 1$ mm is selected here in accordance with the experimental results of Fuller et al. (2016); and z_{lmax} is obtained from the distribution of the height z_l of all impacts.

The impact area within each grid A_w is

$$A_w = d\Delta z \qquad \text{(Equation 2.34)}$$

The lateral erosion rate E_z for a given elevation range $z + \Delta z$ can be calculated as a sum of the volume eroded by impacts that fall within that elevation range divided by the impact area A_w

$$E_z = \frac{\sum_{z_l \in z} E_c(z_l)}{A_w} \qquad \text{(Equation 2.35).}$$

2.2.5. Co-evolution of lateral erosion rate, wall morphology and shear stress

As the wall is eroded over time, the travel distance, and hence the potential for loss of momentum of bedload particles after collision with the roughness element, increase, resulting in lower instantaneous lateral erosion rates. Meanwhile, the flow becomes wider and shallower as the wall is eroded. This results in a somewhat lower bed shear stress and hence lower lateral erosion rate. In turn, the lower lateral erosion rate will slow down the wall evolution. Without considering the co-evolution between shear stress and lateral erosion rate, the model will exaggerate wall evolution.

To model the effects of wall evolution, we break the simulation into a sequence of time periods, each time period T lasting 10 minutes. Smaller time periods were tested, but did not influence the results. During each period we assume that the flow depth, and thus shear stress, do not change. We average the erosion rate from impacts that occur during that time period. Then for the next period we update the depth and shear stress, and calculate new erosion rates. At beginning of the simulation ($T = 1$), the initial depth and shear stress are obtained from assuming a rectangular cross section from Equations 2.1-2.8. As the wall is eroded over time, the channel cross section and hence the wetted area become irregular. Therefore, $Q_w(T)$ is not simply a product of $W(T)$, $h(T)$, and $\bar{u}(T)$ at the time period $T > 1$. Instead, $Q_w(T)$ needs to calculated from the wetted area $A_a(T)$ over the irregular cross section of the flow

$$Q_w(T) = A_a(T)\bar{u}(T) \qquad \text{(Equation 2.36)}$$

where $A_a(T)$ is a function of flow depth $h(T)$ and needs to be obtained from integrating the flow width over $h(T)$ for a given cross section shape. We assume that the friction factor f is constant over the run period, because the changes of flow depth are relatively small. Combining Equation 2.36 with Equations 2.1-2.6, $h(T)$ can be expressed as

$$h(T) = \frac{1}{8gS}\left(\frac{Q_w}{A_a(T)}\right)^2 [(1-F_r)f_b + F_r f_r] \quad \text{(Equation 2.37)}$$

$h(T)$ and $A_a(T)$ can be solved from Equation 2.40 by starting with an initial guess of $h(T)$, integrating the flow width over $h(T)$ for the current cross section shape to get $A_a(T)$ and iteratively changing the values of $h(T)$ and $A_a(T)$ until these two solutions converge in Equation 2.37. $\bar{u}(T)$ will then be back-calculated from Equation 2.39, and used to get the total shear stress $\tau(T)$ and shear stress available for sediment transport $\tau_s(T)$ from total friction factor $f = (1-F_r)f_b + F_r f_r$ and bedrock friction factor $(1-F_r)f_b$ using Equation 2.2, respectively

$$\tau(T) = \frac{\rho_w[(1-F_r)f_b + F_r f_r]\bar{u}(T)^2}{8} \quad \text{(Equation 2.38)}$$

$$\tau_s(T) = \frac{\rho_w(1-F_r)f_b\bar{u}(T)^2}{8}. \quad \text{(Equation 2.39)}$$

For each period, we calculated the suite of particle deflections and resulting erosion rates, then updated the wall morphology, used it recalculate the water depth, water velocity and shear stress available for sediment transport in the next time period from Equations 2.36-2.39, and updated the particle impact velocity, particle impact rates and erosion rates at next period.

2.3. Results

We assessed model performance using results from laboratory experiments reported by Fuller et al. (2016). Fuller et al. (2016) constructed three experimental channels (referred to as channels C1, C2 and C3), held the water discharge and sediment supply constant for each channel throughout the experiment, but varied the roughness element size over six classes: no

roughness elements (smooth sections); 2.4 mm; 4.3 mm; 7.0 mm; 10.0 mm; and 16.0 mm (roughness sections). Table 2.1 and Table 2.2 list the initial hydraulic and sediment transport conditions in the Fuller Experiments, and the values of parameters used in the model calculations. These experiments provide an ideal test case for our model because the flow depth and thus initial shear stress available for sediment transport was measured, and erosion rates and patterns are measured for the various roughness element sizes. However, the rock tensile strength σ_T which controls the magnitude of the erosion rate was not measured. For the model calculations we use a value of 5.5 × 10^4 Pa for σ_T, which is calibrated from the bulk erosion rate of 10 mm roughness elements ($E_b = 74$ mm2/hr) in Channel C3. This value is reasonable for the weak concrete used in the Fuller Experiments (Sklar & Dietrich, 2001), and is used for predicting the erosion rate and assessing the model performance for other roughness element sizes.

Table 2.1 Initial hydraulic and bedload transport conditions used in the simulation of the Fuller Experiments

Channel section	D_r[b] (mm)	F_r[b]	d[c] (mm)	W[b](1[a]) (mm)	Q_w[b] (×10^{-3}m^3/s)	q_s[b] (kg/m/s)	τ[b](1[a]) (Pa)	τ_g[b](1[a]) (Pa)	f_r[d]	f_b[d]
C2	2.4	0.34	3.65	183	12.9	0.21	18.6	14.9	0.10	0.21
C3	4.3	0.47	5.58	165	12.9	0.19	14	13	0.009	0.10
C1	7.0	0.50	8.75	160	12.7	0.19	12	11.6	0.002	0.07
C2[e]	10.0	0.51	13.2	181	12.9	0.21	18.3	9.2	0.16	0.16
C2	16.0	0.56	19.5	183	12.9	0.21	26.4	8	0.61	0.34

[a] 1 indicates the initial conditions, prior to wall evolution.

[b] directly from Fuller et al. (2016).

[c] calculated from F_r by Fuller et al. (2016) assuming the roughness elements are uniformly distributed.

[d] calibrated from τ and τ_s by Fuller et al. (2016).

[e] 10.0 mm roughness elements are located both in C2 and C3 by Fuller et al. (2016), the one in C3 is used for calibration of σ_T and the one in C2 is used for model performance.

Table 2.2 Parameters used in simulation of the Fuller Experiments

Variable	Value
Bedload particle size D (mm)	4.3 [a]
Channel slope S	0.025 [a]
Critical Shields stress τ_c^*	0.045 [b]
Water density ρ_w (kg/m^3)	1000 [b]
Sediment density ρ_s (kg/m^3)	2650 [b]
Rock elastic modulus Y (Pa)	5×10^{10} [c]
Restitution coefficient C_r	0.9 [b]
Dimensionless rock resistance parameter k_v	10^6 [c]
Rock tensile strength σ_T (Pa)	5.5×10^4 [d]
Time period ΔT (min)	10 [b]
Time step Δt (s)	10^{-5} [b]

[a] From Fuller et al. (2016).

[b] Assumed.

[c] From Sklar and Dietrich (2004).

[d] From calibration with the 10 mm roughness element in C3 by Fuller et al. (2016).

2.3.1. Model performance

We assessed three aspects of the model performance when comparing to the Fuller Experiments: 1) shape of the eroded profile, 2) peak erosion and 3) bulk (integrated) cross-section erosion rate. Figure 2.8 shows the erosion rates measured in the Fuller Experiments. An undercut wall morphology occurred, falling within a range of 25-30 mm above the bed for all roughness sections.

Lateral erosion was concentrated in the lower half of the undercut (5 mm to 10 mm above the bed) and decreased progressively up to the maximum height of erosion. The peak erosion was similar for each roughness section, occurring between a height of 0 mm and 5 mm over 2.15 hr.

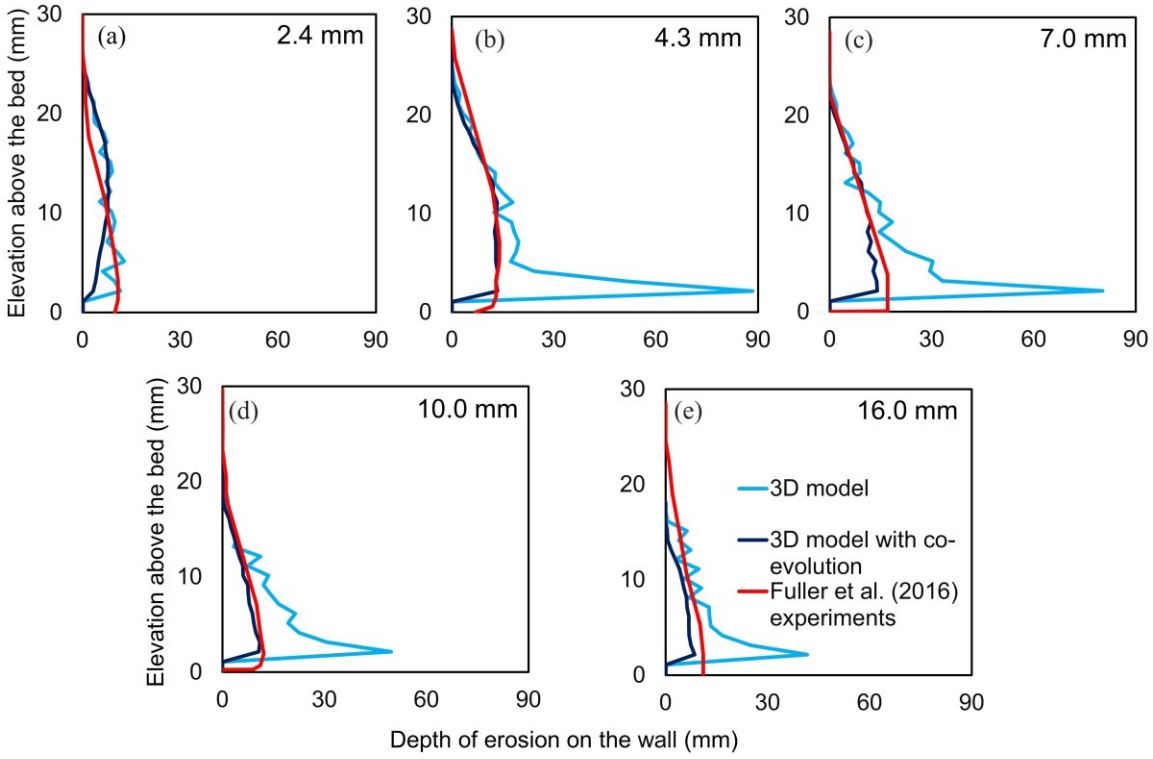

Figure 2.8 Comparison of modelled cross section shape and peak erosion rate to the Fuller et al. (2016) experiments for a) 2.4 mm, b) 4.3 mm, c) 7.0 mm, d) 10.0 mm and e) 16.0 mm roughness sections.

The model without co-evolving the shear stress, wall morphology and erosion rate captures the concentration of erosion in the lower half of the wall observed in the Fuller Experiments (Figure 2.8). However, it overpredicts the peak erosion by 3 to 5 times, except the 2.4 mm roughness element where the measured peak erosion is slightly larger (~ 10%). The lateral erosion concentrates in a smaller zone near the bottom of the wall (below 5 mm above the bed), while the Fuller Experiments show a wider concentration zone of erosion spreading from the base of the wall to 10 mm above the bed. The erosion below the radius of bedload particles (4.3 mm) is under-predicted by the model compared with the substantial undercut on the wall observed in the Fuller

Experiments (Figure 2.8) due to the assumption of spherical bedload particles, which cannot impact on the wall below their radius.

The Fuller Experiments produced a roughly parabolic relation between the roughness element size and integrated cross-section erosion (Figure 2.9), which increases with roughness size below 4.3 mm, peaks at 4.3 mm, and then gradually decreases with larger roughness element sizes. This relation results from a trade-off between more frequent particle deflections and less shear stress available for sediment transport due to an increase in form drag when the roughness elements get larger (Fuller et al., 2016). Although the model captures this parabolic relation observed in the Fuller Experiments, it overpredicts the erosion for all roughness sections by 1.2 to 2 times (Figure 2.9).

The deviation in the erosion profile and peak erosion rate between the model predictions and the Fuller Experiments can occur because changes in wall morphology cause a decline in shear stress applied to the bed. As the wall is eroded over time, the shear stress drops and the travel distance for individual particles increases, resulting in a lower erosion rate over time. We explored the hypothesis that shear stress needs to co-evolve with morphology to accurately predict erosion rate by dividing the model run into 10 minute periods. Figure 2.10 shows the decline in mean velocity and shear stress that occurs due to the increase in cross-sectional area as the wall is undercut and the channel is widen. The change in cross-sectional area, velocity, and shear stress is subtle. Shear stress declines most over the first time period (10 min) but barely changes for the rest of the time, because the erosion rate is largest in that first time period, when the bedload particle travel distance is smallest. The overall decline in shear stress is ~10%, because the changes in wall morphology are relatively small. Only the bottom of the wall is eroded and the maximum eroded length is only ~ 10% of the total river width. Our assumption of constant friction factor f may also slow down the change of shear stress.

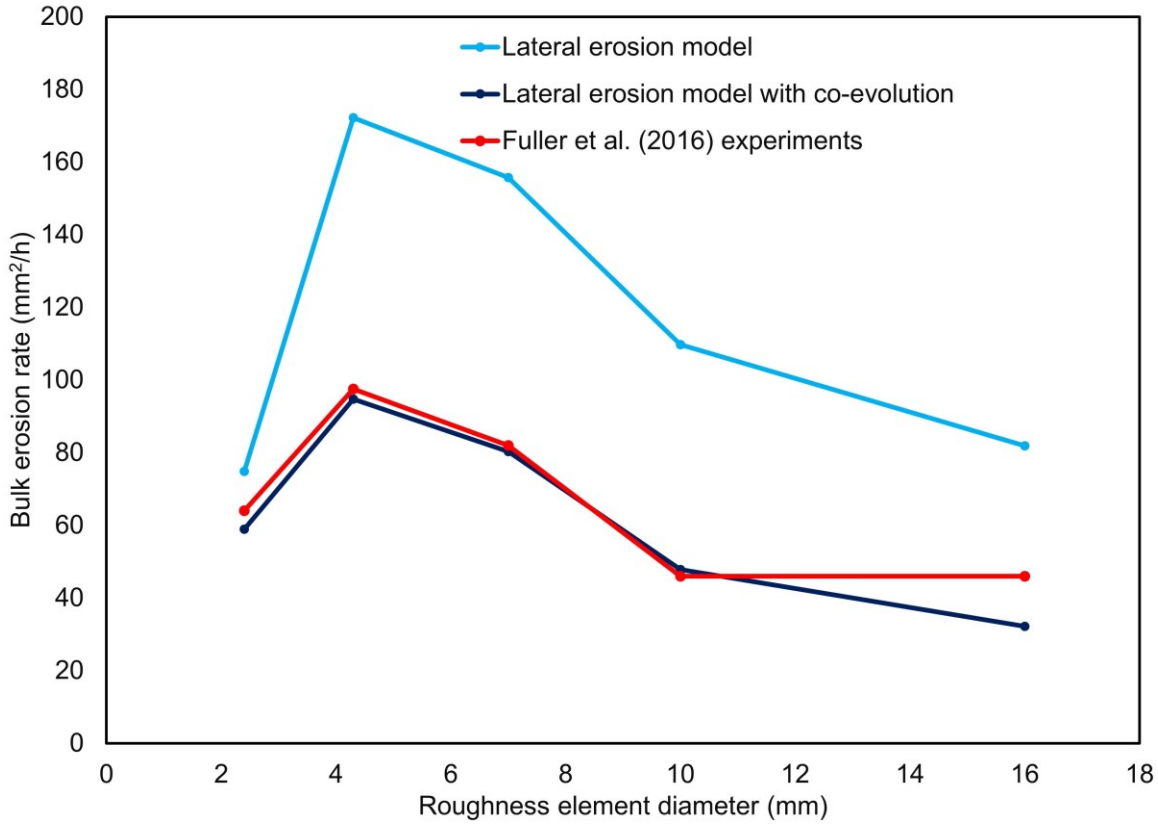

Figure 2.9 Comparison of the total (integrated) cross-section erosion between model predictions and the Fuller Experiments for 2.4 mm, 4.3 mm, 7.0 mm, 10.0 mm and 16.0 mm roughness sections.

The model, when coupled with wall evolution, reproduces both the magnitude of erosion and the undercut wall shape that were observed in the Fuller Experiments well (Figure 2.8). The simulated erosion concentrates in the lower half of the erosion zone and tapers off with increasing height on the walls. The predicted peak erosion depth on the wall generally ranges from 8 mm to 15 mm for all roughness sections, as in the experiments. However, the peak erosion is slightly less than that in the experiments, by ~ 2 mm over the total time period. We suspect this is because we neglected the influence of turbulence on lateral bedload particle deflection into the wall. The Fuller Experiments with a planar bed and no deflectors had a wall erosion depth of ~2 mm over the 2.15 hr run duration (See Figure 2.6d by Fuller et al., 2016), while the wall cannot be eroded without deflectors in our model. The model with evolution of the wall and shear stress also successfully reproduces the parabolic relation between the roughness

element size and integrated cross-section erosion, and the magnitude of erosion over all roughness sections (Figure 2.9).

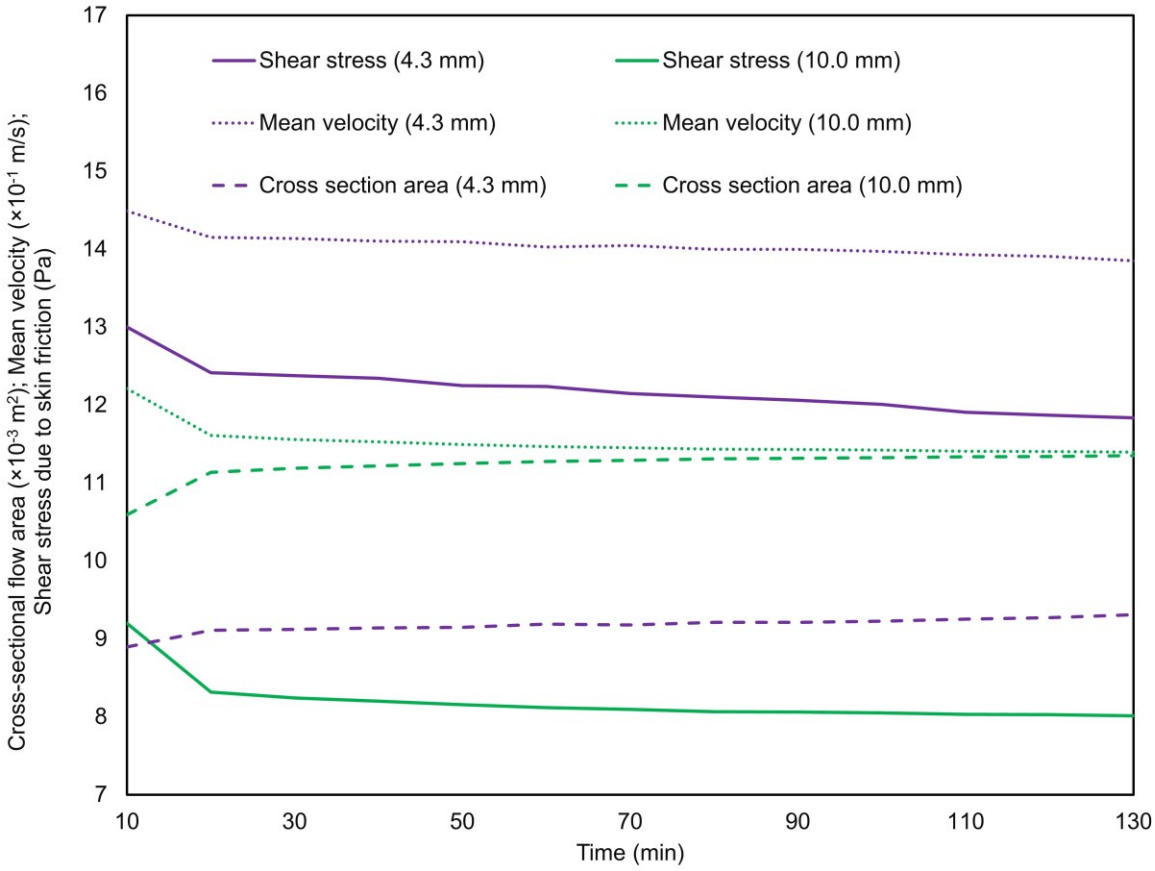

Figure 2.10 Cross section area of flow, mean velocity and shear stress evolution for 4.3 mm and 10.0 mm roughness element.

The model is suitable for predicting the instantaneous lateral erosion rate on the wall. To successfully predict the change of wall morphology over time, however, the model needs to be coupled with co-evolution of shear stress, wall morphology and lateral erosion rate.

2.3.2. Evolution of instantaneous lateral erosion rate and wall morphology

The modelled evolution of erosion rate and wall morphology is similar for all channels in the Fuller Experiments. Representative profiles, for the 4.3 and 10 mm roughness elements, of lateral erosion rate and wall morphology evolution

through time are obtained from our model and shown in Figure 2.11 and Figure 2.12, respectively. The instantaneous erosion rate declines over time (Figure 2.11). The erosion rate is roughly 10 times lower in the final time period compared to the initial time period. As the wall is eroded over time, the shear stress declines with the mean flow velocity (Figure 2.9), which leads to a lower erosion rate by decreasing the impact velocity on the wall in later time periods. However, the shear stress at the end of the time period is ~ 90 % of the initial shear stress (Figure 2.9), indicating the influence of the decreasing shear stress on erosion rate is almost negligible over the time period here. The decreasing erosion rate over time is largely due to the longer travel distance from deflection on the roughness element to impact on the wall as the wall is eroded over time (Figure 2.12). The erosion rates do not decline to zero over the 2.15 hr model runs, which means the wall can still be eroded if the model continues to run (Figure 2.12).

At the beginning of the time period, the erosion rate is roughly 10 times smaller in the upper half of the erosion zone, compared to its lower half (Figure 2.11). The erosion rate decreases in the lower half of the erosion zone because the undercutting makes the wall further from the roughness elements. In the upper erosion zone, the lower rates of erosion continue because the wall is not as far from the roughness elements at the end of the experimental time. At the end of the time period, the erosion rate in the upper and lower halves of the erosion zone are similar (Figure 2.11). The combined effect of this vertical variation through time is a uniform erosion pattern on the wall over the 2.15 hr simulation time (Figure 2.12).

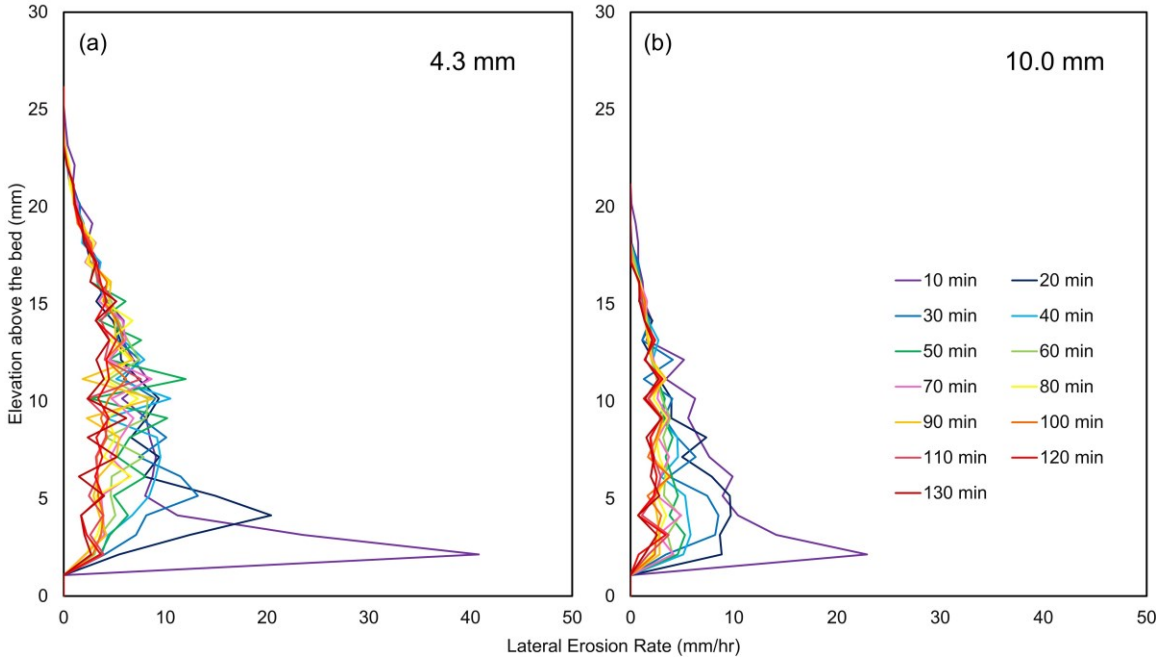

Figure 2.11 Evolution of instantaneous lateral erosion rate on the wall for a) 4.3 mm and b) 10.0 mm roughness sections over 2.15 hr.

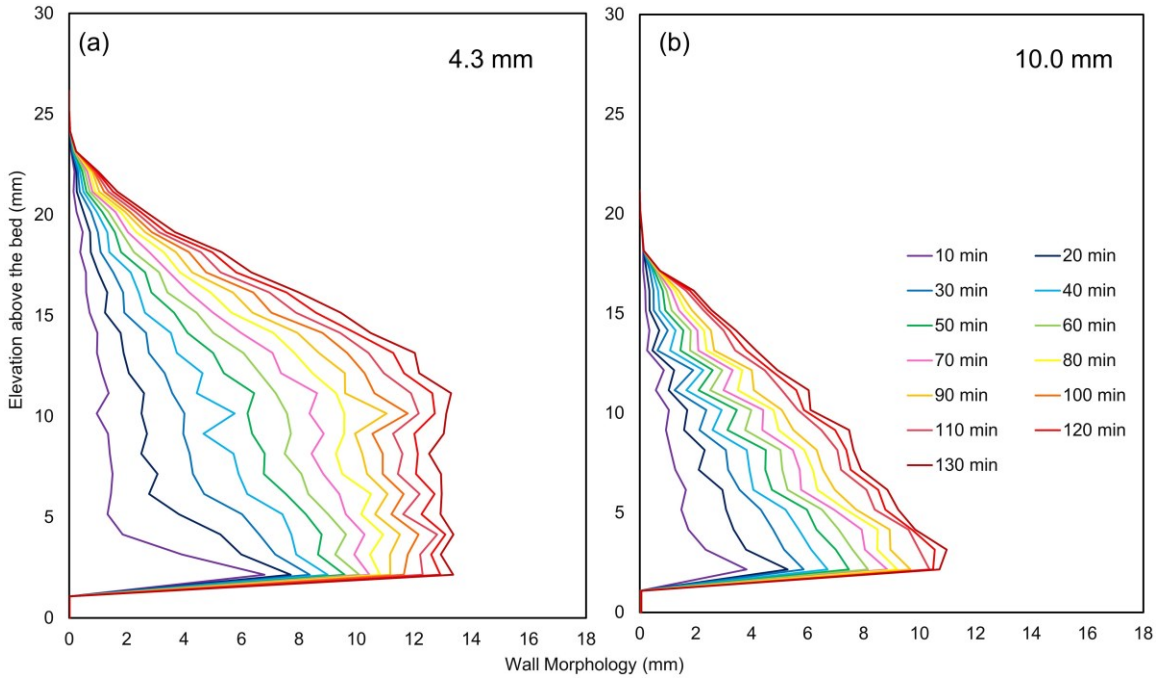

Figure 2.12 Evolution of wall morphology for a) 4.3 mm and b) 10.0 mm roughness sections over 2.15 hr.

The elevation of the peak erosion rate on the wall gets higher from ~2.5 mm to ~8 mm above the bed (Figure 2.11). Initially, the maximum erosion rate is

mostly created by impacts of downward moving bedload particles, which concentrates in a zone near the base of the wall. As the wall is eroded over time, however, the corner between the bed and the wall is protected as it has been undercut. Instead, more bedload particles will either impact higher on the wall or impact on the bed, obtain upward momentum and bounce up on the wall. The elevated position of the peak erosion rate on the wall elevates the concentration of erosion zone on the wall (Figure 2.12).

2.4. Coupled Lateral and Vertical Erosion Model

Both field observations (Hartshorn et al., 2002; Turowski et al., 2008b; Fuller et al., 2009; Finnegan & Balco, 2013) and laboratory experiments (Shepherd, 1972; Finnegan et al., 2007; Johnson & Whipple, 2010) have shown that low sediment supply rates promote vertical erosion and high sediment supply rates promote lateral erosion. Vertical erosion is relatively high when bare exposed bedrock is exposed to sediment impact, but relatively low when the bed is protected by the alluvial cover. Lateral erosion is thought to be high when the bed is alluviated and able to deflect bedload particles into the wall (Gilbert, 1877; Shepherd, 1972; Finnegan et al., 2007; Johnson & Whipple, 2010; Fuller et al., 2016). However, studies of the competition between lateral and vertical erosion for sediment-flux-driven incision remain qualitative.

Our lateral erosion model replicates the essential lateral erosion patterns that were observed in the Fuller Experiments by explicitly accounting for bedrock erosion from bedload particle impacts. We couple the lateral erosion model with a vertical erosion model to quantify the changes in vertical and lateral erosion due to impacts from bedload particles for a range of hydraulic and sediment transport conditions. We generalize the lateral erosion model by treating the roughness elements as alluvial cover that has the same grain size as the bedload particles ($D_r = D$) and use a nondimensional form of the model to show that for a given grain size the full model behavior collapses to a unique functional surface in the parameter space defined by two nondimensional quantities: the

relative sediment supply (q_s/q_t) and the transport stage (τ_s^*/τ_c^*). We then combine the lateral erosion model with the Sklar & Dietrich (2004) vertical erosion model and quantify the competition between lateral and vertical erosion by looking at the ratio of lateral to vertical erosion rate as a function of relative sediment supply (q_s/q_t) and the transport stage (τ_s^*/τ_c^*).

2.4.1. Nondimensional framework of coupled numerical model

The nondimensional framework for the lateral erosion model is intended to explore the variation of instantaneous lateral erosion rate for the given hydraulic and transport conditions, rather than the co-evolution of lateral erosion rate, wall morphology and shear stress over time. We start by determining the size and distribution of roughness elements on the bed. Assuming the alluvial cover provides the only roughness elements capable of deflecting bedload particles, and has the same size as the bedload particles ($D_r = D$), the fraction of roughness elements F_r increases with sediment supply rate and can be calculated from the relative sediment supply q_s/q_t using the method proposed by Sklar & Dietrich (2004)

$$F_r = \frac{q_s}{q_t} \qquad \text{(Equation 2.40)}$$

where the fraction of roughness elements (alluvial cover). F_r is assumed to be a linear function of relative sediment supply. Turowski et al., (2007) developed an exponential formula for F_r, and Turowski & Hodge (2017) built a probabilistic framework for the description of the cover effect that contained the linear and exponential models as special cases. For simplicity and consistency with the Sklar & Dietrich (2004) vertical erosion model we elected to use the linear model.

The transport capacity q_t can be estimated from the Fernandez Luque & Van Beek (1976) bedload sediment transport relation

$$q_t = 5.7\rho_s(R_b g D^3)^{0.5}(\tau_s^* - \tau_c^*)^{1.5} \qquad \text{(Equation 2.41)}$$

where $R_b = \rho_s/\rho_w - 1$ is nondimensional buoyant density. Assuming the alluvial cover is uniformly distributed on the bed, the distance between two adjacent roughness elements d is expressed as

$$d = \frac{D}{F_r} \qquad \text{(Equation 2.42)}$$

Substituting Equation 2.40 into Equation 2.42, d can be obtained from the given grain size D and relative sediment supply rate q_s/q_t

$$d = D\frac{q_t}{q_s} \qquad \text{(Equation 2.43)}$$

We then determine the initial saltation trajectories and deflection trajectories from discrete roughness elements from Equations 2.9-2.15, for a given transport stage τ_s^*/τ_c^* and grain size D. These results are then applied in a continuum model by calculating the deflection rates I_c on each cell of the roughness surface from Equation 2.16-2.22, the impact rate I_w on the wall from I_c, the impact velocities v_i and positions on the wall from Equation 2.23-2.25 and the resultant total erosion rates E_t for all impact locations on the wall from combining Equations 2.29-2.32 for the given rock parameters (k_v, σ_T and Y), relative sediment supply rate q_s/q_t, transport stage τ_s^*/τ_c^* and grain size D

$$E_t = \sum \frac{\pi\rho_s D^3 v_i^2 Y}{6k_v\sigma_T^2} I_w. \qquad \text{(Equation 2.44)}$$

The downstream velocity after deflection in Equation 2.23 is assumed to be constant here for simplification, without considering the variation of deflection trajectories in the longitudinal direction. To account for the transition from bedload to suspension that is equivalent to a particle taking a hop of infinite length, Sklar & Dietrich (2004) assume that the impact rate on the bed and the impact velocity become negligible as u^* approaches w_f (see their Equation 2.21 and 22). When l_s becomes infinite in our lateral erosion model, the impact velocity on the bed w_s (Equation 2.12) before deflection, and hence the impact velocity on the wall v_i (Equation 2.30) monotonically increases with higher transport stage. This is problematic because the lateral erosion rate should

decline as the transport stage approaches the suspension threshold. To keep the lateral erosion model consistent with the Sklar & Dietrich (2004) vertical erosion model, v_i is set to be negligible by multiplying it with $(1-(u^*/w_f)^2)^{0.5}$ in Equation 2.44 as u^* approaches w_f and rearranging Equation 2.44

$$E_t = \frac{\pi \rho_s D^3 Y}{6 k_v \sigma_T^2}(1-(u^*/w_f)^2)\sum(v_i^2 I_w). \quad \text{(Equation 2.45)}$$

To evaluate the average lateral erosion rate E_l on the wall, E_t is averaged over the maximum impact elevation on the wall z_{lmax} which is obtained from the distribution of z_l of all deflection trajectories on the wall

$$E_l = \frac{\pi \rho_s D^3 Y}{6 k_v \sigma_T^2}\frac{(1-(u^*/w_f)^2)}{dz_{lmax}}\sum(v_i^2 I_w) \quad \text{(Equation 2.46)}$$

The variable u^*/w_f is a function of transport stage τ_s^*/τ_c^* for a given grain size D, so E_l is a function of four variables, including rock parameters (σ_T and Y), relative sediment supply rate q_s/q_t, transport stage τ_g^*/τ_c^* and grain size D. The influence of rock parameters (σ_T and Y) in Equation 2.46 can be erased when E_l is non-dimensionalized as (Sklar & Dietrich, 2004)

$$E_l^* = \frac{E_l \sigma_T^2}{\rho_s Y (gD)^{1.5}} = \frac{\pi (D/g)^{1.5}}{6 k_v}\frac{(1-(u^*/w_f)^2)}{dz_{lmax}}\sum(v_i^2 I_w) \quad \text{(Equation 2.47)}$$

Therefore, E_l^* can be considered as a function of just two nondimensional quantities, the relative sediment supply q_s/q_t and the transport stage τ_s^*/τ_c^* for a constant grain size D. Meanwhile, an analytical solution for the non-dimensional vertical erosion rate E_v^* has been proposed to be a function of q_s/q_t and τ_s^*/τ_c^* by Sklar & Dietrich (2004)

$$E_v^* = \frac{E_v \sigma_T^2}{\rho_s Y (gD)^{1.5}} = \frac{0.046(R_b \tau_c^*)^{1.5}}{k_v}\frac{q_s}{q_t}(1-\frac{q_s}{q_t})(\frac{\tau_s^*}{\tau_c^*}-1)(1-(\frac{u^*}{w_f})^2)^{1.5} \quad \text{(Equation 2.48)}$$

Vertical and lateral erosion can be coupled from the ratio e

$$e = \frac{E_l^*}{E_v^*} \quad \text{(Equation 2.49)}$$

because both erosion rates can be related to two variables q_S/q_t and τ_s^*/τ_c^* for a given D.

2.4.2. Competition between vertical and lateral erosion

In order to explore the competition between vertical and lateral erosion with varied q_S/q_t and τ_s^*/τ_c^* , we assume that channel erosion is disconnected from the hillslopes. The most direct analogue for the coupled model here is a bedrock canyon or gorge that is deeply incised into a river valley and largely disconnected from the hillslopes. In order to implement lateral and vertical erosion in a coupled format, we must specify various parameters, including the grain-size of transported material, transport thresholds and various sediment, rock and water properties. For convenience, we use values reported by Sklar & Dietrich (2004) for the South Fork Eel River in Northern California (Table 2.3).

Table 2.3 Reference site and the model parameter values used as inputs for vertical, lateral and coupled erosion models.

Variable	Value
Bedload particle size D (m)	0.060 [a]
Channel width W (m)	18.0 [a]
Critical Shields stress τ_c^*	0.045 [b]
Water density ρ_w(kg/m^3)	1000 [b]
Sediment density ρ_s (kg/m^3)	2650 [b]
Rock elastic modulus Y (Pa)	5×10^{10} [a]
Dimensionless rock resistance parameter k_v	10^6 [a]
Rock tensile strength σ_T (Pa)	7×10^6 [a]

[a] From Sklar and Dietrich (2004).

[b] Assumed.

The first step in exploring the competition between vertical and lateral erosion involved calculating how E_v^* varies with q_s/q_t and τ_s^*/τ_c^* for the grain size $\mathrm{D} = 0.06$ m at the reference site, using the Sklar & Dietrich (2004) model. E_v^* has an analytical solution for q_s/q_t and τ_s^*/τ_c^*, so we can simply determine E_v^* for each combination of q_s/q_t and τ_g^*/τ_c^* from Equation 2.45. Figure 2.13 shows that E_v^* collapses to a unique functional surface in the parameter space created by q_s/q_t and τ_s^*/τ_c^*. As in Sklar & Dietrich (2004), E_v^* goes to zero at the threshold of motion and suspension along the τ_s^*/τ_c^* axis, and the threshold of full cover and no cover along the q_s/q_t axis. The decline in erosion rate at the threshold for suspension is adopted for simplicity here, but we recognize that this is not strictly correct and that there is some reduced bedrock erosion beyond the suspension threshold (Lamb et al., 2008a; Scheingross et al., 2014). E_v^* peaks at the intermediate transport stages (Figure 2.14a) where the growth in the impact energy is balanced by a decline in the impact frequency as the saltation hop length increases with shear stress, and at moderate relative sediment supply (Figure 2.14b), where the growth in impact rate is balanced by the reduction in the extent of bedrock exposure with increasing sediment supply.

The second step in examining the competition between vertical and lateral erosion was to explore how E_l^* varies with q_s/q_t and τ_s^*/τ_c^* for the grain size $\mathrm{D} = 0.06$ m at the reference site. We varied τ_s^*/τ_c^* from 1 to 22, and for each value of τ_s^*/τ_c^* calculated the initial saltation trajectories (Equations 2.9-2.12) before deflection by roughness elements and the transport capacity q_t (Equation 2.38). We also varied q_s/q_t from 0 to 1, and for each value of q_s/q_t calculated the distance between two adjacent roughness elements d (Equation 2.40). For each combination of q_s/q_t and τ_s^*/τ_c^* , we calculated the sediment supply rate q_s (Equation 2.37) and used the deflection model to get all the possible individual deflection trajectories from discrete parts of the roughness elements (Equations 2.13-2.15). We then applied these results in the continuum model by calculating the deflection rates on each cell of the roughness surface (Equation 2.16-2.22), the maximum erosion height z_{lmax} (Equation 2.23-2.25), and the resultant E_l

(Equation 2.43) and E_l^* (Equation 2.44). Using this nondimensional framework, the lateral erosion model also collapses to the unique functional surface in the parameter space defined by q_s/q_t and τ_s^*/τ_c^* (Figure 2.15).

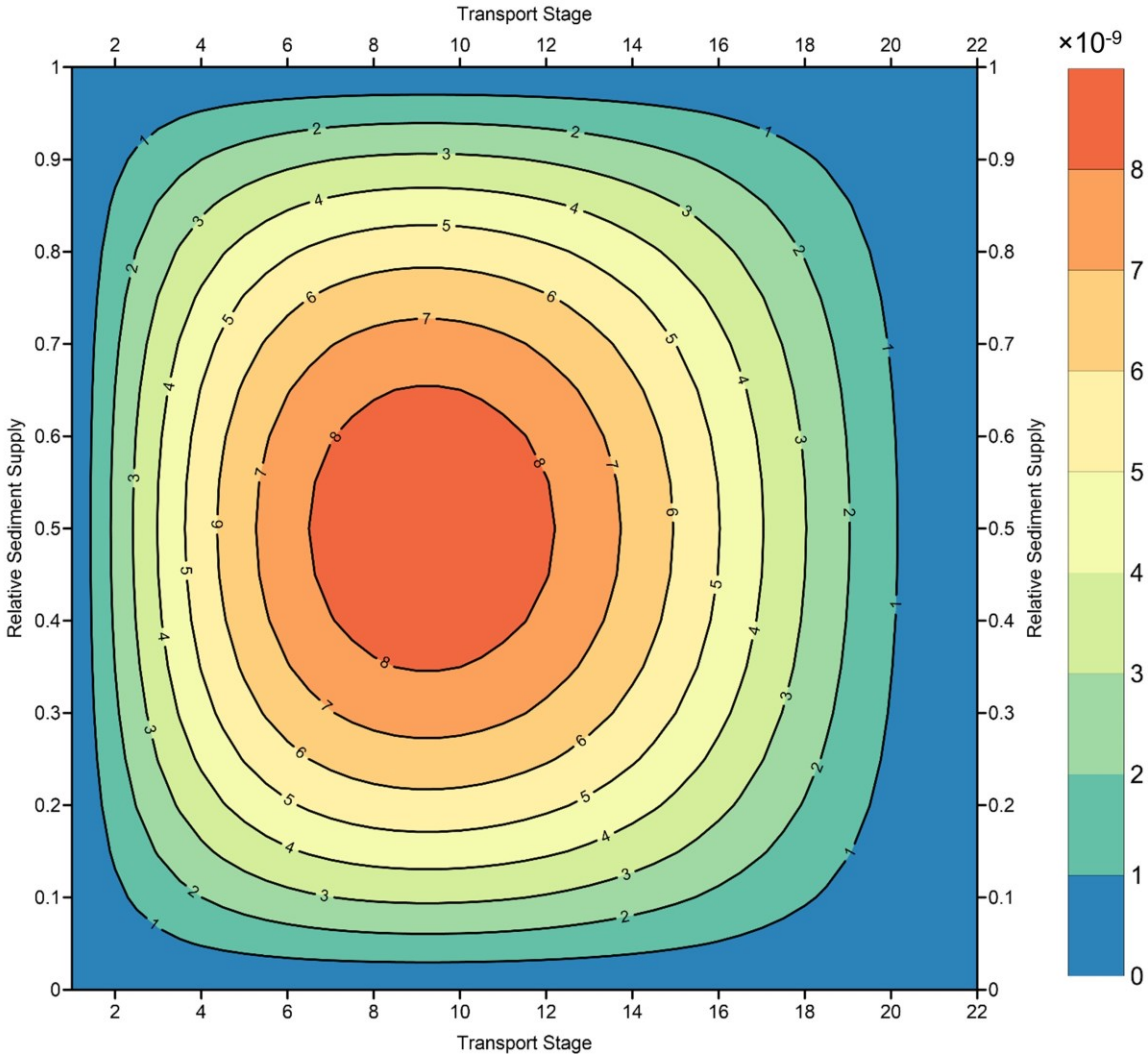

Figure 2.13 Non-dimensional vertical erosion rate (E_v^*) as a function of transport stage and relative sediment supply.

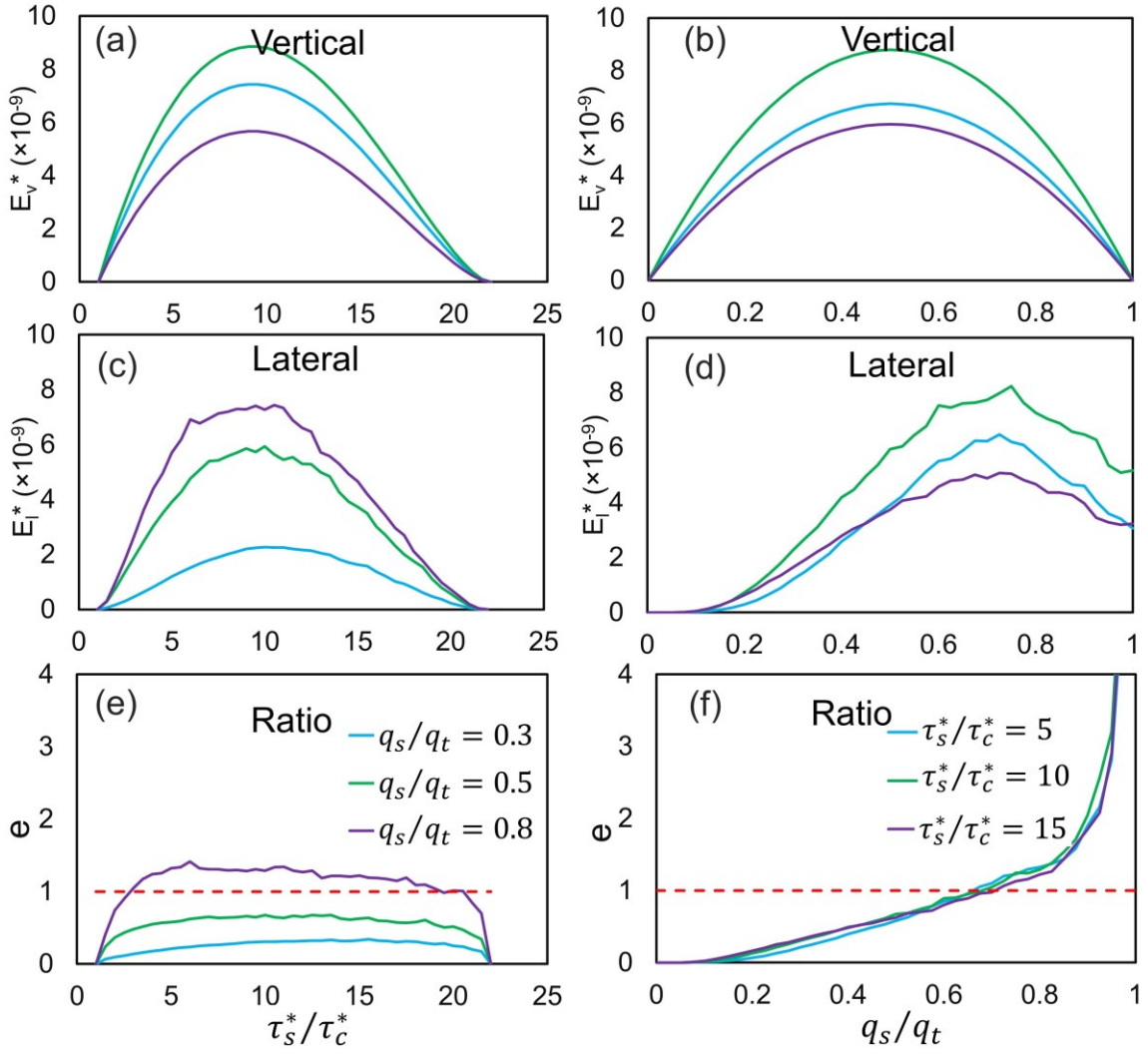

Figure 2.14 Non-dimensional vertical erosion rate as a function of a) transport stage τ_s^*/τ_c^* and b) relative sediment supply q_s/q_t; non-dimensional lateral erosion rate as a function of c) transport stage τ_s^*/τ_c^* and d) relative sediment supply q_s/q_t,and the ratio of lateral to vertical erosion rate as a function of e) transport stage τ_s^*/τ_c^* and f) relative sediment supply q_s/q_t.

Figure 2.15 reveals that E_l^* goes to zero at the threshold of motion and suspension along the τ_s^*/τ_c^* axis, and the threshold of no cover along the q_s/q_t axis, but is relatively high at the threshold of full cover. As with E_v^*, E_l^* peaks at an intermediate transport stages, however, E_l^* peaks at high relative sediment supply rate (~ 0.7; Figure 2.15). Figure 2.14c-d illustrates the pattern of E_l^* with increasing shear stress and relative sediment supply rate more clearly. E_l^* shows a parabolic variation with transport stage, where E_l^* is zero at the threshold of

motion due to a lack of particle movement along the transport stage axis (Figure 2.14c). As the transport stage exceeds the threshold for motion, E_l^* increases gradually with transport stage due to the growth in impact velocity. However, the impact frequency of bedload particles on the roughness element decreases with transport stage, because the saltation trajectories tend to grow more elongated with increasing shear stress. The growth in the particle impact energy and the reduction in the impact frequency with increasing shear stress results in a peak E_l^* at intermediate transport stages. E_l^* goes to zero at the threshold of suspension, because no impacts between roughness elements and bedload particles occur in our model. This is an artifact of the saltation model used. Some limited lateral erosion is possible from deflected particles above the suspension threshold, but E_l^* would be low. Along the relative sediment supply axis, a parabolic variation of E_l^* also exists. E_l^* is zero when the bed is free of cover and remains negligible when the relative sediment supply is <0.15 (Figure 2.14d). This occurs because when the relative sediment supply is low, the fraction of bed coverage is low, and there are relatively few deflectors on the bed. E_l^* gradually grows with the relative sediment supply rate above 0.15 due to the increase of the number of saltating bedload particles and the extent of roughness. However, E_l^* peaks at the relative sediment supply of ~ 0.7 (Figure 2.14d) due to a competition between the impact area A_c and wall-normal velocity v_o and the number of deflections on each cell of the roughness surface. When q_s/q_t increases, the distance between two adjacent roughness elements starts to decline, which will reduce the deflections near the bottom of the roughness surface and force bedload particles to impact near the top of the roughness surface. The concentration of impacts near the top of the roughness surface will lead to lower impact area on each cell as the cell starts to get close to the flux surface (Figure 2.5) and lower wall-normal velocity v_o after deflection by the cell as the vertical velocity w_s before deflection declines and the normal vector increasingly points upward. However, the number of deflections on each cell increases with higher sediment supply rates as q_s/q_t increases. The decrease in impact area A_c and wall-normal velocity v_o and the increase of the number of

deflections on each cell of the roughness surface with higher q_s/q_t will lead to a peak in E_l^* when they are balanced. E_l^* starts to decline for q_s/q_t above ~ 0.7 and is ~ 75% of the peak lateral erosion rate at the threshold of full cover.

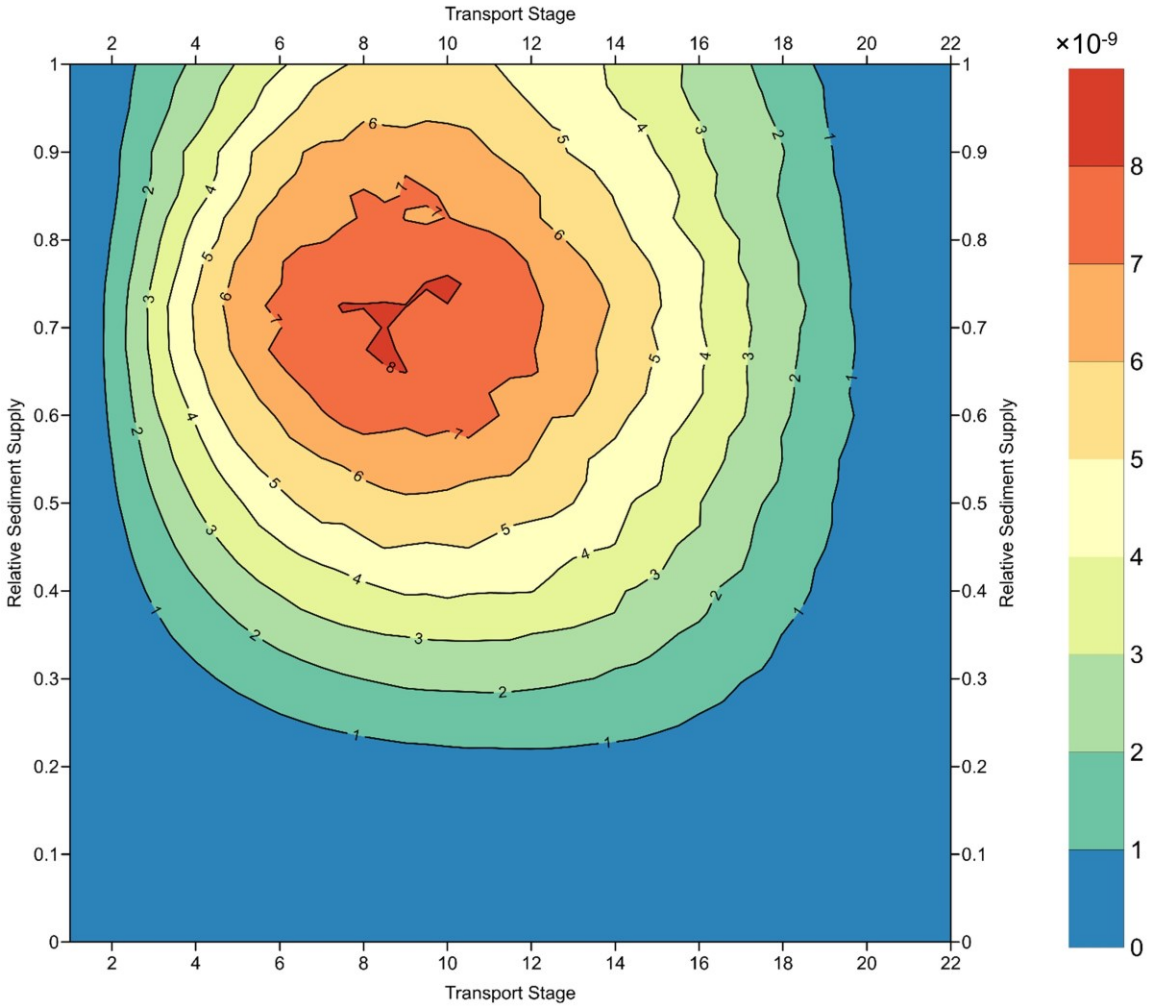

Figure 2.15 Non-dimensional lateral erosion rate ($\overline{E_l^*}$) as a function of transport stage and relative sediment supply.

The contour lines of non-dimensional lateral erosion rate are not smooth. This is not improved by using smaller time steps and space grids. The roughness element surface is discretized into nearly uniform triangular grid cells to model the collision with a finite number of bedload particles, which leads to variations in the modelled erosion rate. Some variation is also caused by our numerical approach. We track the movement of each particle to obtain the impact velocity and the impact position on the wall under every combination of relative sediment

supply rate and transport stage instead of deriving explicit empirical correlations, resulting in a lateral erosion model that varies irregularly with control variables.

The competition between vertical and lateral erosion was calculated from the ratio of E_l^* to E_v^* for each combination of q_s/q_t and τ_s^*/τ_c^*. The ratio e collapses to a unique functional surface in the parameter space created by q_s/q_t and τ_s^*/τ_c^* (Figure 2.16). e goes to zero with no bed cover, at the thresholds of motion and suspension, and is infinite when the bed has full cover. Figure 2.14e-f illustrates the patterns in e with changes of τ_s^*/τ_c^* and q_s/q_t. Along the τ_s^*/τ_c^* axis, e is parabolic, with a peak at an intermediate transport stage. This occurs because E_l^* increases more rapidly than E_v^* at lower transport stages (<10), and decreases more rapidly than E_v^* at high transport stages (Figure 2.14a-b), for a constant q_s/q_t. In contrast, e shows a monotonic increase with increasing q_s/q_t (Figure 2.14f); e goes to zero when q_s/q_t = 0 and gradually increases with relative q_s/q_t (> 0.15), because E_l^* grows faster than E_v^* when the relative sediment supply rate is below 0.5, and E_l^* continues to increase but E_v^* start to decrease when the relative sediment supply is between 0.5 and 0.7 (Figure 2.14b and d). The ratio e continues to increase at high relative sediment supply (> 0.7), because E_l^* decreases more slowly than E_v^*. When the bed is fully covered, the ratio goes to infinity as the lateral erosion rate is relatively high, but the vertical erosion rate goes to zero.

The coupled model shows that the lateral erosion rate is lower than the vertical erosion rate under nearly 75% of the transport and supply conditions (Figure 2.16). Lateral erosion is negligible at low sediment supply rates when the bed coverage is less than 20% and gradually increases with the extent of alluvial cover, but only dominates at high sediment supply rates when the bed is largely covered by roughness elements. The ratio e is ultimately controlled by the change in E_v^* and E_l^* and where it is high does not necessarily correspond to where either E_v^* or E_l^* are largest. Nevertheless, lateral erosion only dominates over vertical erosion under a limited range of conditions.

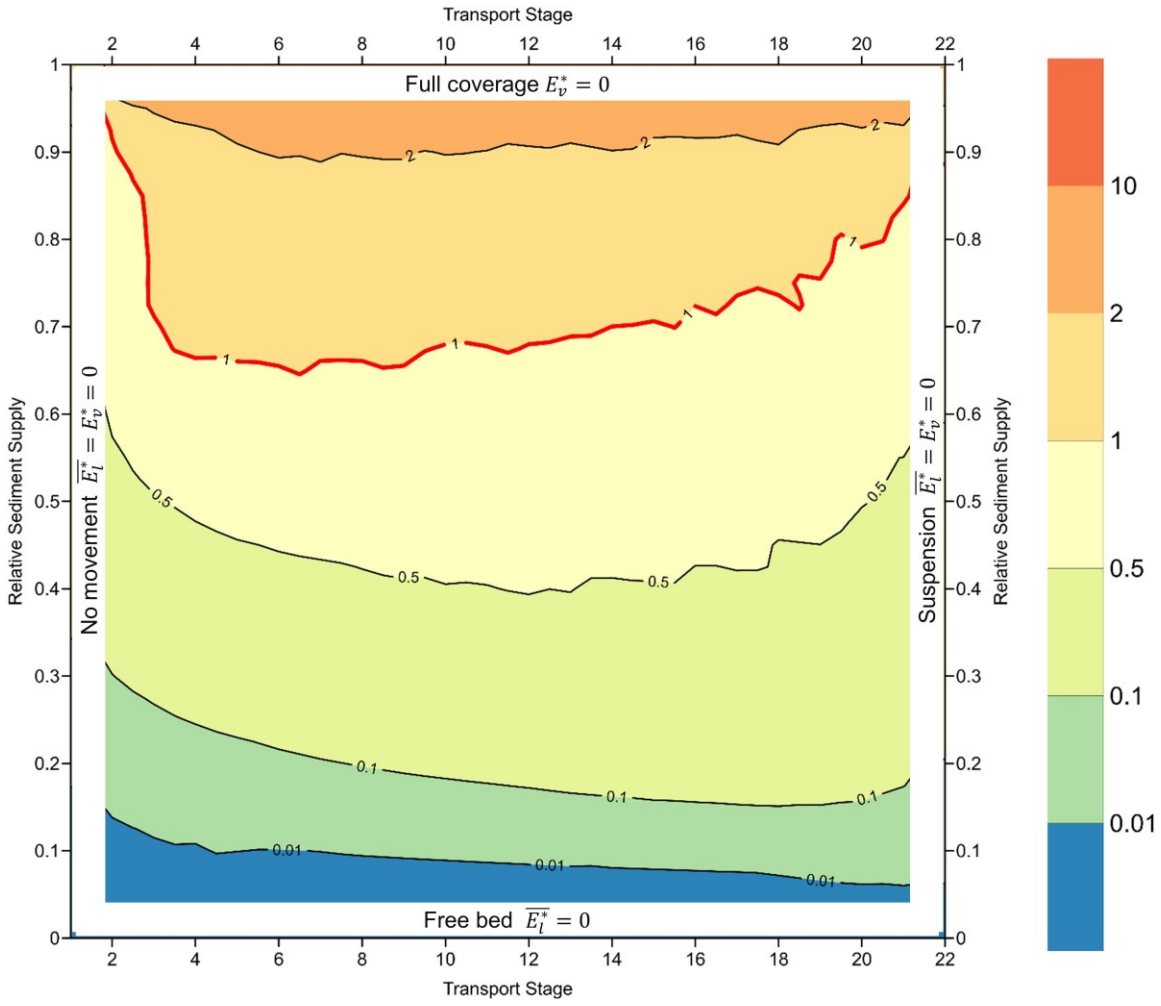

Figure 2.16 The ratio of lateral to vertical erosion rate $e = E_l^*/E_v^*$ as a function of transport stage and relative sediment supply.

2.5. Discussion

The lateral erosion model confirms that bedload particle impact is a viable mechanism for lateral erosion in bedrock rivers by reproducing key patterns in lateral erosion from the Fuller Experiments, including the undercut wall shape, the peak erosion and the total erosion rate. Saltating bedload particles obtain lateral momentum to erode the wall by colliding with the roughness elements on the bed. The bedload particle impacts concentrate in a zone near the bottom of the walls, thereby creating an undercut wall shape.

2.5.1. Limiting conditions on lateral erosion

While our model can reproduce key features of lateral rock erosion in channels, it is useful to consider some limiting conditions on the process of lateral erosion by abrasion. During periods when wall erosion can be effective, there are limits to how far lateral erosion by abrasion may occur before one of the following happens: 1) changes in channel geometry cause the stress to fall below the threshold of motion to maintain bedload; 2) the undercut becomes so deep that deflected particles can no longer reach the wall; or 3) the undercut is so deep that the rock mass above it fails into the channel (as in Figure 2.1a).It is unlikely that the first limitation will actually occur in a river undergoing undercutting. As the wall is undercut over time, mean velocity and shear stress drop due to the increase in cross-sectional area. The lateral erosion rate will go to zero when the shear stress is below the threshold for particle motion. However, this is unlikely to happen because the stress and wall morphology co-evolve. At low stresses, where changes in the wall would affect the shear stress, the erosion rate would be low, so the wall evolution would be very slow. It would therefore take an excessively long time for the shear stress to drop below the threshold of motion.

The lateral momentum for bedload particles to reach the wall drops due to the increase in travel distance as the wall gets undercut over time. To explore how this affects further undercutting, we ran the lateral erosion model over 15 hr using the 10 mm roughness element section. The lateral erosion stops after 12 hr, although the transport stage (~2.5) at the end of the time period is still enough to transport bedload particles (Figure 2.17). This occurs because the wall is eroded over 18 mm at the end of the time period, which is too far for bedload particles to impact on the wall at transport stage of ~2.5. As such, the increase in travel distance provides a greater limiting condition on lateral erosion than the drop of shear stress. Using a constant resistance coefficient over the run may overpredict the shear stress because the hydraulic roughness may increase as the wall is undercut. Also, the calculation shown in Figure 2.17 does not include

any roughness elements within the undercut. If the newly exposed bed by channel undercutting becomes alluviated, those deflectors would allow lateral erosion to continue.

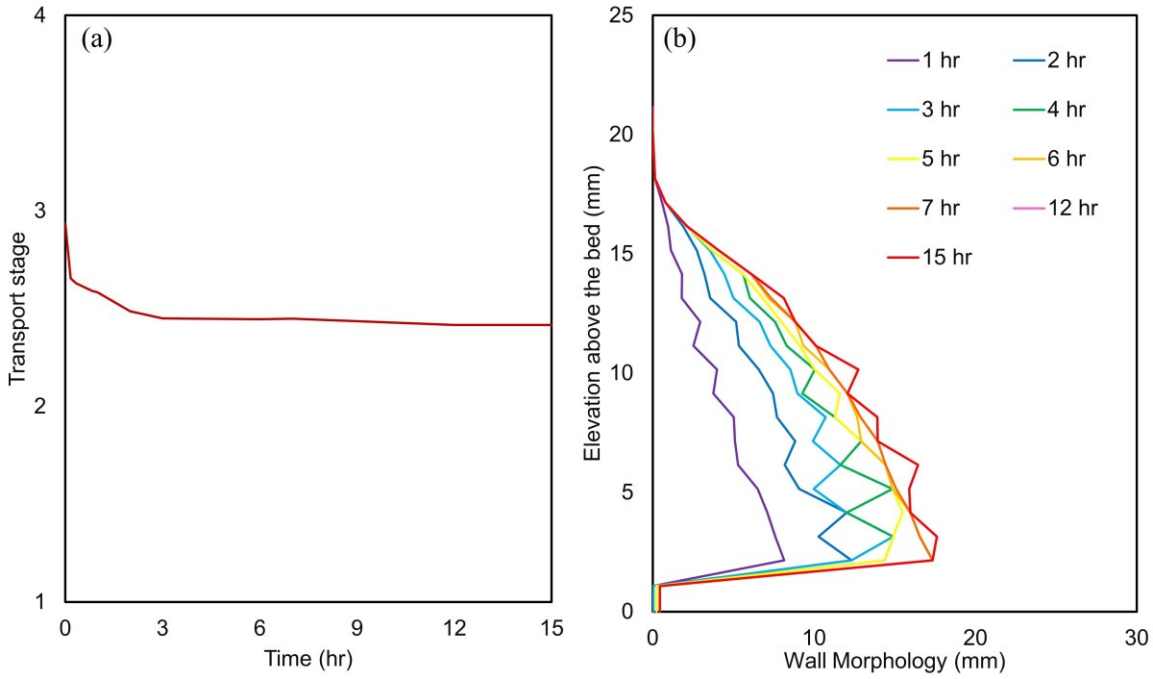

Figure 2.17 a) Shear stress evolution and b) wall morphology of 10.0 mm roughness section (C2) over 15 hr.

Continued undercutting of the lower wall creates an imbalance on the wall and may cause the upper part to collapse and to widen the whole channel. Such a mechanism of channel widening has been documented in both experiments (Carter & Anderson, 2006) and field data (Cook et al., 2014). However, the question of how far the wall needs to be undercut before it fails remains unanswered. Bedrock walls with lesser rock mass strength can fail more easily as the lower part of the wall is undercut. The degree of fracturing and jointing on the bedrock walls influences the rate of rock sliding and toppling and hence channel width. Bedrock bedding may play a dominant role in controlling the wall collapse. Undercut bedrock walls with vertical bedding can cause a channel to widen more effectively than with horizontal bedding, which may remain intact for deeper undercuts.

2.5.2. Undercut wall shape dynamics

One of the key findings of our model is that in bedrock channels with a planar bed, the competition between vertical and lateral erosion is controlled by the extent of alluvial cover under different sediment supply conditions, which agrees with the experimental and field measurements (Finnegan et al., 2007; Fuller et al., 2009, 2016; Johnson & Whipple, 2010; Finnegan & Balco, 2013). Our model provides the opportunity to quantify how different wall shapes are formed under different sediment supply conditions. In a low sediment supply environment, the channel bed is more exposed and vertical erosion will dominate, with lateral erosion relatively negligible, resulting in a near straight wall shape. At an intermediate to high sediment supply where the bed is 50%-90% covered, both the bed and walls can be cut by bedload particle impacts. The continuing lowering of the channel bed will shift down the lateral erosion zone by preventing the bedload particles impacting on a fixed elevation on the walls. This will create an undercut wall shape that keeps the same width but spreads more deeply over time. However, when the bed is near fully covered (>90%), the bed is relatively static due to the protection of alluvium, leading to an undercut wall shape that gets wider over time. As such, the wall shape would change from near straight to deeply undercut as the sediment supply increases.

The undercut wall shape may be modified by roughness elements made of the bedrock surface. The bedrock rivers have a wide range of sculpted bed morphologies (Wohl, 1993; Montgomery & Buffington, 1997; Wohl & Merritt, 2001; Richardson & Carling, 2005), such as potholes, flutes, furrows, runnels, etc. In a bedrock channel with bedrock obstacles near the walls, bedload particles can be deflected toward the walls by bedrock obstacles even when no alluvial cover exists. Beer et al. (2017) mapped the lateral erosion patterns in a bedrock gorge in the Swiss Alps under three bedrock obstacle conditions: 1) no bedrock obstacle; 2) low bedrock obstacle; 3) high bedrock obstacle. Bedrock walls without bedrock obstacles were only slightly eroded, while in sections with low and high bedrock obstacles, the walls were undercut deeper and higher

above the bed. The occurrence of bedrock obstacles to deflect bedload particles to higher elevations than the alluvium may have the effect of elevating the undercut zone. The size of bedrock roughness obstacles can influence the erosion rate from two opposite effects. Small bedrock obstacles do not have large surface area to deflect bedload particles but tend to have high impact velocity due to low form drag. Larger bedrock obstacles have more surface area for deflections, but the impact velocity will be reduced because of higher form drag. Intermediate bedrock obstacles that balance the tradeoff between surface area and impact velocity may result in highest lateral erosion rates.

One implication of our model would suggest is that the extreme magnitude of supply events may not be the most effective in eroding bedrock walls. Instead, the more frequent high moderate sediment supply events may be responsible for the majority of bedrock wall erosion. This occurs because the reduced impact area on each roughness element and the reduced impact velocity with increasing alluvial cover (> 75% coverage; Figure 2.15).

It is possible to infer the relative width to depth ratio and degree of incision of a channel cross-section from Figure 2.16. A bedrock channel with a high sediment supply rate, which can be found near the upper part of Figure 2.16, is mostly covered by alluvium. This channel would be dominated by lateral erosion with negligible vertical erosion, allowing for a wide bedrock channel, relative to its depth. In contrast, a channel that receives relatively little sediment supply should plot near the lower part of Figure 2.16, will preferentially incise the bed and have a lower relative width to depth ratio. Of course, the sediment supply and transport stage conditions of bedrock rivers change over time with hydrographs and sedigraphs in a basin. The ultimate shape of a channel is determined by how long it spends in particular positions on Figure 2.16. A channel that spends the vast majority of its time in the lower corner of Figure 2.16 is likely to be narrow and deeply incised. A channel that is in the upper corner of Figure 2.16 most of the time will be relatively wider. Tracking a channel through time on Figure 2.16

requires a full morphodynamic implementation of the model presented herein, which requires imposed hydrographs and sedigraphs.

2.5.3. Model limitations and further prospects

There are a number of simplifications in our model, which were necessary to produce a result, that may affect the outcomes. Our model is a sediment flux-driven incision model that is most applicable to rivers flowing through massive crystalline rock, that does not take into account any other lateral erosion mechanisms. Plucking may dominate bedrock erosion where rock is weak or well-jointed (Chatanantavet & Parker, 2009, 2011), or where shear stresses are large enough to entrain or transport large blocks (Montgomery, 2004; Stock et al., 2005; Lamb et al., 2015; Beer et al., 2017). Plucking is particularly effective in erosion of columnar basalts (Dubinski & Wohl, 2013; Larsen & Lamb, 2016) and may be possible by fluid shear stresses plucking pieces of weak rocks from channel walls (Montgomery, 2004; Stock et al., 2005).

Our model uses a uniform grain size with spherical shape for sediment particles to represent the wide distribution of grain sizes supplied to bedrock rivers. Grain size controls the threshold for motion and hence the transport stage, and hence impact velocity and impact rates. Grain size of the alluvial cover determines the elevation of collision, thereby influencing the transfer of momentum during collision and the impact height on the wall. High points of the alluvial cover that protrude above the saltation layer do not deflect bedload particles into the wall. Therefore, the distribution of grain sizes supplied by the upstream catchment (Sklar et al., 2017) may influence the lateral erosion rate by changing the fraction of total load that is transported as bedload and the momentum transfer of bedload particles during collision with the alluvial cover. The shape of sediment particles determines the distribution of impact angles during collision between roughness elements and bedload particles, thereby influencing the direction of movement after collision. Given that our assumption of a uniform grain size with spherical shape has well reproduced the erosion

patterns observed in the Fuller Experiments, which used non-spherical deflectors, the influence of the non-spherical shapes of natural particles on lateral erosion rate may be negligible.

Our lateral erosion model uses numerical formulations to track the movement of individual bedload particles. The potential for bedrock erosion by bedload impacts at transport stages above the suspension threshold is ignored. It is possible that particle impacts might be viscously damped for fine grains that are transported as suspended load. Yet, bedload transport remains a significant, but decreasingly important component of the total load as transport stages increase above the suspension threshold (Lamb et al., 2008a; Scheingross et al., 2014). Suspended load has been proposed to be responsible for lateral erosion through turbulent fluctuations that laterally sweep particles to impact on the wall (Whipple et al., 2000). It is not possible for us to track particle movements above the suspension threshold, so we force the lateral erosion rate to zero at the suspension threshold, which is consistent with the Sklar & Dietrich (2004) vertical erosion model. Further work is necessary to develop a version of our model to handle lateral erosion by sediment suspension.

The simplified treatment of flow dynamics in the model may influence the result as well. Movement of sediment after collision is modelled by assuming that the influence of turbulence on trajectories is negligible. However, local turbulent fluctuations can be intense above a bed with significant roughness (Richardson & Carling, 2005). We assume that flow advection is negligible near the bed so that particles impact on roughness elements and subsequently on the wall without being swept away with the flow. The advective component of the impact velocity can be significant over roughness elements (Tinkler, 1997; Johnson & Whipple, 2007), where flow goes around large roughness elements and advects the sediment toward the wall, potentially increasing the impact velocity and rates on the wall. Some caution should be exercised in applying the model where the cross-section is irregular or where the flow field is non-uniform.

An important simplification in the lateral erosion model is our assumption that bedload particles are uniformly transported in a rectangular channel with a planar bed and straight walls. At low relative sediment supply rates, the bedload layer self organizes into a concentrated filament along the channel centerline. In a rectangular bedrock channel, the shear stress is higher in the channel center than near the wall due to the wall drag (Gary Parker, 1978). This flow structure results in faster bedload particle velocity in the channel center than near the walls. Nelson & Seminara (2011) modelled the Finnegan et al. (2007) experiments and showed that the formation of a bed load filament along local channel depressions is capable of forming an incised channel with strath terraces because bedload is gravitationally drawn to the lowest part of the channel cross-section, forming preferential pathways for bed load in bedrock channels (Finnegan et al., 2007; Chatanantavet & Parker, 2008; Nelson & Seminara, 2011; 2012; Inoue et al., 2014; Inoue et al., 2016; Turowski & Hodge, 2017). The higher speed and greater concentration of bedload particles in the channel center will increase the impact energy and frequency and accelerate the vertical erosion rate in the channel center, but slow down the lateral erosion rate due to the increasing travel distance for the particles to impact on the wall. This can have a self-reinforcing effect where the bed load pathways are topographically steered by an incised groove, so that bedload concentrates vertical erosion in the channel center until the incised groove is alluviated (Cao, 2018). Alternatively, the areal concentration of bed load can enhance the lateral erosion on the groove walls because sediment particles can be deflected by the alluvium to impact on the sidewalls and to widen the incised groove. The organization of bedload layers is not presently considered in our model because there is no analytical solution to predict this phenomenon, but this needs to be addressed to understand complex channel cross-sections.

Our model also does not consider the self-organization of bedload layers that may lead to the formation of persistent alluvial patches at high relative sediment supply rates. Relative sediment supply in the Fuller Experiments was kept below the patch formation threshold. Field observations and flume

experiments have shown that partial alluvial cover tends to self-form in patches in bedrock rivers and may form alternating gravel bars (e.g. Lisle, 1986; Chatanantavet & Parker, 2008). Turowski (2020) developed a lateral erosion model that more explicitly treats the effects of self-organized alluvium. The model does not track particle deflections and evolution of the wall, as in our model. Instead, a deflection length is defined as saltation hop length times its defection angle and if the deflection length is less than the distance between the bar and the opposite wall, lateral erosion is thought to occur, increasing the channel width to a steady state reach width. Our model would predict the opposite erosion pattern predicted by the Turowski (2020) model. Our model would underpredict erosion on the wall adjacent to a bar because the bar will have densely packed deflectors and it would overpredict erosion on the wall opposite to the bar because the bare bedrock will have few immobile deflectors. Inclusion of flow patterns associated with alternate bars may produce the erosion patterns predicted by the Turowski (2020) model. Flow in bends directs coarser particles towards the outer bank (Dietrich & Smith, 1984; Dietrich & Whiting, 2011), which has been shown experimentally to enhance lateral erosion downstream of the bend apex (e.g. Mishra et al., 2018). Future development of our model will need to more faithfully treat the self-organization of alluvial cover and flow in bends to predict the effects of channel curvature and self-organized alluvium.

Despite the simplifications in our model, it agrees well with experiments that have relatively simple geometries (Fuller et al., 2016), which suggests that the model captures the fundamental mechanism correctly. Furthermore, the model generates undercut wall shapes that are qualitatively similar to field observations (Beer et al., 2017). Application of the model to a natural channel needs to consider time scales of effectiveness for both the vertical and lateral erosion processes, which are ultimately controlled by discharge and sediment supply variations (Lague et al., 2005, 2010; Finnegan et al., 2005; Finnegan & Balco, 2013; Inoue et al., 2014, 2016). Wall erosion is the integrated result of intermittent periods of variable discharge and sediment supply. Ultimately, application of our model to natural channels with variability in discharge and

sediment supply requires a morphodynamic model by: 1) developing a lateral erosion model by suspended load; 2) finding an analytical solution of the model to make the calculations tractable through geologic time, and 3) developing a way to parameterize our flow resistance submodel.

2.6. Conclusion

We have developed a mechanistic model for lateral erosion of bedrock channel banks by bedload particle impacts using well established empirical relations for initial velocities of bedload particles, a simplified reflection methodology for collision with roughness elements, and a numerical model for tracking the motion of bedload particles from collision to impacts on the wall. Simulations of the Fuller Experiments show that the model successfully predicts the essential undercut wall shape, the dynamics of peak erosion rate and total cross-sectional erosion rate with roughness element size, which not only validates the formulation of our lateral erosion model but also supports the bedload particle impacts as an effective mechanism for lateral incision in bedrock rivers. The predicted lateral erosion rate can be further expressed in non-dimensional form as a function of transport stage and relative sediment supply for the given grain size by assuming that the alluvial cover due to deposition of sediment particles is effective at deflecting downstream transport particles. The non-dimensional lateral erosion model defines a unique functional surface bounded by four thresholds, including the threshold of motion, the threshold of suspension, the threshold of no cover, and the threshold of full cover. The lateral erosion is relatively high at the threshold of full cover, but turns to be zero at all other three thresholds. The model also predicts a peak lateral erosion rate when the bed is near 70% covered, due to a trade-off of deflection rates and deflection angles as the sediment supply increases. A coupled model that combines vertical erosion with lateral erosion due to bedload particle impacts is further developed. The coupled model predicts that vertical erosion dominates under ~ 75% of transport and supply conditions on the unique functional surface. The lateral erosion only outpaces the vertical erosion when the bed is near fully covered.

Chapter 3. An Analytical Model for Lateral Erosion from Saltating Bedload Particle Impacts

Abstract

The width of bedrock rivers is set by the competition between vertical and lateral erosion in uplifting landscapes. Compared with vertical erosion rates, less is known about the lateral erosion rates that are thought to dominate when river beds are alluviated. Here, we derive an analytical model for lateral erosion by saltating bedload particle impacts that are deflected by alluvial cover. The analytical model is a simplification of the Li et al. (2020) numerical model of the same process. The analytical model predicts a nonlinear dependence of lateral erosion rate on sediment supply, shear stress and grain size, revealing the same behaviour observed in the numerical model, but without tracking particle movements through time and space. The analytical model considers both uniformly distributed and patchy partial cover that are implemented with a fully alluviated patch along one bank and bare bedrock along the other. The model predicts that lateral erosion rate peaks when the bed is ~70% covered for uniformly distributed alluvium, or when the bed is fully covered for patchy alluvium. Vertical erosion dominates over lateral erosion for ~75% and >90% of sediment supply and transport stage conditions for uniformly distributed cover and patchy cover, respectively. We use the model to derive a phase diagram of channel responses (steepening, flattening, narrowing, widening) for various combinations of transport stage and relative sediment supply. Application of our model to Boulder Creek, CA captures the observed channel widening in response to increased sediment supply and steepening in response to larger grain size.

3.1. Introduction

In unglaciated landscapes, bedrock rivers are ultimately responsible for driving landscape response to tectonic uplift and climate change through the

coupling of vertical and lateral incision processes (Whipple et al., 2000, 2013). Climate change drives changes in magnitude and frequency of discharge and sediment flux, which largely controls the changes in the degree and frequency of alluviation of the channel bed. Field observations, laboratory experiments, and modeling have shown that vertical erosion dominates in low sediment supply environments due to the exposure of bed but is outpaced by lateral erosion in high sediment supply environments due to the alluvial cover on the bed (Beer et al., 2017; Finnegan & Balco, 2013; Finnegan et al., 2007; Fuller et al., 2009, 2016; Gilbert, 1877; Hancock & Anderson, 2002; Hartshorn et al., 2002; J.P. L. Johnson & Whipple, 2010; Lague, 2010; Shepherd, 1972; Sklar & Dietrich, 2004; Turowski et al., 2008; Yanites, 2018). At high sediment supply rates, the bed is protected by the alluvial cover, but particles can be deflected by the alluvial cover into channel banks. In order to reach steady state, vertical erosion rate in bedrock rivers needs to keep pace with increasing uplift rate. Rivers have been observed to narrow with increasing uplift rates in some settings (Amos & Burbank, 2007; Duvall et al., 2004; Lavé & Avouac, 2001; Tomkin et al., 2003) but not in others (Pazzaglia & Brandon, 2001; Snyder et al., 2003; Tomkin et al., 2003). A model that couples vertical erosion with lateral erosion is needed to capture the complex adjustments of bedrock rivers in response to change of boundary conditions.

There have been some attempts to couple vertical with lateral erosion. They can be divided into three categories: (1) stream power models for both vertical and lateral erosion (referred to as pure stream power model hereafter); (2) mechanistic model for vertical erosion but stream power model for lateral erosion (referred to as hybrid model hereafter); and (3) mechanistic models for both vertical and lateral erosion (referred to as pure mechanistic model). The pure stream power model scales vertical and lateral erosion rate with unit stream power or shear stress (Hancock & Anderson, 2002; Lague, 2010; Langston & Tucker, 2018; Stark, 2006; Turowski et al., 2009; Wobus et al., 2006, 2008), which allows for computationally tractive, large-scale landscape evolution modeling. However, the pure stream power model masks physical processes

responsible for bedrock incision, making it difficult to predict bedrock river dynamics at reach scale, where active incision occurs (Venditti et al., 2020). The hybrid model (Yanites, 2018) couples the mechanistic saltation–abrasion model for vertical erosion (Sklar & Dietrich, 2004) with the stream power model for lateral erosion. The hybrid model provides physical explanations of vertical adjustment by explicitly introducing the influence of sediment supply, discharge, grain size, rock strength, and rock uplift rate but lumps the influence of these variables responsible for lateral erosion into poorly constrained parameters not related to a specific physical mechanism. Turowski (2018, 2020) developed a reach scale lateral erosion model based on particle deflections, but does not explicitly model particle deflections. More recently, Li et al. (2020) developed a mechanistic lateral erosion model based on the experiments of Fuller et al. (2016), which demonstrated substantial bank erosion by deflected bedload particle impacts. Li et al. (2020) coupled the lateral erosion model with the Sklar and Dietrich (2004) vertical erosion model to investigate the role of relative sediment supply and transport stage on the competition between vertical and lateral erosion. However, the pure mechanistic model is computationally intensive because it tracks the movement of each particle over space and time to get the instantaneous lateral erosion rate. The lack of an analytical solution for the Li et al. (2020) numerical model makes it difficult to explore the sensitivity of lateral abrasion rates to input variables and to apply the model to natural bedrock rivers that experience a wide range of discharges and sediment supply events.

Here, we derive an analytical solution for the Li et al. (2020) lateral erosion model, which captures the essential physics of lateral erosion by bedload particle impacts with a uniform grain size and reproduces the numerical solution but is simple enough to couple with the Sklar and Dietrich (2004) vertical erosion model for simulating bedrock river morphodynamics. We are motivated by an interest in determining what controls width variation in bedrock rivers. Boulder Creek, CA, serves as a prototype for our work. Boulder Creek is a small bedrock channel (drainage area ~30 km^2) in the Santa Cruz Mountains that is actively incising into sedimentary rock. Finnegan et al. (2017) described the channel as becoming

abruptly wider and steeper downstream of a tributary that supplies coarser sediment. Upstream of the tributary, the river transports relatively fine bedload (median grain size ~20 mm) derived from weak sedimentary rock and sustains partial alluvial cover. Downstream of the tributary, the river is 2 times wider and 3 times steeper than upstream, and transitions from partial to nearly continuous alluvial cover where it starts to transport coarser diorite bedload (median grain size ~220 mm). Finnegan et al. (2017) argued that the increase in sediment supply magnitude and caliber causes the channel widening because of the increase in bed coverage and lateral particle deflections into the channel banks. We explore this explanation using our analytical model to see if the model predicts an increase in channel width and slope in response to the change in sediment supply rate and grain size.

Our analytical model considers both uniformly distributed and patchy bed cover. While alluvial cover may be uniformly distributed, it often covers some parts of the bed, leaving other areas exposed. Patches of sediment deposited may be transient features, but they are often also persistent features that may grow and shrink in size depending on sediment supply and transport stage. Both field observations (Cook et al., 2009, 2013; Inoue et al., 2014) and laboratory experiments (Chatanantavet & Parker, 2008; Fernández et al., 2019; Finnegan et al., 2007; Johnson & Whipple, 2007, 2010) show that transient deposits coexist with persistent deposits. It is persistent patches that are most likely to cause lateral erosion over long time scales. Herein, our treatment of patchy cover considers bank-attached deposits of sediment, akin to a lateral bar developed in a bedrock river, but our analytical model can be used for any geometry of sediment patches in bedrock rivers, hence our use of the term patch rather than a specific deposit type.

We begin by briefly reviewing the Li et al. (2020) lateral erosion model. Next, we derive empirical correlations for key elements of the Li et al. (2020) numerical model and combine them with established formulas to derive analytical solutions for both uniformly distributed and patchy alluvial bed cover. We then

couple the lateral erosion model with the Sklar and Dietrich (2004) vertical erosion model to find the ratio of lateral to vertical erosion rate. We further compare the numerical model with the analytical model for lateral erosion rate and use the analytical model to explore the sensitivity of predicted bedrock abrasion rates to variations in sediment supply, shear stress, and grain size. Finally, we return to our motivating field study and use the analytical model to discuss the observed changes in Boulder Creek.

3.2. Analytical Model Development

3.2.1. Review of Li et al. (2020) numerical model

Li et al. (2020) developed a numerical model for lateral erosion of bedrock walls by bedload particle impacts that are deflected by alluvium on the bed, which is briefly outlined below. The model assumes a uniform distribution of bedload particles and alluvium in a channel with a planar bed and vertical walls (Figure 3.1a-b), discretizes the surfaces of particles making up the alluvium into uniform triangular grid cells, and tracks the movement of each bedload particle from the moment it is deflected by the alluvium to when it impacts the walls. The model calculates the lateral erosion rate E_l as the sum of all local erosion rates due to individual bedload particles deflected by each deflector of the alluvium E_i

$$E_l = \sum E_i. \qquad \text{(Equation 3.1)}$$

The local erosion rate due to impacts of individual bedload particles E_i is scaled by the kinetic energy transferred, which is the product of particle mass M and the square of impact velocity v_i, on the walls, and the impact rate per unit area on the walls I_w

$$E_i = \frac{Y}{k_v \sigma_T^2} M v_i^2 I_w (1 - (u^*/w_f)^2)^{1.5}, \qquad \text{(Equation 3.2)}$$

where Y is Young's modulus of elasticity of the bedrock, k_v is the dimensionless bedrock strength coefficient, σ_T is the tensile yield strength, u^* is shear velocity and w_f is fall velocity calculated from the empirical method developed by Dietrich

(1982), assuming values of Cory shape factor (0.8) and Powers scale (3.5) typical for natural gravel particles. The model ignores abrasion by suspended sediment, assuming E_i is zero if $u^*/w_f \geq 1$.

The impact velocity v_i is calculated by tracking particle movement from being deflected by the alluvium to impacting on the wall over time, assuming fluid drag is the dominant force on lateral velocity deceleration rate dv/dt

$$-\frac{dv}{dt} = C_d v^2, \qquad \text{(Equation 3.3)}$$

where $C_d = 0.75 C_1 \rho_w/(D\rho_s)$ is the drag deceleration coefficient, C_1 (0.45) is the drag parameter, ρ_w is water density, ρ_s is sediment density, D is grain size. The initial condition for Equation 3.3, $v(t=0)$, is the lateral component v_o of the outgoing velocity vector after being deflected by the alluvium surface $\boldsymbol{i_o} = (u_o, v_o, w_o)$ (u_o, v_o and w_o are the longitudinal, lateral and vertical components of $\boldsymbol{i_o}$, respectively). $\boldsymbol{i_o}$ is calculated from a deflection method, assuming the incoming and outgoing angles are symmetrical about the unit vector that is normal to the alluvium surface at the point of deflection $\hat{\boldsymbol{n}}$

$$\boldsymbol{i_o} = (-\mathbf{2}(\frac{\boldsymbol{i_s}\cdot\hat{\boldsymbol{n}}}{\hat{\boldsymbol{n}}\cdot\hat{\boldsymbol{n}}})\hat{\boldsymbol{n}})C_r, \qquad \text{(Equation 3.4)}$$

where C_r is the restitution coefficient (set to 0.9) that describes the loss of particle momentum during the collision between bedload particle and alluvium, $\hat{\boldsymbol{n}} = (n_x, n_y, n_z)$, n_x, n_y and n_z are downstream, lateral and vertical component of $\hat{\boldsymbol{n}}$, respectively, and $\boldsymbol{i_s}$ is the incoming velocity vector before deflection. $\boldsymbol{i_s}$ has two non-zero components:

$$\boldsymbol{i_s} = (u_s, 0, w_s), \qquad \text{(Equation 3.5)}$$

where u_s is the downstream saltation velocity and w_s is the vertical saltation velocity, assuming the lateral saltation velocity is negligible. u_s and w_s are given as empirical correlations by Sklar & Dietrich (2004) and Lamb et al. (2008a)

$$u_s = 1.56(R_b g D)^{0.5}(\frac{\tau^*}{\tau_c^*} - 1)^{0.56}, \qquad \text{(Equation 3.6)}$$

$$w_s = -\sqrt{\frac{C_g}{C_d}(1 - e^{-2C_d(h_s - h_d)})}, \qquad \text{(Equation 3.7)}$$

where $R_b = \rho_s/\rho_w - 1$ is non-dimensional buoyant density, g is gravitational acceleration, τ^* is the non-dimensional form of shear stress τ, τ_c^* is the value of τ^* at the threshold of sediment motion, $C_{\mathrm{g}} = (1 - \rho_w/\rho_s)g$ is the gravitational acceleration coefficient, h_s is the saltation height, h_d is the height of bedload particle during collision with the deflector. h_s is predicted from the empirical relation developed by Sklar & Dietrich (2004)

$$\frac{h_s}{D} = 1.44\left(\frac{\tau^*}{\tau_c^*} - 1\right)^{0.50}. \qquad \text{(Equation 3.8)}$$

The impact rate per unit area on the walls I_w is given by

$$I_w = \frac{q_s}{M\sqrt{h_s^2 + l_{su}^2}}\frac{A_p}{d h_{max}}, \qquad \text{(Equation 3.9)}$$

where q_s is the mass sediment flux per unit channel width, d is the distance between two adjacent particles (Figure 3.1), h_{max} is the maximum impact height on the wall, A_p is the total projected area of the deflector surface onto the plane that is parallel to the upward motion of saltation particles, following the plane that is parallel to the downward motion of saltation particles (Figure 3.2), and l_{su} is the hop length of the upward motion of saltation particles (Figure 3.2).

d is given by Li et al. (2020) as

$$d = D\frac{q_t}{q_s}. \qquad \text{(Equation 3.10)}$$

where d is inversely proportional to the fraction of alluvium F_a which is assumed to be a linear function of relative sediment supply q_s/q_t (defined as the ratio of sediment supply q_s to transport capacity q_t). Turowski et al. (2007) developed an exponential formula for F_a, and Turowski & Hodge (2017) built a probabilistic framework for the description of the cover effect that contained the linear and exponential models as special cases. For simplicity and consistency with the Sklar & Dietrich (2004) vertical erosion model and Li et al. (2020) numerical

lateral erosion model, we elected to use the linear model ($F_a = q_s/q_t$). The bedload sediment transport equation by Fernandez Luque & Van Beek (1976) is used to estimate q_t as $q_t = 5.7\rho_s(R_b g D^3)^{0.5}(\tau^* - \tau_c^*)^{1.5}$.

l_{su} can be obtained from the empirical relation by Sklar & Dietrich (2004)

$$\frac{l_{su}}{D} = 2.67(\frac{\tau^*}{\tau_c^*} - 1)^{0.88}. \qquad \text{(Equation 3.11)}$$

Combining Equations 3.1, 3.2 and 3.9 yields the composite expression of the saltation abrasion model

$$E_l = \sum \frac{Y}{k_v \sigma_T^2} v_i^2 \frac{q_s}{\sqrt{h_s^2 + l_{su}^2}} \frac{A_p}{dh_{max}} (1 - (u^*/w_f)^2)^{1.5}. \qquad \text{(Equation 3.12)}$$

Calculation of E_l requires discretizing the surface of particles making up the alluvium into grid cells that incorporate the variation of normal vectors $\hat{\boldsymbol{n}}$, the resultant outgoing velocity v_o and the projected area A_p. Solving for the impact velocity v_i and the maximum impact height h_{max} on the walls requires tracking the movement of particles over space and time. The lack of an analytical solution for Equation 3.12 makes it too computationally intensive to implement in models of bedrock river morphodynamics at reach or larger scales for the wide range discharges and sediment supply events that an incising channel might experience.

In order to derive an analytical solution to Equation 3.12, we assume that the various normal vectors $\hat{\boldsymbol{n}}$ and the impact height h_d on the alluvium surface can be represented by the mean normal vector and mean impact height, respectively, for given sediment supply and transport conditions. We also assume that the loss of momentum of bedload particles is negligible if they are rebounded by the bed or other deflectors before impacting on the walls. We therefore develop relations to describe the impact velocity v_i, the maximum impact height h_{max}, the projected area A_p, and hence the lateral erosion rate E_l in Equation 3.12.

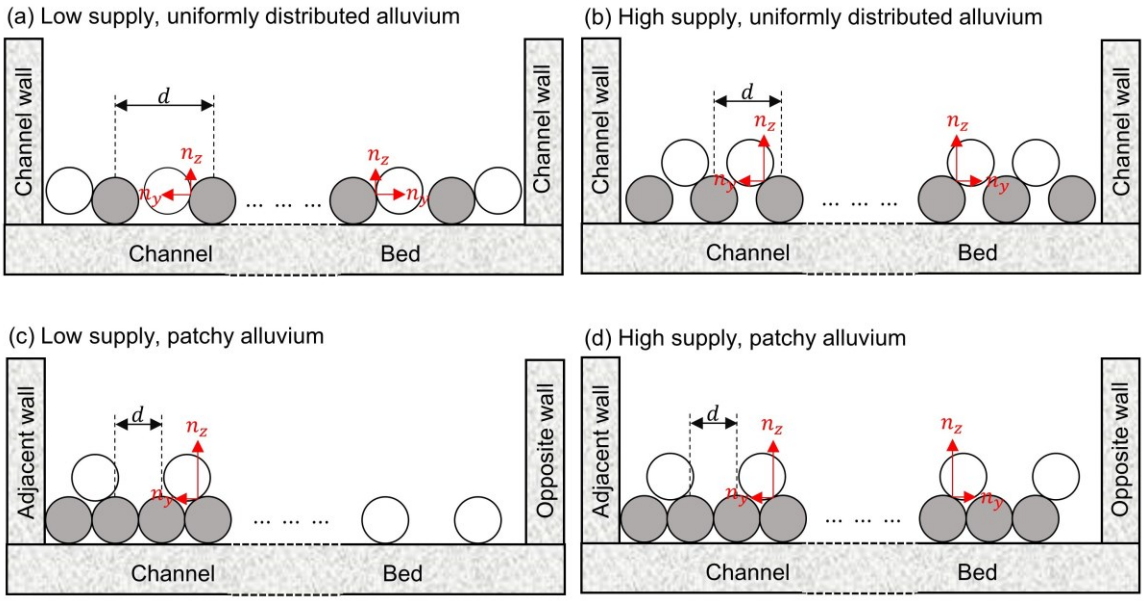

Figure 3.1 Schematic showing cross section view (looking downstream) of model setup in an idealized rectangular channel eroded by saltating bedload particle (white circle) impacts that are deflected by alluvium (gray filled circle) distributed on the channel bed. Two types of alluvium are shown here: uniformly distributed alluvium at a) low and b) high sediment supply rates, and alluvium formed in a continuous patch at c) low and d) high sediment supply rates. Also shown here are the distance between two adjacent deflector d, lateral n_y and vertical n_z components of the normal vector at the point of deflection.

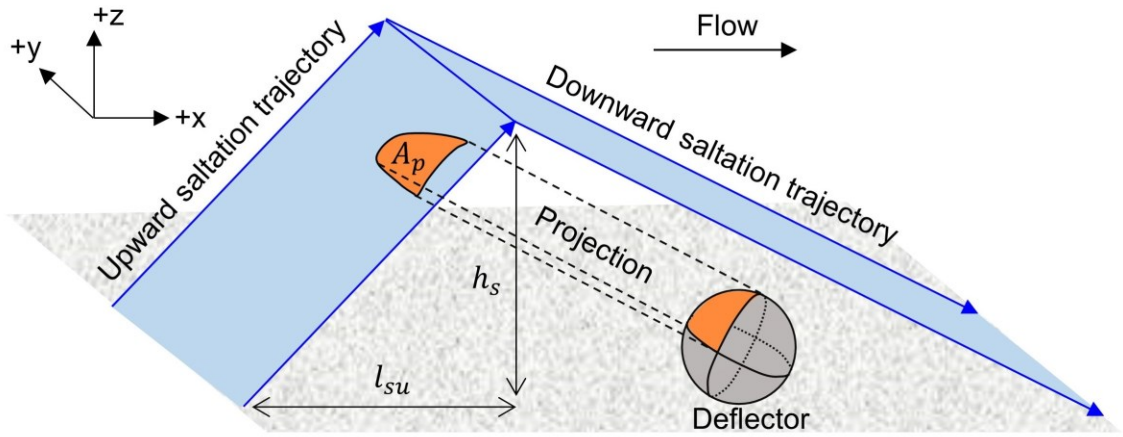

Figure 3.2 Schematic of upward and downward trajectories based on the saltation height h_s and hop length l_{su}, and the projected area of the deflector surface A_p onto the plane parallel to the upward saltation trajectory, following the downward saltation trajectory.

3.2.2. Expression of lateral erosion rate for uniformly distributed cover

3.2.2.1 Impact Velocity v_i

Substituting Equation 3.5 into Equation 3.4 and solving for the outgoing lateral velocity v_o, we obtain

$$v_o = 2C_r n_y (n_x u_s + n_z w_s) \qquad \text{(Equation 3.13).}$$

For uniformly distributed alluvium, Li et al. (2020) showed that the deflection locations and hence the normal vector $\hat{\boldsymbol{n}}$ shifts with relative sediment supply rate q_s/q_t. For example, the vertical component n_z moves towards the top of the deflector as the relative sediment supply rate q_s/q_t increases (Figure 3.1a-b). This occurs because the longitudinal distance between each row of deflectors reduces with increasing q_s/q_t, which leads to more shielding by the upstream row of the deflectors and hence shifts the vertical impact position higher. To derive an expression for the relation between $\hat{\boldsymbol{n}}$ with q_s/q_t, we assume that the various impact locations on the deflectors for the given hydraulic and supply conditions can be represented by the mean deflection location. Figure 3.3 shows the variation in mean downstream n_x, lateral n_y and vertical n_z components of $\hat{\boldsymbol{n}}$ with relative sediment supply q_s/q_t for different values of transport stage τ^*/τ_c^*, calculated from the Li et al. (2020) numerical simulations of saltating particle deflections. The normal vector components are near constant for different transport stages, but change linearly with relative sediment supply rate (Figure 3.3). The best fit linear regression relations between $\hat{\boldsymbol{n}} = (n_x, n_y, n_z)$ and q_s/q_t for uniformly distributed alluvium are shown in Figure 3.3.

The change in lateral velocity, after deflection, can be written in terms of lateral distance y between the deflector and the wall by substituting $dt = dy/v$ into Equation 3.3 to give

$$\frac{dy}{dv} = -\frac{1}{C_d}\frac{1}{v}. \qquad \text{(Equation 3.14)}$$

Assuming that the loss of momentum induced by being rebounded by the bed or other deflectors is negligible, we can derive an analytical solution for the impact velocity on the wall v_i as a function of distance y by integrating both sides of Equation 3.14,

$$v_i = v_o e^{-C_d y}. \qquad \text{(Equation 3.15)}$$

A minimum wall-normal velocity v_{min} is adopted here to distinguish between impacts that can cause erosion and impacts that do not because they are viscously damped. Viscous damping is a function of the particle Stokes number S_t (Davis et al., 1986; Schmeeckle et al., 2001; Joseph & Hunt, 2004), such that the minimum velocity can be expressed as

$$v_{min} = \frac{9 S_t \rho_w \eta}{\rho_s D} \qquad \text{(Equation 3.16)}$$

where η is the kinematic viscosity of the fluid (10^{-6} $m^2 s^{-1}$). Collisions of glass spheres in water become partially damped for $S_t < \sim 100$ (Schmeeckle et al., 2001b; Joseph & Hunt, 2004). At the transition from elastic and viscously-damped collisions, observations of S_t is more scattered for natural particles. The value of $S_t = 100$ is selected here for simplicity. The maximum distance y_{max} over which a deflector can cause wall erosion can be solved for by substituting Equation 3.16 into Equation 3.15

$$y_{max} = \frac{1}{C_d} \ln \frac{v_o}{v_{min}} \qquad \text{(Equation 3.17)}$$

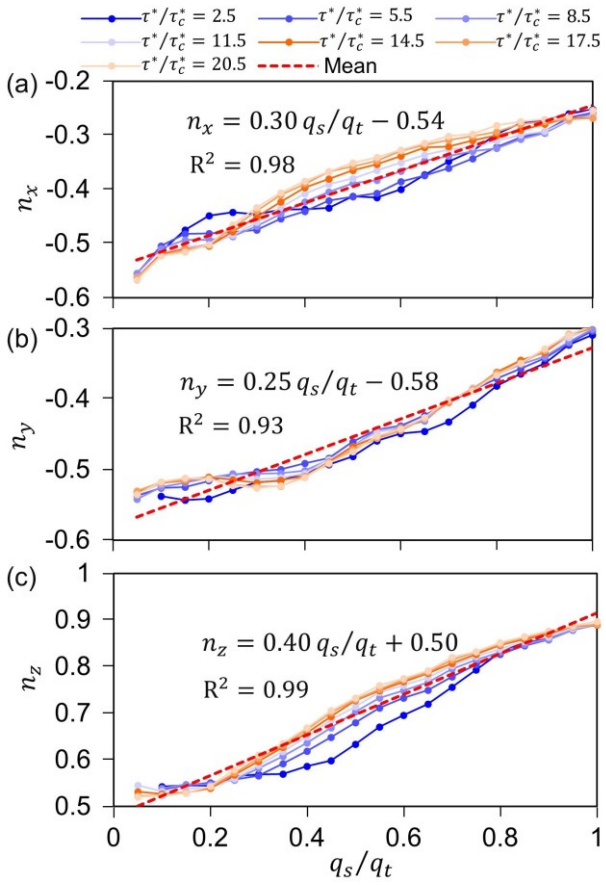

Figure 3.3 The mean downstream component n_x, mean lateral component n_y, and mean vertical component n_z of the normal vector $\hat{n}$ as a function of relative sediment supply q_s/q_t for various transport stages τ^*/τ_c^*, which were obtained from the Li et al. (2020) simulations of saltating particle deflections. n_x is negative in the upstream direction, n_y is negative towards the wall closest to the deflector and n_z is positive upwards.

3.2.2.2 Maximum impact height h_{max}

The maximum impact height h_{max} can be calculated from the vertical movement of bedload particles after being deflected by the alluvium. Assuming that negligible vertical momentum is lost by bedload particles colliding with the bed or other deflectors, the deceleration of an upward moving particle can be calculated simply from the force balance between fluid drag and gravity

$$-\frac{dw}{dt} = C_d w^2 + C_g, \qquad \text{(Equation 3.18)}$$

where w is the velocity in the vertical dimension (positive upwards). Equation 18 can be written in terms of vertical distance z by substituting $dt = dz/w$, which yields

$$-w\frac{dw}{dz} = C_d w^2 + C_g. \qquad \text{(Equation 3.19)}$$

The maximum erosion height h_{max} can be solved by integrating Equation 3.19 when w reduces from the initial outgoing velocity w_o to 0

$$h_{max} = 1.5D + \frac{1}{2C_d}\ln\left(\frac{C_d {w_o}^2}{C_g} + 1\right), \qquad \text{(Equation 3.20)}$$

where the boundary condition of the maximum impact height of the bedload particle center on the alluvium surface $z(w = w_o) = 1.5D$ is applied, and w_o can be solved by substituting Equation 3.5 into Equation 3.4

$$w_o = C_r(w_s - 2n_z(n_x u_s + n_z w_s)). \qquad \text{(Equation 3.21)}$$

The calculation of h_d to determine w_s from Equation 3.7 requires discretizing of the deflector surface into grid cells for each combination of transport stage τ^*/τ_c^* and relative sediment supply rate q_s/q_t in the Li et al. (2020) numerical model. To derive an expression for h_d, we assume that the impact height for the given hydraulic and supply conditions can be represented by the mean impact height. We find the best data collapse when we non-dimensionlize impact height h_d by dividing by saltation height h_s. Figure 3.4a shows the best fit regression of the variation in mean h_d/h_s with transport stage τ^*/τ_c^* and relative sediment supply rate q_s/q_t calculated from Li et al. (2020) numerical simulations of saltating particle deflections. h_d/h_s exponentially decreases with transport stage τ^*/τ_c^* due to the increase in hop height with larger shear stress but linearly increases with relative sediment supply rate due to the shift of impact height towards the top of the deflector with larger extent of alluvial cover. The residuals of estimates of h_d/h_s from the regression are below 0.1 for more than 95% of the transport stage τ^*/τ_c^* and relative sediment supply rate q_s/q_t combinations (Figure 3.4b). The error range of the prediction from the regression is below 15% for the full range of transport and supply conditions. The

largest residuals (~15%) are located near the threshold of motion where lateral erosion rate is relatively small.

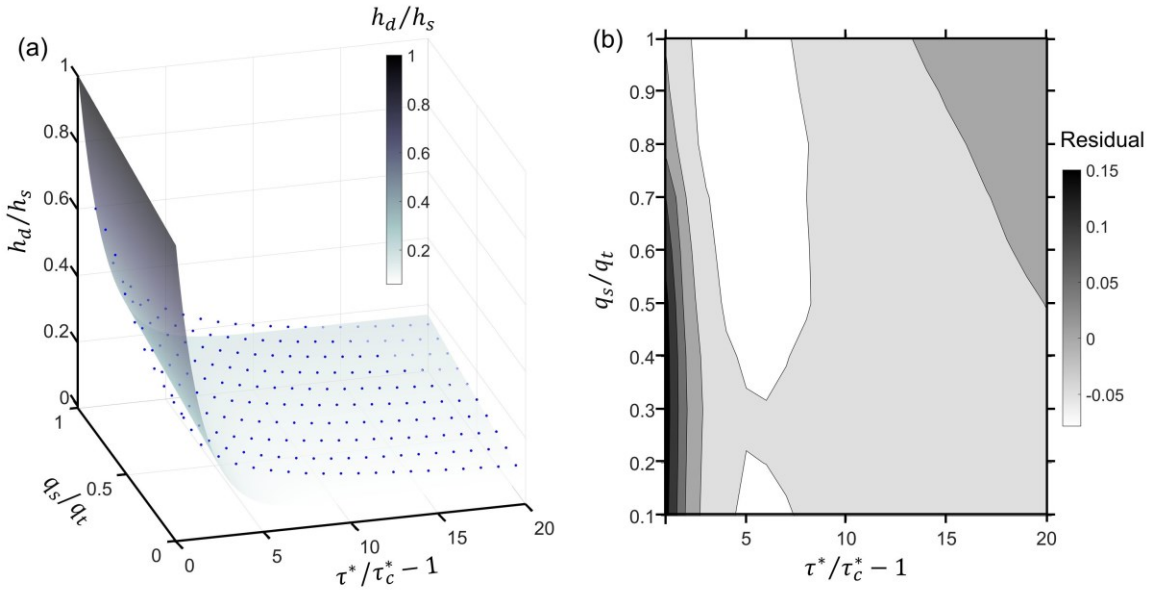

Figure 3.4 a) Variation in h_d/h_s with transport stage τ^*/τ_c^* and relative sediment supply rate q_s/q_t , and b) residuals of the regression as a function of transport stage τ^*/τ_c^* and relative sediment supply rate q_s/q_t.The regression that is shown as the 3D surface of a) is $h_d/h_s = 0.83e^{-0.68(\tau^*/\tau_c^*-1)} + 0.11\,q_s/q_t + 0.06$.The data used to derive the regression are shown as dots, which are obtained from the Li et al. (2020) model.

3.2.2.3 Projected area A_p

The projected area A_p can be obtained by integrating the projected area on each slice of the deflector surface. It has been shown that only ¼ of the semi-spherical deflector surface that faces upstream and the wall closer to the deflector is effective at deflecting bedload particles toward the wall (Li et al., 2020). Therefore, we choose to integrate the projected area on each slice of ¼ of the semi-spherical deflector surface and solve the projected area A_p as

$$A_p = \frac{\pi}{24} D^2 \left(\frac{l_{su}}{h_s} + \frac{1}{2}\right) \frac{\sqrt{h_s^2 + l_{su}^2}}{l_{su}}. \qquad \text{(Equation 3.22)}$$

The impact area on each deflector decreases with higher relative sediment supply rate as the vertical normal vector n_z shifts up. To account for this effect, A_p in Equation 3.22 is multiplied by $(1 - n_z)$

$$A_p = \frac{\pi}{24} D^2 \left(\frac{l_{su}}{h_s} + \frac{1}{2}\right) \frac{\sqrt{h_s^2 + l_{su}^2}}{l_{su}} (1 - n_z). \qquad \text{(Equation 3.23)}$$

3.2.2.4 Composite expression for the lateral erosion rate

All deflectors located to the wall closer than the maximum distance (i.e. $y \leq \mathrm{y_{max}}$) can effectively deflect bedload particles to erode the wall. Substituting Equations 3.19 and 3.23 into Equation 3.2, the total erosion rate for uniformly distributed alluvium E_{lu} is a sum of erosion rates caused by each deflector within $y_u(i) \leq y_{max}$ ($i = 1,2,3, \dots, N_u$, N_u is the total number of deflectors, $y_u(i)$ is the distance between the ith deflector and the eroded wall), given as

$$E_l = \sum_{i=1}^{N_u} \frac{\pi Y}{24 k_v \sigma_T^2} \frac{D^2}{d h_{max}} q_s \left(\frac{1}{h_s} + \frac{1}{2 l_{su}}\right)(1 - n_z)\, v_0^2 e^{-2C_d y_u(i)} \left(1 - (u^*/w_f)^2\right)^{1.5}.$$

(Equation 3.24)

The distance $y_u(i)$ between the ith deflector and the eroded wall can be determined from the distance between two adjacent deflectors d, using $d/2$ as the distance between the center of the first deflector to the wall (Figure 3.1a-b)

$$y_u(i) = \left(i - \frac{1}{2}\right) d. \qquad \text{(Equation 3.25)}$$

N_u can be calculated from the number of deflectors located within the maximum distance y_{max} for uniformly distributed deflectors

$$N_u = y_{max}/d. \qquad \text{(Equation 3.26)}$$

Substituting Equations 3.25 and 3.26 into Equation 3.24, the lateral erosion rate for uniform distributed deflectors E_{lu} can be solved for from the sum of a geometric sequence with a common ratio of $e^{-2C_d d}$ and a total number of N_u

$$E_{lu} = \frac{\pi Y}{48 k_v \sigma_T^2} \frac{D}{h_{max}} \frac{q_s^2 (1 - 0.8 q_s/q_t)}{q_t} \left(\frac{1}{h_s} + \frac{1}{2 l_{su}}\right) v_0^2 \frac{1 - e^{-2 C_d D q_t / q_s}}{e^{C_d D q_t/q_s} - e^{-C_d D q_t/q_s}} \left(1 - (u^*/w_f)^2\right)^{1.5}.$$

(Equation 3.27)

3.2.3. Expression of lateral erosion rate for patchy cover

We also consider the alluvium formed in a continuous patch that begins at the adjacent wall and expands toward the opposite wall (Figure 3.1c-d). We assume that the zone of patchy cover is persistent for given sediment supply and transport conditions. The patchy cover is a special case of uniformly distributed coverage where particles are immediately adjacent one another (Figure 3.1c-d). At low sediment supply rates, the cover is clustered to one side of the channel (referred to as the adjacent wall hereafter, Figure 3.1c). The alluvium moves toward the opposite wall as the sediment supply increases (Figure 3.1d). The distance between two adjacent deflectors d and the normal vector $\hat{\boldsymbol{n}}$ can be treated as a special case of uniformly distributed alluvium when the bed is fully covered ($q_s/q_t = 1$), which gives $d = D$ and $\hat{\boldsymbol{n}} = \left(n_x, n_y, n_z\right) = (-0.24, -0.33, 0.90)$.

For patchy cover, the alluvium and hence lateral erosion concentrate near the adjacent wall at low sediment supply, but will move towards the opposite wall so that the opposite wall starts to be eroded when the bed is near fully covered. Therefore, both sides of the walls need to be considered. For the erosion rate on the adjacent wall, the total number of deflectors that contribute to lateral erosion increases with the fraction of alluvium, until the distance between the furthest deflector and the adjacent wall y_a is bigger than y_{max}. This occurs because the bedload particle impacts that are deflected by a deflector located from the wall further than y_{max} are assumed to be viscously damped. Following the same procedure for calculating E_{lu}, the erosion rate on the adjacent wall E_{lpa} can be obtained from introducing the viscously damping effect and replacing d and $\hat{\boldsymbol{n}}$ for uniformly distributed cover with $d = D$ and $\hat{\boldsymbol{n}} = (-0.24, -0.33, 0.90)$, given as

$$E_{lpa} = \begin{cases} \frac{\pi Y}{240 k_v \sigma_T^2} \frac{D}{h_{max}} q_s \left(\frac{1}{h_s} + \frac{1}{2 l_{su}}\right) v_0^2 \frac{1-e^{-2C_d y_a}}{e^{C_d D} - e^{-C_d D}} (1 - (u^*/w_f)^2)^{1.5}; & \text{if } y_a < y_{max} \\ \frac{\pi Y}{240 k_v \sigma_T^2} \frac{D}{h_{max}} q_s \left(\frac{1}{h_s} + \frac{1}{2 l_{su}}\right) v_0^2 \frac{1-e^{-2C_d y_{max}}}{e^{C_d D} - e^{-C_d D}} (1 - (u^*/w_f)^2)^{1.5}; & \text{otherwise} \end{cases},$$

(Equation 3.28)

where $y_a = W\, q_s/q_t$, and W is the channel width.

On the opposite wall, there is no erosion when the distance between the furthest deflector and the opposite wall y_o is bigger than y_{max} ($y_o > y_{max}$) due to viscously damping effect, and starts to increase with increasing bed coverage when $y_o \leq y_{max}$. Following the same procedure for calculating E_{lu}, the erosion rate on the opposite wall E_{lpo} can also be obtained from replacing d and $\hat{\boldsymbol{n}}$ for uniformly distributed cover with $d = D$ and $\hat{\boldsymbol{n}} = (-0.24, -0.33, 0.90)$, given as

$$E_{lpo} = \begin{cases} 0; & \text{if } y_o > y_{max} \\ \frac{\pi Y}{240 k_v \sigma_T^2} \frac{D}{h_{max}} q_s \left(\frac{1}{h_s} + \frac{1}{2 l_{su}}\right) v_0^2 \frac{e^{-2C_d y_o} - e^{-2C_d y_{max}}}{e^{C_d D} - e^{-C_d D}} (1 - (u^*/w_f)^2)^{1.5}; & \text{otherwise} \end{cases},$$

(Equation 3.29)

where $y_o = W - y_a$.

3.2.4. Coupled erosion models

Sklar & Dietrich (2004) developed a model of vertical bedrock erosion E_v by bedload particle impacts from sediment supply and shear stress

$$E_v = \frac{0.08 R_b g Y}{k_v \sigma_T^2} q_s \left(1 - \frac{q_s}{q_t}\right) \left(\frac{\tau^*}{\tau_c^*} - 1\right)^{-0.5} \left(1 - \left(\frac{u^*}{w_f}\right)^2\right)^{1.5}. \quad \text{(Equation 3.30)}$$

Vertical and lateral erosion can be coupled from the ratio of lateral erosion rate to vertical erosion rate for uniformly distributed alluvium E_{lu}/E_v, for the adjacent wall of the continuous patchy cover E_{lpa}/E_v, and for the opposite wall of the continuous patchy cover E_{lpo}/E_v.

Vertical erosion rate (E_v) and lateral erosion rates for uniformly distributed alluvium (E_{lu}) and patchy alluvium (E_{lpa} and E_{lpo}) can also be non-dimensionalized by multiplying by $\sigma_T^2/\rho_s Y (gD)^{1.5}$ (Sklar & Dietrich, 2004)

$$E_v^* = \frac{0.046(R_b\tau_c^*)^{1.5}}{k_v}\frac{q_s}{q_t}(1-\frac{q_s}{q_t})(\frac{\tau^*}{\tau_c^*}-1)(1-(\frac{u^*}{w_f})^2)^{1.5} \quad \text{(Equation 3.31a)}$$

$$E_{lu}^* = k\frac{D}{h_{max}}(\frac{q_s^2}{q_t^2}-\frac{4q_s^3}{5q_t^3})(\frac{\tau^*}{\tau_c^*}-1)^{1.5}(\frac{1}{h_s}+\frac{1}{2l_{su}})v_0^2\frac{1-e^{-2C_2y_{max}}}{e^{C_2Dq_t/q_s}-e^{-C_2Dq_t/q_s}}(1-(u^*/w_f)^2)^{1.5}$$

(Equation 3.31b)

$$E_{lpa}^* = \begin{cases}\frac{k}{5}\frac{D}{h_{max}}\frac{q_s}{q_t}\left(\frac{1}{h_s}+\frac{1}{2l_{su}}\right)(\frac{\tau^*}{\tau_c^*}-1)^{1.5}v_0^2\frac{1-e^{-2C_2y_a}}{e^{C_2D}-e^{-C_2D}}(1-(u^*/w_f)^2)^{1.5}; \text{if } y_a < y_{max} \\ \frac{k}{5}\frac{D}{h_{max}}\frac{q_s}{q_t}\left(\frac{1}{h_s}+\frac{1}{2l_{su}}\right)(\frac{\tau^*}{\tau_c^*}-1)^{1.5}v_0^2\frac{1-e^{-2C_2y_{max}}}{e^{C_2D}-e^{-C_2D}}(1-(u^*/w_f)^2)^{1.5}; \quad \text{otherwise}\end{cases}$$

(Equation 3.31c)

$$E_{lpo}^* = \begin{cases}0; & \text{if } y_o > y_{max} \\ \frac{k}{5}\frac{D}{h_{max}}\frac{q_s}{q_t}\left(\frac{1}{h_s}+\frac{1}{2l_{su}}\right)(\frac{\tau^*}{\tau_c^*}-1)^{1.5}v_0^2\frac{e^{-2C_2\,y_o}-e^{-2C_2y_{max}}}{e^{C_2D}-e^{-C_2D}}(1-(u^*/w_f)^2)^{1.5}; & \text{otherwise}\end{cases}$$

(Equation 3.31d)

where $k = \frac{0.12\pi {R_b}^{0.5}{\tau_c^*}^{1.5}}{k_v g}$. Equations 3.31a-d reveal that, for given critical non-dimensional shear stress τ_c^* and grain size D, both non-dimensional vertical and lateral erosion rate can be considered as a function of just two dimensionless quantities: transport stage τ^*/τ_c^* and relative sediment supply rate q_s/q_t because the saltation trajectory parameters h_{max}, y_{max}, h_s and l_{su} all depend on τ^*/τ_c^* and q_s/q_t.

3.2.5. Model Implementation

In order to use Equations 3.27-3.31, we must specify water discharge Q_w, sediment supply rate Q_s, channel width W, channel slope S and the bedload particle diameter D. We must also invoke a hydraulic model. Assuming steady uniform flow, the total shear stress τ can be expressed as a function of hydraulic radius R or Darcy-Weisbach hydraulic friction factor f

$$\tau = \rho_w g R S = \frac{\rho_w f \bar{u}^2}{8} \quad \text{(Equation 3.32)}$$

where $R = hW/(W + 2h)$, h is water depth and $\bar{u}$ is flow velocity. Following Johnson (2014), we specify the Darcy-Weisbach hydraulic friction factor f as a weighted average of the spatial fractions of bedrock and alluvium

$$f = F_a f_a + (1 - F_a) f_b, \qquad \text{(Equation 3.33)}$$

where f_a and f_b are friction factors for alluvium and bedrock, respectively. They can be calculated from alluvium k_a and bedrock k_b roughness length scales as

$$f_a = \frac{1}{8(\frac{R}{k_a})^{1/3}} \qquad \text{(Equation 3.34a)}$$

$$f_b = \frac{1}{8(\frac{R}{k_b})^{1/3}} \qquad \text{(Equation 3.34b).}$$

In Equation 3.34, $k_a = nD(1 + (\kappa - 1)F_a)$ where the empirical coefficient $n = 2$ is used to relate hydraulic roughness to fractions of grain size that are coarser than the median grain size (e.g., Ferguson & Paola, 1997; Millar, 1999) and the non-dimensional alluvial roughness coefficient $\kappa = 2$ represents the average amplitude of topographic variations of alluvium (Chatanantavet & Parker, 2008; Johnson, 2014), and $k_b = \xi D$ where ξ scales bedrock roughness to grain size D (Johnson, 2014). Water depth h and shear stress τ can be solved by combining the continuity Equation $Q_w = WhU$ with Equations 3.32-3.34.

3.3. Model Results

3.3.1. Comparison between numerical and analytical model

The non-dimensional lateral erosion rate E_{lu}^* from both the Li et al. (2020) numerical model (Figure 3.5a) and our analytical model (Figure 3.5b) are similar. Inputs of both models are drawn from the South Fork Eel River (Table 3.1). The analytical model (Figure 3.5b) captures all the fundamental behaviors of the numerical model (Figure 3.5a), including the zero erosion rate at the thresholds of motion and suspension along the transport stage axis, the zero erosion rate when the bed is composed of bare bedrock, and the substantial erosion rate when the bed is fully alluviated along the relative sediment supply rate axis. It

also reproduces the maximum E_{lu}^* (~ 8×10^{-9}) at intermediate transport stage (τ^*/τ_c^*~10) where the growth in the impact energy is balanced by a decline in the impact frequency as the saltation hop length increases with shear stress, and at relatively high bed coverage (q_s/q_t~0.7) where the increase in the number of mobile bedload particles is balanced by the decrease in the deflection efficiency when the deflection location shifts towards the top of deflectors with increasing relative sediment supply rate.

On the functional surface bounded by q_s/q_t and τ^*/τ_c^*, the analytical model slightly over-predicts the erosion rate near three boundary conditions, including near the boundary of no motion, suspension and no cover, but under-predicts the erosion rate for the rest of the supply and transport conditions, yet the analytical model is always within 25% deviation of the numerical model (Figure 3.5c). The error range of the prediction from the analytical model is below 10% for ~85% of transport and supply conditions. The error range is above 10% at a small zone where E_{lu}^* is between 3×10-9 and 6×10-9. We used the Nash–Sutcliffe model efficiency coefficient (NSE) to assess the predictive power of the analytical model. The accuracy of the model increases with increasing NSE, and corresponds to a perfect prediction when NSE = 1. Our analytical model has a NSE value of 0.93, showing good agreement with the numerical model. This supports our assumptions that impact normal vectors and impact heights can be represented by the mean normal vector and mean impact height, respectively, and that the loss of momentum of bedload particles impacting alluvium and the bed prior to being deflected into the wall is negligible.

Table 3.1 Reference Site Values and Model Parameter Values for South Fork Eel River and Boulder Creek, CA.

Variable	South Fork Eel River	Boulder Creek	
		Upstream	Downstream
Bedload particle size D (m)	0.06 [a]	0.02 [b]	0.22 [b]
Channel width W (m)	18.0 [a]	4.5 [b]	9.6 [b]
Channel Slope S	0.0053 [a]	0.007 [b]	0.019 [b]
Sediment supply Q_s (kg/s)	42.6 [a]	39 [c]	145 [c]
Discharge (m^3/s)	39.1 [a]	59 [c]	74 [c]
Critical Shields stress τ_c^*		0.045 [d]	
Bedrock roughness scale ξ		0.1 [d]	
Water density ρ_w(kg/m^3)		1000 [d]	
Sediment density ρ_s (kg/m^3)		2650 [d]	
Rock elastic modulus Y (Pa)		5×10^{10} [a]	
Dimensionless rock resistance parameter k_v		10^6 [a]	
Rock tensile strength σ_T (Pa)		7×10^6 [d]	

[a] From Sklar & Dietrich (2004) .

[b] From Finnegan et al. (2017).

[c] Calibrated from values reported in Finnegan et al. (2017).

[d] Assumed.

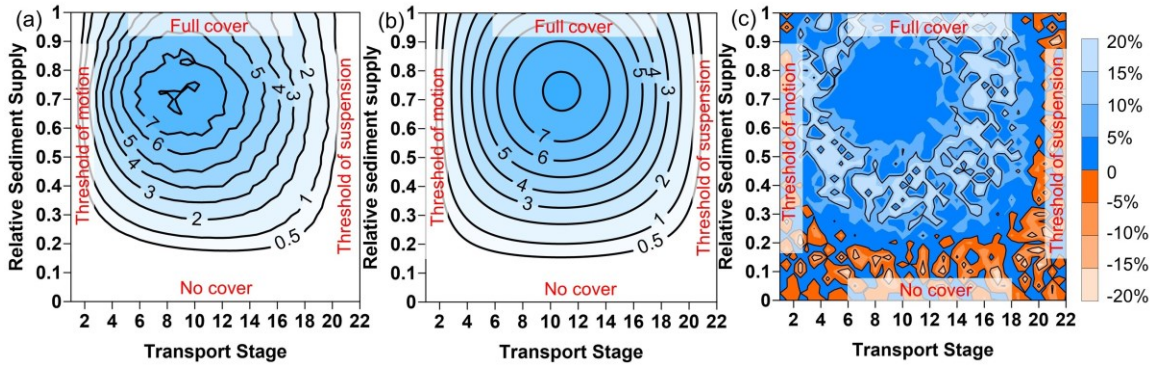

Figure 3.5 Contour plots of non-dimensional lateral erosion rate (×10^{-9}) as a function of transport stage and relative sediment supply rate predicted from a) the Li et al. (2020) numerical model and b) our analytical model for uniformly distributed alluvium. The percentage difference between contour plot a) and b) is shown in c). Model inputs are from South Fork Eel River listed in Table 3.1.Thresholds of motion and suspension may shift boundaries for other rivers.

3.3.2. Comparison between uniformly distributed and patchy cover models

Figure 3.6 shows the non-dimensional lateral erosion rate on the adjacent wall E^*_{lpa} (Figure 3.6a) and the opposite wall E^*_{lpo} (Figure 3.6b) as a function of transport stage τ^*/τ^*_c and relative sediment supply rate q_s/q_t, assuming the alluvium is formed in a continuous patch. The patchy cover model (Figure 3.6) predicts the same lateral erosion patterns as the uniformly distributed cover model (Figure 3.5b) at four τ^*/τ^*_c and q_s/q_t limits, where lateral erosion rate goes to zero at the threshold for entrainment, suspension and no cover, but is substantial at full bed coverage. On the adjacent wall, our patchy cover model shows a monotonic increase in E^*_{lpa} with increasing q_s/q_t (Figure 3.5a), because deflection location and hence the deflection efficiency are constant for the continuous patchy cover (Figure 3.1c-d), but the number of saltating bedload particles increases with increasing q_s/q_t, for given τ^*/τ^*_c. E^*_{lpa} peaks at full coverage (when the adjacent wall patch reaches the opposite wall) when the impact rate is the highest and at intermediate τ^*/τ^*_c when the tradeoff between energy and frequency of particle impacts is balanced. On the opposite wall, our patchy cover model predicts negligible erosion when the bed is <95% covered,

because there are no deflectors close enough to opposite wall to cause erosion. When bed coverage is >95%, E^*_{lpo} increases with increasing q_s/q_t because the number of deflections of bedload particles increases with bed coverage. E^*_{lpo} peaks at the same position with E^*_{lpa} on the functional surface where the bed is fully covered and the distribution of alluvium is symmetrical.

In contrast to the uniformly distributed cover model, the patchy cover model predicts different erosion rates on the two channel walls (E^*_{lpa} and E^*_{lpo}) as a result of the asymmetrical distribution of alluvium along the channel cross section, except when the bed is fully covered. E^*_{lpa} is higher than E^*_{lpo} for the full range of sediment supply and transport conditions due to more deflections towards the adjacent wall, except for the fully coverage where E^*_{lpa} equals to E^*_{lpo} (Figure 3.6a-b).

When the bed is <20% covered, E^*_{lpa} is higher than E^*_{lu} (Figure 3.6c) because the alluvium is clustered to the adjacent wall for the patchy cover but is scarcely distributed in the channel for the uniformly distributed cover at low coverage (Figure 3.1a&c). However, E^*_{lpa} becomes lower than E^*_{lu} when the coverage is >20%, because the deflection efficiency for uniformly distributed cover is higher than that for continuous cover for a given transport stage. E^*_{lpo} is lower than E^*_{lu} for the full range of bed coverage because the alluvium is further to the opposite wall and the impact efficiency is lower for the continuous patchy cover (Figure 3.6d), except at full bed coverage where $E^*_{lpa} = E^*_{lpo} = E^*_{lu}$.

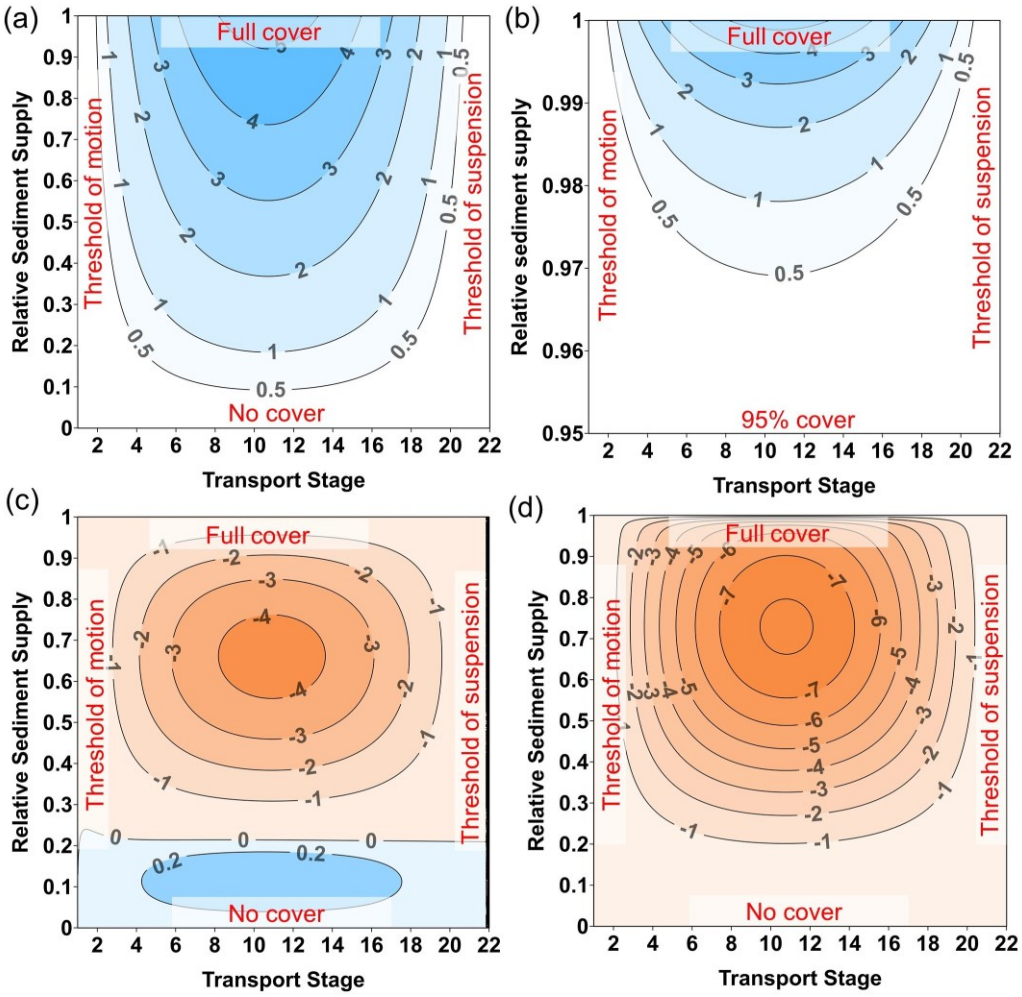

Figure 3.6 Contour plots of non-dimensional lateral erosion rate (×10^{-9}) on a) the adjacent wall E^*_{lpa} and b) the opposite wall E^*_{lpo} for patchy cover, and contour plots of the difference between patchy and uniformly distributed cover c) $E^*_{lpa} - E^*_{lu}$ and d) $E^*_{lpo} - E^*_{lu}$. The relative sediment supply rate axis in panel b) starts at 0.95 because the erosion rate is otherwise negligible. Model inputs are from South Fork Eel River listed in Table 3.1.

3.3.3. Competition between vertical and lateral erosion

The Sklar & Dietrich (2004) vertical erosion model predicts zero E^*_v at all four boundaries of the functional surface defined by τ^*/τ^*_c and q_s/q_t (Figure 3.7a). E^*_v peaks at intermediate bed coverage where the increase in bedload particle impacts and the decrease in bed exposure with increasing q_s/q_t are well balanced, and at intermediate τ^*/τ^*_c where the increase in particle impact energy

and the reduction in frequency of particle impact with increasing shear stress are well balanced as the saltation hop length gets longer (Sklar & Dietrich, 2004).

For the uniformly distributed cover model, the ratio of lateral erosion rate to vertical erosion rate E_{lu}^*/E_v^* increases with increasing q_s/q_t and peaks when the bed is fully covered (Figure 3.7b), regardless of the variations of E_v^* (Figure 3.7a) and E_{lu}^* (Figure 3.5b) with q_s/q_t. This occurs because the ratio E_{lu}^*/E_v^* is ultimately controlled by the change in E_v^* and E_{lu}^* together. E_{lu}^*/E_v^* increases for $q_s/q_t < 0.5$ because E_{lu}^* increases faster than E_v^*, continues to increase for $0.5 < q_s/q_t < 0.7$ because E_{lu}^* continues to increase but E_v^* starts to decrease, and goes to infinity as q_s/q_t approaches 1 because E_v^* declines to zero. E_{lu}^*/E_v^* also shows a monotonic increase with increasing τ^*/τ_c^* because E_{lu}^* increases faster than E_v^* when τ^*/τ_c^* is below 10 but decreases slower than E_v^* when τ^*/τ_c^* is above 10. E_{lu}^* is negligible when bed coverage is below 20% where $E_{lu}^*/E_v^* < 0.1$, and dominates over E_v^* for ~25% of the transport and supply conditions when the bed is largely covered by alluvium (Figure 3.7b).

For patchy cover, the ratios E_{lpa}^*/E_v^* (Figure 3.7c) and E_{lpo}^*/E_v^* (Figure 3.7d) increase monotonically with increasing q_s/q_t for given τ^*/τ_c^* because E_{lpa}^* and E_{lpo}^* increase faster than E_v^* when $q_s/q_t < 0.5$, and E_{lpa}^* and E_{lpo}^* continues to increase but E_v^* decreases when $q_s/q_t > 0.5$. E_{lpa}^*/E_v^* and E_{lpo}^*/E_v^* also grow with increasing τ^*/τ_c^* for given q_s/q_t because E_{lpa}^* and E_{lpo}^* increases faster than E_v^* when $\tau^*/\tau_c^* < 10$ but decrease slower than E_v^* when $\tau^*/\tau_c^* > 10$. E_{lpa}^* is negligible at low transport stages ($\tau^*/\tau_c^* < 2$) where $E_{lpa}^*/E_v^* < 0.1$. E_{lpa}^* is less than E_v^* for bed coverages below ~ 85% where $E_{lpa}^*/E_v^* < 1$, but dominates over E_v^* when the bed is more than ~ 85% covered where $E_{lpa}^*/E_v^* > 1$. In contrast, E_{lpo}^* is negligible for almost 95% of transport and supply conditions ($q_s/q_t < 0.95$) and only becomes higher than E_v^* when the bed is more than ~98% covered where $E_{lpo}^*/E_v^* > 1$.

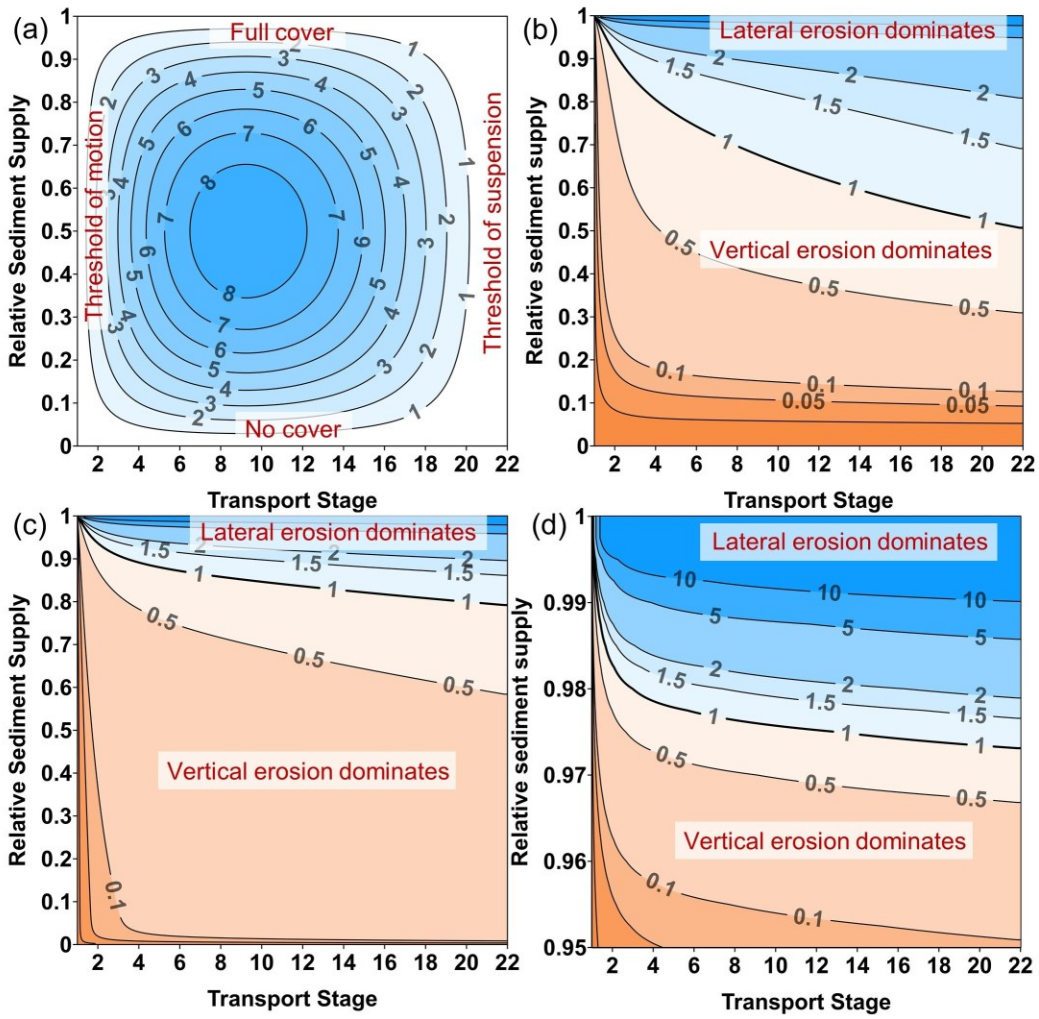

Figure 3.7 Contour plots of a) non-dimensional vertical erosion rate E_v^* (×10^{-9}), b) the ratio of lateral erosion rate predicted by the uniformly distributed cover model to vertical erosion rate (E_{lu}^*/E_v^*), c) the ratio of lateral erosion rate on the adjacent wall predicted by the patchy cover model to vertical erosion rate (E_{lpa}^*/E_v^*), and d) the ratio of lateral erosion rate on the opposite wall predicted by the patchy cover model to vertical erosion rate (E_{lpo}^*/E_v^*), as a function of transport stage and relative sediment supply rate. Model inputs are from South Fork Eel River listed in Table 3.1.

3.3.4. Sensitivity Analysis

The saltation-abrasion model (Equations 3.27-3.29) suggests that the lateral erosion rate depends on three principal variables: sediment supply, shear stress and grain size, for a given rock strength. Here, we explore the behavior of

the lateral erosion rate for uniformly distributed alluvium and continuous patchy alluvium as we systematically vary each of these three variables, while holding others constant. To help guide our selection of model input values for the sensitivity analysis, we use the reach of Boulder Creek, CA, that is upstream of the tributary that causes the change in sediment supply and grain size, as a reference site (Finnegan et al., 2017).

Table 3.1 lists the hydraulic and sediment supply conditions in upstream and downstream reaches of the Boulder Creek. The net effect of the wide distribution of discharge and sediment supply is assumed to be represented by the reference discharge and sediment supply acting over a limited duration. Finnegan et al. (2017) reported the channel width, depth, slope, median grain size, alluvial coverage and shear stress, with no direct measurement of discharge and sediment supply in upstream and downstream reaches of the Boulder Creek. Here we calculate the sediment supply rate from alluvial coverage and shear stress using the linear relation between bed alluvial coverage and relative sediment supply ($F_a = q_s/q_t$). The discharge is calculated from channel width, depth, slope and median grain size using hydraulic friction equations (Equations 3.32-3.34). The intermittency factor (0.27%) for Boulder Creek is calibrated from the uplift rate of the Boulder Creek (~ 0.15 mm yr^{-1}), given that the river is found at near steady state where the uplift rate is balanced by the vertical erosion rate (Finnegan et al., 2017).

3.3.4.1 Uniformly distributed cover model

We varied sediment supply Q_s for a series of constant transport stages using the uniformly distributed cover model (Figure 3.8a). Holding transport stage constant is equivalent to selecting a constant shear stress and grain size. There is no lateral erosion where the sediment supply is zero because there are no tools to abrade the channel walls (and no alluvial cover). At low supply rates, E_{lu} increases with increasing Q_s, due to the growth in the extent of alluvium to deflect bedload particles and the increase in concentration of mobile particles. At high Q_s, E_{lu} decreases with increasing Q_s, due to the shift of deflection locations

towards the top of deflectors (Figure 3.1a-b) and hence the decrease in the efficiency of deflecting bedload particles when deflectors become densely packed. When Q_s is higher than the transport capacity, E_{lu} becomes constant because the bed is fully covered. E_{lu} peaks at a critical level of sediment supply where the bed is ~ 70% covered (Figure 3.5b). The sediment supply required to initiate erosion increases with increasing transport stage, because greater transport stage requires greater sediment supply to cover the bed. As the transport stage increases, the magnitude of the peak E_{lu} increases, but begins to decline at high transport stages because the increase in impact velocity with increasing shear stress is more than offset by the decrease in impact rate as saltation hop length approaches infinity at the threshold of suspension.

When sediment supply and grain size are held constant, the uniformly distributed cover model predicts an inverse U-shaped variation of lateral erosion rate with shear stress (Figure 3.8b). There is an increase in E_{lu} with increasing shear stress until the transport capacity exceeds the sediment supply and then a decline in E_{lu} because the transport capacity exceeds the sediment supply. There is an inflection in the inverse U-shaped curves that occurs where there is enough excess shear stress to expose bed. At that point, E_{lu} increases more rapidly due to the growth in both the impact velocity and the deflection efficiency when the bed gets more exposed. E_{lu} goes to zero at high transport stages as the saltation hop length approaches infinity at the threshold of suspension (Figure 3.8b). All E_{lu} curves are the same until the inflection points because the bed is fully covered and the sediment is transported at its capacity before the slope break, regardless of variations in Q_s for different curves. The peak E_{lu} occurs at higher τ^*/τ_c^* for larger Q_s because greater rates of Q_s require greater excess transport capacity to achieve the optimal bed coverage for lateral erosion (~ 70%). Greater rates of sediment supply also require greater excess transport capacity to expose bedrock and shut down lateral erosion. A maximum in the peak E_{lu} occurs for an intermediate level of sediment supply, where the increase

in the number of saltating bedload particles and the extent of alluvial cover and the decrease in the deflection efficiency are balanced.

We explored the variation of E_{lu} with D, by holding shear stress constant for different sediment supply rates (Figure 3.8c). E_{lu} is zero for finer grain sizes because they are transported in suspension, and is also zero for larger grain sizes because they are too large to be transported by the given shear stress. The uniformly distributed cover model predicts a peak in E_{lu} for intermediate D. Peak E_{lu} occurs at smaller D for larger Q_s because greater rates of Q_s require greater excess transport capacity and hence smaller grain size to achieve the optimal bed coverage for lateral erosion. The magnitude of the peak E_{lu} increases and then declines with increasing Q_s. These are similar to the pattern of erosion rate peaks shown in Figure 3.8b, except that the direction of increase in transport stage along the horizontal axis is reversed because smaller grain size corresponds to higher transport stages for given shear stress.

3.3.4.2 Patchy cover model

We also varied sediment supply for a series of constant transport stages using the patchy cover model, which is equivalent to selecting a constant shear stress and grain size (Figure 3.9a-b). For given shear stress and grain size, E_{lpa} grows with increasing Q_s at low supply rates due to the increase in the extent of alluvium close to the adjacent wall, then peaks and remains constant at high supply rates, because Q_s is equal to the transport capacity and the bed becomes fully covered (Figure 3.9a). In comparison with E_{lpa}, E_{lpo} is negligible at low and intermediate supply rates due to the lack of alluvium close enough to cause deflections into the opposite wall (Figure 3.9b). When Q_s is close to the transport capacity, E_{lpo} increases rapidly with increasing Q_s because the cover extends across the channel towards the opposite wall (Figure 3.9b). The magnitude of peak E_{lpa} is the same as the peak E_{lpo} for given transport stage because the bed coverage is symmetrical along the channel cross section when the bed is fully covered (Figure 3.9a-b). Both E_{lpa} and E_{lpo} peak at higher Q_s for higher τ^*/τ_c^*

because higher shear stress requires higher supply rates to fully alluviate the bed. A maximum in the peak E_{lpa} and E_{lpo} occurs for an intermediate level of τ^*/τ_c^*, where the tradeoff between the energy and frequency of particle impacts with increasing shear stress are well balanced.

Holding sediment supply and grain size constant, E_{lpa} increases with increasing shear stress at low τ^*/τ_c^* due to the increase in transported sediment, but starts to decrease at high τ^*/τ_c^* where the extent of alluvial cover declines and the bed gets exposed with increasing transport capacity (Figure 3.9c). E_{lpa} peaks when the sediment supply is equal to the transport capacity. At low τ^*/τ_c^*, E_{lpo} also grows with increasing shear stress until the bed is fully alluviated (Figure 3.9d). Once the transport capacity exceeds the sediment supply, E_{lpo} decreases abruptly and becomes negligible at intermediate and high τ^*/τ_c^* due to the lack of alluvium close to the opposite wall (Figure 3.9d). Both E_{lpa} and E_{lpo} peak at larger τ^*/τ_c^* for larger Q_s because of the greater excess transport capacity required to transport the larger supplied sediment. The magnitude of the peak E_{lpa} and E_{lpo} rises with increasing Q_s (Figure 3.9c-d) due to the increased number of impacts caused by greater sediment transport rates.

The dependence of E_{lpa} and E_{lpo} on D and hence transport stage is also explored by holding all other variables constant (Figure 3.9e-f). E_{lpa} is zero for $D < 3.8$ mm as these grain sizes are transported in suspension for the input conditions. For $D > 3.8$ mm, E_{lpa} grows with increasing D due to the increase in the extent of alluvial cover. E_{lpa} peaks at the intermediate grain size where the transport capacity is equal to the supplied sediment, and starts to decline for larger grain sizes because sediment becomes less mobile for constant shear stress. E_{lpa} goes to zero for $D > 150$ mm because the shear stress is below the threshold of motion. In comparison with E_{lpa}, E_{lpo} is zero even when particles are transported as bedload for small grain sizes because of the lack of alluvium deposited close to the opposite wall (Figure 3.9f) . E_{lpo} increases with D rapidly once the alluvium moves towards the opposite wall and peaks at full bed

coverage when transport capacity is equal to the supplied sediment. Once the bed is fully covered, E_{lpo} follows the same trend of E_{lpa} for large D. Peak E_{lpa} and E_{lpo} occur at smaller D for larger Q_s and their magnitudes increase with increasing Q_s (Figure 3.9e-f). Figure 3.9e&f mirror Figure 3.9c&d, respectively, because the direction of increase in transport stage along the horizontal axis is reversed.

3.4. Discussion

3.4.1. Effect of width perturbations on erosion rates and feedbacks

Application of our model to Boulder Creek predicts that E_{lu} decreases slightly from 0.1 mm/yr to 0.09 mm/yr in response to the increase in Q_s from the upstream reach to the downstream reaches of the Boulder Creek, holding other variables constant. This occurs because the deflection efficiency decreases when the bed coverage shifts from partial coverage to full coverage. The patchy model predicts that E_{lpa} increases from 0.045 mm/yr to 0.09 mm/yr on the adjacent wall and E_{lpo} increases from 0 to 0.09 mm/yr on the opposite wall. The vertical erosion rate E_v goes to zero in response to the increase in Q_s from the upstream reach to the downstream reach of the Boulder Creek, holding other variables constant. This occurs because the bed becomes fully covered by the increasing sediment flux from the tributary, so the ratio E_l/E_v goes to infinity for both the uniformly distributed and patchy models. While the magnitude of lateral erosion is somewhat different using the uniformly distributed and patchy models, the pattern of change in E_l/E_v is consistent.

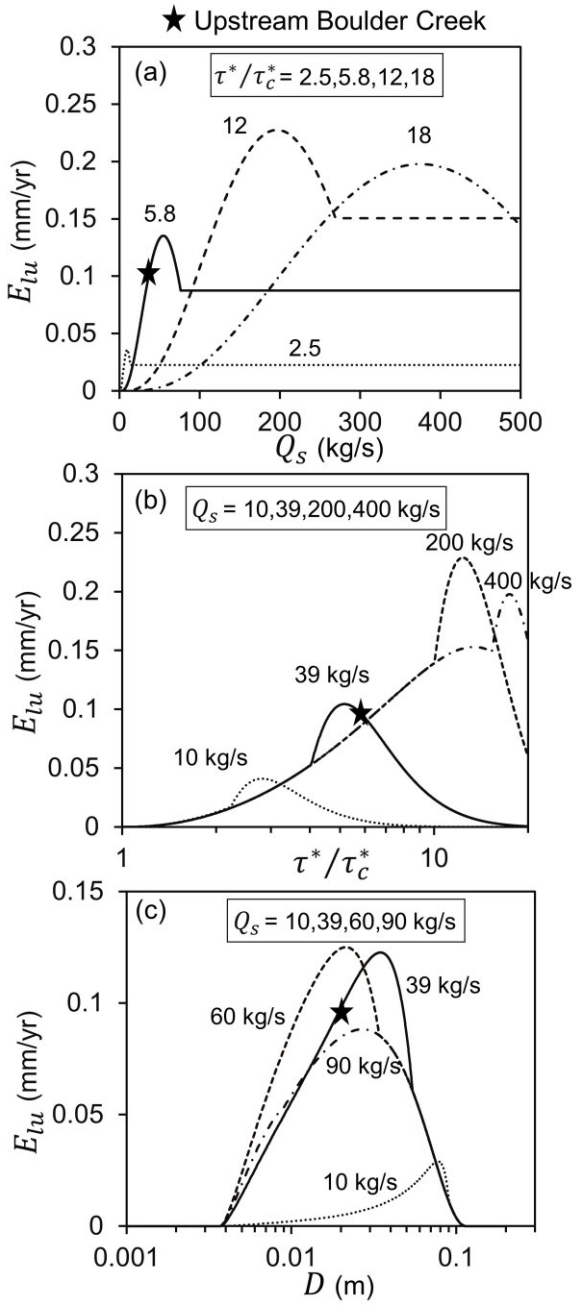

Figure 3.8 Lateral erosion rate for uniformly distributed cover E_{lu} a) as a function of Q_s for a series of constant transport stages τ^*/τ_c^*, holding grain size constant, b) as a function of τ^*/τ_c^* for a series of constant Q_s, holding grain size constant, and c) as a function of D for a series of constant Q_s, holding shear stress constant. The black stars represent the upstream reach of Boulder Creek (Table 3.1).

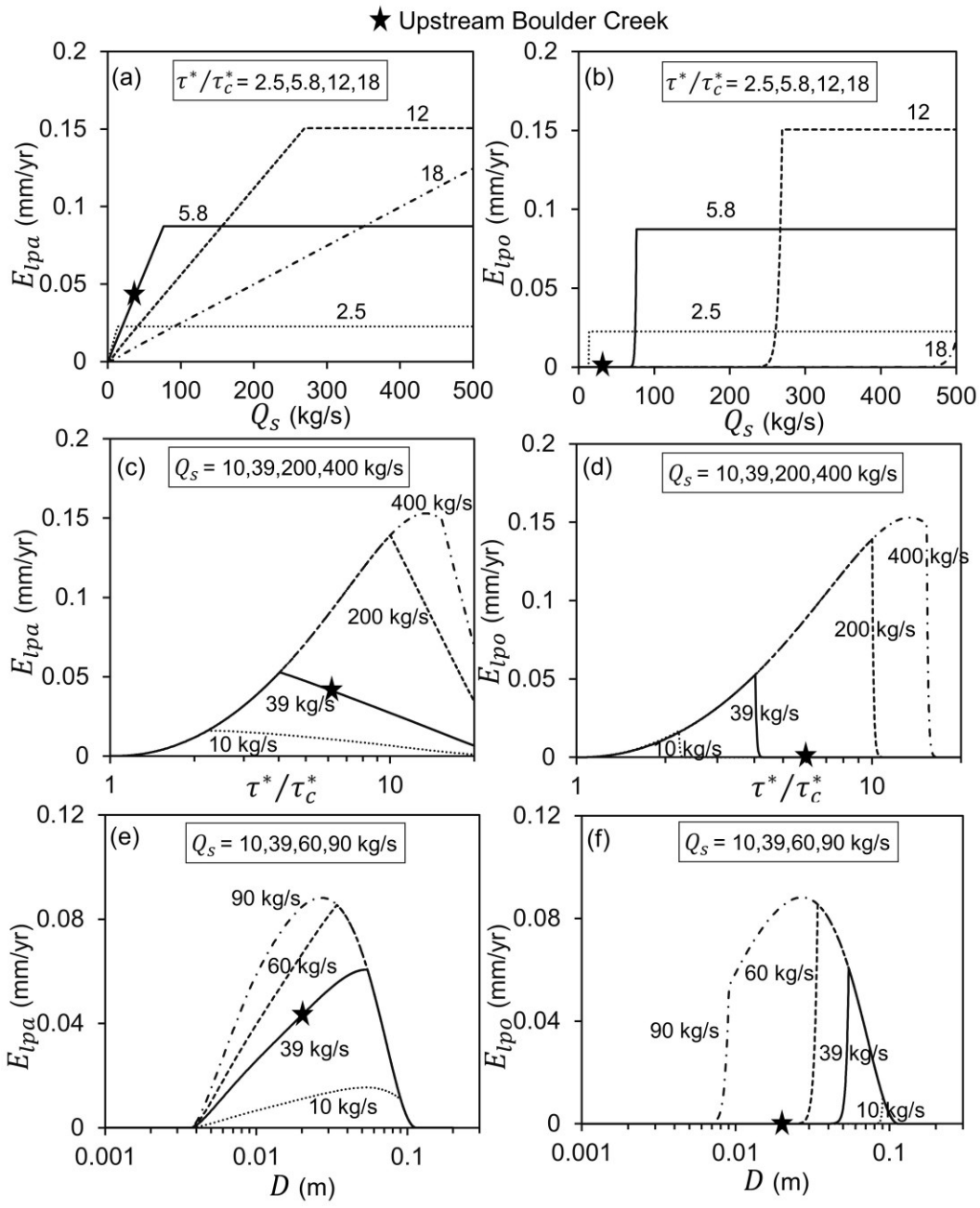

Figure 3.9 a) Lateral erosion rate on the adjacent wall E_{lpa} and b) on the opposite wall E_{lpo} as a function of Q_s for a series of constant transport stages τ^*/τ_c^*, holding grain size constant, c) E_{lpa} and d) E_{lpo} as a function of τ^*/τ_c^* for a series of constant Q_s, holding grain size constant, and e) E_{lpa} and f) E_{lpo} as a function of D for a series of constant Q_s, holding shear stress constant. The black stars represent the upstream reach of Boulder Creek (Table 3.1).

Coupled with the Sklar & Dietrich (2004) vertical erosion model, our analytical model for lateral erosion can be used to indicate how Boulder Creek achieves a stable width in the downstream reach that is two times that of the upstream reach. To examine how Boulder Creek achieves different stable widths, we examine how E_l/E_v responds to a width perturbation (a small change in channel width) by widening or narrowing and how the change in E_l/E_v affects the channel width. The influence of width perturbation on E_l/E_v is explored by varying width independently, holding discharge, sediment supply, grain size and slope to constant values specified for the Boulder Creek (Table 3.1). We elected to use the uniformly distributed model given the similarity in patterns of change in E_l/E_v. An increase in width causes an inverse U-shaped variation in τ^*/τ_c^* because as channels get wider, the effects of the wall roughness declines, increasing bed shear stress and exposing the bed, but that effect is eventually counteracted by decreasing depth, which decreases stress and alluviates the bed. This variation in τ^*/τ_c^* causes an inverse U-shaped variation in E_v and E_{lu} with width (Figure 3.10). However, E_{lu} peaks at a lower channel width than E_v (Figure 3.10) because the optimal bed coverage is higher for E_{lu} (~ 70%; Figure 3.5b) than for E_v (~ 50%; Figure 3.7a). Additionally, the range of channel widths experiencing lateral erosion is wider than for vertical erosion (Figure 3.10). This occurs because at very small or large widths, the bed is alluviated, but lateral erosion may continue as long as $\tau^*/\tau_c^* > 1$.

The ratio of lateral to vertical erosion rate E_{lu}/E_v is a U-shaped function of width (Figure 3.10). At low channel width E_{lu}/E_v is infinity because $E_v = 0$ when the transport stage is below the threshold to transport the supplied sediment and the bed is fully covered. As width increases, the bed becomes exposed and E_{lu}/E_v declines rapidly because bed exposure is beneficial for E_v, then more gently when both E_{lu} and E_v decline with decreasing τ^*/τ_c^*, forming the declining limb of the U-shaped function of E_{lu}/E_v with width. At large channel width, bed coverage starts to increase with decreasing τ^*/τ_c^*, which enhances lateral

erosion relative to vertical erosion, forming the increasing limb of the U-shaped function of E_{lu}/E_v with width.

The U-shaped variation in E_{lu}/E_v causes feedbacks on channel width adjustment. On the declining limb of the U-shaped variation, positive perturbations in width (widening) decrease E_{lu}/E_v causing relatively more vertical than lateral erosion. This would have a negative feedback on width (narrowing) to push channel back toward the pre-perturbation width (before the change), assuming channels can narrow by cutting vertically over some central portion of the channel width less than the full width (e.g., Finnegan et al., 2007; Johnson & Whipple, 2010; Nelson & Seminara, 2011). Negative perturbations (narrowing) on the declining limb increase E_{lu}/E_v (Figure 3.10), causing more lateral than vertical erosion and hence also creates a negative feedback to push channel back toward the pre-perturbation width. On the rising limb of the U-shaped variation, the opposite feedbacks would happen and width perturbations would tend to grow. To reach steady width, slope adjustments will occur on the rising limb. Continued channel widening would eventually shut down vertical erosion, because the bed would become alluviated. In order to pass the incoming sediment supply without filling up the channel, gradient would need to increase, producing a channel steepening response.

Application of width perturbation feedback to Boulder Creek reveals that the upstream reach is on the declining limb of the U-shaped curve (Figure 3.10a) where negative feedbacks on channel width adjustment will occur. If the channel gets wider or narrower, vertical erosion will return the channel to its original stable width without the need for slope adjustment. The downstream reach, however, is on the rising limb of the U-shaped curve (Figure 3.10b) where positive feedbacks on channel width adjustment will occur. The river has widened until the bed is covered with sediment and the slope steepened to pass the sediment load.

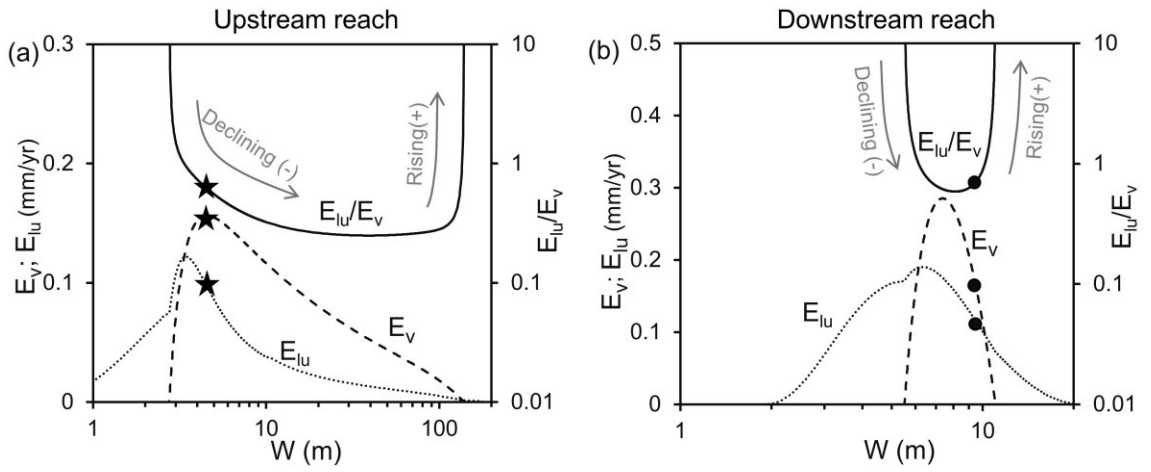

Figure 3.10 Influence of width perturbations on vertical erosion rate E_v, lateral erosion rate E_{lu} and the ratio of lateral to vertical erosion rate E_{lu}/E_v in the a) upstream and b) downstream reaches of the Boulder Creek. The upstream and downstream reaches are shown as black stars and dots, respectively.

3.4.2. Generalized model of width dynamics in bedrock rivers

The coupled vertical and lateral erosion model describes width dynamics for a wide range of sediment supply and transport conditions in bedrock channels. We propose a generalized phase diagram for width dynamics in bedrock rivers (Figure 3.11) based on our width perturbation analysis and the unique functional surface of E_l/E_v with variation in transport stage and sediment supply (Figure 3.7b-d). When $E_v \approx E_l$ ($E_l/E_v \approx 1$), the channel geometry is stable without significant changes in channel width, despite changes in sediment supply and transport conditions. If lateral erosion dominates over vertical erosion the channel would get wider by preferentially eroding the banks. If vertical erosion dominates, however, the channel would get narrower by cutting vertically over some central portion of the channel width less than the full width. On our phase diagram, we chose to represent the threshold of E_l/E_v between widening and narrowing as a range between 0.5 and 1.5, acknowledging the assumptions made in derivation of our model (e.g. bank angle, grain shape, deflection angles) and the uncertainty in transport thresholds used in the model.

At transport stages just above the threshold of motion and near the suspension threshold, we expect a somewhat different channel adjustment. Near the transport threshold, channel width cannot be adjusted because both lateral and vertical erosion rates go to zero. Instead, the channel slope changes because channels near the threshold of motion fill up with sediment and the gradient has to increase (steepening) to pass the supplied sediment. Near the threshold of suspension, we might expect a flattening behavior to occur. Sediment carried in suspension in one reach will eventually transition to bedload downstream and start to erode the bed through abrasion. It is reasonable to expect that increased erosion at this point may cause an upstream migrating knickpoint that could work through a reach, reducing or flattening the gradient.

The conceptual phase diagram has implications for exploring the current state of channel width and slope depending on where they plot in the widening, steady, narrowing, steepening and flatting phase spaces. An actively incising channels can be plotted somewhere on the phase diagram, based on the transport stage, bed coverage and the ratio of lateral to vertical erosion rates. Application of the phase diagram to the Boulder Creek example shows that both upstream and downstream reaches exist within the steady channel width phase space with the downstream reach being closer to the steepening and widening phase than the upstream reach (Figure 3.11). The conceptual phase diagram also has the potential to predict channel responses by isolating the control variables in bedrock rivers, such as grain size, sediment supply and discharge. Taking Boulder Creek as an example, increasing grain size causes a decrease in transport stage, encouraging the channel to get steeper. Increasing sediment supply causes an increase in bed coverage, encouraging the channel to get wider.

Bedrock rivers have been observed to get narrower with increasing vertical erosion rates in some setting but not in others (Lavé & Avouac, 2001; Pazzaglia & Brandon, 2001; Snyder et al., 2003; Tomkin et al., 2003; Duvall et al., 2004; Amos & Burbank, 2007). Turowski (2018) suggested that bedrock

channels tend to narrow with increasing uplift rates at transient state based on vertical erosion models, but did not incorporate the coupling of vertical and lateral erosion models. The conceptual phase diagram can be used to understand relations between controlling variables that give rise to the complex relation between incision rate and channel width. If an increase in vertical erosion rate causes E_l/E_v to drop below 0.5, the channel starts to get narrower as it shifts from steady state to narrowing state. Conversely, if there is a decrease in the vertical erosion rate that causes E_l/E_v to rise above 1.5 the channel will get wider. However, the channel will maintain a steady channel width if an increase or decrease in vertical erosion rate is too small to shift E_l/E_v outside of the 0.5 to 1.5 envelope.

The sensitivity of channel states to changes in discharge and sediment supply rates also differs depending on the phase state in Figure 3.11. If a bedrock river plots near the upper left corner of Figure 3.11 where narrowing states occur, small changes in sediment supply or discharge would shift the channel from narrowing into widening states and vice versa because widening and narrowing states are close to each other here. This striking change of channel states has been found in bedrock rivers of Tian Shan foreland, where varying water and sediment fluxes cause narrow, steep-wall canyons to widen abruptly by influencing the lateral erosion rate (Bufe et al., 2016). However, if a bedrock river has a more moderate sediment supply and transport stage, it would plot near the middle of our phase diagram and be relatively less sensitive to small changes in sediment supply and discharge. In Boulder Creek, the downstream reach is more sensitive to changes in sediment supply and transport stage than the upstream reach because it plots in the upper left corner of our phase diagram. A significant change in either transport stage or sediment supply could shift it out of stead state and into widening, narrowing, or steepening states. The upstream reach is less sensitive to changes in transport stage or sediment supply, but a substantial decrease in sediment supply or a decrease in transport stage could lead to channel narrowing. Widening of the upstream reach would require a substantial increase in the sediment supply.

3.4.3. Future work

Further work is needed to calibrate the value of E_l/E_v to natural bedrock channels and test the hypotheses presented in our conceptual phase diagram. For example, our conceptual phase diagram hypothesizes that channel slope is more difficult to adjust than channel width so that channels only adjust slope when the transport stage is near the threshold of motion or suspension. This behavior makes intuitive sense, and is consistent with the Boulder Creek case, but is hard to test without a full morphodynamic implementation of our model.

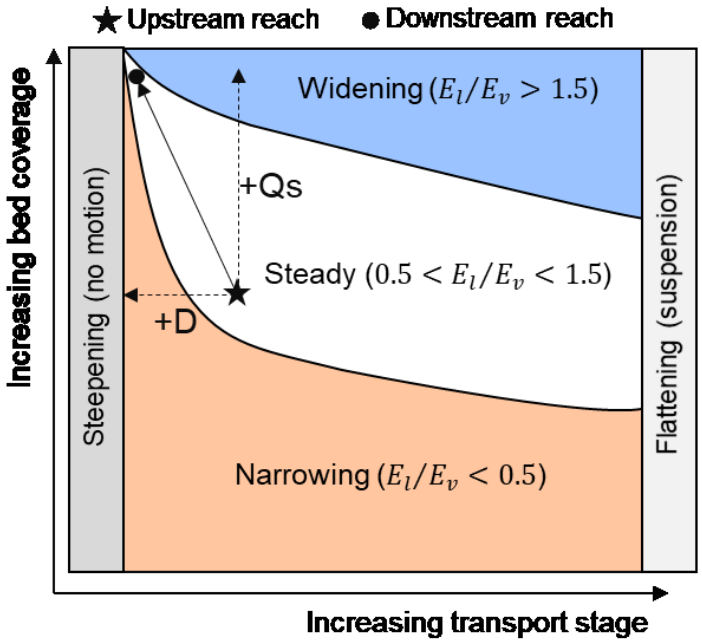

Figure 3.11 Schematic channel widening, steady, narrowing, steepening and flattening response on the functional surface bounded by transport stage and relative sediment supply, based on the variation of E_l/E_v shown in Figure 3.7b-d. The conditions of the upstream and downstream reaches of Boulder Creeak, CA, are shown as black star and dot, respectively. The resultant trajectory from upstream to downstream reaches is shown by the black solid arrow, which can be resolved into two components shown by the black dashed arrows: the component due to increasing grain size (+D) and the component due to increasing sediment supply rate (+Qs).

Our model has also assumed persistent patchy alluvium in the form of lateral bars that expand and contract with sediment supply, yet transient deposits coexist with persistent patches in bedrock rivers (Chatanantavet & Parker, 2008;

Cook et al., 2009, 2013; Fernández et al., 2019; Finnegan et al., 2007; Inoue et al., 2014; Johnson & Whipple, 2007, 2010; Turowski et al., 2007; Turowski, 2020). How these persistent and transient patches interact and affect vertical and lateral erosion rates is not known. Freely migrating bars have been found to cause vertical erosion through sediment particle impacts (e.g., Fernández et al., 2019), so some effect on lateral erosion is expected. Further work is needed to incorporate the self-organization of transient alluvium as in the reach scale models of Turowski (2018, 2020). Presently our analytical model only considers channel erosion by bedload particle impacts, ignoring all other mechanisms such as plucking and particle impacts by suspension. We use a uniform grain size to represent the wide distribution of grain sizes supplied to incising channels. Further work is necessary to develop models for lateral erosion by those processes and to incorporate the grain size distribution. We also need to make the model morphodynamic and incorporate the influence of channel curvature on flow, sediment deposition, and bedload paths (Inoue et al., 2016, 2017). Nevertheless, our analytical model for lateral erosion offers insight into channel dynamics in response to changes in sediment supply and transport conditions and can be scaled up to simulate bedrock river morphodynamics at reach or larger scales by introducing a distribution of discharges and sediment supply events, which the Li et al. (2020) numerical model was too computationally intensive to do.

3.5. Conclusion

We have derived analytical solutions for the Li et al. (2020) numerical model of lateral erosion by impacts of saltating bedload particles that are deflected by uniformly distributed and patchy alluvium. The uniformly distributed and patchy cover models predict that the non-dimensional lateral erosion rate is a function of two dimensionless quantities for a given grain size: relative sediment supply and transport stage. The uniformly distributed cover model reproduces the maximum lateral erosion rate occurring at ~ 70% relative sediment supply and intermediate transport stage, as observed in the numerical

model. The patchy cover model, however, predicts the peak erosion rate at full bed coverage. When our lateral erosion model is coupled with the Sklar & Dietrich (2004) vertical erosion model, the ratio of lateral to vertical erosion rate increases with increasing relative sediment supply for both uniformly distributed and patchy alluvium. Vertical erosion dominates ~75% of transport and supply conditions for uniformly distributed cover, but ~ 85% and ~98% of transport and supply conditions on the adjacent and opposite walls for the patchy cover, respectively.

The analytical model has the benefit of allowing prediction of lateral erosion rate as a function of sediment supply, shear stress and grain size. We find inverse U-shaped variations of lateral erosion rate with shear stress and grain size for both uniformly distributed and patchy alluvium. The lateral erosion rate varies with sediment supply in an inverse U-shaped curve for uniformly distributed alluvium, but monotonically grows with increasing sediment supply until the bed is fully covered for patchy alluvium.

Application of our model in the Boulder Creek explains downstream channel widening due to the dominance of lateral erosion and the shutdown of vertical erosion in response to the increase in sediment supply rates. Downstream channel steepening also occurs in Boulder Creek in order to pass the sediment load. The coupled vertical and lateral erosion model predicts feedbacks between width perturbations and the ratio of lateral to vertical erosion rate. A negative feedback causes a narrowing response that will return a channel back to the pre-perturbation width. A positive feedback encourages the channel width to grow until the channel steepens and achieves a new stable width.

Chapter 4. Bed and Bank Stress Partitioning in Bedrock Rivers

Abstract

Approximation of bed and wall (bank) stresses in confined, narrow bedrock rivers is key to accurately assessing hydraulic roughness, sediment transport, bedrock erosion and the morphodynamics of bedrock channels. Here, we partition bed and wall stresses using the ray-isovel model (RIM) and field observations. We used the RIM to calculate the distribution of shear stress across an idealized trapezoidal channel and found that the ratio of wall to bed stress (φ) grows slightly with increasing bank angles, but exponentially declines with increasing width-to-depth ratio. We applied the RIM to 26 of the canyons along the Fraser River and found that RIM predicts $0.60 \leq \varphi \leq 0.98$. We used field observations of bed and total stress to calculate wall stress in each canyon. The total stress was calculated from 1D momentum balance (depth-slope product). The distribution of bed stress was calculated from near-bed velocity profiles and showed that bed stress spikes as water enters constriction-pool-widening (CPW) sequences. For the majority of studied canyons, the observed wall stress is larger than the total stress and the observed bed stress. The maximum observed bed stress through a CPW sequence is ~7.5 times the mean bed stress and ~4.9 times the total stress. Compared with the observed stresses, the model systematically over-predicts the observed bed stress and under-predicts the observed wall stress by ~55%. Our results reveal that the complex flow structure in bedrock canyons influences the distribution of bed and wall stresses and that bedrock walls contribute more hydraulic roughness than predicted with RIM.

4.1. Introduction

Partitioning shear stress is a key part of calculating hydraulic roughness, sediment transport rates, rock erosion rates and morphodynamic modelling of

bedrock rivers. These are all key elements of landscape evolution models, which range in scale from the stream power model applied at large scales to mechanistic erosion models applied at local scales. The flow parameterization used in landscape evolution models is based on stream power, which assumes that the erosion rate scales with boundary shear stress (e.g., Howard & Kerby, 1983; Howard et al., 1994; Whipple & Tucker, 1999). Bedrock incision in canyons at the local scale happens through a combination of abrasion by sediment impacts of bedload or suspended load, plucking from the river bed or banks by hydraulic forces, chemical and physical weathering, and debris flow scour (Whipple et al., 2000; Whipple et al., 2013). Detailed models of the physics of individual incision processes have been developed to predict bedrock river dynamics, including a saltation abrasion model (Sklar & Dietrich, 2004; Li et al., 2020, 2021; Turowski, 2020), a total-load abrasion model (Lamb et al., 2008a), a plucking model based on the block topple-sliding mechanism (Lamb & Dietrich, 2009; Lamb et al., 2015; Hurst et al., 2021), a bedload abrasion, macroabrasion and plucking model (Chatanantavet & Parker, 2009), and a weathering model (Hancock et al., 2011). All these mechanistic models scale the erosion rate with shear stress with various degrees of sophistication. The relevant shear stresses in these models are the bed shear stress τ_{bed} and the wall shear stress τ_{wall}, partitioned from the total shear stress τ_{Tot}, although in practice this is rarely done because methods to do so are not well developed. The inability to partition shear stress into bed and wall components makes it difficult to make accurate predictions of local-scale channel dynamics, and their influence on larger-scale landscape evolution.

In alluvial channels, partitioning shear stress is rarely done because the wall stress is assumed to be negligible in wide channels where the width-to-depth ratio is much larger than 20. It is common for the bed stress τ_{bed} to be approximated as the total stress τ_{Tot} in bedrock rivers, as is done in alluvial rivers (e.g., Seidl & Dietrich, 1992; Anderson, 1994; Tucker & Slingerland, 1994; Willett, 1999; Hancock & Anderson, 2002; Inoue et al., 2014; Johnson, 2014).

This approach assumes that the walls bear a negligible part of the total shear force because the walls form a negligible proportion of the wetted perimeter, which is not true in narrow bedrock channels. Recognizing this, Stark (2006) split the shear stress across the channel into shear stress on the bed and the walls, assuming that the total shear stress τ_{Tot} is the sum of the bed stress τ_{bed} and the wall stress τ_{wall} ($\tau_{Tot} = \tau_{bed} + \tau_{wall}$). While intuitively correct, it is actually physically incorrect because it is the total force applied to the boundary that equals the sum of the force applied to the bed and the walls. Shear stress is force per unit area. Therefore, τ_{bed} is equal to the force applied to the bed divided by the bed area and τ_{wall} is equal to the force applied to the walls divided by the wall area. If the bed and the walls area and the forces acting on them are known, the total shear stress τ_{Tot} can be calculated from the total force applied to the bed and the walls divided by the total area of the bed and the walls, which is not equal to the sum of τ_{bed} and τ_{wall}. Wobus et al. (2006) calculated the shear stress distribution across the channel cross section from the velocity gradient, assuming that the velocity gradient near the bed scales with the mean velocity gradient between wall and centerline by employing the law of the wall. This approach is easy to implement, but it is not yet clear that the stress applied to the walls is accurately reflected in the cross channel velocity gradient. There have been attempts to characterize wall friction in narrow ducts or flume channels where the ratio of wall stress to bed stress is estimated by dividing the cross-sectional area into a number of sub-areas and each sub-area is assigned a component Manning's n value (e.g., Flintham & Carling, 1988, 1989; Knight & Macdonald, 1979; Lotter, 1933). However, this approach does not accurately resolve the velocity field by assuming zero net momentum transfer across the sub-area boundary lines (Flintham & Carling, 1989).

Vanoni & Brooks (1957) developed a shear stress partitioning framework in a trapezoidal channel that was reformulated by Ferguson et al. (2019) as

$$\tau_{Tot} = \frac{w_b \tau_{bed} + 2h/\sin\alpha \tau_{wall}}{w_b + 2h/\sin\alpha}, \qquad \text{(Equation 4.1)}$$

where w_b is the bottom channel width, h is the water depth, and α is the angle of channel wall inclination (Figure 4.1a). Equation 4.1 balances the total force applied to the bed and the banks, according to the relative areas of the bed and banks, per unit downstream distance. The bed stress τ_{bed} and wall stress τ_{wall} can be obtained from rearranging Equation 4.1

$$\tau_{bed} = \frac{w_b+2h/sin\,\alpha}{w_b+2\varphi h/sin\,\alpha}\tau_{Tot}, \qquad \text{(Equation 4.2)}$$

$$\tau_{wall} = \frac{w_b+2h/sin\,\alpha}{w_b/\varphi+2h/sin\,\alpha}\tau_{Tot}, \qquad \text{(Equation 4.3)}$$

where $\varphi = \tau_{wall}\,/\tau_{bed}$. It is important to recognize from Equations 4.2-4.3 that either the bed or wall shear stresses can be greater than the total shear stress, depending on the ratio of wall to bed stress φ (Ferguson et al., 2019). When $\varphi > 1$, τ_{bed} is smaller than τ_{Tot} because $(w_b + 2h/sin\,\alpha)/(w_b + 2\varphi h/sin\,\alpha)$ is <1 in Equation 4.2 and τ_{wall} is larger than τ_{Tot} because $(w_b + 2h/sin\,\alpha)/(w_b/\varphi + 2h/sin\,\alpha)$ is >1 in Equation 4.3, leading to $\tau_{wall} > \tau_{Tot} > \tau_{bed}$. The opposite relation occurs ($\tau_{bed} > \tau_{Tot} > \tau_{wall}$) when $\varphi < 1$. All three stresses are equal ($\tau_{bed} = \tau_{Tot} = \tau_{wall}$) when $\varphi = 1$. The stress partitioning in Equations 4.2-4.3 is conceptually attractive to apply in bedrock rivers due to its physical basis, but it is difficult to solve τ_{bed} and τ_{wall} from Equations 4.2-4.3 because the ratio $\varphi = \tau_{wall}\,/\tau_{bed}$ is unknown.

Here we seek to improve our understanding of the variation of bed stress τ_{bed}, wall stress τ_{wall} and the ratio of wall to bed stress φ from two methods, including model simulations and field measurements in bedrock rivers. We select 26 bedrock canyons along the Fraser River, British Columbia (Venditti et al., 2020a) as the study site because centerline flow and bed topography measurements are available (Rennie et al., 2018), which permit the calculation of τ_{bed} distributions in canyons. We calculate τ_{Tot} from the 1D momentum balance (depth-slope product) for each canyon. The total stress applied to a channel cross-section is typically estimated using the hydraulic radius instead of depth. In narrow channels with simple, uniform cross-sections, the area of the walls may be large relative to the bed area and the total stress applied to a cross-section

calculated from the depth is larger than the stress calculated from the hydraulic radius. However, in bedrock canyons with complex wall and bed topographies, the total stress is the total force per unit surface area of the whole reach, which is a measure of the weight of a slab of water moving downslope due to gravity against friction under steady uniform flow. Without high resolution measurements of channel bed and wall morphologies, it is impossible to calculate the total surface area, wetted perimeter and hence the averaged hydraulic radius of a channel reach.

Our calculation of τ_{Tot} uses the mean centerline depth because it is well constrained by our measurements, instead of the hydraulic radius (R), which is a cross-section-based measure. We are unable to reliably constrain R with our data because we do not have measurements of the cross-sections throughout the canyon, which are highly variable. We use mean measured centerline depth under the assumption that the channels are trapezoidal with steep banks and near flat beds, which is consistent with our observations of channel morphology (e.g.,Venditti et al., 2014). We acknowledge that the centerline depth is likely to be larger than the hydraulic radius, which will cause an overestimate of τ_{Tot}. Therefore, we treat τ_{Tot} calculated from the centerline depth as an upper limit of the true τ_{Tot}. To assess the potential bias of this approach, we calculate total shear stress using depths that are a fraction of the centerline depth to determine the magnitude of bias introduced by using centerline depth. We calculate the observed τ_{bed} from the near bed velocity profile, and calculate the observed τ_{wall} from τ_{bed} and τ_{Tot} using Equation 4.1, then calculate observed ratio $\varphi = \tau_{wall}/\tau_{bed}$. To obtain modelled shear stresses, we start by exploring the influences of bottom channel width, discharge, roughness length scale and bank angles on the modelled ratio φ using the ray-isovel model (RIM), and develop a simplified equation to predict modelled φ as a function of width to depth ratio. We then calculate modelled bed and modelled wall stresses in the Fraser canyons using the modelled φ. We compare the modelled and observed shear stresses, discuss deviations of the model predictions from the field measurements and call

for further research on the influence of complex wall and bed roughness and flow fields on shear stress partitioning in bedrock canyons.

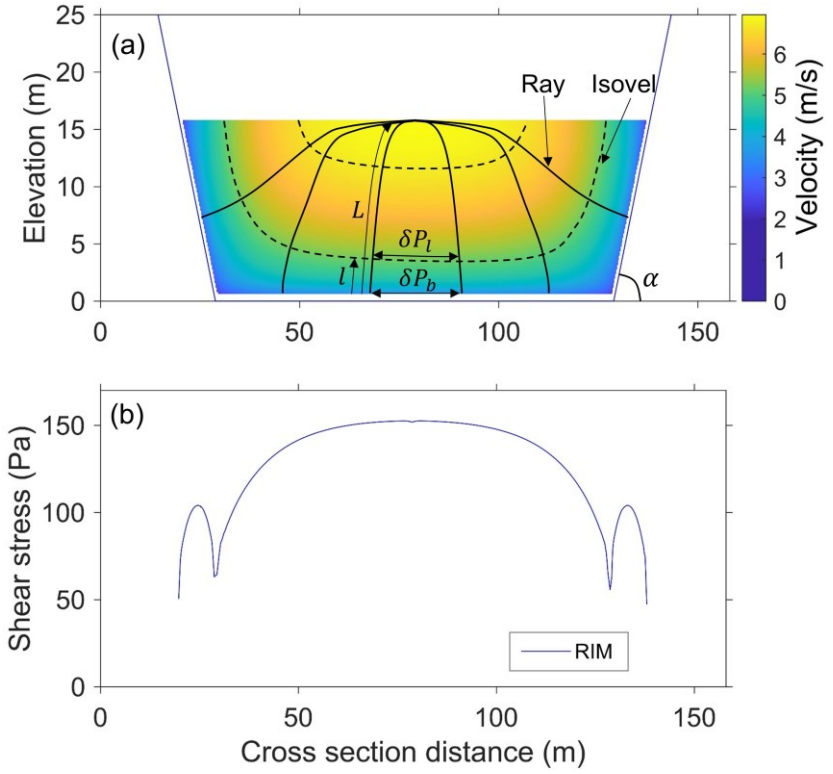

Figure 4.1 Distribution of a) velocity and b) boundary shear stress computed with the RIM for a cross-section typical of the canyons of the Fraser River. Also shown in a) is schematic for the RIM setup. Rays begin perpendicular to the channel boundary and are perpendicular to contours of constant velocity (isovels).

4.2. Theory

4.2.1. Ray-Isovel Model (RIM) Description

In order to predict values of φ, we use RIM to calculate the shear stress distribution in a trapezoidal channel (see Kean & Smith, 2004 for details of RIM). We selected RIM for this exercise because it explicitly calculates the shear stress applied to the channel walls and because it has been used previously in bedrock canyons to partition stress in a bedrock channel (e.g., Wobus et al., 2006, 2008; DiBiase & Whipple, 2011; Nelson & Seminara, 2011). RIM defines the distribution of fluid stress throughout the whole cross section using the curvilinear

coordinate system of the flow. This coordinate system consists of rays that are perpendicular to isovels (Figure 4.1a). RIM solves the momentum equation for steady, uniform flow averaged over turbulence along curves (rays) that are perpendicular to lines of constant velocity (isovels) (Figure 4.1a). The stress and eddy viscosity fields are defined in the orthogonal ray-isovel coordinate system and the velocity field is defined in a Cartesian coordinate system. Local shear stress τ_l is calculated from the downstream weight of water between adjacent rays divided by the wetted perimeter separating them as $\tau_l = \rho g S \int_0^L \delta P_l dl / \delta P_b$, where is l the distance along the ray from the boundary, L is the length of the ray, δP_l is the length along an isovel between adjacent rays, δP_b is the perimeter along the boundary between adjacent rays, S is the channel slope (Figure 4.1a; Kean & Smith, 2004). Wall and bed stresses are obtained from averaging local shear stresses along the walls and bed, respectively. RIM incorporates the effects of the channel cross-section shape and roughness on the flow field and has been supported by laboratory flume data and natural channel data with fixed cross-sectional geometries (Griffin et al., 2005; Kean & Smith, 2005; Kean et al., 2009). Numerical simulations of the co-evolution of shear stress distribution, cross-section shape and erosion rate on the basis of RIM have captured erosional patterns of bedrock observed in flume experiments (Nelson & Seminara, 2011) and width-discharge-slope relations observed in natural bedrock channels at steady state (Wobus et al., 2008).

RIM inputs include channel slope S, discharge Q_w, roughness length scale k_s, bottom channel width w_b and bank angles α. We use the same roughness length scale k_s for channel bed and banks in the following RIM calculations. Flow depth, velocity and shear stress are determined iteratively until the output value of discharge is equal to its input value. The water surface width w is calculated from w_b, h and α as $w = w_b + 2h \cot \alpha$ in a trapezoidal channel. The wall and bed stresses are calculated by averaging shear stress across the channel walls and bed, respectively.

4.2.2. Composite expression for φ

In order to simplify application of the RIM model in studies of bedrock rivers, we develop a composite expression for φ by simplifying RIM model outputs. Figure 4.1 shows an example of the computed velocity field, depth, and boundary shear stresses using model inputs that are typical of the canyons in the Fraser River (S = 0.001, α = 60°, w_b = 100 m, k_s = 0.5 m, Q_w = 9000 m3/s; Rennie et al., 2018). Rennie et al. (2018) found that mean k_s was on the order of 10-10^2 m in the rock bound section of the Fraser River, but this value represents complex non-uniform flow conditions that are not represented in the model. So we selected a conservative k_s value of 0.5 m, which is a modest multiple of the grain sizes transported in the alluvial reaches of the Fraser Canyon (Rennie et al., 2018). RIM predicts h ~ 16 m, which makes water surface width w ~ 118 m, and the width-to-depth ratio w/h ~ 7.4. Water velocity is highest in the channel center and decreases towards all boundaries (Figure 4.1a). Shear stress is highest in the center of the channel bed and decreases towards the channel banks, except for the low stresses at the boundary between the bed and walls due to a corner effect (Figure 4.1b). The average wall and bed stresses are 92 Pa and 136 Pa, respectively, which gives φ = 0.68.

To explore the sensitivity of the ratio of wall shear stress to bed shear stress φ_m from the RIM, we vary the discharge Q_w, roughness length scale k_s, bottom channel width w_b and bank angles α independently (Figure 4.2). Figure 4.2a shows that φ_m increases with increasing Q_w, holding k_s, w_b and α constant. The increase in φ_m with larger Q_w occurs because there is an increase in wall flow resistance as more area of the sidewalls is submerged with increasing water depth. In contrast, φ_m decreases with increasing w_b due to greater bed resistance as w_b increases, holding all other variables constant (Figure 4.2b). As the bank angle α increases, more area of the sidewalls is submerged as the water depth increases and the velocity gradient on the walls increases as the high velocity core at the center-top of water surface gets closer to the walls. The increase in the velocity gradient on the walls leads to more shear stress on the

walls, and hence higher φ with increasing bank angle α (Figure 4.2c). In contrast to the variation of φ_m with Q_w, w_b and α, φ_m is near constant with variation in k_s, over more than three orders of magnitude from 0.01 to 10 m (Figure 4.2d). Therefore, we assume the influence of k_s on φ_m is negligible.

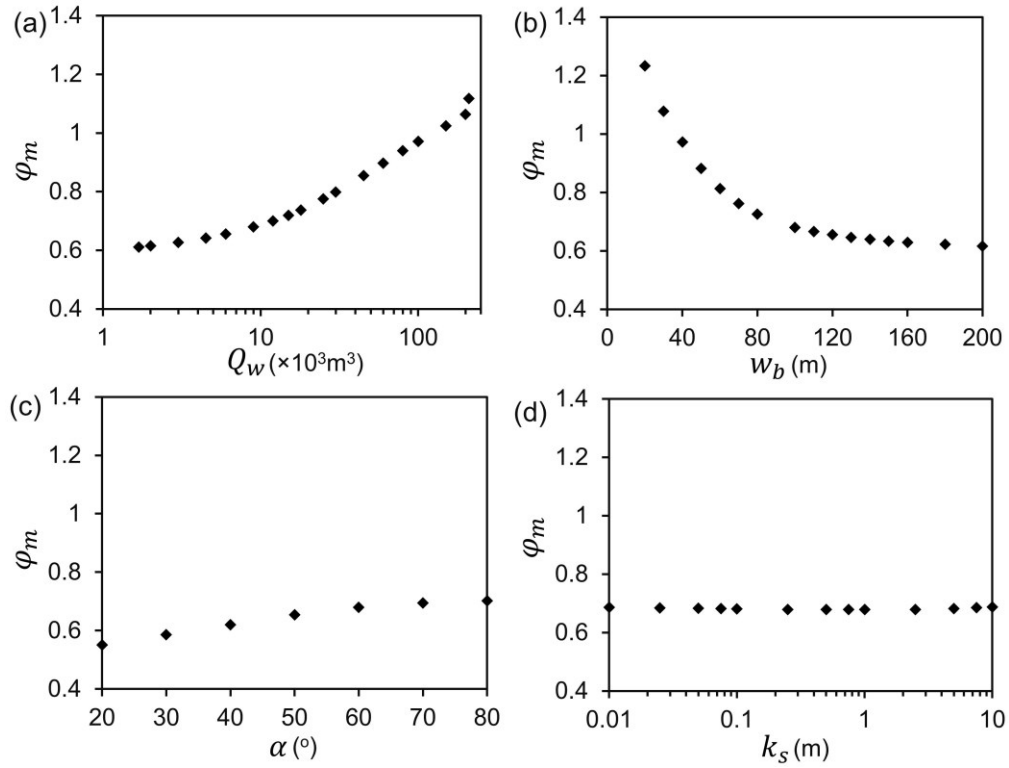

Figure 4.2 The ratio of wall to bed stress as a function of a) discharge Q_w, b) bottom channel width w_b, c) bank angle α and d) roughness height k_s. Each variable is explored independently by holding all other variables constant.

The influence of Q_w and w_b on φ_m can be non-dimensionalized to one variable: width-to-depth ratio w/h (Figure 4.3), because w/h increases with increasing discharge and decreasing bottom channel width. Varying discharge and bottom channel width predict the same φ_m for the same w/h, holding bank angles constant (Figure 4.3a). Figure 4.3 shows the regressions for φ_m including our best fitting one- (w/h) and two-parameter (w/h and α) models. The best-fit one-parameter model shows an exponential function exists between w/h and φ_m, which has the following form (Figure 4.3a):

$$\varphi_m = 1.148e^{-0.4219(w/h)} + 0.5988, \qquad \text{(Equation 4.4)}$$

where $R^2 = 0.96$. The best fit two-parameter model that includes w/h and α is (Figure 4.3b):

$$\varphi_m = 1.094e^{-0.414(w/h)} + 0.0008536\alpha + 0.577, \qquad \text{(Equation 4.5)}$$

where $R^2 = 0.97$. The two-parameter model is only a slight improvement over the one-parameter model, indicating the influence of α on φ_m is negligible, compared with w/h. It is difficult to measure bank angle in natural bedrock rivers with complex topography, making parameterization of the two parameter model challenging. Therefore, we recommend the one-parameter model (Equation 4.4) for simplicity. Equation 4.4 indicates that bed stress dominates over wall stress in wide channels, but is outpaced by wall stress in narrow channels with $w/h < 2.5$.

4.3. Field Site

We test our composite relation for φ against a field dataset from the Fraser Canyon that was initially reported in Rennie et al. (2018). The Fraser River drains 232, 000 km^2 of south-central British Columbia and runs through a 375 km reach from Soda Creek to Yale, British Columbia known colloquially as the Fraser Canyon. At the downstream end of the Fraser Canyon, the river has a mean annual flow of ~ 3000 m^3/s, a mean annual flood flow of ~ 9000 m^3/s and a historic flood of record discharge of ~ 17, 000 m^3/s. Through the Fraser Canyon, the channel alternates irregularly between being alluvial (for 45% of the 375 km length), bedrock-constrained (bedrock on one bank; for 29% of the 375 km length) and bedrock-bound (bedrock on both banks; for 26% of the 375 km length). The 'alluvial' reaches are parts of the river where the bed and banks are formed in alluvium, or the river flows through colluvial or unconsolidated Quaternary deposits (Rennie et al., 2018). Of the bedrock-bound sections, there are 42 individual canyons that are conspicuously deep and narrow, and long enough that they have been named, which occupy just 16% of the total distance (Venditti et al., 2020a).

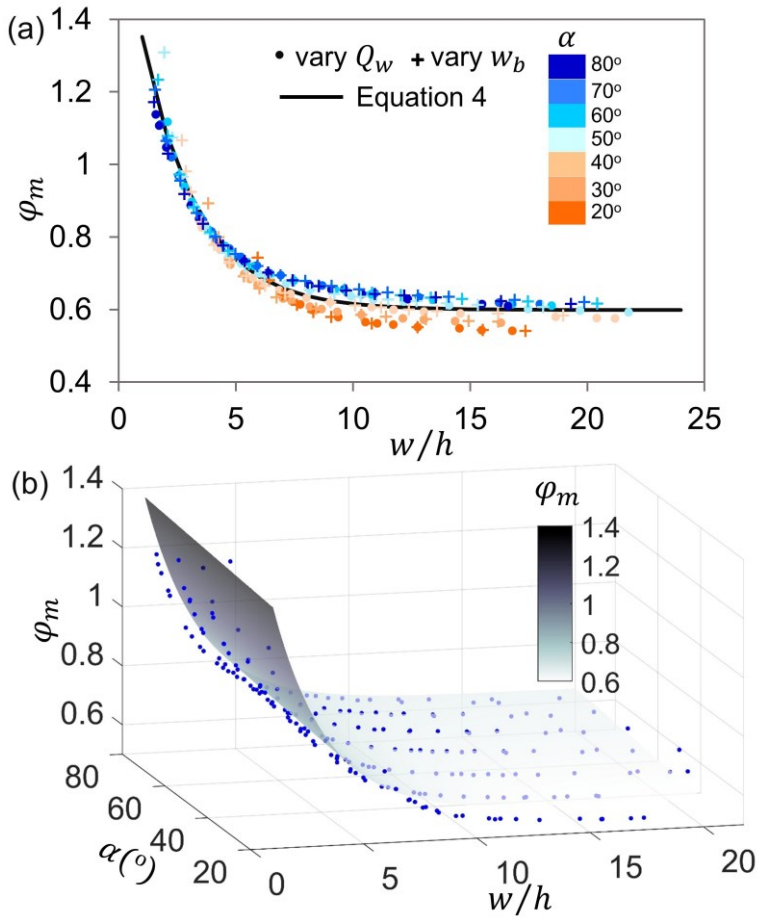

Figure 4.3 a) Variation of φ_m as a function of width-to-depth ratio w/h for different bank angles α, shown by the black line (Equation 4), b) best fit surface of φ_m as a function of width-to-depth ratio w/h and bank angles α, shown by the color-filled surface (Equation 4.5).

The reach scale morphology of these 42 bedrock canyons in the Fraser River exhibits a constriction-pool-widening morphology (e.g., Dolan et al., 1978; Venditti et al., 2014, 2020b). As the river enters a canyon, flow is laterally constricted, which causes an upstream backwater effect and sediment-laden flow spills through the constriction cutting a deep pool downstream (Cao, 2018; Hunt et al., 2018). At the distal end of the pool, sediment accumulates, deflecting incoming sediment into the canyon walls, which undercut the walls and cause them to widen (Li et al., 2020, 2021; Turowski, 2020). This constriction-pool-widening (CPW) morphology recurs through bedrock canyons forming CPW sequences (Venditti et al., 2020b).

Rennie et al. (2018) reported observations of channel depth, water velocity, water surface and bed elevations that were measured near continuously along a centerline traverse of the Fraser Canyon, using a SonTek M9 acoustic Doppler current profiler (aDcp) from motorized rafts in 2009. They also reported the boundary shear stress calculated from the near bed velocity gradient. We extracted observations of flow through the named canyons and identified 26 canyons that have reasonably continuous depth, velocity and shear stress measurements. We calculated the one-dimensional momentum balance (depth-slope product) for each of these canyons as $\tau_{Tot} = \rho g \bar{h} S$ where ρ is water density (~ 1000 kg/m^3), g is gravity acceleration coefficient (~ 9.81 N/kg), $\bar{h}$ is the mean centerline-depth. $\bar{h}$ was obtained from averaging the local water depths through each canyon reach. The local water depths were filtered by removing depth spikes that exceeded 50 m when all neighboring points were less than 20 m deep. S was derived by differencing water surface elevations at the entrance and exit of each canyon. Mean channel width $\bar{w}$ for each canyon was obtained by averaging the local channel width measured continuously along the centerline traverse of each canyon at an interval of 10 m, using LandSat satellite imagery (Wright et al., 2022). Following Venditti et al. (2014) and Rennie et al. (2018), we use the mean flow depth rather than the hydraulic radius to calculate τ_{Tot}. Using depth simplifies the calculation because accurately constraining the mean hydraulic radius in the absence of detailed wall topography along each canyon reach in the Fraser River at the same resolution as bed topography is not possible. The true mean hydraulic radius is highly variable in the canyons. Nevertheless, we also roughly estimated the hydraulic radius using the mean width, mean depth and slope through the canyon for comparison, assuming the canyon morphology is uniform along the whole reach with a trapezoidal cross section. Table 4.1 summarizes $\bar{w}$, $\bar{h}$, S and τ_{Tot} for the 26 bedrock-bound canyons.

We separate τ_{Tot} into its constituent parts using RIM and the field measurements. Using the RIM, we subdivided τ_{Tot} into modelled bed stress

τ_{bed_m} and modelled wall stress τ_{wall_m} using Equation 4.4 and calculated the modelled ratio $\varphi_{\mathrm{m}} = \tau_{wall\_m}/\tau_{bed\_m}$. We also calculated the observed bed stress τ_{bed_o} by averaging the shear stress τ_{bed_nb} that is estimated from the near bed velocity gradient over the canyon ($\tau_{bed\_o} = \overline{\tau_{bed\_nb}}$). Bed shear stresses calculated from the velocity gradient (τ_{bed_nb}) are obtained from the slope (m) of a log law fit using least squares regression of u on $\ln(z)$, where u is the velocity at an elevation z above the bed. The shear velocity u_* is calculated as $u_* = \kappa m$ where κ is the von Karman constant (~ 0.41) and the shear stress is calculated as $\tau_{bed\_nb} = \rho {u_*}^2$. This procedure is done for only the near bed velocity profile from the bed to the velocity maximum. Alluvial rivers are depth-limited and the velocity profile is typically log-linear over the full water depth. In rivers with large bed and wall roughness features, this is often not true (e.g. McLean et al., 1994) and the log-linear velocity profile extends to some limited height above the bed. Velocity inversions are known to occur through CPW sequences in bedrock canyons (Venditti et al., 2014). This phenomenon leads to errors in the calculated boundary shear stress if the data representing the full velocity profile are used in the calculations. However, using the lower portion of the velocity profile that is below the maximum velocity makes the shear stress dependent on the velocity gradient near the boundary and gives improved estimates of bed stresses (Venditti et al., 2014; Rennie et al, 2018). We first calculated the observed wall stress τ_{wall_o} from τ_{bed_o} and τ_{Tot} using Equation 4.1 and then estimated the observed ratio $\varphi_{\mathrm{o}} = \tau_{wall\_o}/\tau_{bed\_o}$ from τ_{wall_o} and τ_{bed_o}. To predict shear stress from Equations 4.1-4.3, the bank angle α for each canyon needs to be specified. Subaqueous bank angles cannot be easily measured in the bedrock-bound parts of the Fraser Canyon. Wright et al. (2022) report α ~ 60° based on bathymetric maps of Black and Alexandra Canyons which have $\overline{w}/\overline{h}$ ratios of 3.71 and 4.80 respectively (Venditti et al, 2021). In the absence of other information, we assume bank angles of Black and Alexandra Canyons are representative of all the canyons and use $\alpha = 60°$ for all calculations below.

Table 4.1 Characteristics of the 26 bedrock-bound canyons studied in the Fraser River.

Canyon	$\overline{w}$	$\overline{h}$	$\overline{w}/\overline{h}$	S	φ_m	τ_{Tot}	τ_{bed_o}	τ_{wall_c}	φ_o
Hawks Creek Canyon	102	9.41	10.8	0.0005	0.61	47.4	35.3	102	2.88
West Williams Lake Canyon	130	9.73	13.4	0.001	0.60	93.8	38.5	405	10.5
Chimney Creek Canyon	80.8	17.7	4.56	0.001	0.77	166	88.1	293	3.33
Doc English Canyon	97.0	11.2	8.69	0.001	0.63	115	110	131	1.18
Iron Canyon	65.9	21.2	3.11	0.0007	0.91	143	99.8	186	1.87
Alkali Rapids	99.3	13.8	7.22	0.001	0.65	136	77.4	304	3.92
McEwan Rapids	81.6	19.0	4.28	0.001	0.79	220	67.9	452	6.65
Grinder Creek North Canyon	135	12.8	10.5	0.0009	0.61	112	67.5	304	4.51
French Bar Canyon	149	10.0	14.9	0.0020	0.60	176	158	293	1.85
Chisholm Canyon	99.5	12.7	7.86	0.0005	0.64	63.3	77.3	19.3	0.25
Kelly Creek Canyon	74.9	16.4	4.56	0.002	0.77	264	201	369	1.84
White Canyon	69.9	16.9	4.13	0.0009	0.80	142	195	65.2	0.33
Fountain Canyon West	80.8	19.1	4.24	0.001	0.79	188	71.0	363	5.11
West Fountain Canyon	85.7	14.5	5.93	0.002	0.69	328	98.2	847	8.63
Bridge River Confluence Canyon	83.1	21.4	3.88	0.001	0.82	261	158	398	2.52
Lillooet Rapid	99.1	18.0	5.51	0.0004	0.71	60.8	69.9	42.0	0.60
Lochore-Nesikep Canyon	106	13.2	8.00	0.0008	0.64	98.4	99.9	93.7	0.94
McGillvray Creek Rapid	108	14.6	7.37	0.001	0.65	139	82.1	305	3.71
Hull Arden Creek Canyon	118	13.2	8.90	0.001	0.63	141	93.0	315	3.39
Keefer Canyon	136	17.6	7.73	0.0005	0.64	94.1	37.2	269	7.25
Inkahtsaph Canyon	106	30.1	3.51	0.0008	0.86	232	47.2	448	9.50
Kahmoose Canyon	83.9	27.9	3.00	0.0008	0.92	219	58.5	370	6.33
Paul's Rapid	63.2	24.4	2.59	0.002	0.98	445	573	348	0.61
Little Hell's Gate Canyon	103	11.6	8.92	0.003	0.63	298	243	498	2.05
Black Canyon	72.4	19.5	3.71	0.001	0.84	284	172	426	2.47
Lamb's View Canyon	128	16.0	8.03	0.001	0.64	181	150	279	1.86

4.4. Results

4.4.1. Flow structure and observed shear stresses

We select three canyons as exemplars of flow structure and shear stress distributions in the Fraser Canyon, based on the relation between τ_{bed_o} and τ_{Tot}. Paul's Rapid is an example where $\tau_{Tot} < \tau_{bed\_o}$ (Table 4.1). The total shear stress τ_{Tot} (~ 445 Pa) is 77.7% of the bed stress τ_{bed_o} (~ 573 Pa). The wall stress τ_{wall_o} required to balance the bed stress in Paul's Rapid is 348 Pa, which is 60.7% of the bed stress τ_{bed_o} and 78.3% of the total stress τ_{Tot}. Of the 26 canyons studied, Paul's Rapid is the narrowest canyon with a mean width to depth ratio $\overline{w}/\overline{h} = 2.59$ (Table 4.1). The canyon bed has a series of deep pools, the first of which occurs at the entrance with a local maximum depth h_{max} ~ 25 m, the second occurs midway along the canyon with h_{max} ~ 32 m and the third occurs at the canyon exit with h_{max} ~ 36 m (Figure 4.4a). The pools are coincident with width constrictions (especially the one midway through the canyon) that create CPW sequences. At the entrance of the CPW, plunging flow occurs where high-velocity fluid from the water surface follows along the channel bed down into scour pools (Figure 4.4a). The high-velocity core dissipates with distance downstream, but reappears with each CPW (Figure 4.4a). The high-velocity core is largest within the CPW that is in the middle of the canyon where the constriction is greatest. The distribution of bed stress in Paul's Rapid shows elevated bed stresses τ_{bed_nb} (Figure 4.4b) at the entrance of the canyon (0 to 60 m), at several locations through the CPW sequence in the middle of the canyon (300 to 600 m), and near the exit of the canyon (700 to 800 m). Increases in shear stress are caused by plunging flows that increase near bed velocity gradients. The peak τ_{bed_nb} in Paul's Rapid is similar in each pool (~ 1750 Pa) and occurs near the maximum pool depths. Minor spikes in τ_{bed_nb} also occur in minor pools where flow gets deeper (e.g. between 140 to 160 m and 200 to 240 m from the canyon entrance). τ_{bed_nb} is negligible at the exit of each pool in Paul's Rapid (e.g., between 650 m and 700 m), where the plunging flow

dissipates and the adverse velocity gradient disappears as the flow shallows and the canyon widens (Venditti et al., 2014).

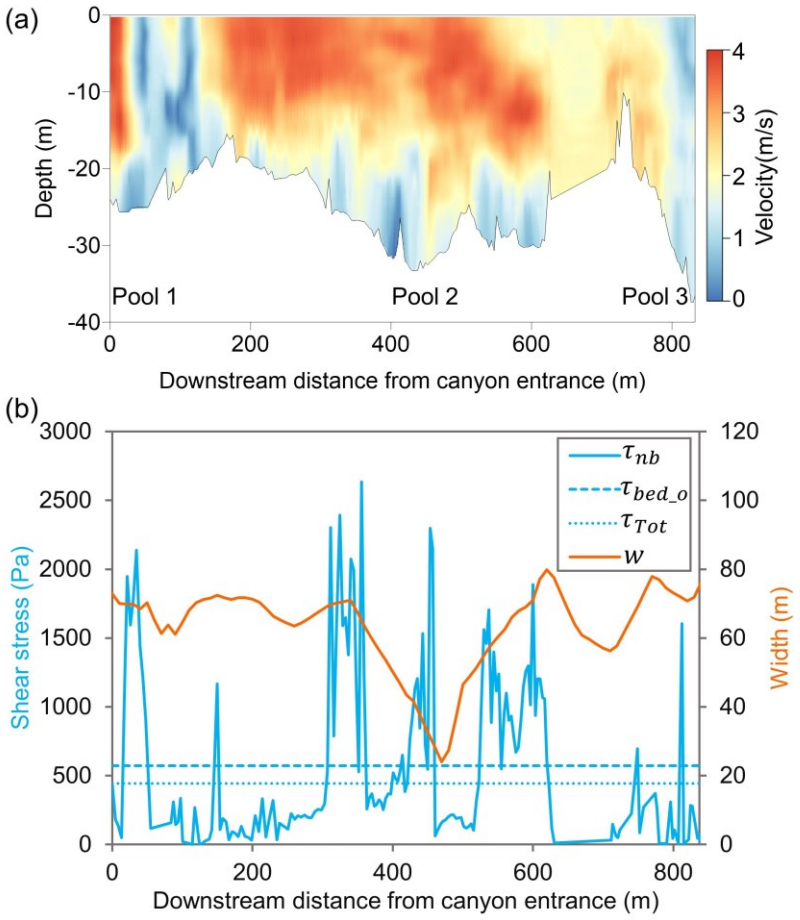

Figure 4.4 a) Streamwise velocity in Paul's Rapid. b) Shear stress distribution τ_{bed_nb} calculated from near bed velocity, mean bed stress τ_{bed_o}, total stress τ_{Tot} and the width w variation throughout Paul's Rapid.

Lamb's View Canyon is an example where $\tau_{Tot} > \tau_{bed\_o}$, which is typical of most canyons. The total stress τ_{Tot} (~ 181 Pa) is 1.21 times the observed bed stress τ_{bed_o} (~ 150 Pa). The wall stress τ_{wall_o} required to balance the bed stress in Lamb's View Canyon is 279 Pa, which is 1.86 times the bed stress τ_{bed_o} and 1.55 times the total stress τ_{Tot}. Of the 26 canyons studied, Lamb's View Canyon has a moderate $\overline{w}/\overline{h}$ = 8.03 (Table 4.1). While Lamb's View Canyon is bedrock on both sides of the channel, there are some lateral sediment inputs from hillslopes making it somewhat more discontinuous than Paul's Rapid.

Lamb's View Canyon has four deep pools (Figure 4.5a). The distribution of bed stress shows large spikes of τ_{bed_nb} (Figure 4.5b) around the deepest pools through these four CPW sequences due to the high velocity gradients near the bed. Minor spikes in τ_{bed_nb} are coincident with local constrictions or deep parts of pools (e.g., between 700 and 1000 m; 2400 and 2700 m). τ_{bed_nb} is negligible at the exit of each CPW sequence (e.g., between 1700 m and 1800 m) where the plunging flow dissipates and the adverse velocity gradient disappears.

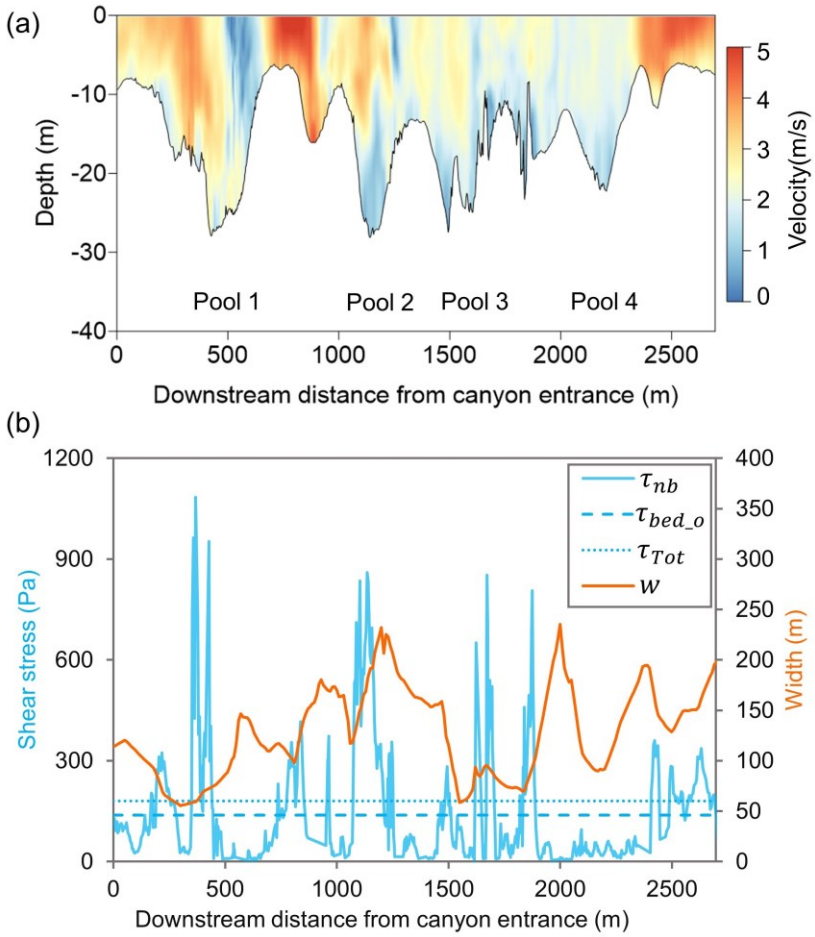

Figure 4.5 a) Streamwise velocity in Lamb's View Canyon. b) Shear stress distribution τ_{bed_nb} calculated from near bed velocity, mean bed stress τ_{bed_o}, total stress τ_{Tot} and the width w variation throughout Lamb's View Canyon.

Lochore-Nesikep Canyon is an example where the total stress τ_{Tot} (98.4 Pa), the bed stress τ_{bed_o} (99.9 Pa) and the wall stress τ_{wall_o} (93.7 Pa) are all

similar (Table 4.1). Lochore-Nesikep Canyon has a moderate $\overline{w}/\overline{h}$ = 8.00 (Table 4.1). The canyon bed has one deep pool at the canyon exit with h_{max} ~ 27m (Figure 4.6a). The pool is coincident with a width constriction that creates one CPW. A plunging flow develops bringing high speed fluid toward the bottom of the pool, and dissipates as the canyon gets wider and shallower at the canyon exit. The distribution of bed stress in Lochore-Nesikep Canyon shows large spikes in τ_{bed_nb} at the canyon entrance where water depth starts to increase and at the canyon exit at the deepest pool.

All 26 studied canyons have a similar unimodal distribution of τ_{bed_nb} (Figure 4.7). The distributions are heavy-tailed because shear stress is low through most of the canyon, with notable spikes in stress associated with the CPW sequences. The narrowest canyon ($\overline{w}/\overline{h} = 2.6$), Paul's Rapid, has the widest range of τ_{bed_nb} (1 to 2635 Pa) and the highest mode (550 Pa), and also stands out as an outlier from the rest of the dataset (Figure 4.8). More typically, the range is 1 to 2000 Pa with the mode lying between 75 and 150 Pa. Several canyons have a narrower distribution and lower mode of τ_{bed_nb} including Hawks Creek, West Williams Lake and Keefer canyons, in which the width constrictions occur somewhat before or after the deep pools instead of being coincident with the deep pools.

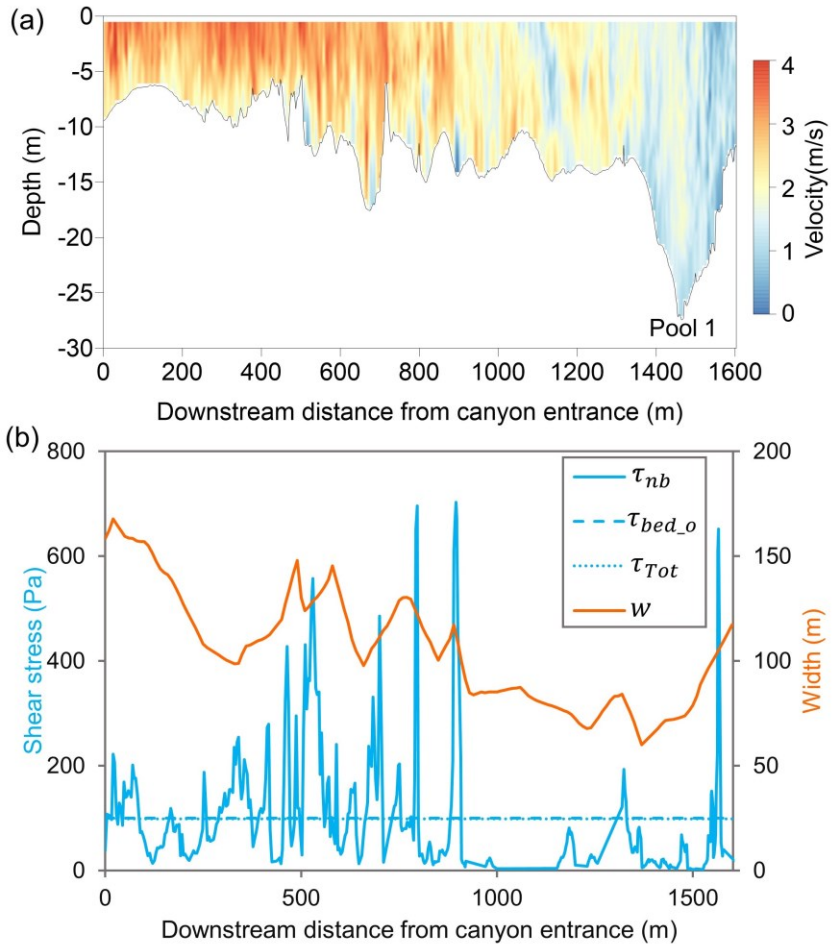

Figure 4.6 a) Streamwise velocity in Lochore-Nesikep Canyon. b) Shear stress distribution τ_{bed_nb} calculated from near bed velocity, mean bed stress τ_{bed_o}, total stress τ_{Tot} and the width w variation throughout Lochore-Nesikep Canyon.

Of 26 canyons studied, 21 canyons have $\tau_{wall\_o} > \tau_{Tot} > \tau_{bed\_o}$, one canyon has $\tau_{Tot} \approx \tau_{bed\_o} \approx \tau_{wall\_o}$ and four canyons had $\tau_{wall\_o} < \tau_{Tot} < \tau_{bed\_o}$ (Figure 4.8). Regression analysis reveals roughly linear relations between τ_{bed_o}, τ_{wall_o} with τ_{Tot} (Figure 4.8). Paul's Rapid is not included in the regression analysis because the observed bed stress in Paul's Rapid ($\tau_{bed\_o} = 573$ Pa) differs significantly from the rest of observed bed stresses τ_{bed_o} and does not follow the trend of the rest of the data. Including the Paul's Rapid data would bias the relations. The relation between τ_{bed_o} and τ_{Tot} shows considerable variability, however 30% of the variance in τ_{bed_o} is explained by τ_{Tot}. There is also considerable variability in the relation between τ_{wall_o} and τ_{Tot}, yet 68% of the

variance in τ_{wall_o} is explained by τ_{Tot}. The relations have non-zero intercepts, but we force the regression through zero because total stress should be zero if the bed and wall stress are zero. We find that τ_{bed_o} is roughly 42% (± standard error 5%) less than τ_{Tot}, and τ_{wall_o} is roughly 74% (±11%) larger than τ_{Tot}. This result is counterintuitive because most models of landscape evolution assume that the bed stress can be approximated as the total stress (e.g., Seidl & Dietrich, 1992; Anderson, 1994; Tucker & Slingerland, 1994; Willett, 1999; Hancock & Anderson, 2002; Yanites, 2018), and therefore assume that the bed stress, wall stress and total stress are equal (Equation 4.1). Our result also shows that the wall stress is not negligible in bedrock canyons. Instead, wall stress dominates over bed stress in most studied canyons in the Fraser River.

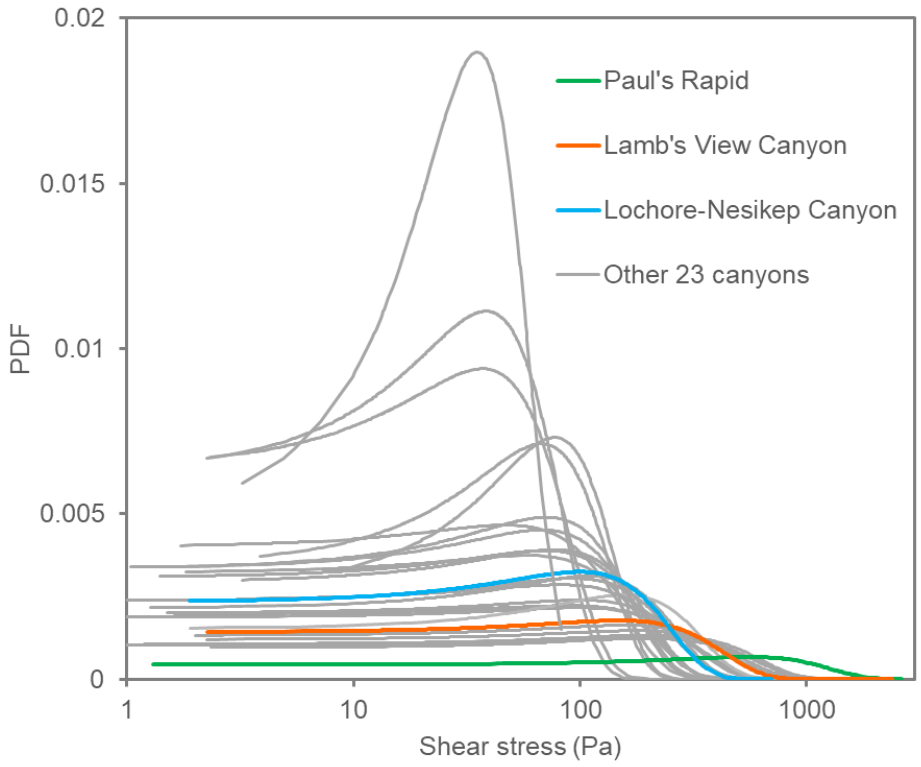

Figure 4.7 Probability density function (PDF) of measured local bed shear stress along each canyon reach studied in the Fraser River.

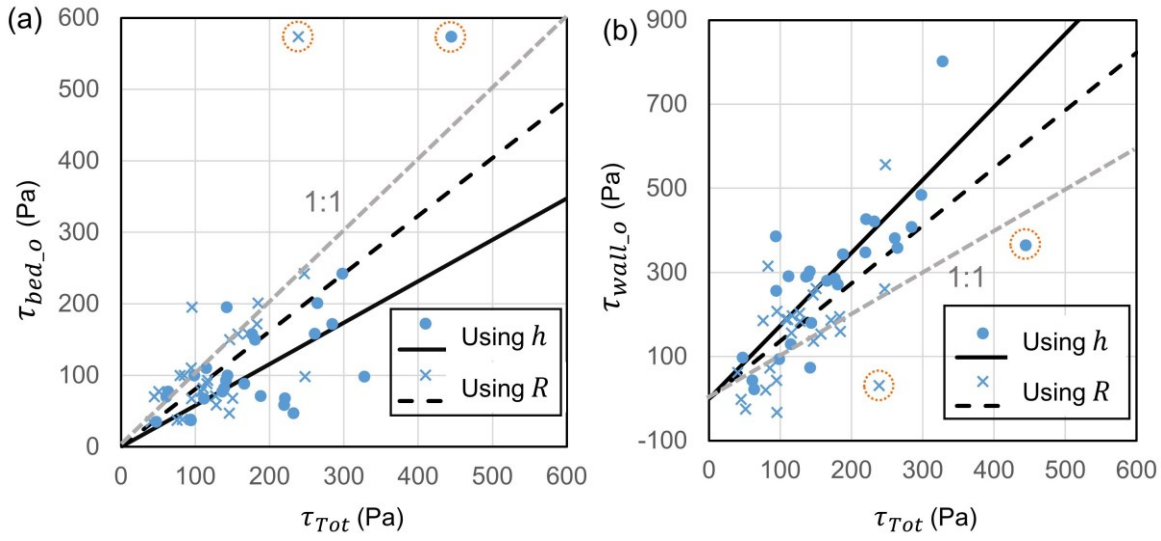

Figure 4.8 a) Relations between observed bed stress τ_{bed_o} and total shear stress τ_{Tot} calculated using depth h ($\tau_{bed\_o} = 0.58\tau_{Tot}$) and hydraulic radius R ($\tau_{bed\_o} = 0.81\tau_{Tot}$). b) Relations between the observed wall stress τ_{wall_o} and total shear stress τ_{Tot} calculated using h ($\tau_{wall\_o} = 1.74\tau_{Tot}$), and hydraulic radius R ($\tau_{wall\_o} = 1.37\tau_{Tot}$). Paul's Rapid (plotted within the orange circle) is not incorporated in the regression. Regressions are forced through zero.

4.4.2. Modelled shear stresses

All 26 canyons studied here have φ_m < 1, ranging from 0.60 to 0.98 (Table 4.1). τ_{bed_m} and τ_{wall_m} are estimated from φ_m, τ_{Tot}, and α (60°) using equations 2 and 3, respectively. Regression analysis reveals linear relations between τ_{bed_m}, τ_{wall_m} and τ_{Tot} (Figure 4.9). Nearly all the variation in τ_{bed_m} is explained by τ_{Tot} (> 99%) (Figure 4.9a) and the proportion of τ_{wall_m} explained by τ_{Tot} is 93% (Figure 4.9b). With the relation fit through zero, τ_{bed_m} is systematically ~9% (± standard error 0.3%) larger than τ_{Tot} and τ_{wall_m} is ~19% (±2%) smaller than τ_{Tot}.

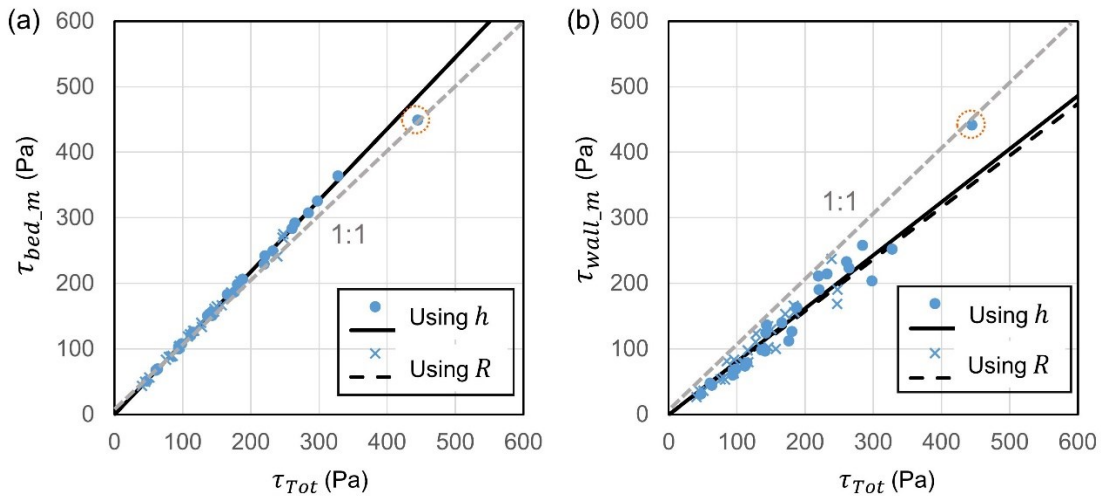

Figure 4.9 a) Relations between the modelled bed stress τ_{bed_m} and total shear stress τ_{Tot} calculated using depth h ($\tau_{bed\_m} = 1.09\tau_{Tot}$) and hydraulic radius R ($\tau_{bed\_m} = 1.09\tau_{Tot}$). b) Relations between the modelled wall stress τ_{wall_m} and total shear stress τ_{Tot} calculated using depth h ($\tau_{wall\_m} = 0.81\tau_{Tot}$) and hydraulic radius R ($\tau_{wall\_m} = 0.79\tau_{Tot}$). Paul's Rapid (plotted within the orange circle) is not incorporated in the regression. Regressions are forced through zero.

4.4.3. Comparison of observed and modelled shear stresses

Of 26 canyons studied, τ_{bed_m} is larger than τ_{bed_o} and τ_{wall_m} is smaller than τ_{wall_o} in 22 canyons (Figure 4.10). τ_{bed_m} is smaller than τ_{bed_o} and τ_{wall_m} is larger than τ_{wall_o} in three canyons (Figure 4.10). One canyon has $\tau_{bed\_m} \approx \tau_{bed\_o}$ and $\tau_{wall\_m} \approx \tau_{wall\_o}$ (Figure 4.10). Regression analysis reveals roughly linear relations between τ_{bed_o} and τ_{bed_m} as well as τ_{wall_o} and τ_{wall_m} (Figure 4.10). Paul's Rapid is not included in the regression analysis because it is an outlier from the rest of the dataset. The relation between τ_{bed_o} and τ_{bed_m} shows considerable variability, however 30% of the variance in τ_{bed_m} is explained by τ_{bed_o}. There is also considerable variability in the relation between τ_{wall_o} and τ_{wall_m}, yet 55% of the variance in τ_{wall_m} is explained by τ_{wall_o}. The relations should have a zero intercept, because the modelled stress should be zero when the observed stress is zero. Even though the difference between the modelled and observed shear stresses show wide variations, the model over-predicts the observed bed stress by 56% (± standard error 15%) (Figure 4.10a) and under-

predicts the observed wall stress by roughly 57% (±3.2%) (Figure 4.10b). The deviation between the model and measurement is somewhat smaller using R for the canyon. Modelled bed stress over-predicts the observed bed stress by 16% (±9%) (Figure 4.10a) and under-predicts the observed wall stress by roughly 54% (±5%) (Figure 4.10b) using R.

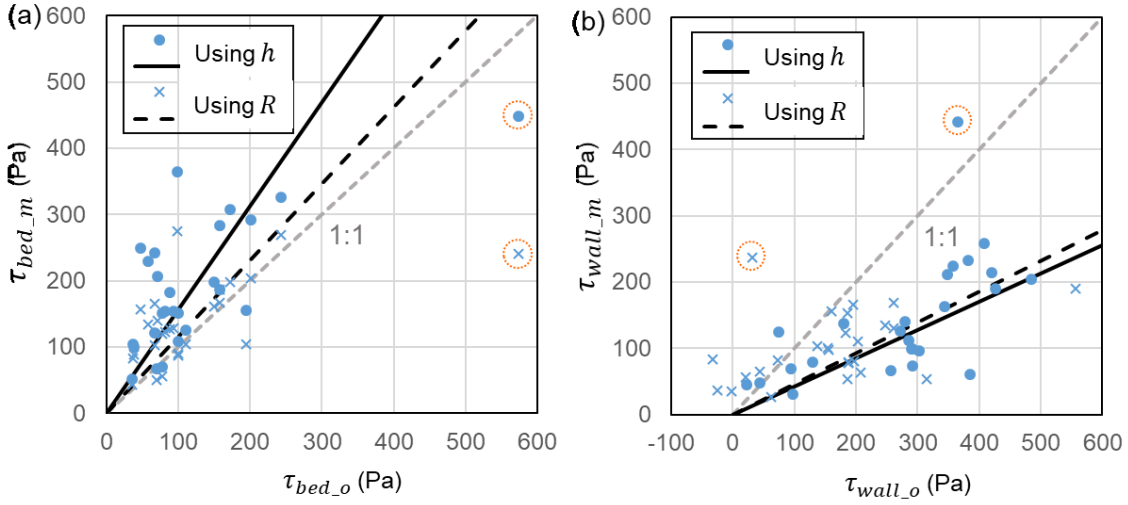

Figure 4.10 a) Relations between observed τ_{bed_o} and modelled bed stresses τ_{bed_m} using τ_{Tot} that is calculated by depth h ($\tau_{bed\_m} = 1.56\tau_{bed\_o}$) and hydraulic radius R ($\tau_{bed\_m} = 1.16\tau_{bed\_o}$). b) Relations between observed τ_{wall_o} and modelled wall stresses τ_{wall_m} using τ_{Tot} that is calculated by depth h ($\tau_{wall\_m} = 0.43\tau_{wall\_o}$), and hydraulic radius R ($\tau_{wall\_m} = 0.46\tau_{wall\_o}$). Paul's Rapid (plotted within the orange circle) is not incorporated in the regressions. Regressions are forced through zero.

4.5. Discussion

4.5.1. Difference between model simulations and field measurements

Of 26 canyons studied here, the bed and the wall stresses are systematically different between model predictions and field observations. The modelled bed stresses are ~ 56% (±15%) larger than the observed bed stresses, and the modelled wall stresses are ~ 57% (±3.2%) smaller than the observed wall stresses. These differences may be explained by three assumptions made in the RIM: 1) the bank angle is assumed to be the same; 2) the bed and the walls

are assumed to be equally rough; 3) the flow is assumed to be steady and uniform.

We assume a constant bank angle (60º) in the RIM in all 26 studied canyons due to the lack of measurements within each canyon. To test the influence of bank angles on the predicted shear stress in the Fraser River, we vary the bank angle from 20º to 80º in the two-parameter model. φ is not sensitive to variation in bank angle, varying by <20%. In response to the variation in bank angles, the range of the ratios $\tau_{bed\_o}/\tau_{bed\_m}$ and $\tau_{wall\_o}/\tau_{wall\_m}$ are similar. We conclude that the difference between the model results and field data is relatively insensitive to bank angle.

RIM uses the same roughness length scale for bedrock bed and walls, assuming that the channel bed and walls are equally rough. RIM predicts the wall stress is smaller than the bed stress for all morphological and hydraulic conditions. However, the wall stress in the field measurements is larger than the bed stress for the majority of studied canyons. This result shows that rock walls are typically rougher than the bed in the Fraser Canyon. Complex wall morphologies can be a substantial momentum sink, leaving less momentum applied to the bed. Bedrock canyon walls may undulate in or out of phase with each other (Wohl et al., 1999; Wohl & Merritt, 2001; Carter & Anderson, 2006). The canyons of the Fraser river typically have irregular undulations superimposed on CPW sequences. Black Canyon, for example, has six CPW sequences with along channel length scales of ~ 1000 m and smaller wall forms with length scales of ~ 50 m (Curran, 2020; Figure 4.11). These wall forvms cause flow separation, secondary flow cells and the formation of large scale coherent flow structures (Venditti et al., 2014; Ansari et al., 2018) that effectively reduce the mean velocity and increase the form drag on the walls (Yang, 1971; Carling, 1989; Wohl, 1993; Wohl et al., 1999; Carter & Anderson, 2006; Carling et al., 2019). The walls may also be rougher than the bed because the bed might be smoothed by alluvium filling depressions. Ferguson et al. (2019) speculated that abrasional smoothing effect decreases with distance above the bed, which

would also tend to make the bed and lower walls smoother where bedload impacts are most common (Fuller et al., 2016; Beer et al., 2017; Li et al., 2020, 2021). The decrease in the ratio of bed to wall roughness length scale in narrow channels has been shown to reduce the ratio of bed to wall stress (Flintham & Carling, 1988). Further experimental and modelling work is needed to explore how the sizes and scales of wall and bed roughness affect the ratio of bed to wall stress.

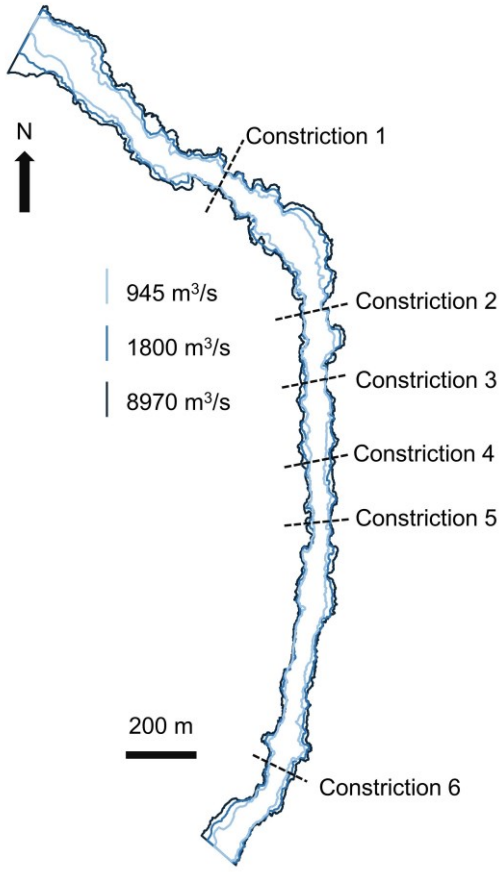

Figure 4.11 Width variations in Black Canyon at three discharges with the six major constrictions marked (modified from Curran, 2020).

RIM solves the distribution of shear stress for steady, uniform flow using a ray-isovel turbulence closure. RIM does not model secondary circulation and calculates a velocity profile that is highest at the center of the water surface. Yet, there are velocity inversions (high velocities near the bed and low velocities at the surface) observed in the Fraser Canyon. The downwelling in the center of the

channel and upwelling along the channel walls result in counter-rotating, along-stream coherent flow structures that diverge near the bed (Venditti et al., 2014). The plunging flow structure leads to the spikes in shear stress as water enters the CPW sequence but muted bed stress as flow shallows downstream of the CPW sequence. These highly non-uniform flows are not reflected in the RIM predictions. Development of three dimensional turbulence resolving models are needed to explore how non-uniform flow structures affect the ratio of bed and wall stresses. Separating the effects of wall roughness and the complex flow structure on wall stress is not possible in our analysis, but we conclude that the combined effect of wall morphology complexities and flow structure can result in the large observed wall stresses relative to the modelled stresses.

4.5.2. Implications for morphodynamic modelling of bedrock rivers

Given the lack of field observations of partitioned bed and wall stresses in large bedrock rivers, morphodynamic models rely on the assumption that bed stress is equal to the total stress (e.g., Whipple & Tucker, 1999; Lague et al., 2005; Sklar & Dietrich, 2008; Yanites, 2018). However, our results show that the wall stress is larger than the total stress and the bed stress is lower than the total stress for the majority of the 26 studied canyons. The majority of landscape evolution models are driven by the simple rule for incision (stream power model) that assumes vertical erosion rate is proportional to the bed stress to a power of 1 (Howard & Kerby, 1983; Howard, 1994; Whipple & Tucker, 1999). The stream power model using the total stress as the bed stress can over-predict the erosion rate by ~42%. The over-estimation of instantaneous erosion rate will overestimate channel response over long time scales. Mechanistic models of erosion by saltating bedload or suspended load largely rely on the transport capacity for determining the bed coverage (Sklar & Dietrich, 2004; Lamb et al., 2008a; Li et al., 2020). The transport capacity and sediment impact velocity on rock in these mechanistic models are proportional to the bed stress to a power larger than 1. Other mechanistic erosion models have a similar non-linear dependence on shear stress with various degrees of sophistication, such as the

plucking and weathering models (Chatanantavet & Parker, 2009; Hancock et al., 2011; Lamb et al., 2015; Larsen & Lamb, 2016). The nonlinear dependence of vertical erosion rate on shear stress in these mechanistic models means that vertical erosion will be overestimated using total stress. The bed stress distribution in bedrock canyons of the Fraser River also has implications for modelling spatial variations of morphodynamics along individual canyon reaches. The bed stress spikes as water enters the CPW sequence, and becomes negligible as water exits the CPW sequence. The spikes in bed stresses along the entrance slope of the CPW sequence would cause high vertical erosion there, leading to the upstream migration of the scour pool. The muted bed stresses along the exit slope of the CPW sequence would cause sediment deposition there, leading to negligible vertical erosion. The peak bed stress within each CPW sequence τ_{peak} is larger than the total shear stress τ_{Tot} for all studied canyons. Venditti et al. (2014) reported that the ratio τ_{peak}/τ_{Tot} was ~3.6 for Iron Canyon using a different and more limited dataset. However, they reduced τ_{Tot} by 50% to account for wall stresses. In our dataset, the ratio τ_{peak}/τ_{Tot} ranges from 1 to 20 with a mean of 4.9 (±0.35). The ratio τ_{peak}/τ_{bed_o} also ranges from 1 to 20 with a mean of 7.5 (±0.45) (Figure 4.12). Given that erosion rate tends to scale with bed stress to a power greater than 1 (Sklar & Dietrich, 2004; Lamb et al., 2008, 2015; Hurst et al., 2021), there would be larger variation of erosion rate than that of bed stress. This result would exaggerate the spikes in erosion rate along the entrance slope of pools, leading to deepening and migration of scour pools. The exaggeration of erosion rate at deep pools would create a positive feedback whereby the higher bed stress deepens the scour pools, which in turn increases the near-bed velocity and the bed stress. The pools of the Fraser Canyon mostly have depths of ~30 m (Venditti et al., 2020a), suggesting that these pools are depth limited. However, the question of how scour pools are depth limited remains unanswered from our analysis. Cao et al. (2022) show that pool depth is limited by development of continuous alluviation, which has also been shown in step-pool channels (Carling et al., 2006).

The lower bed stress than the total stress and the wall stress has implications for the feedbacks amongst bed alluviation, vertical erosion and lateral erosion. A lower bed stress leads to a lower transport capacity and hence a higher extent of alluvial cover at given discharge and sediment supply. The increase in sediment coverage on the bed can reduce the channel-bed erosion due to the decrease in bed exposure, but tends to increase the channel-wall erosion because the alluvium can deflect bedload particles toward the walls (e.g., Fuller et al., 2016; Fernández et al., 2019). Continued channel widening reduces the water depth and further decreases the bed stress (Fuller et al., 2016; Li et al., 2020). This positive feedback would grow until the bed stress is below the threshold of motion so that the channel has to get steeper to transport the supplied sediment (Li et al., 2021).

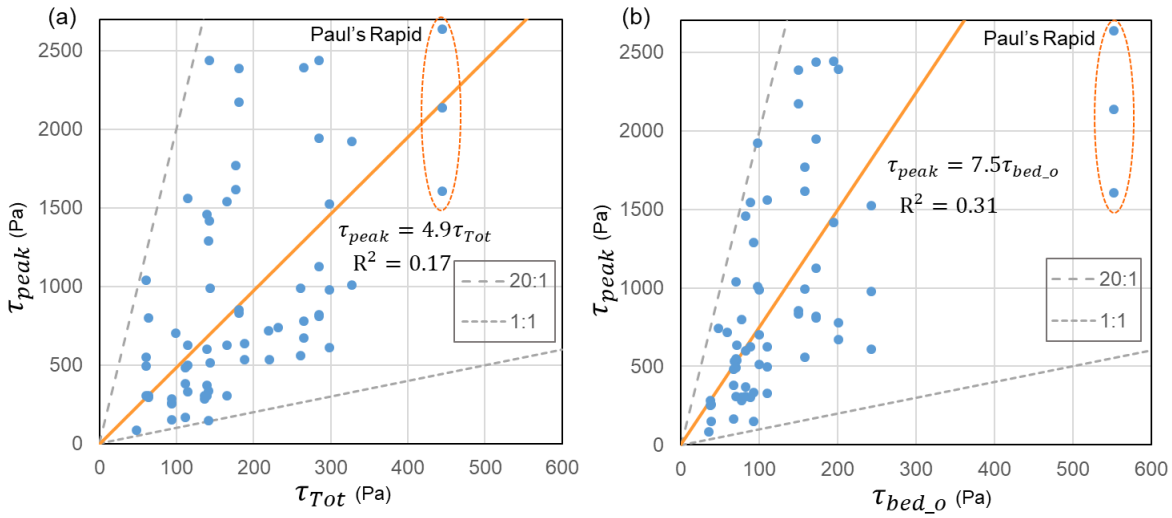

Figure 4.12 Relations between a) peak bed stress τ_{peak} within each pool and total stress τ_{Tot}, and b) peak bed stress τ_{peak} within each pool and mean bed stress τ_{bed_o}. Paul's Rapid (plotted within the orange circle) is not incorporated in the regression.

4.5.3. Application to natural bedrock rivers

Our model results show that wall stress exceeds bed stress in most studied canyons in the Fraser River. Few measurements of bedrock wall morphology are available to help guide a mechanistic parameterization of wall

roughness and calibrate the RIM model. Despite the disagreement between the model and the field data, the difference between the model and observed bed stresses (+56%) and wall shear stresses (-57%) are consistent in the Fraser Canyon (Figure 4.10). There are wide variations in the difference between the model and the observed shear stresses that are caused by variation in the field observations, but the consistency of the difference between modelled and observed shear stresses indicates that the RIM can be used as a first-order estimate of bed and wall shear stresses, which needs to be further adjusted for wall roughness.

To help guide prediction of bed and wall shear stresses in a bedrock river reach, we propose a shear stress partitioning method that includes: 1) measurement of the mean depth $\bar{h}$, slope S and bank angle α (if possible) within the bedrock river reach; 2) calculation of total shear stress from 1-D momentum balance $\tau_{Tot} = \rho g \bar{h} S$; 3) partitioning the initial bed and bank shear stresses from the RIM using Equation 4; 4) dividing the initial bed and bank stresses by correction factors that correct the RIM prediction for wall roughness and complex flow structures. The bed stress correction factor is 1.56 and the wall correction factor is 0.43 for the Fraser Canyon using the centerline depth. The peak bed stress could be further predicted by multiplying the bed stress by 7.5. Where subaqueous bank angle cannot be measured, it can be estimated recognizing that the RIM prediction is not very sensitive to small deviations of bank angle. Although the framework offers insight into the distribution of shear stress, measurements of shear stress in other bedrock rivers are needed to determine whether the coefficients proposed here are suitable. We caution against using the correction factors derived from the Fraser Canyon in systems with very different geology and geological history, different morphologies, or outside of the parameter space used to derive them (e.g. w/h<2.5).

Our proposed framework uses depth-slope product to estimate τ_{Tot} instead of using the hydraulic radius because it is easier to constrain depth from our measurements of channel centerline and because using the hydraulic radius

produces a result that is not physically possible. Comparison of τ_{Tot} calculated using depth and the hydraulic radius reveals that the latter value calculated is smaller than the former (Figure 4.8). Using hydraulic radius, τ_{bed_o} is ~19% smaller than τ_{Tot}, compared with ~42% smaller using depth, and τ_{wall_o} is ~37% larger than τ_{Tot}, compared with ~74% using depth (Figure 4.8). The difference between modelled and measured bed shear stress is smaller using the hydraulic radius than using the depth in calculation of τ_{Tot}. The ratio $\tau_{bed\_m}/\tau_{bed\_o}$ is ~1.56 using the depth but ~1.16 using the hydraulic radius. The ratio $\tau_{wall\_m}/\tau_{wall\_o}$ is ~0.46 using the hydraulic radius compared with ~0.43 using the depth (Figure 4.10).

While the pattern of over-prediction and under-prediction is the same using the hydraulic radius and depth, when τ_{Tot} is calculated from hydraulic radius, we find that $\tau_{wall\_o} < 0$ for three canyons, which is not physically possible. The reason for this is not obvious. It is possible that there is error embedded in our calculation of τ_{Tot} using both depth and hydraulic radius and that the calculation using depth is sufficiently large that it always exceeds the error. We regard this as unlikely because our depths are measured at high resolution over long reaches. In contrast, the hydraulic radius, which is a measure of the channel cross-section, can only be roughly estimated from the mean width, mean depth and bank angles of the canyon. We have no measurement of cross-sections. We suspect that the negative result is because our estimate of the hydraulic radius is not commensurate with the resolution of the bed shear stress observations. It is also not clear that hydraulic radius calculated from cross-sections is capable of capturing the variation in the banks that cause the high stress on the walls (Carling et al., 2019).

The proposed framework above uses the centerline depth to calculate τ_{Tot}, which likely overestimates the bed stress. Bedrock channel cross-sections or the three-dimensional bed topography required to better constrain depth and the hydraulic radius are challenging to obtain in all but the smallest channels. In order to assess the bias caused by using the centerline depth in τ_{Tot}

calculations, we repeat the calculations with depth that is reduced by 10%, 20% and 30%. Reducing depth decreases τ_{Tot}, which increases the ratio of bed stress to total stress by ~14%, per 10% decrease in depth. The ratio of wall stress to total stress reduces by ~11%, per 10% decrease in depth. The correction factor in our proposed framework decreases by ~10% for bed stress and increases by ~5% for wall stress, per 10% decrease in depth (Figure 4.13). It is important to recognize that large decreases (>10%) on flow depth produce negative wall stresses in our analysis and are probably not reasonable. Fortunately, in bedrock channels with a rectangular or trapezoidal cross-section shape, the difference between the mean depth and centerline depth is likely to be small. Nevertheless, the bias induced by using a centerline depth in our framework can be corrected by adjusting the depth used in calculating τ_{Tot} and adjusting the bed stress correction factor and the wall stress correction factor to values shown in Figure 4.13.

Ultimately, detailed measurements of bedrock canyon morphology, wall roughness, and flow structure are necessary to develop a more mechanistic parameterization of wall and bed shear stresses. Such observations can be used to drive hydraulic models that are capable of capturing non-uniform flow structures common in bedrock canyons and that give physical representations of bed and wall stresses. Until such observations and model simulations can be obtained, we recommend using depth to calculate τ_{Tot} rather than hydraulic radius, recognizing that the centreline depth estimate of τ_{Tot} is slightly biased towards larger stresses.

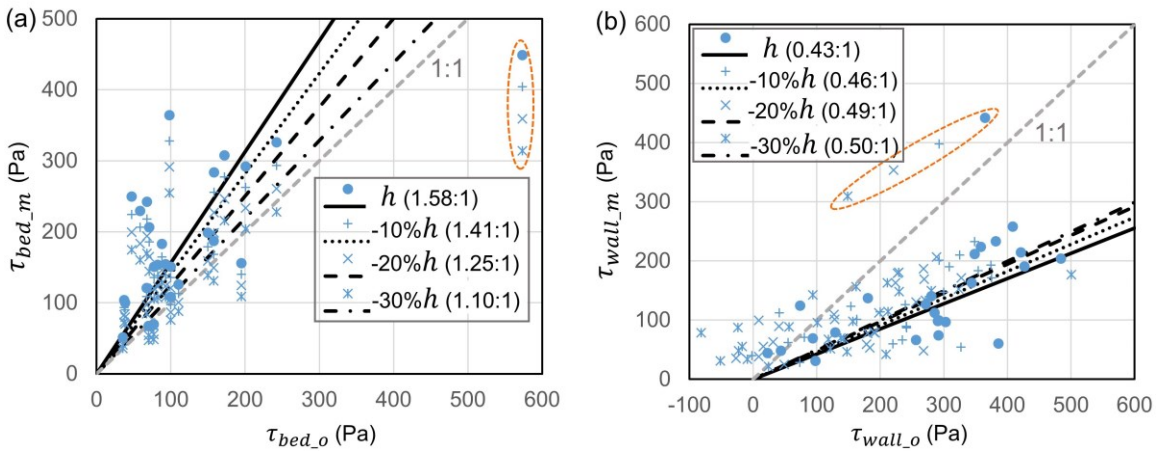

Figure 4.13 Variations of correction factors in our proposed shear stress partitioning framework for a) bed stress and b) wall stress, when we repeat our calculations of total stress using depth that is reduced by 10%, 20% and 30%. Paul's Rapid (plotted within the orange circle) is not incorporated in the regression.

4.6. Conclusion

We have partitioned bed and wall stresses in bedrock rivers from model simulations and field measurements in the major bedrock canyon of the Fraser River. The ray-isovel model (RIM) predicts the ratio of wall to bed stress as a function of the width to depth ratio. The modelled ratio of wall to bed stress exponentially decreases with increasing width-to-depth ratio. Application of the model results to 26 canyons in the Fraser River predicts that the ratio of wall to bed stress varies between 0.60 and 0.98. In general, the modelled bed stress is ~9% larger than the total stress, while the modelled wall stress is ~19% smaller than the total stress.

Measured bed stress distributions through individual bedrock canyons in the Fraser River show that the bed stress spikes as water enters the constriction-pool-widening sequences but is negligible at the downstream exit of pools. Distributions of bed stress are heavy-tailed because shear stress is low through most of the canyon, with notable spikes in stress associated with plunging flows in pools. For the majority of the 26 canyons in our study, the observed wall stress exceeds the total stress, which exceeds the bed stress. This outcome implies

that the bedrock walls are a substantial momentum sink, and the assumption of equal bed and total stress in most bedrock erosion models is not true.

There is variation between the model and the field observations that further complicates morphodynamic modelling of bedrock rivers. Compared with the observed stresses, the model nearly always over-predicts the observed bed stress by ~56% (±15%), but under-predicts the observed wall stress by ~57% (±3.2%). The failure of the model to predict the observed stresses is likely because complex non-uniform flow and morphological structures in bedrock canyons make the walls rougher than the bed, which is not represented in the RIM. Our results provide a first order estimate of bed, wall and peak bed shear stresses and correction factors that permit use of our simplified RIM in bedrock canyons to partition stresses.

Chapter 5. Lateral Erosion of Bedrock Channel Banks by Bedload and Suspended Load

Abstract

Bedrock rivers carry large amounts of fine sediment in suspension. We developed a mechanistic model for erosion of bedrock channel banks by impacting bedload and suspended load particles that are advected laterally by turbulent eddies (advection-abrasion model). The model predicts high lateral erosion rates near the bed, with rates decreasing up to water surface. The model also predicts greater erosion within the suspended load layer than the bedload layer for the majority of sediment supply and transport conditions explored. We compared the advection-abrasion model with a previously derived model for lateral erosion of bedrock banks by bedload particles deflected by stationary bed alluvium (deflection-abrasion model). Erosion rates predicted by the deflection-abrasion model are lower, except within limited conditions where sediment is transported near the threshold of motion and the bed is near fully covered in sediment. Both processes occur in bedrock rivers at the same time, so we combined the advection-abrasion and deflection-abrasion models and found that the lateral erosion rate generally increases with increasing transport stage and relative sediment supply for a given grain size. Application of our combined-abrasion model to a natural bedrock river with a wide distribution of discharge and supply events, and mixed grain sizes, indicates that finer sediment dominates the lateral erosion on channel banks in low sediment supply environments and can be as important as coarser sediment in high sediment supply environments.

5.1. Introduction

Those who have seen the turbid and turbulent flow of a flooding mountain river know that bedrock rivers transport vast quantities of fine sediment in suspension. Could these tiny but energetic particles be responsible for eroding

bedrock river banks and thus govern the width of actively incising channels? Surprisingly, this question has not yet been investigated mechanistically. Much work has focused on mechanistic models for vertical erosion by saltating bedload particle impacts (Sklar & Dietrich, 2004; Huda & Small, 2014). Application of the vertical erosion model by saltating bedload particle impacts (referred to as the saltation-abrasion model hereafter) have led to insights into the controls of channel width, channel slope and knickpoint migration (Sklar & Dietrich, 2006, 2008; Wobus et al., 2006; Nelson & Seminara, 2011; Yanites, 2018). However, the saltation-abrasion model predicts zero vertical erosion rate within the suspension regime, assuming that suspended particles have infinite hop length and do not impact the channel bed. As sediment transport transitions from bedload to suspension, the saltation trajectories become more irregular because they are no longer dominated by the effect of gravity, instead they are strongly influenced by turbulence (Bagnold, 1973; Naqshband et al., 2017). Within the suspension regime, sediment is transported in a near-bed bedload layer with high sediment concentrations and a more dilute suspended-load layer above, with active interchange of these two layers (Rouse, 1937; McLean, 1991). To incorporate the change in sediment transport from bedload to suspension, the saltation-abrasion model has been reformulated in terms of near-bed sediment concentration instead of particle hop length (referred to as the total-load model hereafter; Lamb et al., 2008a). The total-load model predicts higher impact velocity of suspended particles at higher transport stage and hence nonzero erosion rates within the suspension regime, consistent with observations in laboratory experiments (Sklar & Dietrich, 2001; Scheingross et al., 2014).

Previous investigations of the mechanics of lateral erosion of bedrock channel banks have focused on abrasion by bedload particles. Fuller et al. (2016) conducted a set of flume experiments with a non-erodible bed covered with protruding roughness elements and erodible banks composed of weak concrete, and documented lateral erosion by saltating bedload impacts deflected by bed roughness. Using this mechanism, Turowski (2018, 2020) developed a reach-scale lateral erosion model, treating gravel bars as a source of roughness

to deflect bedload particles, but did not explicitly model the deflection process. Another lateral erosion model directly captured the energy transfer of bedload particles deflected by bed roughness to impact the banks (Li et al., 2020, 2021; referred to as the deflection-abrasion model hereafter). These lateral erosion models have been used to explore bedrock channel width and bed slope dynamics in response to change in grain size and sediment supply rate (Li et al., 2021), as well as adjustment timescales to achieve steady-state bedrock channel morphology (Turowski, 2020). One weakness of deflection-abrasion models is that they predict lateral erosion concentrated only in the lower part of bedrock rivers banks, creating undercut banks without eroding the overhanging upper portion of the channel bank (Li et al., 2020). While overhanging banks have been observed in laboratory experiments that included only bedload (Fuller et al., 2016; Mishra et al., 2018; Cao et al., 2022), overhangs are not commonly observed in natural bedrock rivers. Overhanging banks might be removed in natural rivers due to collapse, particularly in highly fractured, weak bedrock. However, overhanging banks may also be rare because the suspended load can be advected by turbulent eddies to erode channel banks above the bedload layer height.

Field observations suggest that erosion by suspended sediment is likely responsible for the formation of sculpted banks of slot canyons (Wohl, 1993; Wohl et al., 1998; Richardson & Carling, 2005; Carter & Anderson, 2006), creation of flutes and scallops on boulders protruding high into flow (Whipple et al., 2000), and wear of bedrock banks above the bedload layer height and near the water surface (Hartshorn et al., 2002; Beer et al., 2017). To explore the efficacy of suspended load on eroding bedrock channel banks in comparison to bedload, we developed a mechanistic model for lateral riverbank erosion due to impacts of bedload and suspended load particles advected by turbulent eddies (referred to as the advection-abrasion model hereafter). We start by deriving the advection-abrasion model, building on the total-load model for vertical incision by bedload and suspended load (Lamb et al. 2008a). Next, we combine the advection-abrasion and deflection-abrasion models for a complete model that

captures both processes of lateral erosion. We investigate the sensitivity of predicted lateral erosion rates within the bedload layer and the suspended load layer to variation in grain size, water discharge, sediment supply and change slope. Finally, we discuss the implications of the combined-abrasion model for the relative importance of finer and coarser sediment in eroding bedrock channel banks.

5.2. Advection-Abrasion Model Development

5.2.1. General expression

The advection-abrasion model is based on the idea that particles are advected toward the banks by turbulent flow fluctuations and cause lateral erosion in bedrock rivers. Given that all bedrock rivers have turbulence and carry suspended sediment in some quantity, the erosion model due to turbulence is not limited to the occurrence of stationary bed alluvium, which is necessary in the Turowski (2020) and Li et al. (2020, 2021) models, to deflect the downstream transport particles to impact the banks. The advection-abrasion model also includes particles transported as both bedload and suspended load, which the deflection-abrasion model does not.

Following the formulation of the saltation-abrasion model (Sklar & Dietrich, 2004) and total-load model (Lamb et al., 2008a; Scheingross et al., 2014) for vertical erosion, the lateral erosion rate predicted by the advection-abrasion model, E_a, can be written as a product of two terms: the eroded volume by per particle impact, V, and the impact rate per unit area and time, I, that is,

$$E_a = VI. \qquad \text{(Equation 5.1)}$$

The eroded volume per particle impact, V, is proportional to the kinetic energy of the impacting particles (Sklar & Dietrich, 2004)

$$V = \frac{\pi \rho_s D^3 Y}{6 k_v \sigma_T^2} {v_p}^2, \qquad \text{(Equation 5.2)}$$

where Y is Young's modulus of elasticity of the bedrock, k_v is the dimensionless bedrock strength coefficient, σ_T is the tensile yield strength, ρ_s is the sediment density, D is the median grain size and v_p is the impact velocity normal to the banks. The time-averaged impact rate, I, is proportional to the product of v_p and the volumetric sediment concentration, c, (Lamb et al., 2008a)

$$I = \frac{\Psi c v_p}{V_p}, \qquad \text{(Equation 5.3)}$$

where Ψ is a dimensionless coefficient describing the portion of particles near the banks that are advected toward the banks. The volume of nominally spherical sediment grains V_p (=$\pi D^3/6$) is used in Equation (3) to convert the mass flux into the volumetric flux. Substituting Equations (5.2)-(5.3) into Equation (5.1) yields

$$E_a = \frac{\Psi \rho_s Y}{k_v \sigma_T^2} c {v_p}^3. \qquad \text{(Equation 5.4)}$$

To estimate the lateral erosion rate in Equation (5.4) directly from control variables in bedrock rivers, we determine local hydraulic conditions from the law of the wall, and then develop expressions for lateral impact velocity and sediment concentration.

5.2.2. Local hydraulic conditions

Local hydraulic conditions are calculated from five input variables: volumetric water discharge: Q_w, channel width: W, channel slope: S, particle diameter: D, and boundary roughness height: z_0. For steady and uniform turbulent flow in open channels, the downstream flow velocity, $u'(z)$, is calculated from the law of the wall

$$u'(z) = \frac{u^*}{\kappa} ln(\frac{z}{z_0}) , \qquad \text{(Equation 5.5)}$$

where κ is von Karman's constant ($\kappa = 0.41$), z is height above the river bed, and z_0 is a function of the boundary roughness (Henderson, 1966). Following Lamb et al. (2008a), we set $z_0 = nD_{84}/30$ with empirical coefficient $n = 3$ (D_{84} is the 84th percentile of the surface bed material). This parameterization of the hydraulic roughness can be modified in natural bedrock rivers with partially covered bed by sediment, and with protruded bedrock roughness on the bed and banks (Finnegan et al., 2007; Johnson & Whipple, 2010; Inoue et al., 2014; Johnson, 2014; Beer et al., 2017; Li et al., 2022). The shear velocity is calculated from the hydraulic radius, R, and channel bed slope, S, as

$$u^* = \sqrt{gRS}, \qquad \text{(Equation 5.6)}$$

assuming steady and uniform flow with uniform roughness of channel bed and banks, where $R = Wh/(W + 2h)$, and h is water depth. Assuming the law of the wall is applicable throughout the water column, the depth-averaged flow velocity is estimated from integrating Equation (5.5)

$$\bar{u} = \frac{1}{h}\int_{z_0}^{h} \frac{u^*}{\kappa} ln(\frac{z}{z_0})dz. \qquad \text{(Equation 5.7)}$$

Depth-averaged flow velocity, $\bar{u}$, and flow depth, h, are solved by combining Equations (5.6)-(5.7) with continuity, $Q_w = Wh\bar{u}$. The non-dimensional shear stress, τ^*, is obtained from shear velocity,

$$\tau^* = \frac{(u^*)^2}{R_b g D}. \qquad \text{(Equation 5.8)}$$

where $R_b = \rho_s/\rho_w - 1$ is non-dimensional buoyant density, ρ_w is water density, and g is the gravitational acceleration.

5.2.3. Impact velocity

The particle impact velocity, v_p, on the banks is induced by lateral turbulent flow velocity fluctuations, v', near the banks that advect particles toward the banks. Turbulent fluctuations embedded in open channel flows are a complex phenomenon. Although numerical and experimental work has been done to explore the complex three-dimensional turbulence structure in open channel

flows (e.g., Nezu, 2005; Venditti, 2013), this level of complexity is arguably not warranted for developing a model for bedrock channel change over geomorphic timescales. For simplicity, we follow Lamb et al. (2008a) and assume that the probability density function, P, of lateral flow velocity fluctuations v' is a Gaussian distribution (Nezu and Nakagawa, 1993)

$$P(v') = \frac{1}{\sqrt{2\pi}\sigma_v} e^{-\frac{(v')^2}{2\sigma_v^2}}, \qquad \text{(Equation 5.9)}$$

where the mean lateral flow velocity is zero, and σ_v is the standard deviation of lateral flow velocity fluctuations and is approximated by the turbulent intensity. The turbulence contributing to lateral flow velocity fluctuations is influenced by both bed and bank roughness. Bank roughness in bedrock rivers can contribute to turbulent fluctuations and hence the impact velocity on the banks (e.g., Carter & Anderson, 2006). The bedrock banks can be rougher than channel bed in bedrock rivers (e.g., Li et al., 2022), which may cause strong turbulence near the bank region (Venditti et al., 2014). However, there is no established relation to predict turbulence fluctuations due to bank roughness. Hence, we only consider the turbulence generated by the bed, assuming that the turbulence generated by bedrock banks is relatively negligible compared with the bed. Nezu & Nakagawa (1993) proposed an exponential expression to describe the vertical variation of lateral flow turbulence intensity σ_v in open channel flows,

$$\frac{\sigma_v}{u^*} = D_v e^{-z/h} \qquad \text{(Equation 5.10)}$$

where D_v is the empirical coefficient, that has a typical value of 1.63 (Nezu & Nakagawa, 1993). Variation in D_v has been reported to depend on channel boundary roughness (Soulsby, 1981; Tominaga et al., 1989; Knight & Shiono, 1990; Sukhodolov et al., 1998; Carling et al., 2002; Sukhodolov et al., 2006) and flow depth relative to boundary roughness (Lamb et al., 2008b; Lamb et al., 2017). However, the range of variations in D_v is narrow (1.39-1.89) and no improvement in scaling σ_v with depth-averaged velocity is found as compared with u^* (Lamb et al., 2017). For simplicity we elected to use D_v =1.63 reported by Nezu & Nakagawa (1993).

The particle impact velocity fluctuations normal to the banks, v_p', is calculated from the acceleration of a particle moving toward the banks laterally due to the fluid drag force, which is given by conservation of linear momentum as

$$\frac{\mathrm{d}v_p'}{\mathrm{d}t} = \frac{1}{2} C_1 \frac{\rho_w}{\rho_s} \frac{A_l}{V_p} (v' - v_p')^2 \qquad \text{(Equation 5.11)}$$

where C_1 (0.45) is the drag parameter and A_l the cross-sectional area of the particle perpendicular to v'.

To solve Equation (5.11) analytically, we assume v' is constant over an eddy turnover timescale, t_l. Under this assumption, $\mathrm{d}v_p'/\mathrm{d}t$ is approximated by $-\mathrm{d}(v' - v_p')/\mathrm{d}t$. Equation (5.11) can then be solved by integration to obtain

$$v_p' = v' - \frac{1}{\frac{3\rho_w C_1}{4\rho_s D} t_l + \frac{1}{v'}} \qquad \text{(Equation 5.12)}$$

where the boundary condition $v_p'(t = 0) = 0$ has been applied and particles are assumed to be spheres (i.e., $A_l/V_p = 1.5/D$).

The mean lateral particle velocity is then found by combining Equations (5.9) and (5.12) and integrating v_p' over all possible velocity fluctuations. However, the lateral erosion rate scales with the cube of individual particle velocity v_p' (Equation 5.4), not the mean lateral particle velocity. Therefore, following Lamb et al. (2008a), we define an effective impact velocity, v_p, by combining Equations (5.9) and (5.12) and nonlinear averaging, as

$$v_p = \left[\int_{v'_{min}}^{6\sigma_v} \left(v' - \frac{1}{\frac{3\rho_w C_1}{4\rho_s D} t_l + \frac{1}{v'}}\right)^3 \frac{1}{\sqrt{2\pi}\sigma_v} e^{-\frac{(v')^2}{2\sigma_v^2}} \, dv' \right]^{1/3}, \qquad \text{(Equation 5.13)}$$

where the upper limit of integration of $6\sigma_v$ is chosen to include near 100% of the possible fluctuations and the lower limit of integration, v'_{min}, is determined from the lower limit of particle velocity, v_{min}, that causes erosion using Equation (5.12). Following Lamb et al., (2008a) and Li et al. (2020), v_{min} is given as

$$v_{min} = \frac{9 S_t \rho_w \eta}{\rho_s D} \qquad \text{(Equation 5.14)}$$

where S_t is the particle Stokes number (~ 100; Schmeeckle et al., 2001; Joseph & Hunt, 2004), and η is the kinematic viscosity of the fluid (10^{-6} m^2s^{-1}).

To solve Equation (5.13), the eddy turnover time t_l needs to be specified. Turbulent energy is extracted from the mean flow in the production subrange, and is transferred from macroscale (energetic) eddies to microscale (dissipative) eddies in the energy-cascade process. The rate at which energy is transferred from macroscale structures to microstructures ϵ (i.e., the energy dissipation rate) can be characterized by the fluctuating velocity σ_v over an integral length scale l (e.g., Batchelor, 1953; Nezu & Nakagawa, 1993; Mouri et al., 2012; Vassilicos, 2015),

$$\epsilon = C_\epsilon \frac{{\sigma_v}^3}{l} \qquad \text{(Equation 5.15)}$$

where C_ϵ is a constant (~1) originating from the Richardson-Kolmogorov cascade under the assumption that turbulence is at equilibrium (Kolmogorov, 1941a, 1941b), and the time scale associated with l is $t_l = l/\sigma_v$.

Assuming the turbulent energy is in local equilibrium (turbulent kinetic energy generation G = turbulence dissipation ϵ), ϵ can be obtained as a function of the distance from the bed, z, using the law of the wall (Grinvald, 1974; Nikora & Smart, 1997)

$$\frac{\epsilon H}{{u^*}^3} = \frac{1}{\kappa}\left(\frac{1-z/h}{z/h}\right). \qquad \text{(Equation 5.16)}$$

Combing Equations (5.15)-(5.16) with $t_l = l/\sigma_v$, t_l can be solved as

$$t_l = \kappa C_\epsilon \frac{{\sigma_v}^2}{{u^*}^3(1/z-1/h)}. \qquad \text{(Equation 5.17)}$$

5.2.4. Sediment concentration

To calculate the vertical distribution of sediment concentration, we partition the supplied sediment flux into a bedload layer and a suspended load layer. We assume the sediment within the bedload layer is well mixed (McLean,

1991; Lamb et al., 2008a; De Leeuw et al., 2020), and use the Rouse-Vanoni equation to predict the vertical profile of sediment concentration above the bedload layer

$$c = \begin{cases} c_b; & (z \le h_s) \\ c_b \left[\frac{h/z-1}{h/h_s-1}\right]^P & (z > h_s) \end{cases}, \quad \text{(Equation 5.18)}$$

where c_b is the volumetric concentration within the bedload layer, h_s is the bedload layer height, $P = w_f/\Upsilon\kappa u^*$ is the Rouse number (Rouse, 1938), Υ is a dimensionless coefficient and w_f is the particle settling velocity. The bedload layer height, h_s, is predicted from the empirical relation developed by Sklar & Dietrich (2004),

$$\frac{h_s}{D} = 1.44\left(\frac{\tau^*}{\tau_c^*} - 1\right)^{0.50}, \quad \text{(Equation 5.19)}$$

where τ_c^* is the value of τ^* at the threshold of sediment motion.

The coefficient Υ is a dimensionless factor that accounts for differences between the diffusivities of momentum and sediment, typically assumed to be a constant of order unity. Previous studies have found that Υ varies with the ratio of settling velocity w_f to shear velocity u^* and flow resistance coefficient (e.g., De Leeuw et al., 2020). To incorporate this effect, we use the best-fit one-parameter model for Υ proposed by De Leeuw et al. (2020), which is $\Upsilon = 2.44(u^*/w_f)^{-0.55}$. We follow Ferguson & Church (2004) to calculate the particle settling velocity w_f,

$$w_f = \frac{R_b g D^2}{C_2\eta + (0.75 C_3 R_b g D^3)^{0.5}} \quad \text{(Equation 5.20)}$$

where $C_2 = 18$ and $C_3 = 1$ are constants set for natural sediment.

Following Lamb et al. (2008a), the volumetric concentration within the bedload layer, c_b, is calculated from continuity as

$$c_b = \frac{q}{\bar{u}h\chi + u_s h_s}, \quad \text{(Equation 5.21)}$$

where q is the total volumetric flux of sediment per unit channel width traveling as both bedload and suspended load, u_s is the longitudinal saltation velocity and χ is the integral relating suspended sediment flux to the parameters of the flow and sediment concentration within the bedload layer, which we calculate according to Lamb et al. (2008a)

$$\chi = \frac{1}{\bar{u}h}\int_{h_s}^{h}\left[\frac{h/z-1}{h/h_s-1}\right]^P \frac{u^*}{\kappa} ln\left(\frac{z}{z_0}\right)dz. \qquad \text{(Equation 5.22)}$$

The longitudinal saltation velocity u_s is estimated from Sklar & Dietrich (2004),

$$u_s = 1.56(R_b g D)^{0.5}\left(\frac{\tau^*}{\tau_c^*}-1\right)^{0.56}. \qquad \text{(Equation 5.23)}$$

5.2.5. Composite expression for the advection-abrasion model

Substituting Equations (5.13) and (5.18) into Equation (5.4) yields the composite expression for the advection-abrasion model,

$$E_a(z) = \begin{cases} \frac{\Psi\rho_s Y}{k_v\sigma_T^2}\frac{q}{\bar{u}h\chi+u_s h_s}\int_{v'_{min}}^{6\sigma_v}\left(v'-\frac{1}{\frac{3\rho_w C_d}{4\rho_s D}t_l+\frac{1}{v'}}\right)^3\frac{1}{\sqrt{2\pi}\sigma_v}e^{-\frac{(v')^2}{2\sigma_v^2}}dv'; & (z\le h_s) \\ \frac{\Psi\rho_s Y}{k_v\sigma_T^2}\frac{q}{\bar{u}h\chi+u_s h_s}\left[\frac{h/z-1}{h/h_s-1}\right]^P\int_{v'_{min}}^{6\sigma_v}\left(v'-\frac{1}{\frac{3\rho_w C_d}{4\rho_s D}t_l+\frac{1}{v'}}\right)^3\frac{1}{\sqrt{2\pi}\sigma_v}e^{-\frac{(v')^2}{2\sigma_v^2}}dv'. & (z>h_s) \end{cases}$$

(Equation 5.24)

where the vertical profile of lateral erosion rate $E_a(z)$ is divided into two layers: the bedload layer ($z \le h_s$) and the suspended load layer ($z > h_s$).

5.3. Combined-Abrasion Model

We propose that lateral erosion should be modeled as a combination of the deflection-abrasion and advection-abrasion mechanisms. To do that, we briefly review the deflection-abrasion model and combined it with the advection-abrasion model (referred to as the combined-abrasion model hereafter).

5.3.1. Expression for the Deflection-Abrasion Model

Li et al. (2021) developed an expression for the lateral erosion rate assuming uniformly distributed alluvium, E_d,

$$E_d = \frac{\pi Y}{48 k_v \sigma_T^2} \frac{D}{h_{max}} \frac{q_s^2 (1 - 0.8 q_s/q_t)}{q_t} \left(\frac{1}{h_s} + \frac{3}{2 l_s}\right) v_o^2 \frac{1 - e^{-2 C_d y_{max}}}{e^{C_d D q_t/q_s} - e^{-C_d D q_t/q_s}} (1 - (u^*/w_f)^2)^{1.5}, \quad \text{(Equation 5.25)}$$

where $C_d = 0.75 C_1 \rho_w/(D \rho_s)$ is the drag deceleration coefficient, q_s is the bedload supply rate, q_t is the bedload transport rate, y_{max} is the maximum distance between the point of deflection and the channel bank above which deflectors will not cause lateral erosion, h_{max} is the maximum impact height on the bank, l_s is the saltation length, and v_o is lateral particle velocity after being deflected by the alluvium surface.

Bedload transport rate, q_t, is estimated from Fernandez Luque & Van Beek (1976),

$$q_t = 5.7 (R_b g D^3)^{0.5} (\tau^* - \tau_c^*)^{1.5}. \quad \text{(Equation 5.26)}$$

The distance, y_{max}, is calculated from the minimum velocity that causes erosion (Li et al., 2021)

$$y_{max} = \frac{4 \rho_s D}{3 \rho_w C_1} \ln \frac{v_o}{v_{min}}. \quad \text{(Equation 5.27)}$$

The saltation length, l_s, is predicted from the empirical relation developed by Sklar & Dietrich (2004)

$$\frac{l_s}{D} = 8.0 \left(\frac{\tau^*}{\tau_c^*} - 1\right)^{0.88}. \quad \text{(Equation 5.28)}$$

The maximum height of erosion, h_{max}, is given as

$$h_{max} = 1.5 D + \frac{1}{2 C_d} ln\left(\frac{C_d {w_o}^2}{C_g} + 1\right), \quad \text{(Equation 5.29)}$$

where $C_g = (1 - \rho_w/\rho_s) g$ is the gravitational acceleration coefficient and w_o is the vertical particle velocity after being deflected by the alluvium surface (Li et al.,

2021). The velocities, w_o and v_o, can be obtained from the momentum transfer at the point of deflection,

$$w_o = C_r(w_s - 2n_z(n_x u_s + n_z w_s)). \quad \text{(Equation 5.30)}$$

$$v_o = 2C_r n_y(n_x u_s + n_z w_s) \quad \text{(Equation 5.31)}$$

where C_r is the restitution coefficient (set to 0.9) that describes the loss of particle momentum during the collision between bedload particle and alluvium surface, n_x, n_y and n_z are downstream, lateral and vertical component of the unit vector that is normal to the alluvium surface at the point of deflection, respectively ($n_x = 0.30\,q_s/q_t - 0.54$; $n_y = 0.25\,q_s/q_t - 0.58$; $n_z = 0.40\,q_s/q_t + 0.50$; Li et al., 2021), and w_s is vertical saltation velocity that is estimated from empirical relations by Lamb et al. (2008a)

$$w_s = -\sqrt{\frac{C_g}{C_d}(1 - e^{-2C_d(h_s - h_d)})}, \quad \text{(Equation 5.32)}$$

where h_d is the height of bedload particle during collision with the deflector. The ratio, h_d/h_s, is a function of transport stage τ^*/τ_c^* and the ratio of bedload sediment supply to bedload transport capacity q_s/q_t (Li et al., 2021)

$$h_d/h_s = 0.83e^{-0.68(\tau^*/\tau_c^* - 1)} + 0.11\,q_s/q_t + 0.06 \quad \text{(Equation 5.33)}$$

The lateral erosion rate predicted by the deflection-abrasion model can be obtained from substituting Equations (5.26)-(5.33) into Equation (5.25). The deflection-abrasion model does not account for the possibility of lateral erosion by suspended load abrasion, assuming lateral erosion rate is zero if u^*/w_f (Equation 5.25).

5.3.2. Expression for the Combined-Abrasion Model

The deflection-abrasion model and the advection-abrasion model predict erosion rates on different parts of the channel banks. The deflection-abrasion model focuses on erosion by saltating bedload particle impacts and hence predicts erosion near the bottom of the banks. The advection-abrasion model

considers the sediment concentration for the whole water column, and thus predicts erosion over the whole bank. To combine these two models, we calculate the cross-sectional area eroded per unit time to obtain an areal erosion rate from each model, which we add to get the total eroded cross-sectional area per unit time.

The cross-sectional area eroded per unit time for the deflection-abrasion model, E_{cd}, is equal to the product of the vertically averaged erosion rate, E_d, and the maximum height above the bed over which erosion occurs, h_{max}

$$E_{cd} = E_d h_{max} \quad \text{(Equation 5.34)}$$

The cross-sectional area eroded per unit time for the advection-abrasion model, E_{ca}, is the sum of the eroded cross-section area per unit time within the bedload layer, E_{cb}, and the suspended load layer, E_{cs},

$$E_{ca} = E_{cb} + E_{cs} \quad \text{(Equation 5.35)}$$

where E_{cb} and E_{cs} are obtained from integrating $E_a(z)$ over the thickness of bedload layer, h_s, and suspended layer, $H - h_s$, respectively. The total cross-sectional area eroded per unit time on the banks is the sum of E_{cd} and E_{ca},

$$E_{ct} = E_{cd} + E_{ca} \quad \text{(Equation 5.36)}$$

To explore the behavor of the advection-abrasion and deflection-abrasion models over a wide range of parameter space, we nondimensionalize areal erosion rates by multiplying by $\sigma_T^2/\rho_s Y g^{1.5} D^{2.5}$ (Sklar & Dietrich, 2004; Lamb et al., 2008a; Li et al., 2020, 2021). In this parameter space, the non-dimensional erosion rates (deflection-abrasion model: E_{cd}^*; advection-abrasion model: E_{ca}^*; and combined-abrasion model: E_c^*) are a function of transport stage, τ^*/τ_c^*, and relative sediment supply, q/q_t, for a given grain size. For given transport stage, E_{ca}^* also depends on flow depth because the vertical distributions of sediment concentration and impact velocity are a function of flow depth (Equation 5.24). In contrast, the deflection-abrasion model only considers the abrasion by saltating bedload particles and does not depend on flow depth (Equation 5.26).

5.4. Model Results

Both the advection-abrasion model and the deflection-abrasion model predict that the lateral erosion rate depends on four principle variables: water discharge Q_w, channel slope S, sediment supply q, and grain size D, for given rock strength. To explore the distribution of lateral erosion on channel banks and the relative importance of lateral erosion within the bedload and the suspended load layers, we vary each of these four variables independently. We also explore the variation of the nondimensionalized erosion rates predicted by the advection-abrasion model, the deflection-abrasion model, and the combined-abrasion model over parameter space defined by transport stage and relative sediment supply.

We selected Black Canyon in the Fraser River, British Columbia as the reference field site to help specify model input variables (Table 5.1). The Fraser River annual hydrograph has peaks within the range between ~6070 and ~12,900 m^3/s over the past 20-years at Hope, British Columbia, the nearest gauging station to Black Canyon. Coarse sediment supply to the gravel bed reach that starts at Hope at the downstream end of bedrock canyons of the Fraser River is ~0.35 Mt/yr (megatons per year), and the annual sediment supply to the river, including gravel, sand, silt and clay is ~17.5 Mt/a (Ferguson & Church, 2009; Ferguson et al., 2015). Modelling of long-term aggradation/degradation in the Fraser canyons by Ferguson et al. (2015) suggests that the modern coarse sediment supply is < 1Mt/a, but the local sediment supply may vary substantially. Nevertheless, 0.35 Mt/a is a reasonable estimate of the coarse sediment supply in Black Canyon because that is how much is transmitted downstream to the gravel bed reach. Ferguson & Church (2009) found that a discharge of 7000 m^3/s operating 15% of the year transported the same amount and size distribution of sediment as the 20-year hydrograph, so we selected the combination of these values as our reference discharge and intermittency. Black canyon has grain diameters that range between 6 mm and 471 mm with a median size of 195 mm and the 84th

percentile of the grain size of 267 mm. The representative discharge can transport grains up to 285 mm in diameter as bedload and size up to 11 mm diameter in suspension. To compare the relative importance of bedload and suspended load, we consider two grain sizes: 10 mm diameter gravel and 195 mm diameter cobbles, which are carried as suspended load and bedload, respectively.

Table 5.1 Reference Site Values and Model Parameter Values for Black Canyon in Fraser River, British Columbia.

Variable	Value
Sediment size D (m)	0.010; 0.195
Channel width W (m)	80
Slope S	0.00234
Water discharge Q_w (m^3/s)	7000 [a]
Sediment supply q (m^2/s)	3.61×10^{-4} [a]
Critical Shields stress τ_c^*	0.045 [b]
Water density ρ_w (kg/m^3)	1000 [b]
Sediment density ρ_s (kg/m^3)	2650 [b]
Rock elastic modulus Y (Pa)	5×10^{10} [b]
Dimensionless rock resistance parameter k_v	10^6 [c]
Rock tensile strength σ_T (Pa)	7×10^6 [b]

[a] From Ferguson & Church (2009). [b] Assumed. [c] Sklar & Dietrich (2004).

5.4.1. Influence of discharge

We explored the effect of varying water discharge while holding sediment supply, grain size and channel slope set to constant values for the reference field site. Like the deflection-abrasion model, the advection-abrasion model predicts an undercut erosional shape on channel banks, where lateral erosion is concentrated near the bottom of channel banks and decreases progressively up to the water surface (Figure 5.1a-b). The maximum erosional height on channel

banks increases with increasing discharge due to the increase in water depth (Figure 5.1a-b). The maximum E_a within the undercut zone increases with increasing discharge due to the the increase in transport stage and hence impact velocity, but starts to decline at high discharge when the increase in impact velocity is outpaced by the decrease in near-bed sediment concentration, as more sediment in held in the upper water column for 10-mm gravel and 195-mm cobbles (Figure 5.1a-b). However, compared with the 195-mm cobbles, a lower discharge is required for E_a to exceed zero and the maximum E_a within the undercut zone to peak for 10-mm gravel (Figure 5.1a-b). This occurs because finer sediment can be transported at lower shear stresses and hence lower discharge for a given channel slope. Overall, the advection-abrasion model predicts similar patterns of erosion on channel banks for 10-mm gravel and 195-mm cobbles (Figure 5.1a-b).

The advection-abrasion model predicts negligible erosion rate within the bedload layer, E_{cb}, compared with the suspended load layer, E_{cs}, for both 10-mm gravel and 195-mm cobbles (Figure 5.1c-d) because the bedload layer is much thinner than the suspended layer. The total load erosion, E_{ca}, is almost the same as the erosion rate within the suspended load layer. For the gravel, E_{ca} increases with increasing discharge once the transport stage is above the threshold of motion (Figure 5.1c) due to the increase in impact velocity and the erosional height on channel banks. However, E_{ca} starts to decline at discharges higher than 2×10^5 m^3/s (Figure 5.1c). This occurs because increases in impact velocity and the erosional height are more than offset by the decrease in near-bed sediment concentration with increasing discharge. For the cobbles, the increase in transport stage is much lower than for the gravel with increasing discharge, resulting in a slower decrease in near-bed sediment concentration. Therefore, E_{ca} is more influenced by the increase in impact velocity and the erosional height on channel banks than the decrease in near-bed sediment concentration for the cobbles, as compared to the gravel, which leads to a near monotonic increase in E_{ca} with increasing discharge (Figure 5.1d).

The deflection-abrasion model predicts an increase in lateral erosion rate, E_{cd}, at low discharge due to the increase in impact energy with increasing shear stress, but starts to decline at high discharge due to the decrease in the extent of alluvial cover with increasing transport capacity for given sediment supply (Figure 5.1c-d; Li et al., 2021). The deflection-abrasion model predicts neglible lateral erosion at discharge higher than ~ 2.5×10^2 m^3/s for the gravel and ~ 3.9×10^3 m^3/s for the cobbles because there is not enough alluvium to deflect bedload particles (Figure 5.1c-d). The advection-abrasion, in contrast, predicts continued lateral erosion at high discharge. The erosion rate predicted by the advection-abrasion model is higher than the deflection-abrasion model except at low discharge when the bed is near fully covered by alluvium. Therefore, the erosion rate predicted by combined-abrasion model shows similar patterns with the deflection-abrasion model at low discharge where the deflection-abrasion mechanism dominates, but becomes fully controlled by the advection-abrasion model at intermediate and high discharges where the advection-abrasion mechanism dominates (Figure 5.1c-d).

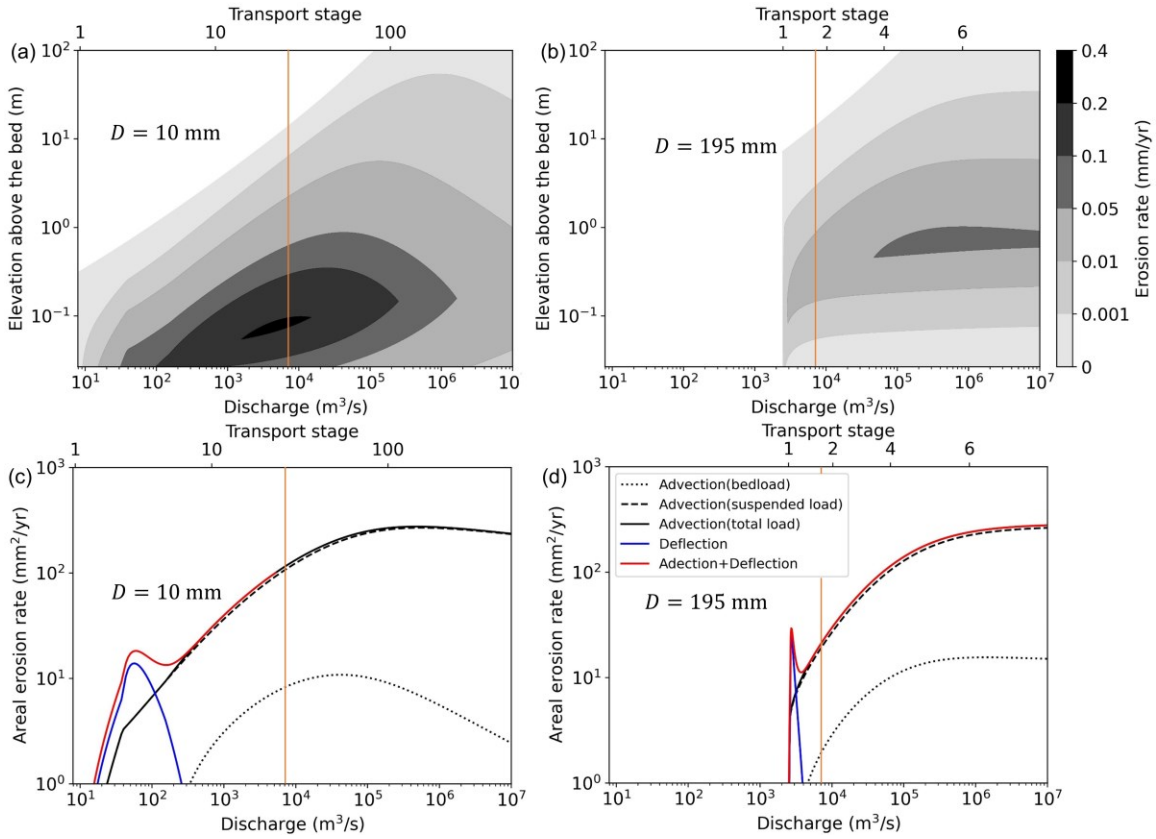

Figure 5.1 Distribution of lateral erosion rate on channel banks predicted by the advection-abrasion model as a function of discharge for (a) 10-mm gravel and (b) 195-mm cobbles. Areal erosion rate predicted by advection-abrasion, deflection-abrasion, and combined-abrasion model as a function of discharge for (c) 10-mm gravel and (d) 195-mm cobbles. The orange lines are the conditions for the representative field case of the Black Canyon.

5.4.2. Influence of slope

Predictions by the advection-abrasion model for 10-mm gravel and 195-mm cobbles are qualitatively similar when slope is varied, with all other parameters held constant (Figure 5.2a-b). The distribution of lateral erosion rate on channel banks predicted by the advection-abrasion model forms an undercut erosional pattern. The maximum E_a within the undercut zone increases with increasing slope due to the increase in transport stage and hence impact velocity. The advection-abrasion model predicts a decrease in height of the undercut zone on channel banks with increasing slope as a result of the

decrease in water depth. In contrast, the height of maximum E_a within the undercut zone increases with increasing slope due to the increase in bedload layer height with increasing transport stage. For the same channel slope, the lateral erosion rate for the gravel is larger than for the cobbles (Figure 5.2a-b) because, for the same shear stress, smaller grains have a higher transport stage and hence higher impact energy.

The advection-abrasion model predicts a monotonic increase in the erosion rate with slope within the bedload layer, E_{cb}, due to the increase in bedload layer height and the impact velocity (Figure 5.2c-d). Compared with E_{cb}, the erosion rate within the suspended load layer, E_{cs}, increases with increasing slope due to the increase in impact energy at low slope values, but starts to decline at $S > 0.8$ for the gravel and $S > 0.06$ for the cobbles due to the decrease in height of suspended load layer as bedload layer height approaches the water surface at steep slopes (Figure 5.2c-d). The total load erosion rate, E_{ca}, monotonically increases with increasing slope for both the gravel and the cobbles, even at steep slopes where E_{cs} declines because E_{cs} declines at a lower rate than the growth of E_{cb} (Figure 5.2c-d). E_{cb} is smaller than E_{cs} at $S < 0.3$ for gravel and $S < 0.04$ for cobbles, but becomes larger than E_{cs} at very steep slopes where the bedload layer grows to encompass most of the flow depth (Figure 5.2c-d). Therefore, E_{cs} dominates the total load erosion at low slopes and E_{cb} dominates at steep slopes, while both bedload and suspended load layers are important in eroding channel banks at intermediate slopes.

The erosion rate predicted by the deflection-abrasion model, E_{cd}, increases with increasing slope once the transport stage is above the threshold of motion, but starts to decline at $S \approx 0.00008$ for 10-mm gravel (Figure 5.2c) and $S \approx 0.0012$ for 195-mm cobbles (Figure 5.2d) due to the decrease in the extent of alluvial cover as the transport stage increases, for given sediment supply. Compared with the advection-abrasion model, the deflection-abrasion model predicts negligible erosion at $S > 0.00021$ for the gravel and $S > 0.0017$ for the cobbles (Figure 5.2c-d). The erosion rate predicted by the deflection-abrasion

model is lower than the advection-abrasion model for the whole range of slope variation, except at $0.000075 < S < 0.00008$ for gravel and $0.00115 < S < 0.0012$ for cobbles (Figure 5.2c-d). Therefore, the erosion rate predicted by the combined-abrasion model E_{ct} follows the advection-abrasion model, except at a narrow range of small gradients where the erosion rate predicted by the deflection-abrasion model dominates.

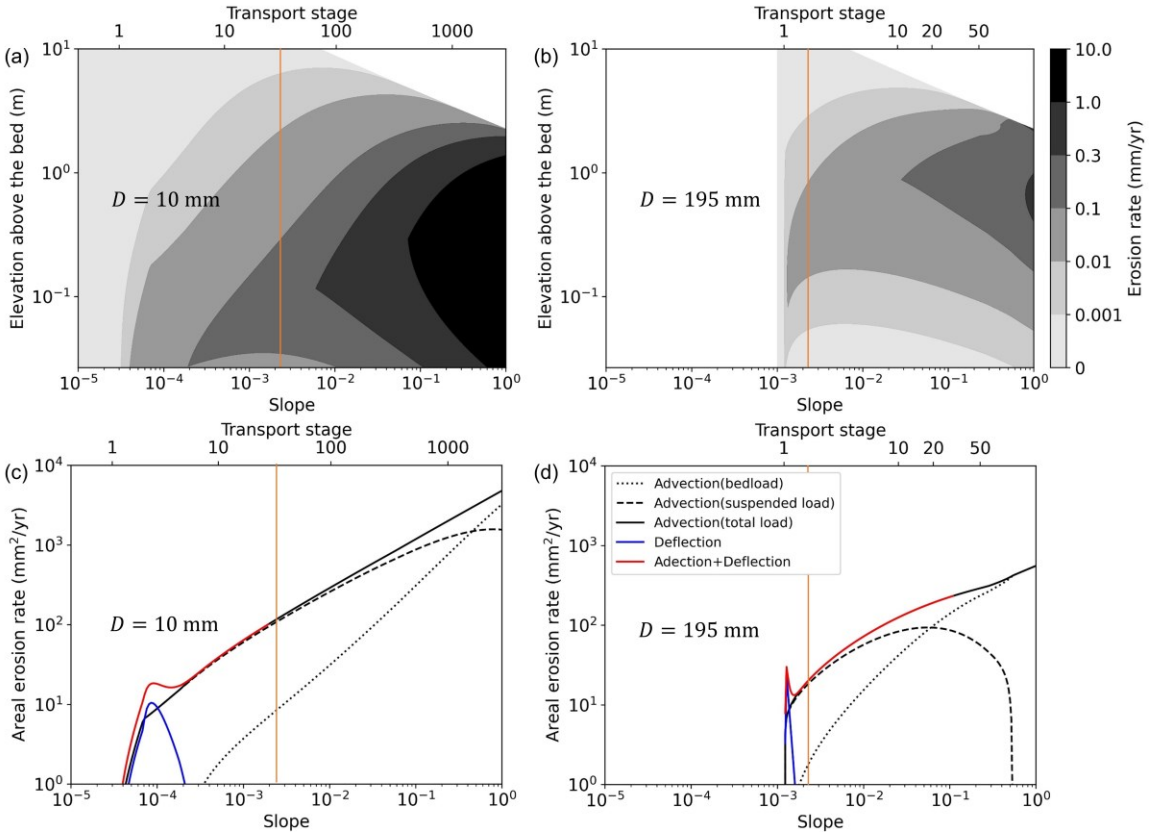

Figure 5.2 Distribution of lateral erosion rate on channel banks predicted by the advection-abrasion model as a function of slope for (a) 10-mm gravel and (b) 195-mm cobbles. Areal erosion rate predicted by advection-abrasion, deflection-abrasion, and combined-abrasion model as a function of discharge for (c) 10-mm gravel and (d) 195-mm cobbles. The orange lines are the conditions for the representative field case of the Black Canyon. The low transport stages for the 10-mm gravel and the large transport stages for the 195-mm cobbles correspond to unlealistic low slopes (<0.0001) and large slopes (>0.1) in natural bedrock rivers , respectively, but are shown here for comprison of the influence of slope on 10-mm gravel and 195-mm cobbles.

5.4.3. Influence of grain size

The advection-abrasion model, E_a, also shows an undercut erosional pattern when grain size is varied with all other parameters held constant at values for the reference site (Figure 5.3a). Within the undercut zone, E_a initially increases with increasing grain size due to the increase in near-bed volumetric sediment concentration for larger sediment and the increase in impact velocity. However, the impact velocity starts to decrease when the increase in grain size is more than offset by the decrease in transport stage, resulting in a decrease in E_a for large grain size.

The advection-abrasion model predicts an increase in the erosion rate within both the bedload layer, E_{cb}, and the suspended load layer, E_{cs}, for grain size smaller than ~4 mm and ~15 mm, respectively, and a decline in these erosion rates for larger grain size (Figure 5.3b). E_{cs} is higher than E_{cb} for the full range of grain sizes that can cause erosion (Figure 5.3b), so the total load erosion E_{ca} is almost fully controlled by E_{cs}. Compared with the advection-abrasion model, the deflection-abrasion model predicts negligble erosion rate at grain size smaller than ~ 280 mm, an increase in erosion rate for larger grain size due to the increase in the extent of alluvial cover, and then a decline in erosion rate at grain size larger than ~ 305 mm due to the decrease in transport capacity (Figure 5.3b). The erosion rate predicted by the deflection-abrasion model is only larger than the advection-abrasion model near the threshold of motion at $D \approx 300\ \mathrm{mm}$ (Figure 5.3b). Therefore, the combined erosion rate follows the similar pattern with the advection-abrasion model, except at $D \approx 300$ mm where the deflection-abrasion model dominates.

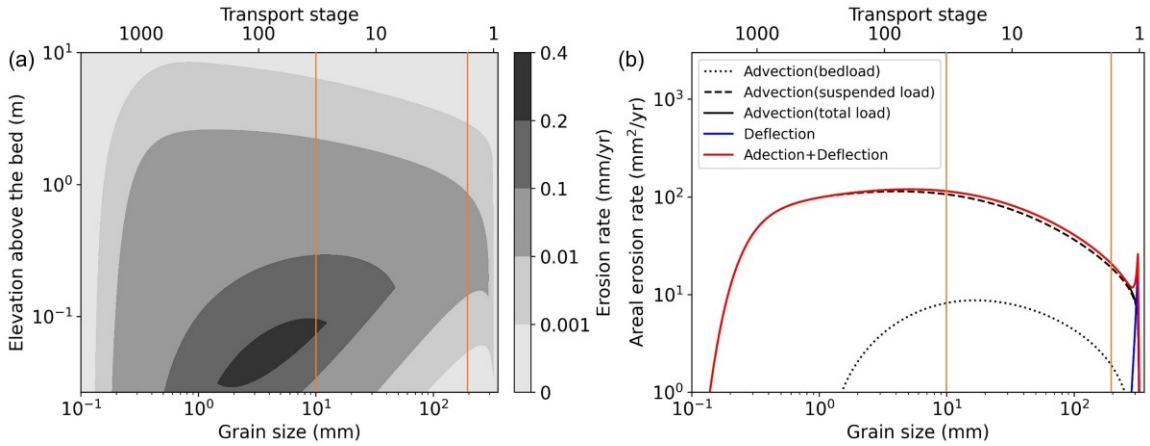

Figure 5.3 a) Distribution of lateral erosion rate on channel banks predicted by the advection-abrasion model and b) areal erosion rate predicted by advection-abrasion, deflection-abrasion, and combined-abrasion model as a function of grain size. The orange lines are the conditions for the representative field case of the Black Canyon.

5.4.4. Influence of sediment supply

Increasing sediment supply in the advection-abrasion model, with all other variables held constant at the reference site values, increases the sediment concentration and hence the erosion rate until the bedload sediment supply exceeds the transport capacity (Figure 5.4a-b). The erosion rate within the suspended load layer E_{cs} is much higher than the erosion rate within the bedload layer E_{cb} for the full range of sediment supply rate (Figure 5.4c-d). Therefore, the total load erosion rate E_{ca} is nearly the same with E_{cs} (Figure 5.4c-d).

Compared with the advection-abrasion model, the deflection-abrasion model predicts zero erosion rate for 10-mm gravel because it is transported in suspension under the hydraulic conditions at the reference site (Figure 5.4c). Therefore, the combined erosion rate E_{ct} is equal to E_{ca} for the gravel (Figure 5.4c). The deflection-abrasion model for the cobbles predicts negligible erosion at $q < 0.0009\ \mathrm{m^2/s}$ (Figure 5.4d) due to the lack of alluvial cover and an increase in erosion rate E_{cd} at larger sediment supply as number of deflections increases with the extent of alluvial cover. E_{cd} for the cobbles starts to decline at $q \approx 0.02\ \mathrm{m^2/s}$ (Figure 5.4d) due to the shift of deflection locations toward the top of

alluvium surface and hence the decrease in the efficiency of deflecting bedload particles when deflectors become densely packed at high sediment supply rate (Li et al., 2021). Compared with the deflection-abrasion model, the advection-abrasion model predicts a higher erosion rate at low supply rate ($q < 0.004\ \mathrm{m^2/s}$) but is outpaced by E_{cd} at high supply rate ($q < 0.004\ \mathrm{m^2/s}$) for the cobbles (Figure 5.4d). Therefore, the combined erosion rate E_{ct} for the cobbles is mainly due to the advection-abrasion mechanism at low supply rate but becomes dominated by the deflection-abrasion mechanism at high supply rate (Figure 5.4d).

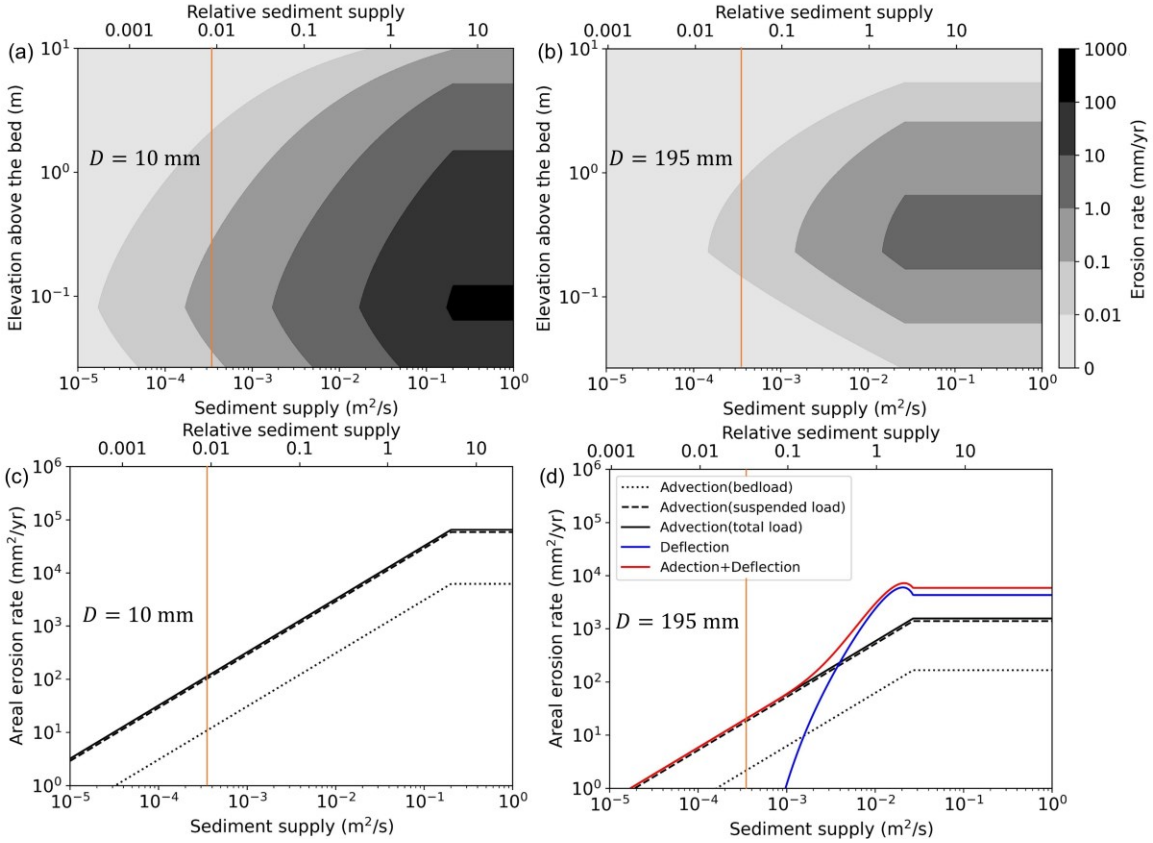

Figure 5.4 ***Distribution of lateral erosion rate on channel banks predicted by the advection-abrasion model as a function of sediment supply for (a) 10-mm gravel and (b) 195-mm cobbles. Areal erosion rate predicted by advection-abrasion, deflection-abrasion, and combined-abrasion model as a function of sediment supply for (c) 10-mm gravel and (d) 195-mm cobbles. The orange lines are the conditions for the representative field case of the Black Canyon.***

5.4.5. Nondimensional erosion rate

We explored the advection-abrasion model, the deflection-abrasion model, and the combined-abrasion model behaviors over a wide range of parameter space defined by transport stage and relative sediment supply (Figure 5.5-5.8). The transport stage is varied in two ways: varying discharge (Figure 5.5-6) and varying slope (Figure 5.7-8), because of the dependency of E_{ca}^{*} on flow depth.

For the constant slope case, the advection-abrasion model predicts an increase in non-dimensional lateral erosion rate with increasing transport stage because the impact velocity increases with increasing discharge at the same relative sediment supply for 10-mm gravel (Figure 5.5a) and 195-mm cobbles (Figure 5.6a). The nondimensional lateral erosion rate predicted by the advection-abrasion model also increases with increasing relative sediment supply due to the increase in impact rate with increasing sediment supply, until when the bedload supply rate reaches bedload transport capacity (Figure 5.5a & Figure 5.6a). The advection-abrasion model predicts an increase in nondimensional lateral erosion rate where the total sediment supply exceeds the bedload transport capacity because some of the sediment is transported as suspended load.

Compared with the advection-abrasion model, the deflection-abrasion model predicts a peak in lateral erosion rate at intermediate transport stage ($\tau^{*}/\tau_{c}^{*} \approx 16$ for the gravel and $\tau^{*}/\tau_{c}^{*} \approx 5.5$ for the cobbles; Figure 5.5b & Figure 5.6b) when the increase in impact velocity and the decrease in impact rate with increasing flow depth are well balanced. The deflection-abrasion model predicts zero erosion at $\tau^{*}/\tau_{c}^{*} \geq 29$ because of the onset of suspension (Figure 5.5b) for

the 10-mm gravel. The erosion rate for the 195-mm gravel predicted by the deflection-abrasion model remains above zero even at extreme, unrealistic discharges (10^7 m^3/s) at our reference site (Figure 5.6b) because the cobbles are transported at a much lower stage than the gravel for given discharge and remain bedload at extreme discharge events (10^7 m^3/s). The deflection-abrasion model predicts a peak in lateral erosion rate at high relative sediment supply (Figure 5.5b & Figure 5.6b) when the increase in the number of deflections is balanced with and the decrease in the deflection efficiency, when the deflection location shifts toward the top of deflectors with increasing sediment supply (Li et al., 2021). The erosion rate predicted by the deflection-abrasion model is higher than the advection-abrasion model at low transport stage ($\tau^*/\tau_c^* < 4.5$) and high relative sediment supply ($q/q_t > 0.5$), but is outpaced by the advection-abrasion model at lower relative sediment supply ($q/q_t < 0.5$) or high transport stage ($\tau^*/\tau_c^* > 4.5$) (Figure 5.5c & Figure 5.6c).

The combined-abrasion model predicts an increase in erosion rate with increasing transport stage and increasing relative sediment supply, except at low transport stage where the erosion rate peaks at high relative sediment supply due to the dominance of the deflection-abrasion model here (Figure 5.5d & Figure 5.6d).

In the parameter space defined by relative sediment supply and transport stage, the non-dimensional erosion rate predicted by the advection-abrasion model for the constant discharge cases (Figure 5.7a & Figure 5.8a) is qualitatively similar to the constant slope case (Figure 5.5a & Figure 5.6a). This occurs because increasing slope decreases the flow depth, resulting in lower impact height on the banks (impact area) but higher near-bed sediment concentration (impact rate), while increasing discharge increases the flow depth, resulting in higher impact height on the banks (impact area) but lower near-bed sediment concentration (impact rate). These opposite effects on impact area and impact rate cause similar patterns of erosion rate for the constant discharge and constant slope case.

When the transport stage is varied by varying slope, the erosion rate for 10-mm gravel is generally higher than the constant slope case (Figure 5.5a & Figure 5.7a), but the opposite relation occurs for 195-mm cobbles at the same transport stage and relative sediment supply (Figure 5.6a & Figure 5.8a). This occurs because the cobbles has a higher bedload layer height than the gravel and hence the increase in impact area with increasing discharge has a larger effect on erosion rate for cobbles. Compared to the constant slope case (Figure 5.6b), the transport stage can go beyond the threshold of suspension for cobbles when the slope is varied, resulting in a peak erosion rate at $\tau^*/\tau_c^* = 16$ and zero erosion rate at $\tau^*/\tau_c^* > 29$ (Figure 5.8b). The advection-abrasion model predicts a higher erosion rate than the deflection-abrasion model in the full range of transport and sediment supply conditions for the gravel, except within a small range where $1.2 < \tau^*/\tau_c^* < 3.5$ and $0.75 < q/q_{bc} < 1.5$ (Figure 5.7c). For cobbles, the deflection-abrasion model predicts higher erosion rate than the advection-abrasion model at low-to-intermediate transport stage ($1 < \tau^*/\tau_c^* < 10.5$) and high relative sediment supply ($q/q_{bc} > 0.5$) but becomes negligible beyond the threshold of suspension (Figure 5.8c).

The combined-abrasion model for 10-mm gravel and 195-mm cobbles predicts a similar erosional pattern with the advection-abrasion model, where erosion rate increases with increasing transport stage and relative sediment supply except at a small range of conditions where the deflection-abrasion model dominates (Figure 5.7d & Figure 5.8d).

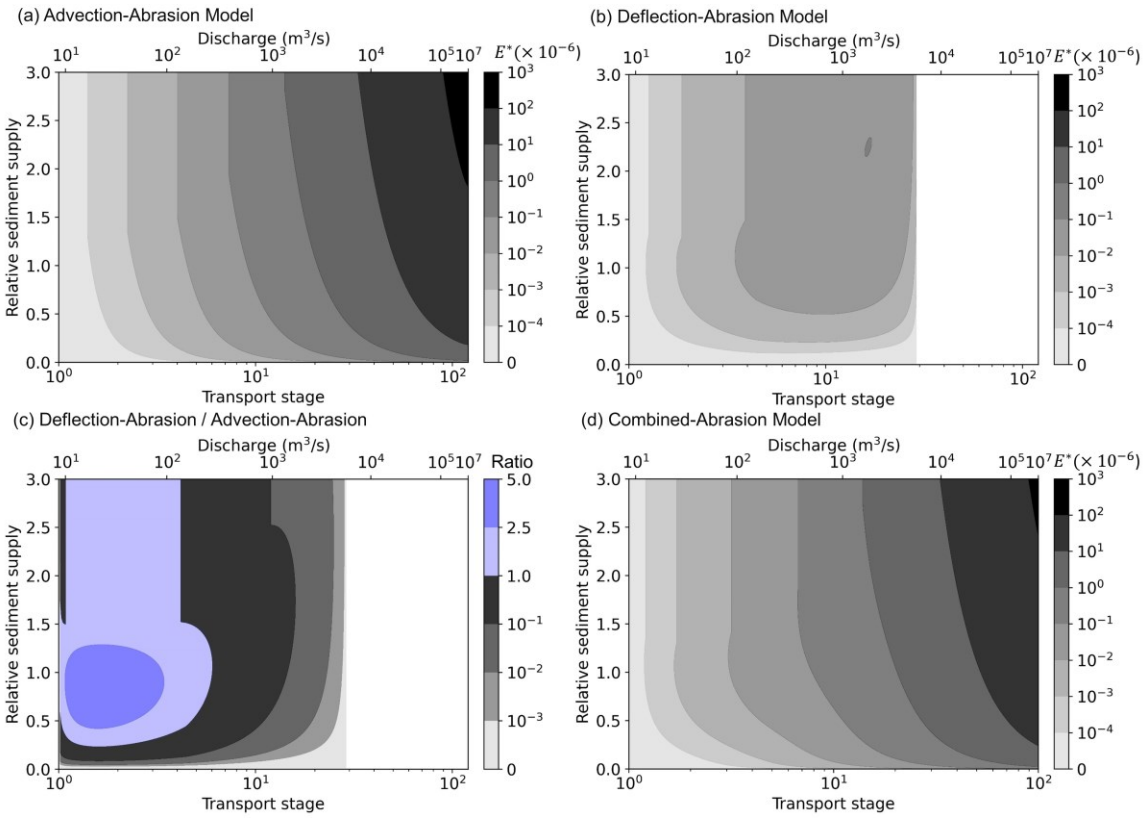

Figure 5.5 a) Non-dimensional erosion rate predicted by the advection-abrasion model E^*_{ca} , b)non-dimensional erosion rate predicted by the deflection-abrasion model E^*_{cd}, c) the ratio E^*_{cd}/E^*_{ca} and d) non-dimension erosion rate predicted by the combined-abrasion model E^*_c for 10-mm gravel as a function of transport stage and relative sediment supply. The transport stage is varied by varying discharge, holding channel slope constant at S=0.00234.

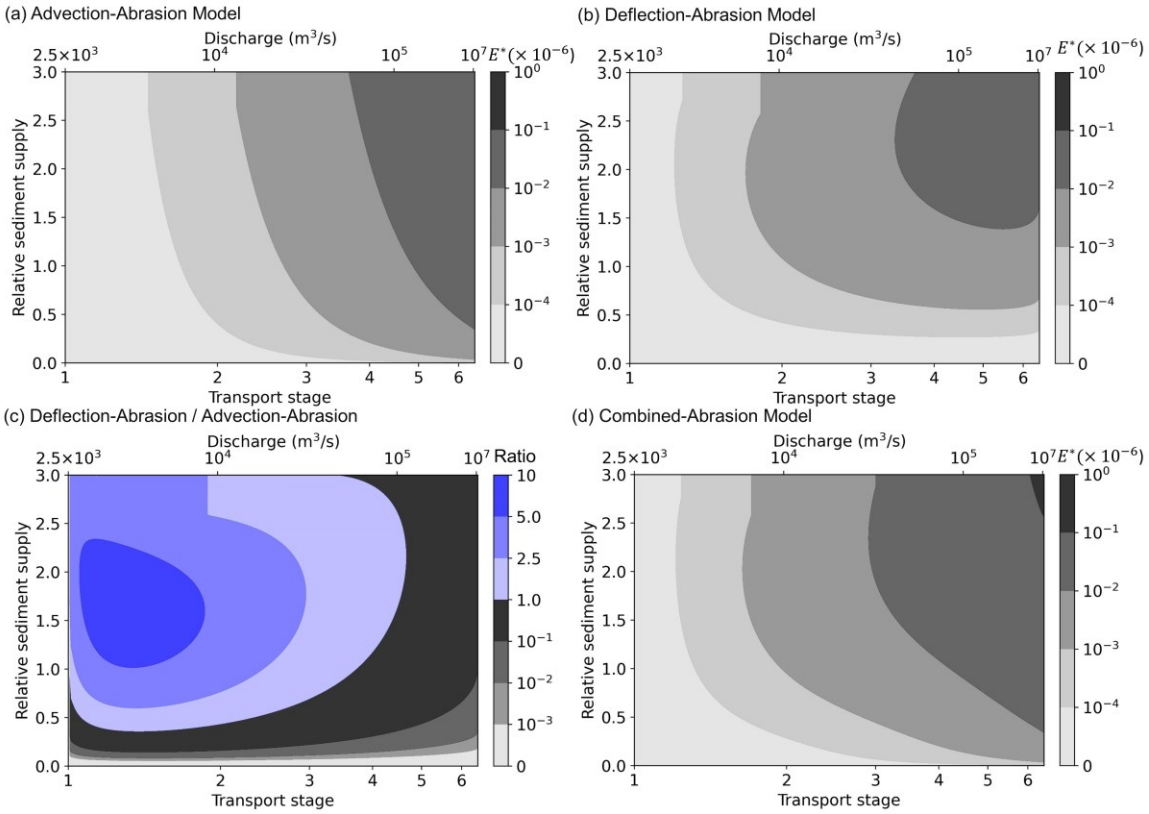

Figure 5.6 a) Non-dimensional erosion rate predicted by the advection-abrasion model E^*_{ca} , b)non-dimensional erosion rate predicted by the deflection-abrasion model E^*_{cd}, c) the ratio E^*_{cd}/E^*_{ca} and d) non-dimension erosion rate predicted by the combined-abrasion model E^*_c for 195-mm cobbles as a function of transport stage and relative sediment supply. The transport stage is varied by varying discharge, holding channel slope constant at S=0.00234.

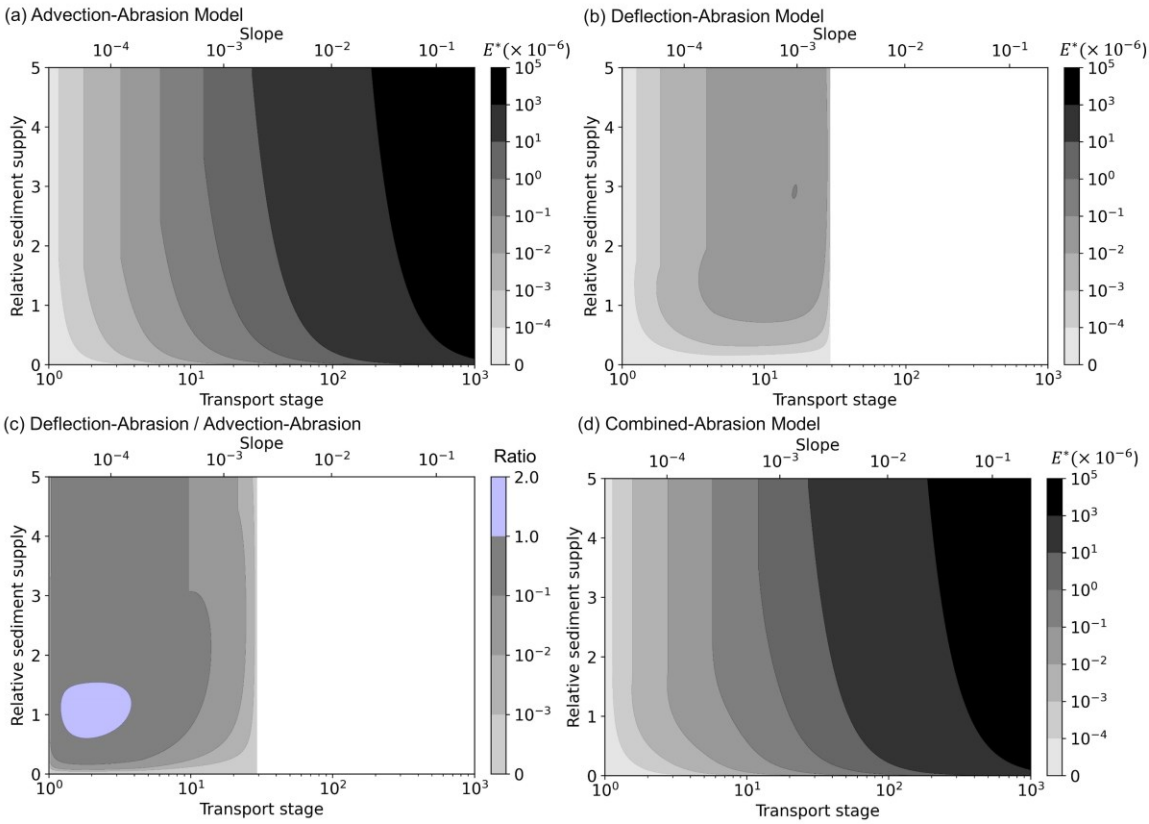

Figure 5.7 Contour plots of non-dimensional erosion rate as a function of transport stage and relative sediment supply for 10-mm gravel, predicted by a) the advection-abrasion model, b) the deflection-abrasion model and c) the combined-abrasion model. Also shown here is d) the ratio of erosion rate predicted by the deflection-abrasion model to erosion rate predicted by the advection-abrasion model. The transport stage is varied by varying slope, holding water discharge constant at Q_w=7000 m^3/s.

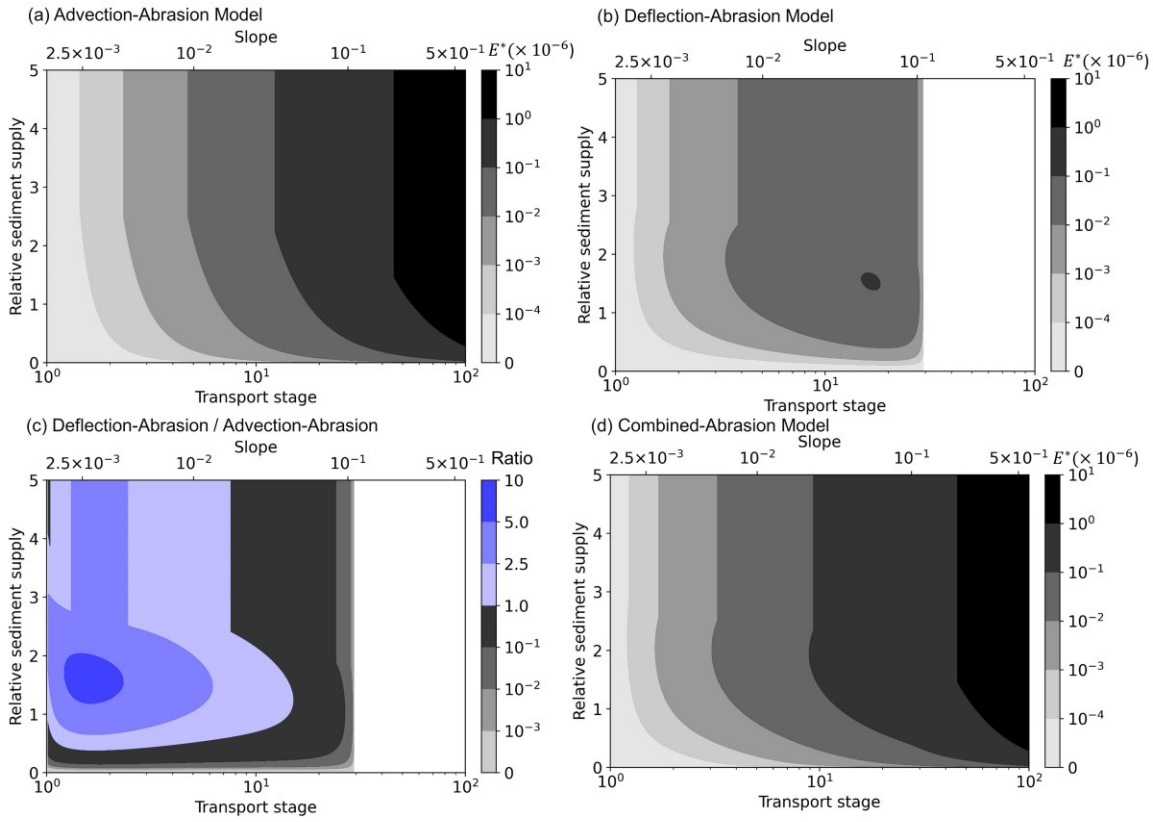

Figure 5.8 Contour plots of non-dimensional erosion rate as a function of transport stage and relative sediment supply for 195-mm cobbles, predicted by a) the advection-abrasion model, b) the deflection-abrasion model and c) the combined-abrasion model. Also shown here is d) the ratio of erosion rate predicted by the deflection-abrasion model to erosion rate predicted by the advection-abrasion model. The transport stage is varied by varying slope, holding water discharge constant at Q_w=7000 m^3/s.

5.5. Discussion

5.5.1. Comparison between advection-abrasion and deflection-abrasion models

The advection-abrasion process is important to consider in sediment-starved or detachment-limited bedrock rivers, where there is not enough alluvial cover to deflect particles to erode the banks. For example, Black Canyon in the Fraser River receives relatively little coarse sediment supply compared to the transport capacity ($q/q_{bc} = 0.034$ for 195-mm cobbles) during a characteristic discharge event (Q_w = 7000 m^3/s). The low sediment supply rate results in

negligible bed coverage and hence a relatively small erosion rate predicted by the deflection-abrasion model. However, the advection-abrasion model relies on the turbulence intensity and predicts a lateral erosion rate of ~60 mm^2/yr for 195-mm cobbles.

The deflection-abrasion model assumes that the saltation hop length is infinite and predicts zero lateral erosion rate for suspended sediment. In contrast, the advection-abrasion model predicts higher lateral erosion rate at larger transport stages, especially beyond the threshold of suspension. This condition mostly occurs for finer grain sizes, in narrow slot canyons that experience flash floods, in coarse-grained bedrock rivers during large flood events, or in steep bedrock rivers or knickzones. For example, Wire Pass, a slot canyon in Utah, is characterized by undulating sidewalls with a wavelength of 5-10 m (Carter & Anderson, 2006). These undulating sidewalls have been suggested to be created by the abrasion of sediment particles during flash floods, where the majority of the sediment (sand) can be easily transported in suspension (Carter & Anderson, 2006). The deflection-abrasion model would predict zero erosion, but the advection-abrasion model can predict the sidewall widening caused by the suspended sediment impacts in these slot canyons. In bedrock rivers, large sediment (e.g., gravel and cobbles) can also be transported in suspension during extreme flood events or in steep reaches. For example, the typhoon induced extreme floods in Taiwan are capable of suspending large sediment with grain size ~ 10 cm in the Liwu River (Hartshorn et al., 2002) and ~57 cm in the narrow knickpoint of the Da'an River (Cook et al., 2009, 2013), causing rapid lateral erosion of bedrock banks above the bedload layer height or near the water surface, which indicates the importance of lateral erosion within the suspension regime.

Compared with the advection-abrasion model, the deflection-abrasion model dominates in a small parameter space where the transport stage is near the threshold of motion and the relative sediment supply is close to the threshold of full bed coverage (Figure 5.5-8). Low transport stage leads to relatively low

turbulence energy and hence low impact energy and impact rate from the advection-abrasion model, but the large extent of alluvial cover on the bed are beneficial for deflecting the bedload particles to erode the channel banks. For example, the bedrock beds of the South Fork Eel River (Sklar & Dietrich, 2004) and the downstream reach of the Boulder Creek (Finnegan et al., 2017), California, USA, are covered by a nearly continuous alluvial cover with bedrock exposed only in isolated patches. Both of these channels have a transport stage below 2 for the median grain size during annual floods. Without considering the advection-abrasion model, application of the deflection-abrasion model in the downstream reach of the Boulder Creek has successfully captured the channel widening and steepening dynamics (Li et al., 2021), supporting that inference that the deflection-abrasion dominates lateral erosion in channels with low transport stage and high bed coverage.

5.5.2. Implications for natural bedrock rivers

Our combined-abrasion model has implications for the relative importance of sediment size in eroding bedrock channel banks. Natural bedrock rivers transport a wide range of grain sizes, where finer sediment can be transported easily in suspension within almost the full distribution of discharge events but coarser sediment can only be mobilized over a limited duration. Previous bedrock lateral erosion models only consider bedload impacts, assuming that the long term lateral erosion rate is controlled by the coarser sediment transported over a limited duration and that the influence of finer sediment is negligible in eroding bedrock cannel banks (Turowski, 2018, 2020; Li et al., 2020, 2021). However, our combined-abrasion model suggests that the finer sediment transported in suspension can be advected toward the banks to cause lateral erosion over a longer period and hence might dominate lateral erosion.

To explore the competition between finer sediment and coarser sediment over the full distribution of discharge and sediment supply events, we use our reference site (Black Canyon) as an example. We calculate the probability

density function (PDF) of the discharge at our reference site (Figure 5.9a-b) using the daily discharge data for the full 1912-2019 period of record from Water Survey of Canada at the Hope Gauge station (08MF005). Mixed grain sizes would complicate the entrainment of each grain size and the interaction amongst them (e.g., Wilcock et al., 2001; Wilcock & Crowe, 2003; Parker, 1990), and extending our model to mixed grain sizes would be more realistic, but would require reevaluation of several formulas, such as the critical shear stress for motion, the boundary roughness, and the transport capacity. For simplicity, we calculate the total erosion on bedrock channel banks from the sum of erosion by 10-mm gravel and 195-mm cobbles.

To incorporate the variability of sediment supply, we assume that the sediment supply $Q_s(t)$ follows a power law relation with, $Q_w(t)$,

$$Q_s(t) = k_{sw}(Q_w(t))^m, \qquad \text{(Equation 5.37)}$$

where k_{sw} is a scaling factor which can be obtained from the annual sediment flux at our reference site, and m can be viewed as a rating exponent which generally varies between 1 and 3 based on sediment transport measurements in several bedrock rivers (Lague, 2010). For simplicity, we choose $m = 2$. We consider two sediment supply conditions: low sediment supply and high sediment supply. We use the annual coarse mass flux of 0.35 Mt/yr for the low sediment supply case where the bed is near fully exposed (reference site condition) and 35.0 Mt/yr for the higher sediment supply case where the bed is near fully covered. In each sediment supply scenario, the 10-mm gravel and the 195-mm cobbles are assumed to have the same mass flux.

For the lower sediment supply scenario, the combined-abrasion model predicts much higher lateral erosion rate for the finer sediment (10-mm gravel) than the coarser sediment (195-mm cobbles) along the whole bedrock channel bank at our reference site (Figure 5.9c). The peak erosion rate for 10-mm gravel (~0.1 mm/yr) is 9 times higher than 195-mm cobbles (~0.01 mm/yr) and occurs at a lower elevation above the bed (~ 0.08 m) than 195-mm cobbles (~ 0.15 m).

The dominance of lateral erosion by the finer sediment causes the total erosion rate to follow the similar pattern with the 10-mm gravel, with 85% of the total erosion caused by the 10-mm gravel. In contrast, at high sediment supply, the bed is near fully covered by alluvium. Therefore, the coarser sediment can be deflected by the alluvium and can cause higher erosion rates (Figure 5.9d). The lateral erosion rate for the coarser sediment is larger than the finer sediment at an elevation of z < 0.4 m above the bed. The maximum erosion rate for the coarser sediment (~ 13 mm/yr) is slightly higher than the finer sediment (~10 mm/yr) (Figure 5.9d). At high sediment supply, the coarser sediment accounts for near the same percentage of the total erosion rate with the finer sediment (~ 50%). Therefore, our combined-abrasion model implies that the finer sediment controls the lateral erosion in bedrock rivers with low sediment supply, and the importance of coarser sediment in eroding bedrock channel banks increases with increasing sediment supply.

An important implication of our advection-abrasion model is that the most frequent, small magnitude events might be more effective in eroding bedrock channel banks than the least frequent, extreme magnitude events (Figure 5.9a-b). For example, the small magnitude events ($Q_w < 2000\ \mathrm{m}^3/\mathrm{s}$) at our reference site are effective in transporting the finer sediment (10-mm gravel) and eroding bedrock channel banks. The small magnitude events are also > 100 times more frequent than the extreme magnitude events ($Q_w > 12000\ \mathrm{m}^3/\mathrm{s}$). The net effect of the magnitude and frequency of discharge events reveals that the smallest events ($Q_w < 2000\ \mathrm{m}^3/\mathrm{s}$) are > 10 times more effective in eroding bedrock channel banks than the extreme events ($Q_w > 12000\ \mathrm{m}^3/\mathrm{s}$) at our reference site (Figure 5.9). Like classic analyses of geomorphic work (Leopold, Wolman & Miller, 1964), moderate magnitude and frequency might be the most effective in eroding bedrock channel banks. This is because of the net effect of the reduced impact velocity for small magnitude events and the reduced frequency of the extreme events. At our reference site, the majority of lateral erosion are caused

by the discharge with a moderate magnitude that is between 6000 m^3/s and 8000 m^3/s.

Our combined-abrasion model includes two lateral erosion mechanisms: lateral erosion by bedload particle impacts that are deflected by the alluvium (deflection-abrasion mechanism) and lateral erosion by bedload and suspended load particle impacts that are advected by turbulence eddies (advection-abrasion mechanism). Our model does not consider other lateral erosion mechanisms, such as plucking (Beer et al., 2017) that may dominate in rivers with weak or well jointed bedrock channel banks. In meandering bedrock rivers, channel curvature can also enhance the sediment transport perpendicular to the bedrock channel banks and hence accelerate the bank abrasion (Cook et al., 2014; Mishra et al., 2018). To build a complete lateral erosion model, future work is needed to develop lateral erosion models by plucking and to incorporate the influence of channel curvature. Furthermore, current lateral erosion models calculate the hydraulic conditions based on the assumption of steady, uniform flow. However, 3D complex flow structure has been observed in laterally constricted bedrock rivers characterized by flow plunging towards the bed, with a high velocity core near the bed, and flow upwelling along the banks, causing counter-rotating secondary flow structure (Venditti et al., 2014; Hunt et al., 2018). The presence of the complex flow structure causes higher and lower local flow velocities, turbulent intensities, shear stresses and erosion rates (Venditti et al., 2014; Hunt et al., 2018; Li et al., 2022; Cao et al., 2022), and hence needs to be coupled with erosion models to predict the morphodynamics of bedrock rivers. Nevertheless, our combined-abrasion model considers both bedload and suspended load, which is a more realistic representation of lateral erosion processes in bedrock rivers than the bedload deflection-only models. Our combined-abrasion model also highlights the importance of tiny but energetic particles in eroding bedrock channel banks.

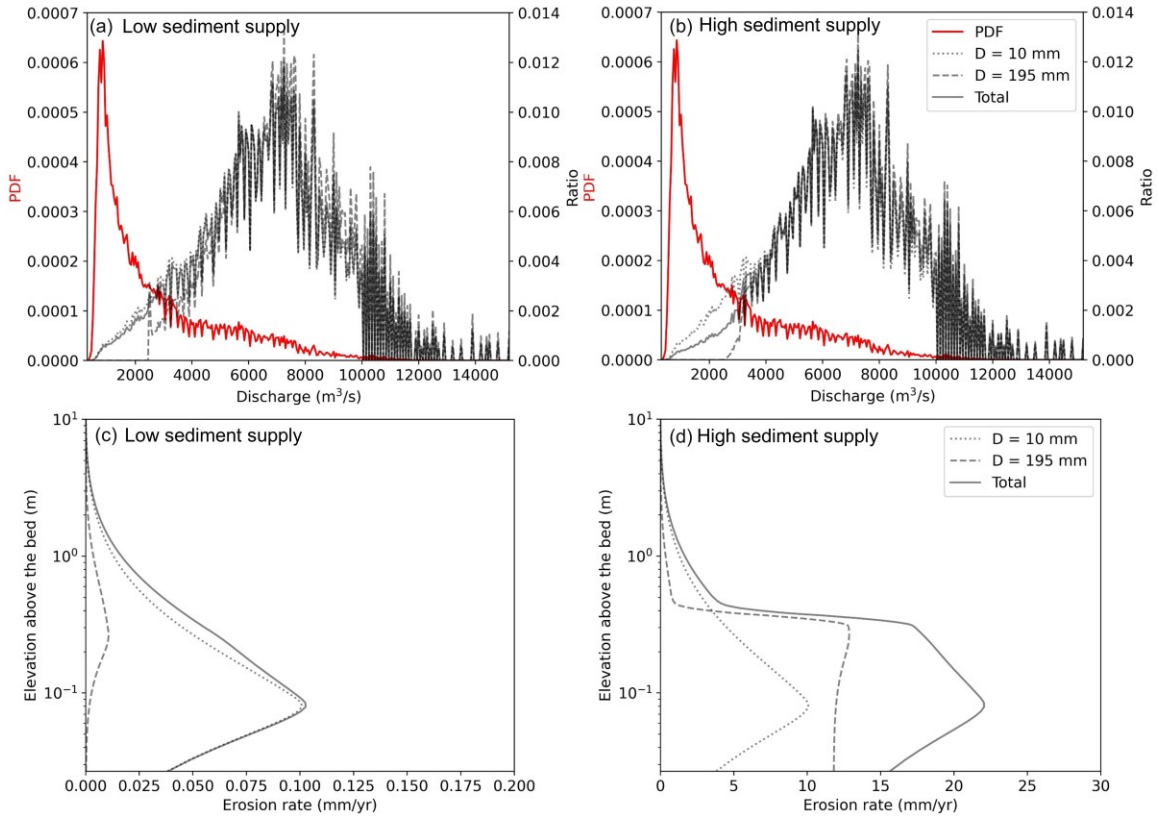

Figure 5.9 The ratio of erosion rate for each discharge event at a) low sediment supply and b) high sediment supply, and the annual erosion rate for the full range of the distribution of discharge events at c) low sediment supply and d) high sediment supply for 10-mm gravel, 195-mm cobbles and these two grain sizes together. Also shown in a-b) is the probability density function of the discharge at our reference site using the daily discharge data for the full 1912-2019 period of record at Hope gauging station from Water Survey of Canada (08MF005).

5.6. Conclusion

We developed an advection-abrasion model for lateral erosion by bedload and suspended load particles impacts that are advected by turbulence eddies. The model calculates lateral erosion rate as a function of sediment concentration and impact velocity that are controlled by sediment supply, discharge, slope and grain size. The model predicts an undercut erosional bank shape, where lateral erosion rate concentrates on the lower part of the banks and decreases progressively up to the water surface. The maximum erosion rate within the

undercut zone peaks at intermediate discharge due to the reduction of near-bed sediment concentration as water depth increases, but increases with increasing slope due to the decline in water depth and hence the increase in near-bed sediment concentration, for given sediment supply. The maximum erosion rate within the undercut zone peaks at intermediate grain size due to the reduction in impact energy with increasing grain size for given shear stress, but increases with increasing sediment supply until the bedload supply approaches the transport capacity due to the increase in sediment concentration. The erosion rate within the suspended layer is larger than the bedload layer for all supply and transport conditions explored, except at steep slopes where bedload layer height approaches water depth.

We combined the advection-abrasion model with the deflection-abrasion model. Both the advection-abrasion and deflection-abrasion models can be nondimensionalized as a function of transport stage and relative sediment supply, for given grain size. The deflection-abrasion model predicts a lower erosion rate than the advection-abrasion model for all supply and transport conditions explored, except within a limited condition where sediment is transported near the threshold of motion and the bedload sediment supply is close or higher than transport capacity. Therefore, the combined-abrasion model follows the similar pattern with the advection-abrasion model, where erosion rate increases with increasing transport stage and increasing relative sediment supply until the bedload sediment supply approaches the transport capacity.

Application of the combined-abrasion model in a natural bedrock river with the wide distribution of discharge and sediment supply events and mixed grain size (finer and coarser sediments) indicates that the finer sediment causes more lateral erosion than coarser sediment in a low sediment supply environment, but coarser sediment becomes as important as finer sediment for eroding bedrock channel banks in rivers with high sediment supply rates.

Chapter 6. What Sets the Width and Slope of Bedrock Rivers?

Abstract

River channel geometry is defined by three simple quantities: velocity, depth and width, the combination of which gives the water discharge (Leopold & Wolman, 1957). There are well-established methods to calculate the depth and velocity of a river that are based in the mechanics of water flow (Parker, 2004; Garcia, 2008). Prediction of river channel width based on the physics of flow and sediment transport remains a stubbornly difficult problem (Whipple, 2004; Dunne & Jerolmack, 2020). This is surprising because there are sophisticated methods for describing flow and sediment transport in rivers, yet the reason why a river channel adopts a particular width remains unknown. Here, we present a method for calculating the width and slope of a bedrock river based entirely on the physics that underly vertical and lateral erosion. We predict observed width and slope for rivers where the necessary input variables are known or can be estimated. We use our new predictive method to explore the controls on bedrock width and slope at a cross-section and scale up our predictions to drainage basin scale to explore what controls the downstream variation of width and slope. We predict the observed scaling relations between river width, slope, and drainage area that underly the stream power model that lies at the heart of landscape evolution models (Perron et al., 2009, 2012; Perron, 2011; Ferrier et al., 2013) and inferences of tectonics and drainage reorganization over geologic time scales (Perron & Royden, 2013; Royden & Perron, 2013; Goren et al., 2014; Willett et al., 2014; Yang et al., 2015).

6.1. Introduction

Alluvial rivers flow through their own deposits and therefore their width is set by deposition and erosion of sediment. The reason a channel adopts a particular width must be linked to the balance between the stress applied to the banks and the strength of the banks, although the exact threshold remains a matter of ongoing debate (Dunne & Jerolmack, 2020). Fortunately, there are well-defined empirical relations that link width and channel discharge (Leopold &

Maddock, 1953; Park, 1977; Parker, 1978; Parker et al., 2007) and semi-theoretical approaches that require an assumption that rivers are optimized systems (Blench, 1952; Ikeda & Izumi, 1991; Millar, 2005; Eaton & Church, 2007; Nanson & Huang, 2017; Ohara & Yamatani, 2019).

In bedrock channels, that are actively incising rock, prediction of the stable width of the river is more difficult because channel width is not set by local erosion and deposition of sediment, but rather a balance between lateral and vertical bedrock incision balanced against uplift, occurring over geologic timescales. There are analytical approaches where bedrock river width is calculated by iteratively solving equations that describe sediment cover on otherwise bedrock beds (Turowski, 2018, 2020). However, lateral erosion in bedrock rivers is caused by sediment particle impacts (Fuller et al., 2016; Turowski, 2020; Li et al., 2020, 2021), the physics of which is not represented by expressions for sediment cover. There are poorly constrained empirical relations that link the width of a bedrock river to discharge (Whipple, 2004; Wohl & David, 2008; Rennie et al., 2018; Wright et al., 2022) or metrics of drainage area and slope (stream power) (Finnegan et al., 2005; Wobus et al., 2006; Turowski et al., 2007). At steady state, width (W) and slope (S) are widely accepted to scale drainage basin area (A) as $W \sim \lambda A^{\mu}$ and $S \sim \delta A^{\theta}$. Compilations of data indicate $\mu = \theta = 0.5$ across a wide range of uplift rates and rock strengths (Whipple et al., 2013; Harel et al., 2016). These relations are the foundation of landscape evolution models (Perron et al., 2009, 2012; Perron, 2011; Ferrier et al., 2013) and inferences of tectonics and drainage reorganization from fluvially-carved topography over geologic time scales (Perron & Royden, 2013; Royden & Perron, 2013; Goren et al., 2014; Willett et al., 2014; Yang et al., 2015). However, there is no consensus what sets the width and slope of a bedrock river due to a lack of mechanistic understanding for why width, slope and drainage area are interrelated.

We present a method for predicting the width and slope of bedrock rivers based entirely on the physics of vertical and lateral erosion occurring at grain-

scales, and validate our calculation against observed river width and slopes. We use our new predictive method to explore what sets the local width and slope of a bedrock river and then predict the scaling relations between width, slope, and drainage area that underly the stream power model.

6.2. Theory

Steady bedrock channel morphology requires a balance between vertical erosion rate and uplift rate so that the channel elevation is constant. Steady state morphology also requires the same lowering rate of the channel bed and banks so that the cross-sectional shape is constant. To predict bedrock channel morphology at steady state, we use a model for vertical erosion by saltating particle abrasion (Sklar & Dietrich, 2004) and a model for lateral erosion by saltating particles deflected by sediment cover into the channel banks (Li et al., 2021) (see Methods). Bedrock erosion is caused by a combination of abrasion, plucking, and weathering processes, but in massive crystalline rock, abrasion is the dominant mechanism. Models for vertical and lateral erosion by particle abrasion directly capture the dominance of vertical erosion at low-to-intermediate sediment supply when the bed is exposed to abrasion and the shift to lateral erosion at high sediment supply when the bed is protected by alluvium deposits. The models also explicitly incorporate the effects of water discharge (Q_w), sediment supply (Q_s), grain size (D), rock strength (k_r), channel slope (S) and width (W). Therefore, steady bedrock channel width and slope can be iteratively solved by combining the equations that describe the balance between vertical erosion rate and uplift rate (U) and the equation that describe the lowering rate of the channel bed and banks, for given Q_w, Q_s, D, k_r and U.

6.3. Prediction of Channel Width and Slope

There are not many rivers where the required variables to predict channel width are known, but there are four rivers where the variables are known or can be constrained. South Fork Eel River is an actively incising bedrock river in

northern California, which has a long-term uplift rate of 0.9 mm/year (Sklar & Dietrich, 2004, 2006). Boulder Creek is a small bedrock river in the Santa Cruz Mountains with a long-term uplift rate of 0.15 mm/year. The upstream reach of Boulder Creek has a low gradient and is narrow, but the downstream reach becomes wide and steep after receiving coarse sediment supply from a tributary (Finnegan et al., 2017). Black Canyon in the Fraser River is a large bedrock river in British Columbia that is capable of transporting large boulders and cobbles. The bedrock canyons in the Fraser River flow along a fault between Cascade and Coast mountain ranges (Venditti et al., 2014; Wright et al., 2022) and experience a long-term uplift rate of 0.35 mm/year (Farley et al., 2001). Channel slopes and widths of South Fork Eel River, upper Boulder Creek and Black Canyon are predicted to be at near steady state (Figure 6.1). Our model predicts that the lower Boulder Creek is adjusting to the sediment input from the tributary by getting wider and a lower gradient than its current morphology which is consistent with field-based interpretations of Finnegan et al. (2017).

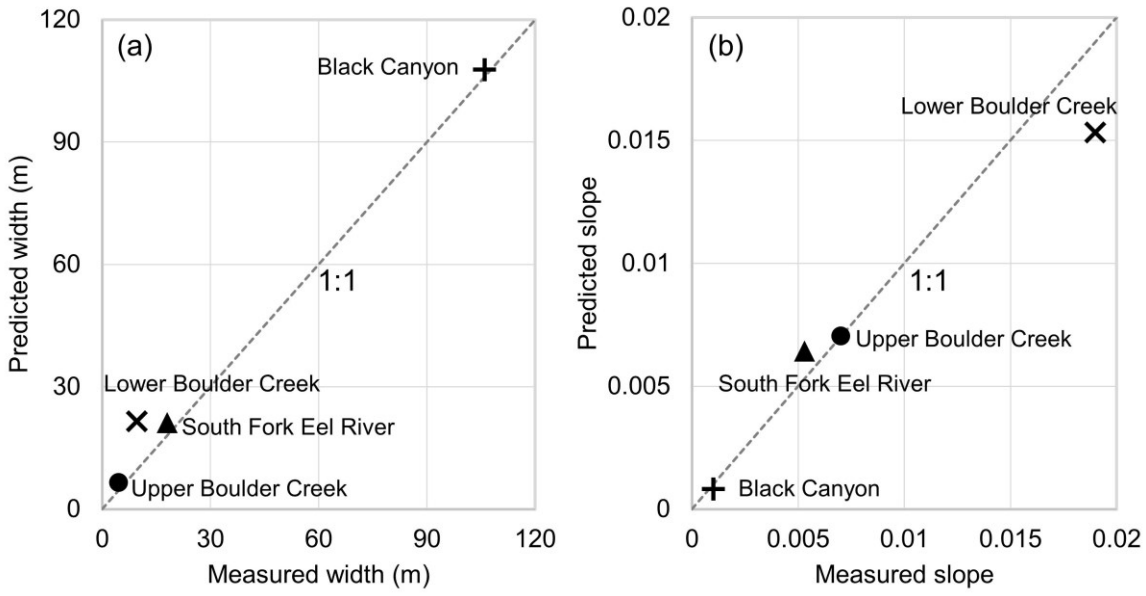

Figure 6.1 Comparisons between a) measured and predicted width, and b) measured and predicted slope (Extended Data Table C.1).

6.4. Local variation of width and slope

We explored controls of Q_w, Q_s, D, k_r and U on steady-state width and slope at a cross-section, which is akin to examining the at-a-station variation, like in classic hydraulic geometry (c.f. Leopold and Maddock, 1953). We varied each variable independently, holding all other variables constant values for the representative field case of the South Fork Eel River (Figure 6.2). Width is a nonlinear function of D, k_r and U (Figure 6.2a-b). Width increases with D for fine sediment due to the increase in impact energy as viscous damping becomes less important, but starts to decrease for coarse sediment due to increasing alluvial bed coverage (Figure 6.2a). Width declines with U and k_r because bed coverage declines at higher vertical erosion rate or rock strength (Figure 6.2b). We found W is not a function of Q_w (Figure 6.2c), but a linear function of Q_s (Figure 6.2d), suggesting that the observed $W - Q_w$ scaling relation is a result of the codependence of sediment supply and discharge. The linear relation between W and Q_s can be used to derive analytical solutions for channel width where

$$W = k_w Q_s \qquad \text{(Equation 6.1)}$$

and $k_w = f_1(D, U, k_r)$ (see Methods for an explicit function).

Slope behaves somewhat differently than width in response to changes in D, k_r, U, Q_w and Q_s. As particles get larger, the slope necessary to maintain transport gets larger (Figure 6.2a). Slope has a parabolic relation with U and k_r with a decline in S at low U and k_r and an increase in S at high U and k_r (Figure 6.2b). This occurs because width adjusts at low U and k_r by channel narrowing but slope adjusts at high U and k_r by steepening (Figure 6.2b). Slope declines with Q_w because of the non-linear relation between water depth and slope (Figure 6.2c). Slope increases with Q_s due to the increase in width, except at low width where shear stress increases with increasing width (Figure 6.2d). The effects of Q_w and Q_s on slope can be captured by combining flow resistance and continuity equations for given transport stage τ^*/τ_c^* because transport stage remains constant for varying Q_w and Q_s. Multiple regression analysis gives

$$S = k_c(\tau^*/\tau_c^*)^{10/7} D^{9/7}(Q_w^{-0.86}(k_w Q_s)^{0.86} + Q_w^{-0.4}(k_w Q_s)^{-0.5}) \quad \text{(Equation 6.2)}$$

where k_c is a parameter describing the water and sediment density, the threshold of motion, and boundary roughness) and $\tau^*/\tau_c^* = f_2(D, U, k_r)$ (see Methods for an explicit function).

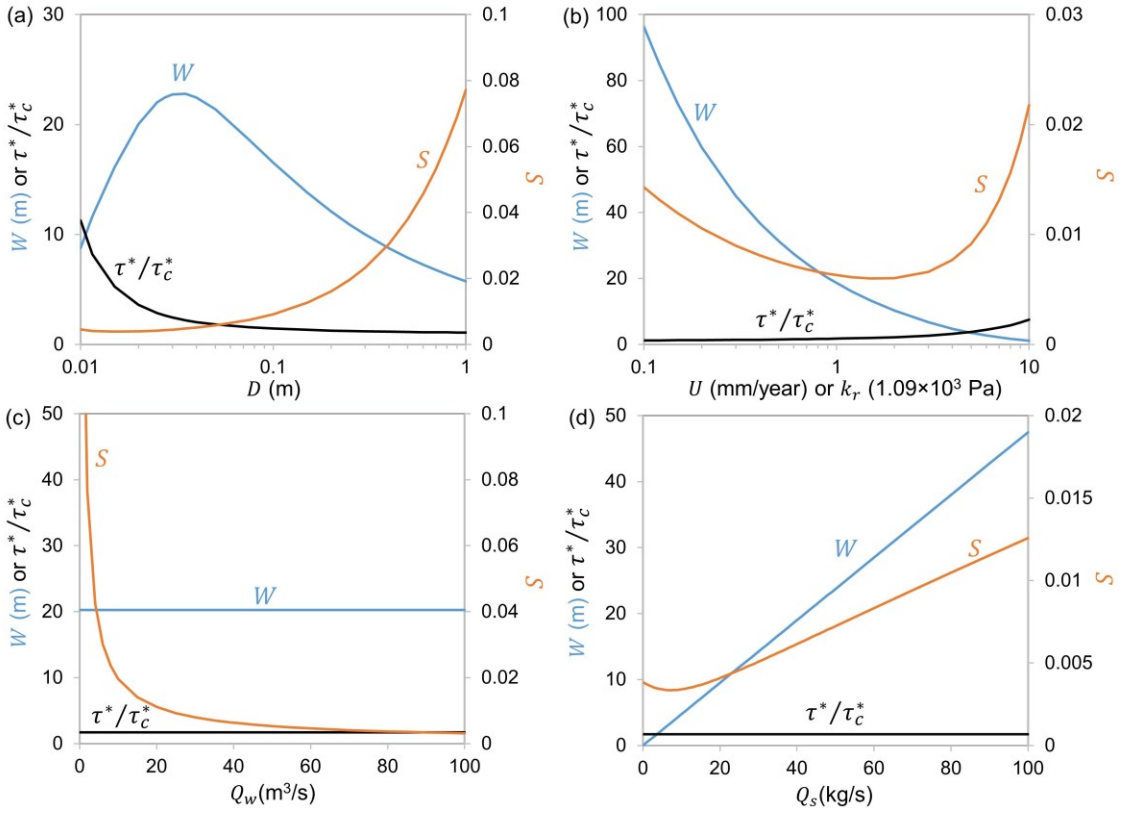

Figure 6.2 Influence of a) water discharge Q_w, b) sediment supply Q_s, c) grain size D and d) uplift rate U or rock strength k_r on channel width W and slope S. Also shown is the variation in transport stage τ^*/τ_c^*. Each variable is varied independently, holding all other variables to constant values for the reference field site (South Fork Eel River).

6.5. Downstream Variation of Width and Slope

The local relations for width and slope (Equations 6.1 & 6.2) can be scaled up to drainage basin scale using explicit functions of k_w and τ^*/τ_c^*, and rewriting downstream variations of discharge, sediment supply and grain size as functions of drainage area. We assume that all the coarse sediments are transported

during a representative high-flow discharge at the reference site and discharge is calculated as a power function of drainage area, $Q_w = k_q A^{m_q}$, where k_q is a measure of river base flow and m_q is the scaling power dependency. At steady state, the uplift rate U is equal to the long-term vertical erosion rate and the coarse sediment supply rate can be expressed as $Q_s = \frac{\rho_s U A F_b}{k_t}$, where ρ_s is sediment density, k_t is the fraction of time that bedload occurs and F_b is the fraction of sediment load that is transported as bedload. Assuming the decline in grain size downstream is due to the production of finer sediments, F_b should decline in the downstream direction (Sklar et al., 2017). A global-scale bedload flux model indicates a power law relation between F_b and distance downstream (Cohen et al., 2022). Therefore, we model F_b as a power function of drainage area, $F_b = F_0 A^{1-m_s}$, where F_0 is the bedload fraction of the total load at the channel head and m_s is an empirical parameter. Downstream grain size fining is treated as a power law relation with distance downstream (Brierley & Hickin, 1985), allowing grain size to be expressed as a power function of drainage area using Hack's law: $D = k_d A^{-0.67 m_d}$, where k_d is a parameter that describes grain size at channel head, and m_d is downstream fining rate (see Methods).

Compilations of data that form the basis of classical downstream hydraulic geometry relations indicate $W = \lambda A^{\mu}$, where the coefficient λ is assumed to be a function of rock strength and runoff rate and the exponent μ has a classical value of 0.50 (Figure 6.3a) (Whipple, 2004; Wohl & David, 2008; Ferguson & Rennie, 2017; Rennie et al., 2018; Baynes et al., 2020; Wright et al., 2022). Upscaling the local relations to drainage basin scale reproduces the $W \sim A$ relation with the the classical value of μ = 0.5 for a wide range values of uplift rates and rock strength (Figure 6.3b-c). The exponent μ is strongly influenced by the downstream change of the portion of sediment carried in suspension m_s with some influence by the downstream variation in grain size m_d so that as $\mu = m_s + 0.27 m_d$ (see Methods). However, at high uplift rates and rock strengths, μ is a nonlinear function of U and k_r (Figure 6.3b-c). The coefficient λ is also a function of uplift

rate and rock strength such that $\lambda = m_1 U^{0.29} k_r^{-0.71}$ (m_1 is a constant, see Methods).

Downstream variation in slope is commonly observed to be an inverse function of drainage area as in the stream power model that predicts $S = \delta A^{-\theta}$, where θ is channel concavity (e.g. Figure 6.3d). Global average θ is 0.51 ± 0.14 (Harel et al., 2016). The coefficient δ is a function of rock erodibility k_e (reciprocal of rock strength, $1/k_r$) and uplift rate U, $\delta = (U k_r)^{0.5}$. Upscaling local width and slope relations to drainage basin scale reproduces the $S \sim A$ relation and the classical value of θ = 0.5 for a wide range of uplift rate and rock strength (Figure 6.3e-f). This occurs because θ is mainly controlled by m_q, m_s, and m_d such that $\theta = 0.86(m_s - m_q - 0.73 m_d)$ (see Methods). At high rock strength, however, θ is a nonlinear function of k_r. The coefficient δ generally increases with uplift rate and decreases with rock strength such that $\delta = m_2 U^{0.25} k_r^{-0.61}$ (m_2 is a constant; see Methods).

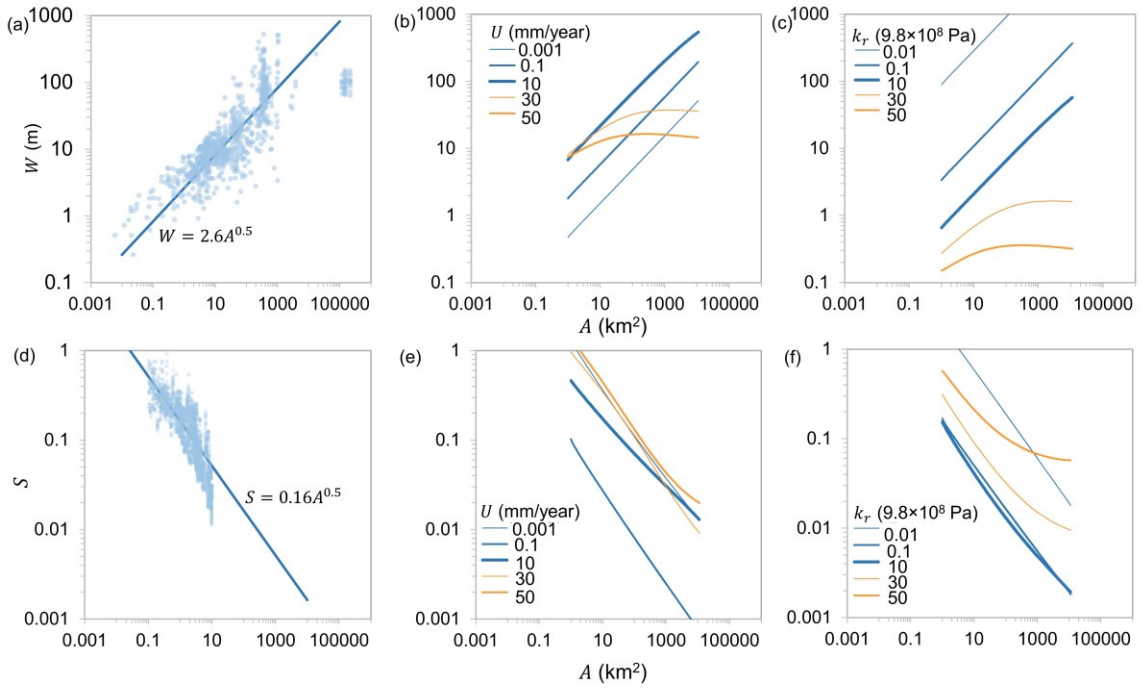

Figure 6.3 a) Measured $W \sim A$ relation across a wide range of uplift rates and rock strength that are compiled by Wright et al. (2022), predicted $W \sim A$ relations across a wide range of b) uplift rates and c) rock strength, D) measured $S \sim A$ at the Mendocino Triple Junction region of northern California, USA (Wang et al., 2017), and predicted $S \sim A$ relations across a wide range of E) uplift rates and F) rock strengths.

6.6. Discussion and Conclusion

Our findings indicate that local bedrock channel width at steady-state is a function of four parameters: sediment supply, grain size, uplift rate and rock strength. Steady-state bedrock channel slope can be predicted by adding water discharge. Scaling up the local bedrock channel width and slope relations reproduces the $W = \lambda A^{\mu}$ and $S = \delta A^{-\theta}$ relations with classical values of $\mu = \theta = 0.5$ and provides mechanistic meanings of all these coefficients. Our results indicate that the classical value of μ and θ emerges across a wide range of tectonic activity and rock strengths at steady state. Both μ and θ are dominantly controlled by coarse sediment supply and caliber, and the increase in width and the decrease in slope downstream is strongly influenced by the portion of sediment carried as bedload and suspended load, the variation of which is poorly understood in drainage basins and need of greater attention. The uplift rate and

rock strength only influences μ and θ at extremely high uplift rates and rock strength.

Explicitly incorporating width and slope adjustment into landscape evolution models will affect how long-term climate change impacts the uplift of mountains ranges. A more erosive climate has been argued to increase eroded mass, which needs to be compensated with isostatic uplift of mountain ranges (Molnar & England, 1990; Gilchrist et al., 1994; Small & Anderson, 1995, 1998; Brozović et al., 1997). Models of landscape evolution only considers eroded mass from channel bed, assuming channel width is constant. However, our model shows that channel width is a linear function of sediment supply. This function leads to a positive feedback between eroded mass and channel widening as climate becomes more erosive. More bedrock is eroded as climates become wetter, which can increase the sediment supply and hence the channel width. The channel widening in turn can cause more mass eroded from bedrock riverbanks and hillslopes, which will cause more isostatically compensated uplift than predicted in current landscape evolution models.

Methods

Steady state bedrock channel morphology. Steady-state bedrock channel morphology requires steady channel elevation and cross-sectional shape. The vertical erosion rate E_v needs to be balanced with the uplift rate U to keep elevation steady:

$$E_v = U \qquad \text{(Equation 6.3)}$$

The channel banks need to lower at the same rate of the channel bed to keep the cross-sectional shape steady:

$$E_l = E_v \cos \alpha \qquad \text{(Equation 6.4)}$$

where E_l is the bank normal erosion rate and α is the bank angle.

Vertical erosion by saltating bedload impacts. We used the model by Sklar & Dietrich (2004) for calculating vertical erosion rate due to saltating bedload impacts. The vertical erosion rate E_v is expressed as

$$E_v = 0.08R_b g \frac{1}{k_r}\frac{Q_s}{W}\left(\frac{\tau^*}{\tau_c^*} - 1\right)^{-0.52}(1 - \frac{Q_s}{Q_t})(1 - (\frac{u_s}{w_f})^2)^{1.5} \quad \text{(Equation 6.5)}$$

where $R_b = \frac{\rho_s - \rho_w}{\rho_w}$ is the submerged specific density of sediment, ρ_s is the sediment density, ρ_w is the water density, g is the acceleration due to gravity, k_r is bedrock strength coefficient that scales with the rock tensile yield strength σ_T, Young's modulus of elasticity of the bedrock and the dimensionless coefficient k_v ($k_r = \frac{k_v \sigma_T^2}{Y}$), Q_s is the mass sediment flux, Q_t is the sediment transport capacity, W is the channel width, $\tau^*$is the nondimensional form of shear stress τ, $\tau_c^* = \frac{\tau}{(\rho_s - \rho_w)gD}$ is the value of τ^* at the threshold of sediment motion, D is the grain size, u_s is the shear velocity, and w_f is the settling velocity. We used the bedload transport equation by Fernandez Luque & Van Beek (1976) to estimate Q_t as $Q_t = 5.7\rho_s W(R_b g D^3)^{0.5}(\tau^* - \tau_c^*)^{1.5}$. The settling velocity w_f was calculated using the Ferguson & Church (2004) relation, $w_f = \frac{R_b g D^2}{C_1 \upsilon + (0.75 C_2 R_b g D^3)^{0.5}}$, where υ is the kinematic viscosity of the fluid, and $C_1 = 18$ and $C_2 = 1$ are constants set for natural sediment.

Lateral erosion by saltating bedload impacts. We calculated the lateral erosion rate due to saltating bedload impacts that are deflected by the alluvial cover based on the Li et al. (2021) model. The lateral erosion rate E_l is expressed as

$$E_l = \frac{\pi}{48k_r}\frac{D \sin\alpha}{h_{max}}\frac{Q_s^2}{WQ_t}(1 - \frac{Q_s}{Q_t})(\frac{1}{h_s} + \frac{3}{2l_s})v_i^2(1 - (u^*/w_f)^2)^{1.5} \quad \text{(Equation 6.6)}$$

where h_s is the saltation height, l_s is the saltation length, h_{max} is the maximum height of erosion on the walls, and v_i is the particle velocity that is perpendicular to the channel banks. The saltation trajectories, h_s and l_s, were calculated using the relation developed by Sklar & Dietrich (2004), $h_s = 1.44D(\frac{\tau^*}{\tau_c^*} - 1)^{0.50}$ and $l_s =$

$8.0D(\frac{\tau^*}{\tau_c^*}-1)^{0.88}$. The maximum height of erosion h_{max} was calculated using the relation developed by Li et al. (2021), $h_{max}=1.5D+\frac{1}{2C_d}ln(\frac{C_d{w_o}^2}{C_g}+1)$, where $C_d=0.75C_1\,\rho_w/(D\rho_s)$ is the drag deceleration coefficient, C_1 (0.45) is the drag parameter, $C_g=(1-\rho_w/\rho_s)g$ is gravitational acceleration coefficient and w_o is the vertical particle velocity after being deflected by the alluvium surface.

The Li et al. (2021) model assumed a rectnagular channel with vertical channel banks ($\alpha=90°$) and hence only considered lateral velocity v_l. However, both lateral velocity v_l and vertical velocity v_v can cause erosion on bedrock banks in a trapezoid channel. The particle velocity that is perpendicular to the channel banks can be obtained from lateral velocity and vertical velocity using trigonometric functions, $v_i=v_l\,sin\,\alpha+v_v\,cos\,\alpha$. We used the relation developed by Li et al. (2021) to estimate the lateral velocity v_l as $v_l=v_o(\frac{(1-v_{min}^2/v_o^2)e^{-C_d h_{max}\,cot\,\alpha}}{e^{C_d DQ_t/Q_s}-e^{-C_d DQ_t/Q_s}})^{0.5}$, where $v_{min}=\frac{9S_t\upsilon\rho_w}{\rho_s D}$ is the minimum impact velocity that distinguishes impacts that can cause erosion and that are viscously damped, S_t is the particle Stokes number (~ 100; Schmeeckle et al., 2001; Joseph & Hunt, 2004), and v_o is the lateral particle velocity after being deflected by the alluvium surface. Assuming the ratio of lateral to vertical velocity is constant and following the method of caluclating v_l by Li et al. (2021), we can derive a relation for the vertical velocity $v_v=k_v w_o(\frac{(1-v_{min}^2/v_o^2)e^{-C_d h_{max}\,cot\,\alpha}}{e^{C_d DQ_t/Q_s}-e^{-C_d DQ_t/Q_s}})^{0.5}$, where k_v is the fraction of particles that move downwards and w_o is the vertical particle velocity after being deflected by the alluvium surface.

We used the relations developed by Li et al. (2021) to calculate the velocities, w_o and v_o, as $w_o=C_r(w_s-2n_z(n_x u_s+n_z w_s))$ and $v_o=2C_r n_y(n_x u_s+n_z w_s)$, where $C_r=0.9$ is the restitution coefficient that describes the loss of particle momentum during the collision between bedload particle and alluvium surface, n_x, n_y and n_z are downstream, lateral and vertical component of the unit vector that is normal to the alluvium surface at the point of deflection,

respectively ($n_x = 0.30\frac{Q_s}{Q_t} - 0.54$; $n_y = 0.25\frac{Q_s}{Q_t} - 0.58$; $n_z = 0.40\frac{Q_s}{Q_t} + 0.50$; Li et al., 2021), u_s is the longitudinal saltation velocity, and w_s is vertical saltation velocity. The longitudinal saltation velocity u_s was calculated using the relation developed by Sklar & Dietrich (2004) as $u_s = 1.56(R_b g D)^{0.5}(\frac{\tau^*}{\tau_c^*} - 1)^{0.56}$. The vertical saltation velocity was calculated using the relation developed by Lamb et al. (2008) as $w_s = -\sqrt{\frac{C_g}{C_d}(1 - e^{-2C_d(h_s - h_d)})}$, where $h_d = (0.83e^{-0.68(\tau^*/\tau_c^* - 1)} + 0.11\frac{Q_s}{Q_t} + 0.06)h_s$ is the height of bedload particle during collision with the deflector.

Shear stress. Assuming steady, uniform flow, shear stress τ can be expressed as

$$\tau = \rho_w g R S \qquad \text{(Equation 6.7)}$$

where S is channel slope and R is hydraulic radius. R was calculated from the channel width W, depth H and bank angle α, $R = \frac{(W + H/\tan\alpha)H}{W + 2H/\sin\alpha}$. Flow depth was calculated using the continuity equation $Q_w = (W + H/\tan\alpha)HU$, where Q_w is water discharge and U is flow velocity. The flow velocity U was calculated using a general Manning-Strickler formula, $\frac{U}{u^*} = a(\frac{R}{k_s})^{1/6}$, in which $u^* = \sqrt{\frac{\tau}{\rho_w}}$ is the shear velocity, $a = 8$ is a coefficient, k_s is a length scale assumed to be a function of grain size, $k_s = nD$ ($n = 3$ is selected here; Kamphuis, 1974)..

Upscaling to drainage basin scale. To scale up from at-a-station variation to drainage basin scale, we assumed that all the coarse sediments are transported during a representative high-flow discharge, which occurs a fraction of the time k_t (4.37%), and no coarse sediment is transported during low flow when the shear stress is below the threshold of motion. We assumed Q_w is a power function of A, $Q_w = k_q A^{m_q}$, where k_q is a measure of river base flow and m_q is the scaling power dependency. In our calculations, we used value of k_q = 1 and m_q = 0.9. Drainage area was related to the distance downstream x using Hack's Law, $A = A_0 + k_A x^b$, where A_0 (1 km^2) is the drainage area at the channel head, k_A (1

km$^{0.5}$) and b (1.5) are empirical parameters. The downstream fining of grain size was calculated from $D = D_0(\frac{x+x_0}{x_0})^{-m_d}$, where D_0 (0.3 m) is the grain size at the channel head, x_0 (1 km) is the unchanneled distance from the drainage divide to the channel head and m_d is an empirical parameter. D can be then approximated as a function of drainage area: $D \approx k_d A^{-0.67m_d}$, where $k_d = D_0 {x_0}^{m_d} {k_A}^{-0.67m_d}$. At steady state, the uplift rate U is equal to the long-term vertical erosion rate ($U = E_v$) and the coarse sediment supply rate can be expressed as $Q_s = \frac{\rho_s U A F_b}{k_t}$, where F_b is the fraction of sediment load that is transported as bedload. We assumed that the downstream fining of the bedload grain size is due to the production of fine sediment that is transported as wash load and the sediment supplied from the hillslopes has been found to shift to finer sediment and less coarse sediment with decreasing elevation. Therefore, the bedload fraction of the total load is assumed to decreases with increasing downstream distance and treated as a power law function of drainage area $F_b = F_0 A^{1-m_s}$, where F_0 (0.9) is the bedload fraction of the total load at the channel head and m_s (0.55) is an empirical parameter that describes the downstream change of the portion of sediment transported as suspended load.

Explicit functions for width and slope. In order to apply our results to predict width and slope of a bedrock river, we derive universal functions for width and slope as a function of Q_w, Q_s, D, k_r and U. The local width is not a function of Q_w (Figure 6.2c) but a linear function of Q_s. Therefore width can be expressed as

$$W = k_w Q_s \qquad \text{(Equation 6.8)}$$

where k_w is a nonlinear function of D, k_r and U. We use multiple nonlinear regression to find an explicit function for k_w as

$$k_w = \left[e^{(-11.56e^{-2.31Uk_r} - 13.4e^{-0.089Uk_r})} D^{(D-3.7)} + 10.3(Uk_r)^{0.711} D^{0.4}\right]^{-1} \qquad \text{(Equation 6.9)}$$

The component $e^{(-11.56e^{-2.31Uk_r} - 13.4e^{-0.089Uk_r})} D^{(D-3.7)}$ describes the narrowing response to decreasing grain size for fine sediment and can be

neglected for coarse sediment (D > 6 mm; Extended Data Figure C.1). Substituting equations for Q_s and D into the equation for W, the downstream width variation can be expressed as an explicit power relation of drainage area, given as $W = m_1 U^{0.29} k_r^{-0.71} A^{m_s + 0.27 m_d}$, where $m_1 = \frac{\rho_s F_0}{10.3 k_t {k_d}^{0.4}}$.

We used multiple nonlinear regression to find an explicit function for local slope expressed as

$$S = k_c (\tau^* / \tau_c^*)^{10/7} D^{9/7} (Q_w^{-0.86} (k_w Q_s)^{0.86} + Q_w^{-0.4} (k_w Q_s)^{-0.5}) \quad \text{(Equation 6.10)}$$

where

$$k_c = 5.9 g^{3/7} n^{-1/7} \left(\frac{\rho_s - \rho_w}{\rho_w} \tau_c^* \right)^{10/7}, \qquad \text{(Equation 6.11)}$$

and τ^* / τ_c^* is a nonlinear function of D, k_r and U that is also derived from multiple nonlinear regression

$$\tau^* / \tau_c^* = e^{(-3.5(Uk_r)^{-0.094} + 0.94) D^{0.18} + (0.37(Uk_r)^{0.32} - 0.055) D^{-0.58} + (0.02(Uk_r)^{-0.05} - 0.028) D^{-1}} + 1). \quad \text{(Equation 6.12)}$$

Equation 6.10 can be simplified to $S = k_c D^{9/7} (Q_w^{-0.86} (k_w Q_s)^{0.86})$ because τ^* / τ_c^* is close to 1, except at high uplift rate and rock strength conditions (Extended Data Figure C.2) and $Q_w^{-0.4} (k_w Q_s)^{-0.5}$ is negligible in rivers that are wider than deep. Replacing Q_w, Q_s, k_w and D with functions of A, the downstream slope variation can be expressed as $S = m_2 U^{0.25} k_r^{-0.61} A^{-0.86(m_s - m_q - 0.73 m_d)}$, where $m_2 = k_c k_q^{-0.86} m_w^{0.86}$.

Chapter 7. Conclusions

The dissertation sought to explore what controls width in bedrock rivers through mechanistic modelling and field observations. The findings of the dissertation are summarized in the context of the proposed objectives.

A numerical model for lateral erosion of bedrock channel banks by bedload particle impacts was developed in Chapter 2 by tracking the movement of bedload particles from collision with the deflectors to impacts on the wall. The model successfully reproduces the patterns of lateral erosion observed in flume experiments by Fuller et al. (2016). The predicted lateral erosion rate is nondimensionalized as a function of transport stage and relative sediment supply, and coupled with the vertical erosion model by Sklar & Dietrich (2004). The coupled model predicts that vertical erosion dominates under ~75% sediment supply and transport conditions, while lateral erosion only dominates when the bed is near fully covered.

An analytical solution for the numerical model of lateral erosion by bedload particle impacts was derived in Chapter 3. The analytical model predicts a nonlinear dependence of lateral erosion rate on sediment supply, shear stress, and grain size, revealing the same behavior observed in the numerical model, but without tracking individual particle movement. The analytical model considers uniformly distributed alluvial cover and patchy partial cover, which is implemented as a fully alluviated patch along one bank with bare bedrock along the other. The uniformly distributed cover model predicts the maximum erosion rate occurring at ~70% bed coverage, but the patchy cover model predicts the peak erosion rate at full bed coverage. When the lateral erosion model is coupled with the Sklar and Dietrich (2004) vertical erosion model, the ratio of lateral to vertical erosion rate increases with increasing relative sediment supply for both uniformly distributed and patchy covers. Application of the analytical model to Boulder Creek, California supports the inference by Finegan et al (2017) that

downstream channel widening occurs due to an increase in sediment supply and caliber.

Bed and wall stresses, which are key elements of erosion rate prediction in bedrock rivers, were partitioned using the Ray-Isovel Model (RIM) (Chapter 4). RIM predicts that the ratio of wall to bed stress exponentially decreases with increasing width-to-depth ratio. Application of RIM results to 26 bedrock canyons of the Fraser River shows that the modelled wall stress is smaller than the modelled bed stress and the ratio of wall to bed stress varies between 0.60 and 0.98. Observations of bed and wall stresses reveal that the observed wall stress is larger than the observed bed stress for the majority of the 26 canyons in the Fraser River. The model nearly always over-predicts the observed bed stress by ~56% (±15%), but under-predicts the wall stress by ~57% (±3.2%). The inconsistency between the model results and field observations is caused by complex three-dimensional flow and rough walls in natural bedrock canyons, which is not represented in the model. Nevertheless, RIM provides a first order estimate of bed and wall stresses, which can be corrected for partitioning bed and wall stresses because the RIM appears to be biased consistently.

A model for lateral erosion by bedload and suspended load advected by turbulence eddies was developed in Chapter 5 (advection-abrasion model). The advection-abrasion model predicts high lateral erosion rates near the bed and decreasing rates up to water surface. The erosion rate within the suspended load layer is higher than the bedload layer for many sediment supply and transport conditions, but is outpaced by the erosion rate within the bedload layer at steep slopes. Compared with the deflection-abrasion model developed in Chapters 2 and 3, the advection-abrasion model predicts higher erosion rate for all sediment supply and transport conditions, except when transport stage is near the threshold of motion and the bedload sediment supply is nearly equal to, or higher than transport capacity. A model that combines the advection- and the deflection-abrasion models predicts an increase in erosion rate with increasing transport stage and sediment supply, until the bedload supply approaches the bedload

transport capacity. The combined-abrasion model was applied to a natural bedrock river with a wide distribution of discharge and sediment supply as well as mixed grain size (finer and coarser sediments). The results indicate that finer sediment causes more lateral erosion than coarser sediment at low sediment supply, but coarser sediment becomes important at high sediment supply.

A method for calculating the width and slope of a bedrock river based entirely on the physics that underly vertical and lateral erosion was developed in Chapter 6. The new method predicts observed width and slope for rivers where the necessary input variables are known or can be estimated. Local and downstream variations of width and slope are explored. The local width is not controlled by discharge, but is a linear function of sediment supply, implying the commonly used width-discharge relation is due to the codependence of discharge and sediment supply. The local width and slope are non-linear functions of uplift rate, rock strength and grain size. Upscaling the local predictions to drainage basin scale reproduces the observed scaling relations between river width, slope, and drainage area underlying the stream power model that lies at the heart of modern landscape evolution models.

References

Amos, C. B., & Burbank, D. W. (2007). Channel width response to differential uplift. Journal of Geophysical Research, 112, F02010. https://doi.org/10.1029/2006JF000672

Anderson, R. S. (1994). Evolution of the Santa Cruz Mountains, California, through tectonic growth and geomorphic decay. Journal of Geophysical Research, 99(B10), 20,161–20,179. https://doi.org/10.1029/94JB00713

Ansari, S., Rennie, C. D., Venditti, J. G., Kwoll, E., & Fairweather, K. (2018). Shore-based monitoring of flow dynamics in a steep bedrock canyon river. In E3S Web of Conferences (Vol. 40, p. 06025). https://doi.org/10.1051/e3sconf/20184006025

Auel, C., Albayrak, I., Sumi, T., & Boes, R. M. (2017a). Sediment transport in high-speed flows over a fixed bed: 1. Particle dynamics. Earth Surface Processes and Landforms, 42(9), 1365–1383. https://doi.org/10.1002/esp.4128

Auel, C., Albayrak, I., Sumi, T., & Boes, R. M. (2017b). Sediment transport in high-speed flows over a fixed bed: 2. Particle impacts and abrasion prediction. Earth Surface Processes and Landforms, 42(9), 1384–1396. https://doi.org/10.1002/esp.4132

Bagnold, R. A. (1973). The nature of saltation and of 'bed-load' transport in water. Proceedings of the Royal Society of London. A. Mathematical and Physical Sciences, 332(1591 (1973)), 473–504. https://doi.org/10.1098/RSPA.1973.0038

Batchelor GK. (1953). The Theory of Homogeneous Turbulence. Cambridge, UK: Cambridge Univ. Press

Baynes, E. R. C., Lague, D., Steer, P., Bonnet, S., & Illien, L. (2020). Sediment flux-driven channel geometry adjustment of bedrock and mixed gravel–bedrock rivers. Earth Surface Processes and Landforms, 45(14), 3714–3731. https://doi.org/10.1002/ESP.4996

Beer, A. R., & Turowski, J. M. (2015). Bedload transport controls bedrock erosion under sediment-starved conditions. Earth Surface Dynamics, 3(3), 291–309. https://doi.org/10.5194/esurf-3-291-2015

Beer, A. R., Turowski, J. M., & Kirchner, J. W. (2017). Spatial patterns of erosion in a bedrock gorge. Journal of Geophysical Research: Earth Surface, 122, 191–214. https://doi.org/10.1002/2016JF003850

Blench, T. (1952). Regime Theory for Self-Formed Sediment-Bearing Channels. Transactions of the American Society of Civil Engineers, 117(1), 383–400. https://doi.org/10.1061/TACEAT.0006641

Brierley, G. J., & Hickin, E. J. (1985). The downstream gradation of particle sizes in the Squamish river, British Columbia. Earth Surface Processes and Landforms, 10(6), 597–606. https://doi.org/10.1002/ESP.3290100607

Brozović, N., Burbank, D. W., & Meigs, A. J. (1997). Climatic limits on landscape development in the northwestern Himalaya. Science, 276(5312), 571–574. https://doi.org/10.1126/SCIENCE.276.5312.571

Bufe, A., Paola, C., & Burbank, D. W. (2016). Fluvial bevelling of topography controlled by lateral channel mobility and uplift rate. Nature Geoscience, 9, 706–710. https://doi.org/10.1038/ngeo2773

Cao, Z. (2018). Scour pool incision in bedrock canyons. (Master's thesis). Retrieved from summit. (http://summit.sfu.ca/item/17995). Burnaby, BC: Simon Fraser University.

Cao, Z. (Eric), Venditti, J. G., & Li, T. (2022). Experiments on Pool Formation in Bedrock Canyons. Journal of Geophysical Research: Earth Surface, 127(5), e2021JF006456. https://doi.org/10.1029/2021JF006456

Carling, P. A. (1989). Hydrodynamic models of boulder berm deposition. Geomorphology, 2, 319–340. https://doi. org/10.1016/0169-555X(89)90018-4

Carling, P. A., Cao, Z., Holland, M. J., Ervine, D. A., & Babaeyan-Koopaei, K. (2002). Turbulent flow across a natural compound channel. Water Resources Research. https://doi.org/10.1029/2001wr000902

Carling, P. A., Huang, H. Q., Su, T., & Hornby, D. (2019). Flow structure in large bedrock-channels: The example of macroturbulent rapids, lower Mekong River, Southeast Asia. Earth Surface Processes and Landforms. https://doi.org/10.1002/esp.4537

Carling, P. A., Tych, W., & Richardson, K. (2006). The hydraulic scaling of step-pool systems. In River, coastal and estuarine mor- phodynamics: RCEM 2005 - Proceedings of the 4th IAHR Symposium on river, Coastal and Estuarine morphodynamics. https://doi. org/10.1201/9781439833896.ch8

Carter, C. L., & Anderson, R. S. (2006). Fluvial erosion of physically modeled abrasion-dominated slot canyons. Geomorphology, 81(1–2), 89–113. https://doi.org/10.1016/J.GEOMORPH.2006.04.006

Chatanantavet, P., & Parker, G. (2008). Experimental study of bedrock channel alluviation under varied sediment supply and hydraulic conditions. Water Resources Research, 44, W12446. https://doi.org/10.1029/2007WR006581

Chatanantavet, P., & Parker, G. (2009). Physically based modeling of bedrock incision by abrasion, plucking, and macroabrasion. Journal of Geophysical Research, 114, F04018. https://doi.org/10.1029/2008JF001044

Chatanantavet, P., & Parker, G. (2011). Quantitative testing of model of bedrock channel incision by plucking and macroabrasion. Journal of Hydraulic Engineering, 137(11), 1311–1317. https://doi.org/10.1061/(ASCE)HY.1943-7900.0000421

Cohen, S., Syvitski, J., Ashely, T., Lammers, R., Fekete, B., & Li, H. (2022). Spatial Trends and Drivers of Bedload and Suspended Sediment Fluxes in Global Rivers. Water Resources Research, 58(6). https://doi.org/10.1029/2021WR031583

Cook, K. L., Whipple, K. X., Heimsath, A. M., & Hanks, T. C. (2009). Rapid incision of the Colorado River in Glen Canyon - insights from channel profiles, local incision rates, and modeling of lithologic controls. Earth Surface Processes and Landforms. https://doi.org/10.1002/esp.1790

Cook, K. L., Turowski, J. M., & Hovius, N. (2013). A demonstration of the importance of bedload transport for fluvial bedrock erosion and knickpoint propagation. Earth Surface Processes and Landforms. 38(7), 683–695. https://doi.org/10.1002/esp.3313

Cook, K. L., Turowski, J. M., & Hovius, N. (2014). River gorge eradication by downstream sweep erosion. Nature Geoscience, 7(9), 682–686. https://doi.org/10.1038/ngeo2224

Croissant, T., Lague, D., & Davy, P. (2019). Channel widening downstream of valley gorges influenced by flood frequency and floodplain roughness. Journal of Geophysical Research: Earth Surface, 124, 154–174. https://doi.org/10.1029/2018JF004767

Cundall, P. A., & Strack, O. D. L. (1979). Discrete numerical model for granular assemblies. Geotechnique, 29(1), 47–65. https://doi.org/ 10.1680/geot.1979.29.1.47

Curran, M. (2020). Bedrock structural influences on river morphology (Master's thesis). Retrieved from http://summit.sfu.ca/item/20434. Simon Fraser University.

Davis, R. H., Serayssol, J.-M., & Hinch, E. J. (1986). The elastohydrodynamic collision of two spheres. Journal of Fluid Mechanics, 163(1), 479. https://doi.org/10.1017/S0022112086002392

De Leeuw, J., P. Lamb, M., Parker, G., Moodie, A. J., Haught, D., G. Venditti, J., & Nittrouer, J. A. (2020). Entrainment and suspension of sand and gravel. Earth Surface Dynamics. https://doi.org/10.5194/esurf-8-485-2020

DiBiase, R. A., & Whipple, K. X. (2011). The influence of erosion thresholds and runoff variability on the relationships among topography, climate, and erosion rate. Journal of Geophysical Research: Earth Surface, 116, F04036. https://doi.org/10.1029/2011JF002095

Dietrich, W. E. (1982). Settling velocity of natural particles. Water Resources Research, 18(6), 1615–1626. https://doi.org/10.1029/ WR018i006p01615

Dietrich, W. E., & Smith, J. D. (1984). Bed load transport in a river meander. Water Resources Research, 20(10), 1355–1380. https://doi.org/ 10.1029/WR020i010p01355

Dietrich, W. E., & Whiting, P. (1989). Boundary shear stress and sediment transport in river meanders of sand and gravel. River meandering (pp. 1–50). Washington, DC: American Geophysical Union (AGU). https://doi.org/10.1029/wm012p0001

Dolan, R., Howard, A., & Trimble, D. (1978). Structural control of the rapids and pools of the Colorado river in the grand canyon. Science, 202, 629–631. https://doi.org/10.1126/science.202.4368.629

Dubinski, I. M., & Wohl, E. (2013). Relationships between block quarrying, bed shear stress, and stream power: A physical model of block quarrying of a jointed bedrock channel. Geomorphology, 180-181, 66–81. https://doi.org/10.1016/j.geomorph.2012.09.007

Dunne, K. B. J., & Jerolmack, D. J. (2020). What sets river width? Science Advances, 6(41). https://doi.org/10.1126/SCIADV.ABC1505/SUPPL_FILE/ABC1505_SM.PDF

Duvall, A., Kirby, E., & Burbank, D. (2004). Tectonic and lithologic controls on bedrock channel profiles and processes in coastal Califor- nia. Journal of Geophysical Research, 109, F03002. https://doi.org/10.1029/2003JF000086

Eaton, B. C., & Church, M. (2007). Predicting downstream hydraulic geometry: A test of rational regime theory. Journal of Geophysical Research: Earth Surface, 112(F3), 3025. https://doi.org/10.1029/2006JF000734

Egholm, D. L., Knudsen, M. F., & Sandiford, M. (2013). Lifespan of mountain ranges scaled by feedbacks between landsliding and erosion by rivers. Nature, 498(7455), 475–478. https://doi.org/10.1038/nature12218

Farley, K. A., Rusmore, M. E., & Bogue, S. W. (2001). Post–10 Ma uplift and exhumation of the northern Coast Mountains, British Columbia . Geology, 29(2), 99–102. Retrieved from https://authors.library.caltech.edu/36884/

Ferguson, R. I., & Church, M. (2004). A simple universal equation for grain settling velocity. Journal of Sedimentary Research. https://doi.org/10.1306/051204740933

Ferguson, R., & Church, M. (2009). A critical perspective on 1-D modeling of river processes: Gravel load and aggradation in lower Fraser River. Water Resources Research, 45(11), 11424. https://doi.org/10.1029/2009WR007740

Ferguson, R. I., & Paola, C. (1997). Bias and precision of percentiles of bulk grain size. Earth Surface Processes and Landforms, 22(11), 1061–1077. https://doi.org/10.1002/(SICI)1096-9837(199711)22:11<1061::AID-ESP809>3.0.CO;2-L

Ferguson, R. I., Hardy, R. J., & Hodge, R. A. (2019). Flow resistance and hydraulic geometry in bedrock rivers with multiple roughness length scales. Earth Surface Processes and Landforms, 44(12), 2437–2449. https://doi.org/10.1002/esp.4673

Ferguson, S. P., & Rennie, C. D. (2017). Influence of alluvial cover and lithology on the adjustment characteristics of semi-alluvial bedrock channels. Geomorphology, 285, 260–271. https://doi.org/10.1016/J.GEOMORPH.2017.01.040

Fernández, R., Parker, G., & Stark, C. P. (2019). Experiments on patterns of alluvial cover and bedrock erosion in a meandering channel. Earth Surface Dynamics, 7, 949–968. https://doi.org/10.5194/esurf-7-949-2019

Fernandez Luque, R., & Van Beek, R. (1976). Erosion and transport of bed-load sediment. Journal of Hydraulic Research, 14(2), 127–144. https://doi.org/10.1080/00221687609499677

Ferrier, K. L., Huppert, K. L., & Perron, J. T. (2013). Climatic control of bedrock river incision. Nature 2013 496:7444, 496(7444), 206–209. https://doi.org/10.1038/nature11982

Finnegan, N. J., & Balco, G. (2013). Sediment supply, base level, braiding, and bedrock river terrace formation: Arroyo Seco, California, USA. Geological Society of America Bulletin, 125(7–8), 1114–1124. https://doi.org/10.1130/B30727.1

Finnegan, N. J., Klier, R. A., Johnstone, S., Pfeiffer, A. M., & Johnson, K. (2017). Field evidence for the control of grain size and sediment supply on steady-state bedrock river channel slopes in a tectonically active setting. Earth Surface Processes and Landforms, 42(14), 2338–2349. https://doi.org/10.1002/esp.4187

Finnegan, N. J., Roe, G., Montgomery, D. R., & Hallet, B. (2005). Controls on the channel width of rivers: Implications for modeling fluvial incision of bedrock. Geology. https://doi.org/10.1130/G21171.1

Finnegan, N. J., Sklar, L. S., & Fuller, T. K. (2007). Interplay of sediment supply, river incision, and channel morphology revealed by the transient evolution of an experimental bedrock channel. Journal of Geophysical Research, 112, F03S11. https://doi.org/10.1029/ 2006JF000569

Finnegan, N. J., & Dietrich, W. E. (2011). Episodic bedrock strath terrace formation due to meander migration and cutoff. Geology, 39(2), 143–146. https://doi.org/10.1130/G31716.1

Flintham, T. P., & Carling, P. A. (1988). In R. White (Ed.), The prediction of mean bed and wall boundary shear in uniform and compositely rough channels. In River Regime (pp. 267–287). John Wiley.

Flintham, T. P., & Carling, P. A. (1989). Manning's-N of composite roughness in channels of simple cross section. In B. C. Yen (Ed.), Proceedings of the International Conference for Centennial of Manning's Formula and Kuichling's Rational Formula (p. 518–529). Am. Soc. Civ. Eng.

Finnegan, N. J., Roe, G., Montgomery, D. R., & Hallet, B. (2005). Controls on the channel width of rivers: Implications for modeling fluvial incision of bedrock. Geology, 3, 229–232. https://doi.org/10.1130/G21171.1

Fuller, T. K., Gran, K. B., Sklar, L. S., & Paola, C. (2016). Lateral erosion in an experimental bedrock channel: The influence of bed roughness on erosion by bed load impacts. Journal of Geophysical Research: Earth Surface, 121, 1084–1105. https://doi.org/10.1002/ 2015JF003728

Fuller, T. K., Perg, L. A., Willenbring, J. K., & Lepper, K. (2009). Field evidence for climate-driven changes in sediment supply leading to strath terrace formation. Geology, 37(5), 467–470. https://doi.org/10.1130/G25487A.1

Garcia, M. (2008). Sedimentation engineering: Processes, measurements, modeling, and practice. (M. Garcia, Ed.). Reston, VA: American Society of Civil Engineers. https://doi.org/10.1061/9780784408148

Gilbert, G. K. (1877). Geology of the Henry Mountains, 170 pp., U.S. Govt.Print. Office, Washington, D. C. https://doi.org/10.3133/ 70039916

Gilchrist, A. R., Summerfield, M. A., & Cockburn, H. A. P. (1994). Landscape dissection, isostatic uplift, and the morphologic development of orogens. Geology, 22(11), 963–966. https://doi.org/10.1130/0091-7613(1994)022<0963:LDIUAT>2.3.CO;2

Goren, L., Fox, M., & Willett, S. D. (2014). Tectonics from fluvial topography using formal linear inversion: Theory and applications to the Inyo Mountains, California. Journal of Geophysical Research: Earth Surface, 119(8), 1651–1681. https://doi.org/10.1002/2014JF003079

Griffin, E. R., Kean, J. W., Vincent, K. R., Smith, J. D., & Friedman, J. M. (2005). Modeling effects of bank friction and woody bank vegetation on channel flow and boundary shear stress in the Rio Puerco, New Mexico. Journal of Geophysical Research: Earth Surface, 110, F04023. https://doi.org/10.1029/2005JF000322

Grinvald, D. I. (1974). Turbulence of Open-Channel Flows. Hydrometeoizdat, Leningrad (former USSR).

Hancock, G. S., & Anderson, R. S. (2002). Numerical modeling of fluvial strath-terrace formation in response to oscillating climate. GSA Bulletin, 114(9), 1131–1142. https://doi.org/10.1130/0016-7606(2002)114<1131:nmofst>2.0.co;2

Hancock, G. S., Small, E. E., & Wobus, C. (2011). Modeling the effects of weathering on bedrock-floored channel geometry. Journal of Geophysical Research, 116, F03018. https://doi.org/10.1029/2010JF001908

Harel, M. A., Mudd, S. M., & Attal, M. (2016). Global analysis of the stream power law parameters based on worldwide10Be denudation rates. Geomorphology. https://doi.org/10.1016/j.geomorph.2016.05.035

Hartshorn, K., Hovius, N., Dade, W. B., & Slingerland, R. L. (2002). Climate-driven bedrock incision in an active mountain belt. Science, 297(5589), 2036–2038. https://doi.org/10.1126/science.1075078

Howard, A. D. (1994). A detachment-limited model of drainage basin evolution. Water Resources Research, 30(7), 2261–2285. https://doi. org/10.1029/94WR00757

Howard, A. D., Dietrich, W. E., & Seidl, M. A. (1994). Modeling fluvial erosion on regional to continental scales. Journal of Geophysical Research: Solid Earth. https://doi.org/10.1029/94JB00744

Howard, A. D., & Kerby, G. (1983). Channel changes in badlands. Geological Society of America Bulletin, 94, 739–752. https://doi.org/ 10.1130/0016-7606(1983)94<739:CCIB>2.0.CO;2

Huda, S. A., & Small, E. E. (2014). Modeling the effects of bed topography on fluvial bedrock erosion by saltating bed load. Journal of Geophysical Research: Earth Surface, 119, 1222–1239. https://doi.org/10.1002/2013JF002872

Hunt, B., Venditti, J. G., & Kwoll, E. (2018). Experiments on the morphological controls of velocity inversions in bedrock canyons. Earth Surface Processes and Landforms. https://doi.org/10.1002/esp.4274

Hurst, A. A., Anderson, R. S., & Crimaldi, J. P. (2021). Toward entrainment thresholds in fluvial plucking. Journal of Geophysical Research: Earth Surface, 126. https://doi.org/10.1029/2020JF005944

Inoue, T., Iwasaki, T., Parker, G., Shimizu, Y., Izumi, N., Stark, C. P., & Funaki, J. (2016). Numerical simulation of effects of sediment supply on bedrock channel morphology. Journal of Hydraulic Engineering, 142(7), 04016014.

Ikeda, S., & Izumi, N. (1991). Stable Channel Cross Sections of Straight Sand Rivers. Water Resources Research, 27(9), 2429–2438. https://doi.org/10.1029/91WR01220

Inoue, T., Izumi, N., Shimizu, Y., & Parker, G. (2014). Interaction among alluvial cover, bed roughness, and incision rate in purely bedrock and alluvial-bedrock channel. Journal of Geophysical Research: Earth Surface, 119, 2123–2146. https://doi.org/10.1002/2014JF003133

Inoue, T., Parker, G., & Stark, C. P. (2017). Morphodynamics of a bedrock-alluvial meander bend that incises as it migrates outward: Approximate solution of permanent form. Earth Surface Processes and Landforms, 42, 1342–1354. https://doi.org/10.1002/esp.4094

Johnson, E. D., & Cowen, E. A. (2017). Estimating bed shear stress from remotely measured surface turbulent dissipation fields in open channel flows. Water Resources Research. https://doi.org/10.1002/2016WR018898

Johnson, J. P., & Whipple, K. X. (2007). Feedbacks between erosion and sediment transport in experimental bedrock channels. Earth Surface Processes and Landforms, 32(7), 1048–1062. https://doi.org/10.1002/esp.1471

Johnson, J. P. L. (2014). A surface roughness model for predicting alluvial cover and bed load transport rate in bedrock channels. Journal of Geophysical Research: Earth Surface, 119, 2147–2173. https://doi.org/10.1002/2013JF003000

Johnson, J. P. L., & Whipple, K. X. (2010). Evaluating the controls of shear stress, sediment supply, alluvial cover, and channel morphology on experimental bedrock incision rate. Journal of Geophysical Research, 115, F02018. https://doi.org/10.1029/2009JF001335

Joseph, G. G., & Hunt, M. L. (2004). Oblique particle-wall collisions in a liquid. Journal of Fluid Mechanics, 510, 71–93. https://doi.org/ 10.1017/S002211200400919X

Joseph, G. G., Zenit, R., Hunt, M. L., & Rosenwinkel, A. M. (2001). Particle-wall collisions in a viscous fluid. Journal of Fluid Mechanics, 433, 329–346. https://doi.org/10.1017/S0022112001003470

Kamphuis, J. W. (1974). Determination of sand roughness for fixed beds. Journal of Hydraulic Research, 12(2), 193. https://doi.org/10.1080/00221687409499737

Kean, J. W., Kuhnle, R. A., Smith, J. D., Alonso, C. V., & Langendoen, E. J. (2009). Test of a method to calculate near-bank velocity and boundary shear stress. Journal of Hydraulic Engineering, 135, 588–601. https://doi.org/10.1061/(ASCE)HY.1943-7900.0000049

Kean, J. W., & Smith, J. D. (2004). Flow and boundary shear stress in channels with woody bank vegetation. In S. J. Bennett & A. Simon (Eds.), Riparian Vegetation and Fluvial Geomorphology, Water Science and Application Series. (Vol. 8, pp. 237–252). AGU. https://doi. org/10.1029/008wsa17

Kean, J. W., & Smith, J. D. (2005). Generation and verification of theoretical rating curves in the Whitewater River basin, Kansas. Journal of Geophysical Research: Earth Surface, 110, F04012. https://doi.org/10.1029/2004JF000250

Knight, D. W., & Macdonald, J. A. (1979). Open channel flow with varying bed roughness. Journal of the Hydraulics Division, 105(9), 1167– 1183. https://doi.org/10.1061/jyceaj.0005274

Knight, D. W., & Shiono, K. (1990). Turbulence measurements in a shear layer region of a compound channel. Journal of Hydraulic Research. https://doi.org/10.1080/00221689009499085

Kolmogorov AN. (1941a). Dissipation of energy in locally isotropic turbulence. Dokl. Akad. Nauk. SSSR 32:16–18

Kolmogorov AN. (1941b). On degeneration (decay) of isotropic turbulence in an incompressible viscous fluid. Dokl. Akad. Nauk. SSSR 31:538–40

Lague, D. (2010). Reduction of long-term bedrock incision efficiency by short-term alluvial cover intermittency. Journal of Geophysical Research, 115, F02011. https://doi.org/10.1029/2008JF001210

Lague, D., Hovius, N., & Davy, P. (2005). Discharge, discharge variability, and the bedrock channel profile. Journal of Geophysical Research,110, F04006. https://doi.org/10.1029/2004JF000259

Lamb, M. P., Brun, F., & Fuller, B. M. (2017). Hydrodynamics of steep streams with planar coarse-grained beds: Turbulence, flow resistance, and implications for sediment transport. Water Resources Research, 53(3), 2240–2263. https://doi.org/10.1002/2016WR019579

Lamb, M. P., & Dietrich, W. E. (2009). The persistence of waterfalls in fractured rock. Bulletin of the Geological Society of America, (121, pp. 1123–1134). https://doi.org/10.1130/B26482.1

Lamb, M. P., Dietrich, W. E., & Sklar, L. S. (2008a). A model for fluvial bedrock incision by impacting suspended and bed load sediment. Journal of Geophysical Research, 113, F03025. https://doi.org/10.1029/2007JF000915

Lamb, M. P., Dietrich, W. E., & Venditti, J. G. (2008b). Is the critical shields stress for incipient sediment motion dependent on channel-bed slope? Journal of Geophysical Research: Earth Surface. https://doi.org/10.1029/2007JF000831

Lamb, M. P., Finnegan, N. J., Scheingross, J. S., & Sklar, L. S. (2015). New insights into the mechanics of fluvial bedrock erosion through flume experiments and theory. Geomorphology, 244, 33–55. https://doi.org/10.1016/j.geomorph.2015.03.003

Langston, A. L., & Tucker, G. E. (2018). Developing and exploring a theory for the lateral erosion of bedrock channels for use in landscape evolution models. Earth Surface Dynamics, 6(1), 1–27. https://doi.org/10.5194/esurf-6-1-2018 Larsen, I. J., & Lamb, M. P. (2016). Progressive incision of the Channeled Scablands by outburst floods. Nature, 538(7624), 229–232. https://doi.org/10.1038/nature19817

Lavé, J., & Avouac, J. P. (2001). Fluvial incision and tectonic uplift across the Himalayas of central Nepal. Journal of Geophysical Research, 106(B11), 26561–26591. https://doi.org/10.1029/2001JB000359

Leopold, L. B., & Maddock Jnr, T. (1953). The Hydraulic Geomtry of Stream Channels and Some Physiographic Implications. US Government Printing Office. https://doi.org/10.3133/PP252

Leopold, L. B., & Wolman, G. M. (1957). River Channel Patterns: Braided, Meandering and Straight. PHYSIOGRAPHIC AND HYDRAULIC STUDIES OF RIVERS. https://doi.org/10.1093/mollus/70.2.123

Li, T., Fuller, T. K., Sklar, L. S., Gran, K. B., & Venditti, J. G. (2020). A mechanistic model for lateral erosion of bedrock channel banks by bedload particle impacts. Journal of Geophysical Research: Earth Surface, 125, e2019JF005509. https://doi.org/10.1029/2019JF005509

Li, T., Venditti, J. G., & Sklar, L. S. (2021). An analytical model for lateral erosion from saltating bedload particle impacts. Journal of Geophys- ical Research: Earth Surface, 126. https://doi.org/10.1029/2020jf006061

Li, T., Venditti, J. G., Rennie, C. D., & Nelson, P. A. (2022). Bed and Bank Stress Partitioning in Bedrock Rivers. Journal of Geophysical Research: Earth Surface, 127(2), e2021JF006360. https://doi.org/10.1029/2021JF006360

Limaye, A. B. S., & Lamb, M. P. (2014). Numerical simulations of bedrock valley evolution by meandering rivers with variable bank material. Journal of Geophysical Research: Earth Surface, 119, 927–950. https://doi.org/10.1002/2013JF002997

Lisle, T. E. (1986). Stabilization of a gravel channel by large streamside obstructions and bedrock bends, Jacoby Creek, northwestern California. GSA Bulletin, 97(8), 999–1011. https://doi.org/10.1130/0016-7606(1986)97<999:soagcb>2.0.co;2

Lotter, G. K. (1933). Considerations on hydraulic design of channels with different roughness of walls.Transactions of the All-Union Scientific Research Institute of Hydraulic Engineering (Vol. 9, pp. 238–241).

McLean, S. R. (1991). Depth-Integrated Suspended-Load Calculations. Journal of Hydraulic Engineering. https://doi.org/10.1061/(asce)0733-9429(1991)117:11(1440)

McLean, S. R., Nelson, J. M., & Wolfe, S. R. (1994). Turbulence structure over two-dimensional bed forms: Implications for sediment transport. Journal of Geophysical Research, 99, 12729. https://doi.org/10.1029/94jc00571

Meshkova, L. V., Carling, P. A., & Buffin-Bélanger, T. (2012). Nomenclature, complexity, semi-alluvial channels and sediment-flux-driven bedrock Erosion. In Gravel-Bed Rivers: Processes, Tools, Environments (pp. 424–431). Chichester, UK: John Wiley. https://doi.org/ 10.1002/9781119952497.ch31

Millar, R. G. (1999). Grain and form resistance in gravel-bed rivers. Journal of Hydraulic Research, 37(3), 303–312. https://doi.org/10.1080/00221686.1999.9628249

Millar, R. G. (2005). Theoretical regime equations for mobile gravel-bed rivers with stable banks. Geomorphology, 64(3–4), 207–220. https://doi.org/10.1016/J.GEOMORPH.2004.07.001

Mishra, J., Inoue, T., Shimizu, Y., Sumner, T., & Nelson, J. M. (2018). Consequences of abrading bed load on vertical and lateral bedrock erosion in a curved experimental channel. Journal of Geophysical Research: Earth Surface, 123, 3147–3161. https://doi.org/10.1029/ 2017JF004387

Moglen, G. E., & Bras, R. L. (1995). The Effect of Spatial Heterogeneities on Geomorphic Expression in a Model of Basin Evolution. Water Resources Research, 31(10), 2613–2623. https://doi.org/10.1029/95wr02036

Montgomery, D. R. (2004). Observations on the role of lithology in strath terrace formation and bedrock channel width. American Journal of Science, 304(5), 454–476. https://doi.org/10.2475/ajs.304.5.454

Montgomery, D. R., & Buffington, J. M. (1997). Channel-reach morphology in mountain drainage basins. Bulletin of the Geological Society of America, 109(5), 596–611. https://doi.org/10.1130/0016-7606(1997)109<0596:CRMIMD>2.3.CO;2

Molnar, P., & England, P. (1990). Late Cenozoic uplift of mountain ranges and global climate change: chicken or egg? Nature 1990 346:6279, 346(6279), 29–34. https://doi.org/10.1038/346029a0

Mouri, H., Hori, A., Kawashima, Y., & Hashimoto, K. (2012). Large-scale length that determines the mean rate of energy dissipation in turbulence. Physical Review E, 86(2), 026309. https://doi.org/10.1103/PhysRevE.86.026309

Nanson, G. C., & Huang, H. Q. (2017). Self-adjustment in rivers: Evidence for least action as the primary control of alluvial-channel form and process. Earth Surface Processes and Landforms, 42(4), 575–594. https://doi.org/10.1002/ESP.3999

Naqshband, S., McElroy, B., & Mahon, R. C. (2017). Validating a universal model of particle transport lengths with laboratory measurements of suspended grain motions. Water Resources Research, 53(5), 4106–4123. https://doi.org/10.1002/2016WR020024

Nelson, P. A., & Seminara, G. (2011). Modeling the evolution of bedrock channel shape with erosion from saltating bed load. Geophysical Research Letters, 38, L17406. https://doi.org/10.1029/2011GL048628

Nelson, P. A., & Seminara, G. (2012). A theoretical framework for the morphodynamics of bedrock channels. Geophysical Research Letters, 39, L06408. https://doi.org/10.1029/2011GL050806

Nezu, I. (2005). Open-channel flow turbulence and its research prospect in the 21st Century. Journal of Hydraulic Engineering, 131(4), 229–246. https://doi.org/10.1061/(ASCE)0733-9429(2005)131:4(229)

Nezu, I., & Nakagawa, H. (1993). Turbulence in open-channel flows. Turbulence in Open-Channel Flows. https://doi.org/10.1061/(asce)0733-9429(1994)120:10(1235)

Nikora, V. I., & Smart, G. M. (1997). Turbulence characteristics of New Zealand gravel-bed rivers. Journal of Hydraulic Engineering, 123(9), 764–773. https://doi.org/10.1061/(ASCE)0733-9429(1997)123:9(764)

Niño, Y., García, M., & Ayala, L. (1994). Gravel saltation: 1. Experiments. Water Resources Research, 30(6), 1907–1914. https://doi.org/ 10.1029/94WR00533

Ohara, N., & Yamatani, K. (2019). Theoretical Stable Hydraulic Section based on the Principle of Least Action. Scientific Reports 2019 9:1, 9(1), 1–6. https://doi.org/10.1038/s41598-019-44347-4

Park, C. C. (1977). World-wide variations in hydraulic geometry exponents of stream channels: An analysis and some observations. Journal of Hydrology, 33(1–2), 133–146. https://doi.org/10.1016/0022-1694(77)90103-2

Parker, G. (1978). Self-formed straight rivers with equilibrium banks and mobile bed. Part 1. The sand-silt river. Journal of Fluid Mechanics, 89(01), 109. https://doi.org/10.1017/S0022112078002499

Parker, G. (2004). 1D sediment transport morphodynamics with applications to rivers and turbidity currents. Retrieved from http://hydrolab.illinois.edu/people/parkerg/morphodynamics_e-book.htm

Parker, G. (2010). Surface-based bedload transport relation for gravel rivers. Journal of hydraulic research, 28(4), 417-436. https://doi.org/10.1080/00221689009499058

Parker, G., Wilcock, P. R., Paola, C., Dietrich, W. E., & Pitlick, J. (2007). Physical basis for quasi-universal relations describing bankfull hydraulic geometry of single-thread gravel bed rivers. Journal of Geophysical Research: Earth Surface, 112(F4), 4005. https://doi.org/10.1029/2006JF000549

Pazzaglia, F. J., & Brandon, M. T. (2001). A fluvial record of long-term steady-state uplift and erosion across the Cascadia forearc high, western Washington State. American Journal of Science, 301, 385–431. https://doi.org/10.2475/ajs.301.4-5.385

Perron, J. T. (2011). Numerical methods for nonlinear hillslope transport laws. Journal of Geophysical Research: Earth Surface, 116(F2), 2021. https://doi.org/10.1029/2010JF001801

Perron, J. T., Dietrich, W. E., & Kirchner, J. W. (2008). Controls on the spacing of first-order valleys. Journal of Geophysical Research, 113, F04016. https://doi.org/10.1029/2007JF000977

Perron, J. T., Kirchner, J. W., & Dietrich, W. E. (2009). Formation of evenly spaced ridges and valleys. Nature. https://doi.org/10.1038/nature08174

Perron, J. T., Richardson, P. W., Ferrier, K. L., & LapÔtre, M. (2012). The root of branching river networks. Nature 2012 492:7427, 492(7427), 100–103. https://doi.org/10.1038/nature11672

Perron, J. T., & Royden, L. (2013). An integral approach to bedrock river profile analysis. Earth Surface Processes and Landforms, 38(6), 570–576. https://doi.org/10.1002/ESP.3302

Rennie, C. D., Church, M., & Venditti, J. G. (2018). Rock control of river geometry: The Fraser canyons. Journal of Geophysical Research: Earth Surface.,123, 1860–1878. https://doi.org/10.1029/2017JF004458

Richardson, K., & Carling, P. A. (2005). A typology of sculpted forms in open bedrock channels. In Special Paper 392: A typology of sculpted forms in open bedrock channels (pp. 1–108). Boulder, CO: Geological Society of America. https://doi.org/10.1130/0-8137-2392-2.1

Royden, L., & Taylor Perron, J. (2013). Solutions of the stream power equation and application to the evolution of river longitudinal profiles. Journal of Geophysical Research: Earth Surface. https://doi.org/10.1002/jgrf.20031

Scheingross, J. S., Brun, F., Lo, D. Y., Omerdin, K., & Lamb, M. P. (2014). Experimental evidence for fluvial bedrock incision by suspended and bedload sediment. Geology, 42(6), 523–526. https://doi.org/10.1130/G35432.1

Schmeeckle, M. W., Nelson, J. M., Pitlick, J., & Bennett, J. P. (2001). Interparticle collision of natural sediment grains in water. Water Resources Research, 37(9), 2377–2391. https://doi.org/10.1029/2001WR000531

Seidl, M. A., & Dietrich, W. E. (1992). The problem of channel erosion into bedrock. Functional geomorphology, 23, 101–124. https://doi. org/10.1002/cssc.201301001

Shepherd, R. G. (1972). Incised river meanders: Evolution in simulated bedrock. Science, 178(4059), 409–411. https://doi.org/10.1126/ science.178.4059.409

Sklar, L. S., & Dietrich, W. E. (2001). Sediment and rock strength controls on river incision into bedrock. Geology, 29(12), 1087. https://doi. org/10.1130/0091-7613(2001)029<1087:SARSCO>2.0.CO;2

Sklar, L. S., & Dietrich, W. E. (2004). A mechanistic model for river incision into bedrock by saltating bed load. Water Resources Research, 40, W06301. https://doi.org/10.1029/2003WR002496

Sklar, L. S., & Dietrich, W. E. (2006). The role of sediment in controlling steady-state bedrock channel slope: Implications of the saltation-abrasion incision model. Geomorphology, 82(1–2), 58–83. https://doi.org/10.1016/j.geomorph.2005.08.019

Sklar, L. S., & Dietrich, W. E. (2008). Implications of the saltation-abrasion bedrock incision model for steady-state river longitudinal profile relief and concavity. Earth Surface Processes and Landforms, 33(7), 1129–1151. https://doi.org/10.1002/esp.1689

Sklar, L. S., Riebe, C. S., Marshall, J. A., Genetti, J., Leclere, S., Lukens, C. L., & Merces, V. (2017). The problem of predicting the size distribution of sediment supplied by hillslopes to rivers. Geomorphology, 277, 31–49. https://doi.org/10.1016/j.geomorph.2016.05.005

Small, E. E., & Anderson, R. S. (1995). Geomorphically Driven Late Cenozoic Rock Uplift in the Sierra Nevada, California. Science, 270(5234), 277–280. https://doi.org/10.1126/SCIENCE.270.5234.277

Small, E. E., & Anderson, R. S. (1998). Pleistocene relief production in Laramide mountain ranges, western United States. Geology, 26(2), 123–126.

Snyder, N. P., & Kammer, L. L. (2008). Dynamic adjustments in channel width in response to a forced diversion: Gower Gulch, Death Valley National Park, California. Geology, 36(2), 187–190. https://doi.org/10.1130/G24217A.1

Snyder, N. P., Whipple, K. X., Tucker, G. E., & Merritts, D. J. (2003). Channel response to tectonic forcing: Field analysis of stream mor- phology and hydrology in the Mendocino triple junction region, northern California. Geomorphology, 53(1–2), 97–127. https://doi. org/10.1016/S0169-555X(02)00349-5

Soulsby, R. L. (1981). Measurements of the Reynolds stress components close to a marine sand bank. Marine Geology. https://doi.org/10.1016/0025-3227(81)90157-2

Sukhodolov, A., Thiele, M., & Bungartz, H. (1998). Turbulence structure in a river reach with sand bed. Water Resources Research. https://doi.org/10.1029/98WR00269

Sukhodolov, A. N., Fedele, J. J., & Rhoads, B. L. (2006). Structure of flow over alluvial bedforms: An experiment on linking field and laboratory methods. Earth Surface Processes and Landforms. https://doi.org/10.1002/esp.1330

Stark, C. P. (2006). A self-regulating model of bedrock river channel geometry. Geophysical Research Letters, 33, L04402. https://doi.org/ 10.1029/2005GL023193

Stark, C. P., Barbour, J. R., Hayakawa, Y. S., Hattanji, T., Hovius, N., Chen, H., et al. (2010). The climatic signature of incised river meanders. Science, 327(5972), 1497–1501. https://doi.org/10.1126/science.1184406

Stock, J. D., Montgomery, D. R., Collins, B. D., Dietrich, W. E., & Sklar, L. (2005). Field measurements of incision rates following bedrock exposure: Implications for process controls on the long profiles of valleys cut by rivers and debris flows. Geological Society of America Bulletin, 117(1), 174. https://doi.org/10.1130/B25560.1

Tanaka, G., & Izumi, N. (2013). The bedload transport rate and hydraulic resistance in bedrock channels partly covered with gravel. Journal of Japan Society of Civil Engineers, Ser. B1 (Hydraulic Engineering), 69(4). https://doi.org/10.2208/jscejhe.69.i_1033

Tinkler, K. J. (1997). Rockbed wear at a flow convergence zone in Fifteen Mile Creek, Niagara Peninsula, Ontario. The Journal of Geology,105(2), 263–274. https://doi.org/10.1086/515918

Tomkin, J. H., Brandon, M. T., Pazzaglia, F. J., Barbour, J. R., & Willett, S. D. (2003). Quantitative testing of bedrock incision models for the Clearwater River, NW Washington State. Journal of Geophysical Research, 108(B6), 2308. https://doi.org/10.1029/2001JB000862

Tominaga, A., Nezu, I., Ezaki, K., & Nakagawa, H. (1989). Three-dimensional turbulent structure in straight open channel flows. Journal of Hydraulic Research. https://doi.org/10.1080/00221688909499249

Tucker, G. E., & Slingerland, R. (1996). Predicting sediment flux from fold and thrust belts. Basin Research, 8(3), 329–349. https://doi.org/ 10.1046/j.1365-2117.1996.00238.x

Tucker, G. E., & Slingerland, R. L. (1994). Erosional dynamics, flexural isostasy, and long-lived escarpments: A numerical modeling study. Journal of Geophysical Research, 99(B6), 12,229–12,243. https://doi.org/10.1029/94JB00320

Turowski, J. M. (2018). Alluvial cover controlling the width, slope and sinuosity of bedrock channels. Earth Surface Dynamics, 6(1), 29–48.https://doi.org/10.5194/esurf-6-29-2018

Turowski, J. M. (2020). Mass balance, grade, and adjustment timescales in bedrock channels. Earth Surface Dynamics, 8, 103–122. https://doi.org/10.5194/esurf-8-103-2020

Turowski, J. M., & Hodge, R. (2017). A probabilistic framework for the cover effect in bedrock erosion. Earth Surface Dynamics, 5(2), 311–330. https://doi.org/10.5194/esurf-5-311-2017

Turowski, J. M., Hovius, N., Hsieh, M. L., Lague, D., & Chen, M. C. (2008). Distribution of erosion across bedrock channels. Earth Surface Processes and Landforms, 33(3), 353–363. https://doi.org/10.1002/esp.1559

Turowski, J. M., Hovius, N., Wilson, A., & Horng, M.-J. (2008). Hydraulic geometry, river sediment and the definition of bedrock channels.Geomorphology, 99(1–4), 26–38. https://doi.org/10.1016/J.GEOMORPH.2007.10.001

Turowski, J. M., Lague, D., & Hovius, N. (2007). Cover effect in bedrock abrasion: A new derivation and its implications for the modeling of bedrock channel morphology. Journal of Geophysical Research, 112, F04006. https://doi.org/10.1029/2006JF000697

Turowski, J. M., Lague, D., & Hovius, N. (2009). Response of bedrock channel width to tectonic forcing: Insights from a numerical model, theoretical considerations, and comparison with field data. Journal of Geophysical Research, 114, F03016. https://doi.org/10.1029/ 2008JF001133

Vanoni, V. A., & Brooks, N. H. (1957). Laboratory studies of the roughness and suspended load of alluvial streams. California Institute of Technology.

Vassilicos, J. C. (2015). Dissipation in turbulent flows. Annual review of fluid mechanics, 47, 95–114. https://doi.org/10.1146/ANNUREV-FLUID-010814-014637

Venditti, J. G., Best, J. L., Church, M., & Hardy, R. J. (2013). Coherent Flow Structures at Earth's Surface. John Wiley & Sons.

Venditti, J., Fairweather, K., Kwoll, E., Wong, M., Lin, C., Rennie, C., & Church, M. (2020). Atlas of the Fraser canyons data archive. Federated Research Data Repository. https://doi.org/10.20383/101.0277

Venditti, J., Kwoll, E., Fairweather, K., Haught, D., Rennie, C., & Church, M. (2021). 2016 Fraser canyon survey data archive. Federated Re- search Data Repository. https://doi.org/10.20383/101.0280

Venditti, J. G., Li, T., Deal, E., Dingle, E., & Church, M. (2019). Struggles with stream power: Connecting theory across scales. Geomorphology. https://doi.org/10.1016/j.geomorph.2019.07.004

Venditti, J. G., Rennie, C. D., Bomhof, J., Bradley, R. W., Little, M., & Church, M. (2014). Flow in bedrock canyons. Nature, 513(7519), 534–537. https://doi.org/10.1038/nature13779

Wang, Y., Zhang, H., Zheng, D., Yu, J., Pang, J., & Ma, Y. (2017). Coupling slope-area analysis, integral approach and statistic tests to steady-state bedrock river profile analysis. Earth Surface Dynamics. https://doi.org/10.5194/esurf-5-145-2017

Whipple, K. X. (2004). Bedrock rivers and the geomorphology of active orogens. Annual Review of Earth and Planetary Sciences, 32, 151–185. https://doi.org/10.1146/annurev.earth.32.101802.120356

Whipple, K. X., DiBiase, R. A., & Crosby, B. T. (2013). Bedrock rivers. In Treatise on geomorphology (1st ed., pp. 550–573). https://doi. org/10.1016/B978-0-12-374739-6.00254-2

Whipple, K. X., Hancock, G. S., & Anderson, R. S. (2000). River incision into bedrock: Mechanics and relative efficacy of plucking, abrasion, and cavitation. Bulletin of the Geological Society of America, 112(3), 490–503. https://doi.org/10.1130/0016-7606(2000)112<490: RIIBMA>2.0.CO;2

Whipple, K. X., & Tucker, G. E. (1999). Dynamics of the stream-power river incision model: Implications for height limits of mountain ranges, landscape response timescales, and research needs. Journal of Geophysical Research, 104, (B8), 17,661–17,674. https://doi.org/ 10.1029/1999jb900120

Wilcock, P. R., & Crowe, J. C. (2003). Surface-based Transport Model for Mixed-Size Sediment. Journal of Hydraulic Engineering. https://doi.org/10.1061/(asce)0733-9429(2003)129:2(120)

Wilcock, P. R., Kenworthy, S. T., & Crowe, J. C. (2001). Experimental study of the transport of mixed sand and gravel. Water Resources Research, 37(12), 3349–3358. https://doi.org/10.1029/2001WR000683

Willett, S. D. (1999). Orogeny and orography: The effects of erosion on the structure of mountain belts. Journal of Geophysical Research, 104(B12), 28,957–28,981. https://doi.org/10.1029/1999JB900248

Willett, S. D., McCoy, S. W., Taylor Perron, J., Goren, L., & Chen, C. Y. (2014). Dynamic reorganization of River Basins. Science. https://doi.org/10.1126/science.1248765

Wobus, C. W., Kean, J. W., Tucker, G. E., & Anderson, R. S. (2008). Modeling the evolution of channel shape: Balancing computational efficiency with hydraulic fidelity. Journal of Geophysical Research, 113, F02004. https://doi.org/10.1029/2007JF000914

Wobus, C. W., Tucker, G. E., & Anderson, R. S. (2006). Self-formed bedrock channels. Geophysical Research Letters, 33, L18408. https://doi. org/10.1029/2006GL027182

Wohl, E. E. (1993). Bedrock channel incision along Piccaninny Creek, Australia. Journal of Geology, 101(6), 749–761. https://doi.org/ 10.1086/648272

Wohl, & E., E. (1998). Bedrock channel morphology in relation to erosional processes. GMS, 107, 133–151. https://doi.org/10.1029/GM107P0133

Wohl, E., & David, G. C. L. (2008). Consistency of scaling relations among bedrock and alluvial channels. Journal of Geophysical Research: Earth Surface, 113(F4). https://doi.org/10.1029/2008JF000989

Wohl, E. E., & Merritt, D. M. (2001). Bedrock channel morphology. Bulletin of the Geological Society of America, 113(9), 1205–1212. https:// doi.org/10.1130/0016-7606(2001)113<1205:BCM>2.0.CO;2

Wohl, E. E., Thompson, D. M., & Miller, A. J. (1999). Canyons with undulating walls (p. 2). Bulletin of the Geological Society of America. https:// doi.org/10.1130/0016-7606

Wright, M., Venditti, J. G., Li, T., Hurson, M., Chartrand, S., Rennie, C. D., & Church, M. (2022). Covariation in width and depth in bedrock rivers. Earth Surface Processes and Landforms. https://doi.org/10.1002/esp.5335

Yang, C. T. (1971). Potential energy and stream morphology. Water Resources Research. https://doi.org/10.1029/WR007i002p00311

Yang, R., Willett, S. D., & Goren, L. (2015). In situ low-relief landscape formation as a result of river network disruption. Nature. https://doi.org/10.1038/nature14354

Yanites, B. J. (2018). The dynamics of channel slope, width, and sediment in actively eroding bedrock river systems. Journal of Geophysical Research: Earth Surface, 123, 1504–1527. https://doi.org/10.1029/2017JF004405

Appendix A. Chapter 2 Supplementary Information

The supporting information describes the details of calculating the limits on impact positions in the process of estimating impact rates. We want to provide enough information for the reader to understand the model, and if necessary reproduce it.

Limits also exist on impact positions on both the downstream and upstream facing parts of the roughness elements. Bedload particles moving downstream cannot impact the downstream face of the roughness element below the tangent point (Figure 2.4) which has a central angle θ_d calculated from

$$\theta_d = \frac{\pi}{2} + \beta \ . \qquad \text{(Equation A.1)}$$

Whether a particle impacts the upstream facing part of the roughness element is controlled by the relation between the downstream distance of the potential impact position on the bed l_u and the distance between the center of the roughness element and the vertex of the upstream face of the successive downstream roughness element l_r (Figure 2.4)

$$l_u = \frac{r}{\sin\beta} \qquad \text{(Equation A.2)}$$

$$l_r = d - r \qquad \text{(Equation A.3)}$$

where r is the semi-circle radius cut along the roughness element in the downstream direction, which decreases from center line of the roughness element laterally. When l_u is equal or smaller than l_r ($l_u \leq l_r$), the downstream trajectory of bedload particles at the tangent line can impact on the bed directly (Figure 2.4). Therefore, the bedload particles can impact any positions on the upstream facing part of the roughness element. However, if $l_u > l_r$, the downstream trajectory of bedload particles at the tangent line is intercepted by the upstream facing part of the subsequent downstream roughness element instead of impacting on the bed.

Appendix B. Chapter 3 Supplementary Information

The supporting information describes the detailed equations of calculating the total projected area A_p from integrating the projected area on each slice of the deflector surface, and the lateral erosion rate on the adjacent wall E_{lpa} and the opposite wall E_{lpo} for bank-attached alluvium. We want to provide enough information for the reader to understand the model, and if necessary reproduce it.

The projected area A_p can be obtained by integrating the impact area on the plane that is parallel to the upward motion of saltation particles. It has been shown that only ¼ of the semi-spherical deflector surface that faces upstream and the wall closer to the deflector is effective at deflecting bedload particles toward the wall (Li et al., 2020). Therefore, we choose to integrate the impacts on ¼ of the semi-spherical deflector surface by dividing it into individual slices with a wall-normal interval of dr where each slice is parallel to the wall and is a semi-circle with a radius $r_s \in (0, D/2)$

$$r_s = \sqrt{(D/2)^2 - r'^2}. \qquad \text{(Equation B.1)}$$

where r' is the lateral distance between each slice of the deflector surface and the center of the deflector. r' is zero for the slice at the center of the deflector, increases as it moves towards the edge of the deflector and becomes $D/2$ for the slice at the edge of the deflector. The projected length L_s of the slice with radius r_s can be obtained from upward saltation length l_{su} and saltation height h_s using trigonometric functions

$$L_s = r_s\left(\frac{l_{su}}{h_s} + 0.5\right)\frac{2\sqrt{h_s^2 + l_{su}^2}}{3l_{su}}. \qquad \text{(Equation B.2)}$$

The projected area on each slice can be written as

$$A_s = L_s\, dr'. \qquad \text{(Equation B.3)}$$

Therefore, the total projected area A_p can be obtained by integrating the projected area on each slice

$$A_p = \int_0^{D/2} L_s \, dr = \left(\frac{l_{su}}{h_s} + \frac{1}{2}\right) \frac{2\sqrt{h_s^2 + l_{su}^2}}{3l_{su}} \int_0^{D/2} \sqrt{(D/2)^2 - r^2} \, dr'. \quad \text{(Equation B.4)}$$

Equation B.4 can then be solved by trigonometric substitution, leading to

$$A_p = \frac{\pi}{24} D^2 \left(\frac{l_{su}}{h_s} + \frac{1}{2}\right) \frac{\sqrt{h_s^2 + l_{su}^2}}{l_{su}}. \quad \text{(Equation B.5)}$$

For the erosion rate on the adjacent wall, the distance between the ith deflector and the adjacent wall $y_{pa}(i)$ can be determined from grain size D, using $D/2$ as the distance between the first deflector and the wall

$$y_{pa}(i) = \left(i - \frac{1}{2}\right) D, \quad \text{(Equation B.6)}$$

where $i = 1,2,3, \ldots, N_{pa}$, and $i = 1$ corresponds to the closest deflector to the wall and increases with increasing extent of alluvium. N_{pa} is the total number of deflectors that contribute to lateral erosion on the adjacent wall. N_{pa} increases with the fraction of alluvium F_a, until the distance between the furthest deflector and the adjacent wall y_a is bigger than y_{max} because the bedload particle impacts that are deflected by a deflector located from the wall further than y_{max} would be viscously damped, so

$$N_{pa} = \begin{cases} y_a/D, & \text{if } y_a \le y_{max} \\ y_{max}/D, & \text{otherwise} \end{cases}. \quad \text{(Equation B.7)}$$

where $y_a = WF_a = W\, q_s/q_t$, and W is the channel width.

The total erosion rate on the adjacent wall for bank-attached alluvium E_{lpa} is a sum of erosion rates caused by all deflections from 1 to N_{pa}, given as

$$E_{lpa} = \sum_{i=1}^{N_{pa}} \frac{\pi Y}{24 k_v \sigma_T^2} \frac{D^2}{dh_{max}} q_s \left(\frac{1}{h_s} + \frac{1}{2l_{su}}\right)(1 - n_z)\, v_0^2 e^{-2C_d y_{pa}(i)} \left(1 - (u^*/w_f)^2\right)^{1.5}.$$

(Equation B.8)

Equation B.8 can be solved from the sum of a geometric sequence with a common ratio of e^{-2C_dD} and a total number of N_{pa}

$$E_{lpa} = \begin{cases} \frac{\pi Y}{240 k_v \sigma_T^2} \frac{D}{h_{max}} q_s \left(\frac{1}{h_s} + \frac{1}{2l_{su}}\right) v_0^2 \frac{1-e^{-2C_d y_a}}{e^{C_d D} - e^{-C_d D}} (1-(u^*/w_f)^2)^{1.5} & \text{if } y_a < y_{max} \\ \frac{\pi Y}{240 k_v \sigma_T^2} \frac{D}{h_{max}} q_s \left(\frac{1}{h_s} + \frac{1}{2l_{su}}\right) v_0^2 \frac{1-e^{-2C_2 y_{max}}}{e^{C_d D} - e^{-C_d D}} (1-(u^*/w_f)^2)^{1.5} & \text{otherwise} \end{cases},$$

(Equation B.9)

As the alluvium extends from the adjacent wall to the opposite wall, the distance between the ith deflector and the opposite wall $y_{po}(i)$ can be treated as a mirror image of that between the deflector and the adjacent wall $y_{pa}(i)$, given as

$$y_{po}(i) = y_{max} - y_{pa}(i) = y_{max} - (i - \tfrac{1}{2})D, \qquad \text{(Equation B.10)}$$

where $i = 1,2,3,\ldots,N_{po}$, and $i = 1$ corresponds to the first deflector that can effectively deflect particle to erode the opposite wall and increases with increasing extent of alluvium. N_{po} is the total number of deflectors that contribute to erosion on the opposite wall. N_{po} is zero when the distance between the furthest deflector to the opposite wall y_o is larger than y_{max}, and can be determined from the distance between the furthest deflector to the opposite wall y_o and the maximum distance y_{max} when $y_o \le y_{max}$

$$N_{po} = \begin{cases} 0, & \text{if } y_o > y_{max} \\ (y_{max} - y_o)/D, & \text{otherwise} \end{cases}. \qquad \text{(Equation B.11)}$$

The total erosion rate on the opposite wall for bank-attached alluvium E_{lpo} is a sum of erosion rates caused by all deflections from 1 to N_{po}, given as

$$E_{lpo} = \sum_{i=1}^{N_{po}} \frac{\pi Y}{24 k_v \sigma_T^2} \frac{D^2}{d h_{max}} q_s \left(\frac{1}{h_s} + \frac{1}{2l_{su}}\right)(1-n_z)\, v_0^2 e^{-2C_d y_{po}(i)} (1-(u^*/w_f)^2)^{1.5}.$$

(Equation B.12)

Equation B.12 can be solved from the sum of a geometric sequence with a common ratio of e^{-2C_dD} and a total number of N_{po}

$$E_{lpo} = \begin{cases} 0; & \text{if } y_o > y_{max} \\ \frac{\pi Y}{240 k_v \sigma_T^2} \frac{D}{h_{max}} q_s \left(\frac{1}{h_s} + \frac{1}{2 l_{su}}\right) v_0^2 \frac{e^{-2C_d y_o} - e^{-2C_d y_{max}}}{e^{C_d D} - e^{-C_d D}} (1 - (u^*/w_f)^2)^{1.5} & \text{otherwise} \end{cases}$$

(Equation B.13)

where $y_o = W - y_a$.

Appendix C. Chapter 6 Extended Data

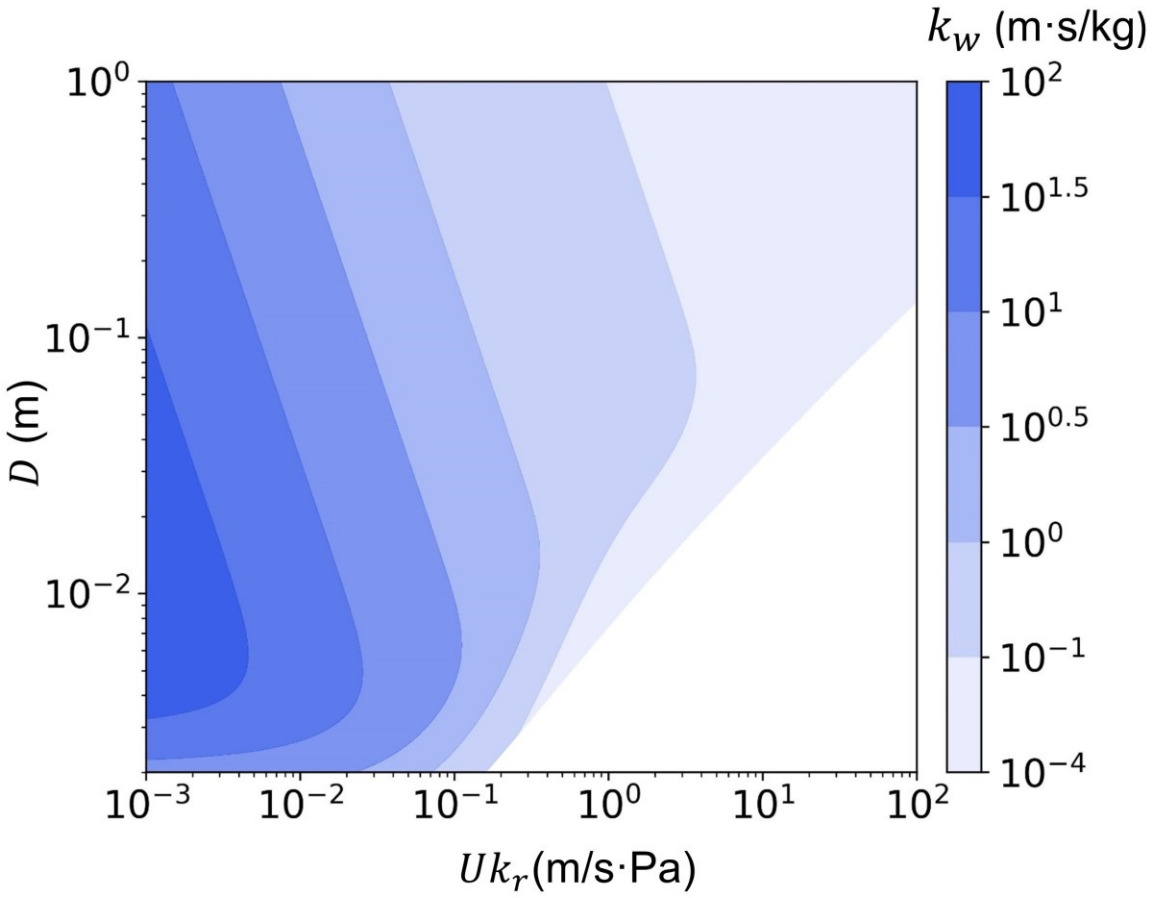

Extended Data Figure C.1. Contours of the ratio of width to sediment supply k_w as a function of D and Uk_r derived from multiple nonlinear regression

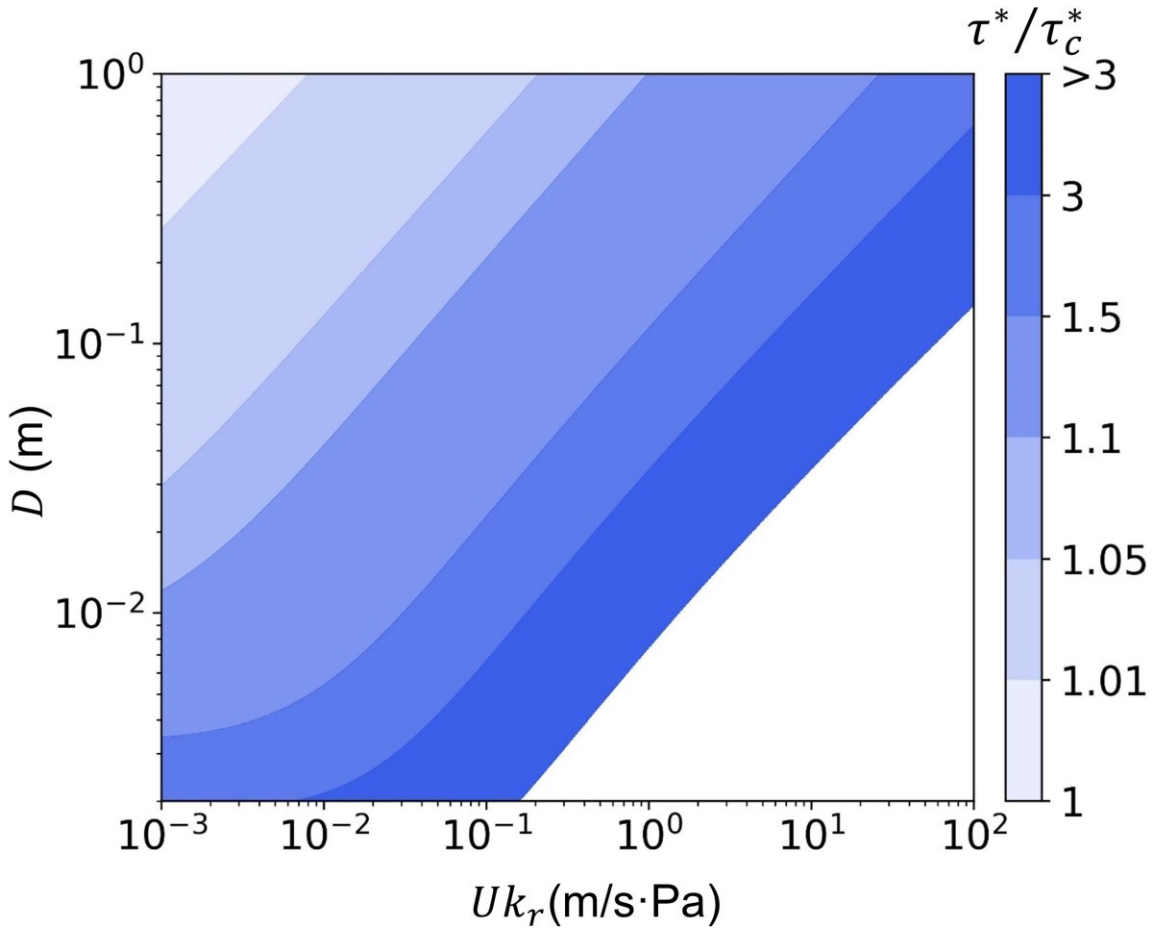

Extended Data Figure C.2. Contours of transport stage τ^*/τ_c^* as a function of D and Uk_r derived from multiple nonlinear regression.

Extended Data Table C.1 Reference Site Values and Model Predictions for South Fork Eel River, Boulder Creek, and Black Canyon.

Variable	South Fork Eel River	Black Canyon	Boulder Creek	
Bedload particle size D (m)	0.06	0.195	0.02	0.22
Sediment supply Q_s (kg/s)	42.6	70	39	145
Discharge (m^3/s)	39.1	7000	59	74
Measured/Predicted width W (m)	18.0/20.2	106/88.7	4.5/4.82	9.6/19.9
Measured/Predicted slope S	0.0053/0.0065	0.001/0.0008	0.007/0.007	0.019/0.015
Fraction of time that bedload occurs k_t	0.0437	0.145	0.00274	0.00274
Critical Shields stress τ_c^*	0.03	0.03	0.03	0.03
Water density ρ_w(kg/m^3)	1000	1000	1000	1000
Sediment density ρ_s (kg/m^3)	2650	2650	2650	2650
Rock strength parameter k_r (Pa)	9.8×10^8	9.8×10^8	9.8×10^8	9.8×10^8